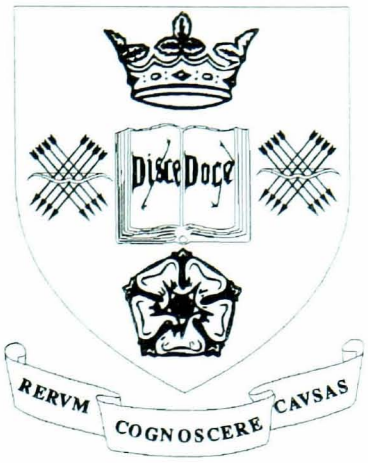

WAVELET BUMP EXTRACTION (WBE) FOR EDITING VARIABLE AMPLITUDE FATIGUE LOADINGS

SHAHRUM ABDULLAH

A thesis submitted for the degree of Doctor of Philosophy

Department of Mechanical Engineering
The University of Sheffield
United Kingdom

July 2005

In memory of my beloved father,

ABDULLAH ABD RAHMAN,

Who left this world on 20th August 2004.

CONTENT

ACKNOWLEDGEMENTS

I would like to convey my greatest gratitude to Professor John R. Yates and Dr. Joseph A. Giacomin for supervising me towards the completion of the Ph.D. degree at The University Of Sheffield, United Kingdom. This special gratitude is also dedicated to Universiti Kebangsaan Malaysia and The Malaysian Government for sponsoring me during the period of Ph.D. programme.

My thanks also for Dr. Paul Wilkinson of Leyland Technical Centre (United Kingdom), Dr. Christoph Leser of Society of Automotive Engineers Fatigue Design and Evaluation (United States of America), Professor David L. DuQuesnay of Royal Military College of Canada, Department of Mechanical Engineering (The University Of Sheffield), Marco Ajovalasit and all my friends for their contributions and supports.

My special thanks are dedicated to my mother and my late father for their everlasting love. I believe not to have enough time to repay all the love they have provided. The most special thanks are dedicated to my lovely wife (Rahimah Hamdan) and son (Imran Hakim Shahrum) for their love, patience and supports during the period of my studies. Finally, thank you to all my brothers and sisters in Malaysia.

Shahrum Abdullah
Department of Mechanical and Materials Engineering
Universiti Kebangsaan Malaysia
43600 UKM Bangi, Selangor
MALAYSIA
+60-3-89216511
Email: shahrum@vlsi.eng.ukm.my or mcabdul@yahoo.com

Nomenclature

a	Wavelet scale
A	Material constant for the ESD strain-life model [MPa]
A_k	Amplitude of power spectral density
b	Fatigue strength exponent
b'	Wavelet translation step
B	Material constant for the ESD strain-life model
c	Fatigue ductility component
$C.F.$	Crest factor
$C1$	Percentage level for determining initial trigger level value in a wavelet group [%]
$C2$	Percentage level for determining the trigger level decrement step [%]
D	Fatigue damage parameter
D_i	Fatigue damage for one cycle
D_T	Total fatigue damage per block
$D1$	Percentage difference in the root-mean-square value between the original and mission signals [%]
$D2$	Percentage difference in the kurtosis value between the original and mission signals [%]
E	Modulus of elasticity [MPa]
f_0	Cyclic frequency [Hz]
f_k	The harmonic frequency [Hz]
$G(f)$	r.m.s. value is the function of PSD of the input signal
H	Material constant in the Ramberg-Osgood relationship [MPa]
$H(f)$	Stress response function
j	Number of point in time series
k	Number of iteration in discrete Fourier transform
K	Kurtosis
KD	Percentage level of target acceptable range for kurtosis [%]
K_f	Fatigue notch factor
K_t	Stress concentration factor
m	Material constant for a stress decay process of the ESD model

$maxg_i$	Maximum amplitude in a wavelet group [microstrain]
n	Number of data points
n'	Strain hardening exponent
N	Number of samples in time series
N_f	Fatigue life [Number of cycles or blocks to failure]
N_{fi}	Number of constant amplitude cycles to failure
N_i	Number of applied cycles
N_T	Number of blocks to failure
q	Notch sensitivity factor
r.m.s.	Root-mean-square [microstrain]
RD	Percentage level of target acceptable range for root-mean-square [%]
S	Skewness
$S(f_k)$	Underlying PSD of the Gaussian signal
S_{cu}	*C*urrent opening stress [MPa]
SD	Standard deviation [microstrain]
S_e	Fatigue limit or endurance limit of a material [MPa]
$S_{e(notched)}$	Fatigue limit or endurance limit of a notched material [MPa]
$S_{e(smooth)}$	Fatigue limit or endurance limit of a smooth material [MPa]
S_i	Intrinsic stress limit under VA loading [MPa]
S_{max}	Maximum stress amplitude [MPa]
S_{min}	Minimum stress amplitude [MPa]
S_{op}	Crack opening stress [MPa]
S_{ss}	Steady-state opening stress [MPa]
S_u	Ultimate strength of a material [MPa]
S_y	Yield strength of a material [MPa]
S_y	0.2% static yield strength [MPa]
t	Time [seconds]
T_p	Period [seconds]
$W_\psi(a,b')$	Wavelet coefficients for continuous wavelet transform
$W_\psi(m,n)$	Wavelet coefficients for discrete wavelet transform
$\bar{x}$	Mean value [mm, microstrain, etc.]

x_j	Instantaneous value in time series [mm, microstrain, etc.]
x_{jmax}	Maximum instantaneous value in time series [mm, microstrain, etc.]
$x(t)$	Instantaneous value at time t [mm, microstrain, etc.]
X_k	Amplitude of discrete Fourier transform
X	Amplitude
$X(\omega)$	Amplitude of Fourier transform in frequency distribution
α	Material constant for steady state opening stress equation
α'	Material constant having dimensions of length for notch sensitivity equation
β	Material constant for steady state opening stress equation
β'	Material constant having dimensions of length for notch sensitivity equation
Δf	Frequency interval in frequency domain [Hz]
$\Delta\varepsilon^*$	Net effective strain range for a closed hysteresis loop related to fatigue crack growth
$\Delta\varepsilon_{eff}$	Effective strain range
$\Delta\sigma$	Stress range [MPa]
ε'_f	Fatigue ductility coefficient
ε_a	Total strain amplitude
ε_{ea}	Elastic strain amplitude
ε_i	Intrinsic strain fatigue limit under VA loading
ε_{op}	Crack opening strain
ε_{pa}	Plastic strain amplitude
ρ	Notch tip radius [mm]
σ	Stress [MPa]
σ_a	Stress amplitude [MPa]
σ'_f	Fatigue strength coefficient and
σ_{max}	Maximum stress [MPa]
σ_{min}	Minimum stress [MPa]
$\psi(t)$	Wavelets
$\psi_{a,b}(t)$	Scaled wavelets

ψ^*	Complex conjugate of ψ
ω	Angular frequency [rad/s]

ARMA	Autoregressive and Moving Average
ASTM	American Society for Testing and Materials
BS	British Standards
BS1	The original order sequence of the bump segments in a mission signal
BS2	Bump segment sequences in a mission signal ordered from the highest expected fatigue damage to the lowest
BS3	Bump segment sequences in a mission signal ordered from the lowest expected fatigue damage to the highest
BT	Linear summation of fatigue damage for all bump segments
CA	Constant amplitude
CWT	Continuous wavelet transform
DFT	Discrete Fourier transform
DWT	Discrete wavelet transform
ESD	Effective Strain Damage
FFT	Fast Fourier transform
HCF	High-cycle-fatigue
IDFT	Inverse Discrete Fourier transform
IFFT	Inverse Fast Fourier transform
LCF	Low-cycle-fatigue
LSB	Log skidder bending
LTC	Leyland Technical Centre, United Kingdom
MNMS	Mildly Nonstationary Mission Synthesis
OL	Overload stress/strain
OL/UL	Overload followed by underload stress/strain
OWT	Orthogonal wavelet transform
PSD	Power spectral density
PV	Peak-valley
SAE	Society of Automotive Engineers
SAEFDE	Society of Automotive Engineers Fatigue Design and Evaluation

S-N	Stress-life
STFT	Short time Fourier transform
SWT	Smith-Watson-Topper
T1	Sinusoidal synthetic test signal
T2	Random synthetic test signal
T3	Experimental test signal measured on public road
T4	Experimental test signal measured on pavé test track having tensile mean strain loading
T5	Experimental test signal measured on pavé test track having compressive mean strain loading
T6	Experimental test signal measured on manoeuvre proving ground
TCFD	Time Correlated Fatigue Damage
TiBSj	Mission signal with a particular bump segment sequences (i denotes number of test signal, i = 1,2, ...,6; j denotes bump segment sequences, j = 1,2,3)
UL	Underload stress/strain
VA	Variable amplitude
WBE	Wavelet Bump Extraction

LIST OF FIGURES

LIST OF TABLES

SUMMARY

In durability testing of automobiles, load histories collected for laboratory testing are often lengthy in time. Therefore, a fatigue data editing technique is needed to summarise the load history. A fatigue mission synthesis algorithm, called Wavelet Bump Extraction (WBE) preserves the original load cycle sequences has been developed. The basis of WBE is to identify the important features or bumps that cause the majority of the fatigue damage. Bumps are identified in the frequency bands of the load spectrum using an orthogonal wavelet transform. Bumps are then extracted and combined to produce a mission signal with an equivalent fatigue damage as the original signal.

The WBE validation was performed by analysing the cycle sequence effects in variable amplitude (VA) loadings. The experimental fatigue lives of the shortened VA loadings (Choi 2004) were compared to those predicted using strain-life fatigue damage models, i.e. Coffin-Manson, Morrow, Smith-Watson-Topper and Effective Strain Damage (ESD). The smallest difference was found between the experiment and ESD model, suggesting it is a suitable model for the use with WBE. Comparison between WBE and the time domain fatigue data editing was also conducted in order to observe its effectiveness for accelerated fatigue tests. Moreover, it is useful to evaluate the fatigue life of the original and mission signals by means of fatigue damage preservation in the mission signal. Finally, an analysis of the bump segments sequence effects was performed in order to determine an appropriate mission signal for accelerated fatigue tests.

The WBE algorithm showed a substantial compression of the VA loadings could be achieved whilst maintaining fatigue damage and the important load sequences. The ability of the WBE algorithm to shorten fatigue loadings would be expected to prove useful in accelerated fatigue testing of automobiles. Finally, the combination of WBE and ESD provides a novel application of the wavelet-based fatigue data editing.

CHAPTER 1

1. Introduction

1.1 Fatigue Design

In engineering there is a type of failure which is caused by the repeated loading of machine components and structures. Such loads cause cyclic stresses that can produce microscopic physical damage to the components. Even at stresses below a given material's ultimate strength, this microscopic damage can accumulate with continued cycling until it develops into a crack that leads to the failure of the component. Failure due to this type of loading is called fatigue.

Fatigue is a highly localised phenomenon that depends on the stresses and strains experienced in critical regions of a component or structure. Mechanical failures due to fatigue have been the subject of durability research for more than 150 years (Mann 1967). Historically, an early fatigue study was performed by W.A.J. Albert in 1829 and the term *fatigue* was first used in 1839 in a book by P.V. Poncelet of France. A well-known study was performed by Wöhler (1860) in which railway axles made of several metals were tested under bending, torsion and axial loads. Wöhler demonstrated that fatigue failure was not only a consequence of cyclic loads, but was also affected by mean stresses.

Research has shown that about 50% of mechanical failures can be attributed to fatigue (Fuchs and Stephens 1980). The economic costs of fracture and its prevention are large, estimating 80% of these costs involve cyclic loading and fatigue failure situations (Dowling 1999). Such statistics provide motivation for improvements in fatigue design, and several guidelines are routinely considered during the design of mechanical components or structures:

1. The elimination or reduction of stress raisers by streamlining the part to produce smooth surfaces;
2. The avoidance of sharp surfaces that might result from punching, stamping, shearing, or similar manufacturing processes;
3. The prevention of the development of surface discontinuities during processing;
4. The reduction or elimination of tensile residual stresses that are caused by manufacturing processes;

1.2 Durability Analysis

Automotive industries increasingly seek to reduce development times while simultaneously achieving higher quality levels for their vehicles (Lin and Heyes 1999). One of the essential elements to achieve these targets is durability analysis. By definition, durability is the capacity of an item to survive its intended use for a suitably long period of time. Therefore, good durability minimises the cost of maintaining and replacing the item, the prevention of failures and the optimisation of automobile or component design (Dowling 1999; Palma and Martins 2004).

Procedures used by the automobile industry for performing fatigue design are continually evolving (Dabell 1997). The main task performed during durability analysis is the fatigue life assessment of components such as engine parts, suspension parts and body structures (Bignonnet 1999). Automotive manufacturers have made large investments in this area so as to achieve products which meet a specified fatigue life target (Smith 1999a).

Figure 1.1 shows the relationship between the elements involved in the durability analysis, as defined by Landgraf (1987). As shown in Figure 1.1, component geometry, service loads and materials properties were identified as the inputs for performing a durability analysis.

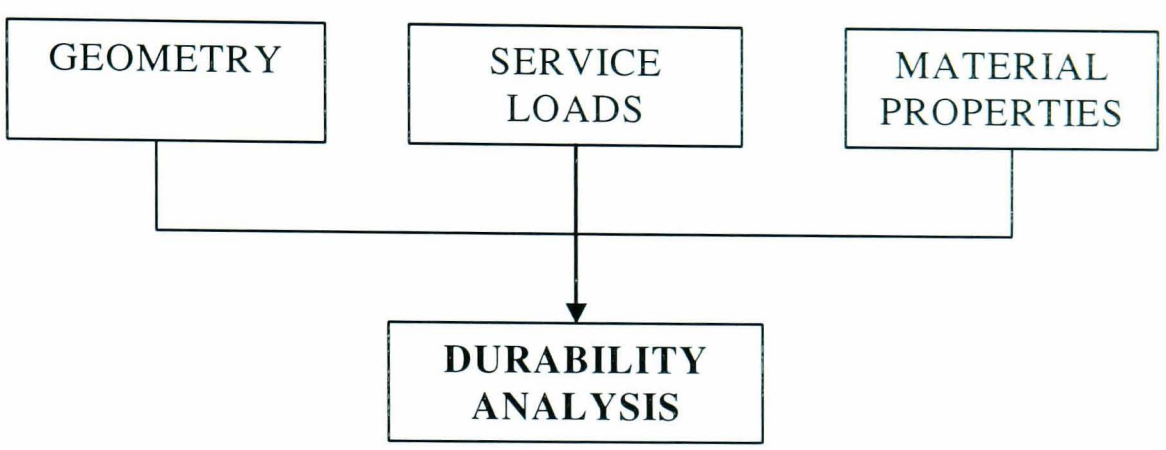

Figure 1.1: Inputs to the durability analysis process (Adapted from Landgraf 1987).

The first required input is the geometry of the automobile component, which is needed so that the component can be fabricated from a specific material and properly fixed to the testing machine. The second type of input consists of the service loads, which are measured on the automobile component while either a physical or numerical simulation prototype automobile is driven over reference road surfaces. In this context, load or loading is used as a generic term to indicate the parameters used in the fatigue data measurement such as forces, movements, strains or stresses. The experimentally measured service loads normally exhibit a variable amplitude pattern and are lengthy in time. Such service loads are generally considered to constitute a variable amplitude (VA) loading. A VA loading is defined as a cyclic load that oscillates between varying maximum and minimum stress amplitudes and these amplitudes changed in an irregular manner (Dowling 1999). Another loading type is constant amplitude (CA) loading, which involves cycles which oscillates between fixed maximum and minimum stress amplitudes (Dowling 1999). Most of the automobile service loads that have been reported in the literature, however, have had the pattern of VA loadings (Fuchs and Stephens 1980; Fatemi and Yang 1998).

Finally, material properties data are used together with the service loads and specimen geometry in order to perform a damage analysis of the component (Landgraf 1987). In the case of durability analysis performed by means of fatigue damage prediction, the properties of a material can be obtained from tensile tests and cyclic tests. By performing tensile tests (BS 10002-1 2001), several parameters can be obtained such as the modulus of elasticity, the ultimate strength, the yield strength, the hardness of material, etc. Such parameters are known as monotonic mechanical properties (Dowling 1999). Using cyclic tests (ASTM E739-91 1988), the mechanical properties which can be determined include the fatigue strength coefficient, the fatigue strength exponent, the fatigue ductility coefficient and the fatigue ductility exponent.

Using the three types of input data, several engineering activities are performed to complete the durability analysis of an automobile. Figure 1.2 lists the three principal activities as defined by Landgraf (1987). Computer modelling is performed using fatigue analysis software codes which can estimate failure life based on component geometry, loading and material properties (Lee *et al.* 1995). Laboratory testing of components is also performed in order to determine the deformation and failure life under a given service load. Road testing of prototype automobiles is also performed by driving them over reference surfaces so as to obtain experimentally measured durability data. Finally, the fatigue life results obtained by means of computer modelling and laboratory testing can be compared.

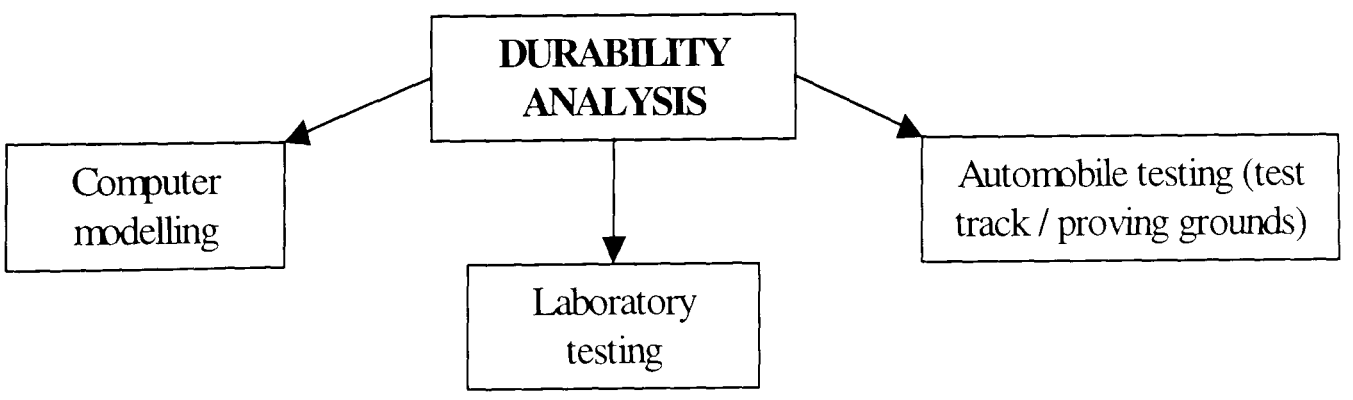

Figure 1.2: Durability analysis activities (Adapted from Landgraf 1987).

1.3 Fatigue Data Editing for Accelerated Fatigue Tests

Durability analysis requires knowledge of service loads since these loads are used for the laboratory testing of the component (Ridder *et al.* 1993; Goswani 1997). The required service loads have traditionally been obtained by testing a prototype automobile, or at least a similar automobile, over reference road surfaces (either proving ground surfaces or public roads). More recently it has also become possible to estimate service loads for the component by means of multi-body dynamics analysis (Shabana 1998)

The objective of laboratory based accelerated testing is to expose the component or the complete automobile to a test loading which is much shorter than the target loading, but which has approximately the same damage potential. Three techniques are used to accelerate laboratory fatigue testing (Frost *et al.* 1974): to increase the frequency of the cyclic loading; to increase the load level; and to remove small amplitude cycles from the time history.

Increasing the frequency of the cyclic loading is one of the alternative solutions for achieving an accelerated fatigue test. For a simple component, changes in loading frequency can be made on the basis that frequency has minimal effect on component fatigue strength. This is often not the case, however, when testing complex structures since the changes in frequency may lead to a resonance being excited (Frost *et al.* 1974).

In the second approach, automobile manufacturers tend to increase load levels by scaling up the service load by a constant value. Using this approach, the fatigue limit of the edited loading can be found at shorter fatigue life compared to the original loading fatigue limit (Frost *et al.* 1974). Therefore, the test of automobile components can be accelerated using the edited loading that has shorter fatigue life. By definition, the fatigue limit is the limiting value of the fatigue strength as fatigue life becomes very

large, for example at approximately 10^6 cycles for steel (Dowling 1999). Fatigue strength is a stress value that is determined at a particular fatigue life as determined from stress-life diagram. Finally, the fatigue life is defined as the number of cycles of stress or strain that a given specimen sustains before failure (Fuchs and Stephens 1980).

The final approach for performing the accelerated fatigue testing is to apply a method to the input VA fatigue loading by removing small amplitude cycles (Frost *et al.* 1974). Such a technique is known as fatigue data editing, which is defined as a method for omitting the small amplitude cycles which provide a minimal contribution to the overall fatigue damage, whilst retaining the high amplitude cycles which are the most damaging sections. In automotive applications, this concept is today often applied for the purpose of achieving accelerated fatigue tests which shorten the total test time required (Rotem 1981; Leese and Mullin 1991). Without editing the service load before performing the tests, test time and cost can become prohibitive.

Using the fatigue data editing approach, large amplitude cycles that cause the majority of the damage are retained and a shortened loading consisting of large amplitude cycles is produced (Conle and Topper 1979; Conle *et al.* 1997). The concept of accelerating a test by removing non-damaging events is distinctly different from the previous two approaches (Leese and Mullin 1991). Using both the previous approaches, the original VA loading is not compressed, so that the edited loading will have the same time length as the original loading. The last approach achieves test acceleration by considering less than the complete set of VA loadings since only a subset of the loading is required to produce the same amount of damage.

Early fatigue data editing research was performed by Conle and Topper (1979) with the small cycle omission procedure using strain loading. In this method, the local strain approach and the linear damage rule were used to select the omission levels. There were three criteria of strain ranges to select the edit levels: the sequential strain ranges with the application of peak-valley (PV) and damage histogram ranges; the rainflow counted strain ranges; and the mean stress parameters. For defining the term of peak-

valley, a peak is a change in the slope from positive to negative, and a valley is a change in the slope from negative to positive (Pompetzki 1993). Evaluation of the criteria was carried out by estimating the amount of fatigue damage generated by each amplitude level of the original history, selecting several strain range levels for history editing and then comparing the amount of damage reduction predicted by each criterion with actual fatigue test results. However, it is apparent that when high overall strain levels are encountered in the total record of the VA loading, great care should be taken to eliminate smaller cycles. A similar technique was performed by Conle and Topper (1980) to edit VA loading but using lower overall strain levels in order to omit smaller cycles. The fatigue damage results obtained from this study indicate the presence of an overstrain effect is much larger than the previous work by Conle and Topper (1997).

A study by Heuler and Seeger (1986) using the aircraft service loading showed the small cycles were omitted from the original loading according to the fatigue limit criteria. In this study, any small cycles with the stress below 50% of the materials CA fatigue limit were found to be allowable levels to be omitted. This omission levels was applicable in the fatigue tests using smooth steel and notched aluminium specimens. Using this approach, the total life for smooth specimen (steel) and for notched specimen (aluminium) was increased by 10-30% and 30-70%, respectively. The omission level, which is 50% of the CA fatigue limit, was chosen as a fraction of the maximum load range because of simplicity and convenience. For producing an accurate fatigue damage result, however, this fatigue data editing method is not appropriate for VA fatigue loadings.

Other fatigue data editing analysis involving the concept of PV reversals conducted by Gunger and Stephens (1995) and Stephens *et al.* (1997). In these studies, the Society of Automotive Engineers Fatigue Design and Evaluation (SAEFDE) committee log skidder bending (LSB) loading was selected due to a large number of small cycles in the total record length. The combination of strain amplitude and mean obtained from the formulation of the Smith-Watson-Topper (SWT) strain-life model was used in order to produce an omission level to remove the small cycles. Using this approach, the PV

domain was used to edit the PV service history where all SWT parameter cycles less than the omission level were removed. This PV editing method showed that almost 90% of the fatigue damage was retained in the edited signal while 89% of the history length was removed.

Research by El-Ratal *et al.* (2002) discussed the application of time correlated damage analysis for time domain fatigue data editing by using the nSoft® software package. Using this approach, the analysed VA loading that was measured from automobile suspension was divided into many small windows and the fatigue damage for each window was calculated. Sections with significant fatigue damage that contained high amplitude cycles were retained. On the other hand, sections with minimal fatigue damage that contained small amplitude cycles were removed. High amplitude sections were then assembled using the available windows joining function of the software. In order to validate the fatigue data editing approach, the authors performed laboratory fatigue tests using a full automobile suspension system. By applying several VA loadings (obtained from a 'potholes and bumps' test surface) to this suspension system, the test was accelerated from eleven days to two days.

The application of the wavelet transform was rarely used for the fatigue data editing technique. The wavelet transform is defined as the mathematical transformation in the time-scale domain and it is a significant tool for presenting local features of a signal. In this type of transform, the data is moved from a space to a scale domain by using wavelets as a basic function in order to provide the localised features of the original signal. This approach was initially performed by Oh (2001) with the application using a VA loading measured on a light railway train component. The author used the wavelet transform for the spike removal and de-noising a contaminated signal in order to compress the light railway VA fatigue loading. In this case approximately 80% of the fatigue damage was retained in the edited signal while 71% reduction in the record length.

Another wavelet-based approach in data editing is the Mildly Nonstationary Mission Synthesis (MNMS) algorithm which was developed by Giacomin *et al.* (1999; 2000; 2001) for performing mission synthesis of vibration of stimuli in comfort applications. The application of MNMS for the fatigue data editing (Abdullah *et al.* 2004) produced statistically accurate fatigue missions when the original signal was substantially shortened. Using this approach, the VA loading was compressed by up to 10 times to produce the edited loading. In terms of fatigue damage potential, however, the edited VA loadings did not have similar fatigue damage as the unedited loading.

For all the fatigue data editing techniques discussed in this section, different VA loadings were used for different techniques. There seem to be no generally agreed rules that clarify which method is the best, or what amplitude should be chosen for load omission (Wang and Chen 1999; Yan *et al.* 2001). Practically, any fatigue data editing technique must reduce the testing period and be technically valid.

1.4 Research Objectives

1.4.1 The Research Topic

Road vehicle manufacturers go to great lengths to measure loadings under a variety of driving conditions. Accelerated fatigue testing is often accomplished by correlating the damage produced by specific test tracks with the damage produced by public roads. Severe, short duration, test tracks are used instead of longer public roads. Testing is often further accelerated by use of a fatigue data editing technique which retains the high amplitude cycles that produce the majority of damage. The need to reduce development time while simultaneously improving confidence in the durability analysis means that it is of interest to investigate the issue of fatigue loading compression. Such a method to summarise VA loadings measured on the automobile component whilst preserving the local load-time cycle sequences is the subject of this thesis.

A new fatigue data editing technique and algorithm, based on a wavelet-based approach has been developed. The algorithm was designed to identify and extract fatigue damaging events, or high amplitude segments, from a VA loading of the type commonly encountered when designing automobile components. The extracted segments are combined to produce a shortened signal which is called a mission signal. The mission signal is a complete signal with shorter time length, but it has equivalent global signal statistics and fatigue damage as the original signal. This algorithm was developed based on the MNMS algorithm that was previously applied for the vibrational comfort studies by Giacomin *et al.* (1999; 2000; 2001), Grainger (2001) and Steinwolf *et al.* (2002).

The research described in this thesis was motivated by the author's belief that the wavelet transform is a suitable method for use in fatigue data editing. Since VA fatigue loadings normally exhibit nonstationary signal behaviour, wavelet time-scale analysis would be expected to be a natural choice of analysis method. With this approach the fatigue loading sections that produce the majority of damage can be identified based on the concept of time-frequency localisation. According to the author's readings and knowledge, no fatigue data editing technique uses the wavelet transform for the identification and extraction of fatigue damaging events.

1.4.2 The Specific Research Objectives

Based on the related background and research overview, the main objective of the Ph.D. research is *to develop a fatigue data editing technique involving a wavelet-based approach.* In order to achieve this objective, several secondary objectives had to be accomplished:

- Perform a literature review in order to find the available fatigue data editing techniques in various domains;

- Find a suitable strain-life fatigue damage model for VA loadings which considers cycle sequence effects;

- Validate the accuracy of the chosen strain-life model by means of laboratory fatigue tests;

- Evaluate the suitability for purposes of fatigue data editing of a mission synthesis algorithm, first developed for use in the area of human vibrational comfort, known as Mildly Nonstationary Mission Synthesis (MNMS);

- Develop a new wavelet-based fatigue data editing algorithm which would be able to identify and extract the damaging sections from the original fatigue loading;

- Evaluate the effectiveness of the algorithm at shortening several VA fatigue loadings, and quantify the retained damage by means of computational analysis;

- Validate the effectiveness of the fatigue data editing algorithm by means of laboratory fatigue tests.

Some of the questions which the research sought to answer were the following:

- What is the suitable fatigue damage model to calculate the fatigue life of a component under VA loadings?

- What is the most appropriate method to edit VA fatigue loadings for the purpose of accelerated fatigue tests?

- Can a new algorithm be developed to improve the accuracy of fatigue data editing with respect to existing techniques?

- What are the main factors that influence the identification of fatigue damaging events in the new algorithm?

- How important are the sequence effects of fatigue cycles and fatigue damaging events to the fatigue life prediction?

- Are the mission signals produced by the new fatigue data editing algorithm suitable for accelerated fatigue testing of vehicle components?

The author hopes that this thesis clarifies some of the above listed questions and that it accurately describes the wavelet-based fatigue data editing algorithm that was developed.

CHAPTER 2

2. Review of Concepts and Approaches

Since in automotive applications the road load data sets are typically nonstationary in their statistics, discussion is dedicated to the definition of the possible signal types and to the influence of signal type on the choice of signal processing method. In addition, the theoretical background behind fatigue life prediction is also presented in this section.

2.1 Signal Analysis

A signal is a series of numbers that come from measurement, typically obtained using some recording method as a function of time (Meyer 1993). In the case of fatigue analysis, the signal consists of a measurement of the cyclic loads, i.e. force, strain and stress against time. A time series typically consists of a set of observations of a variable taken at equally spaced intervals of time (Harvey 1981). Today, most experimental measurements, or data samples, are performed digitally. A signal is normally measured using an analogue-to-digital converter, so as to produce an experimental signal at a series of regularly spaced times as shown in Figure 2.1. This form of time history is known as a discrete time series, which is formed as a function of time. The objective of time series analysis is to determine the statistical characteristics of the original function by manipulating the series of discrete numbers (Newland 1993).

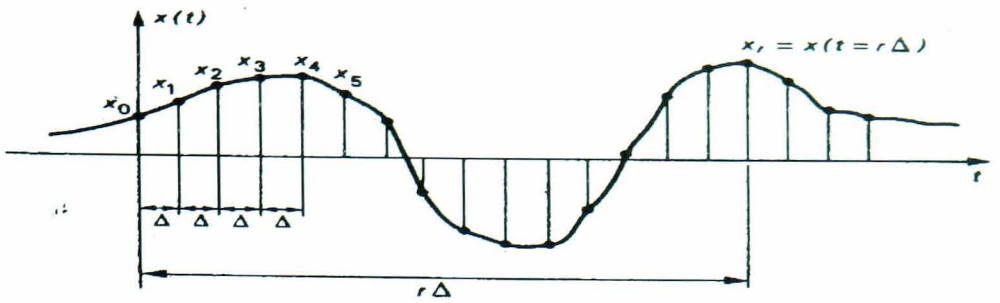

Figure 2.1: Sampling a continuous function of time at regular intervals (Reproduced from Newland 1993).

A signal can also be related to a probability distribution, and one example of the signal distribution is Gaussian or normal. It is an interesting fact of life that many naturally occurring random vibrations have the Gaussian distribution or the well known bell-shaped distribution as illustrated in Figure 2.2 (Newland 1993). The mathematical equation of the Gaussian distribution is given by

$$p(x) = \frac{1}{\sqrt{2\pi}(SD)} \exp^{-(x-\bar{x})^2/2(SD)^2} \tag{2.1}$$

where *p(x)* is probability density function of Gaussian Distribution, *SD* is the standard deviation value, *x* is the instantaneous value and $\bar{x}$ is the mean value. The function is symmetric about the mean, it gains its maximum value at the mean and the minimum value is at plus and minus infinity.

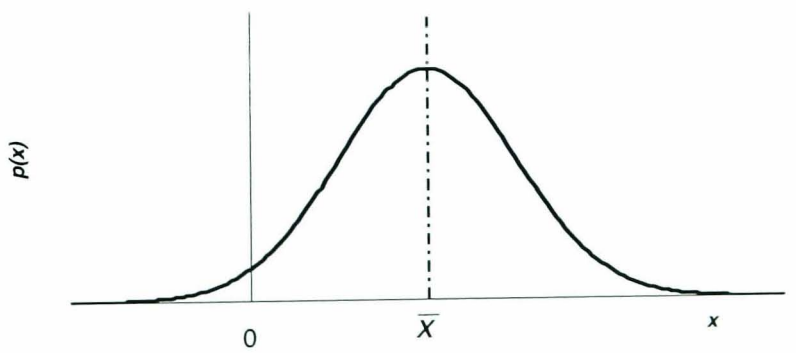

Figure 2.2: The Gaussian distribution.

2.1.1 Signal Types

Signals can be divided into two main categories as shown in Figure 2.3: deterministic and nondeterministic.

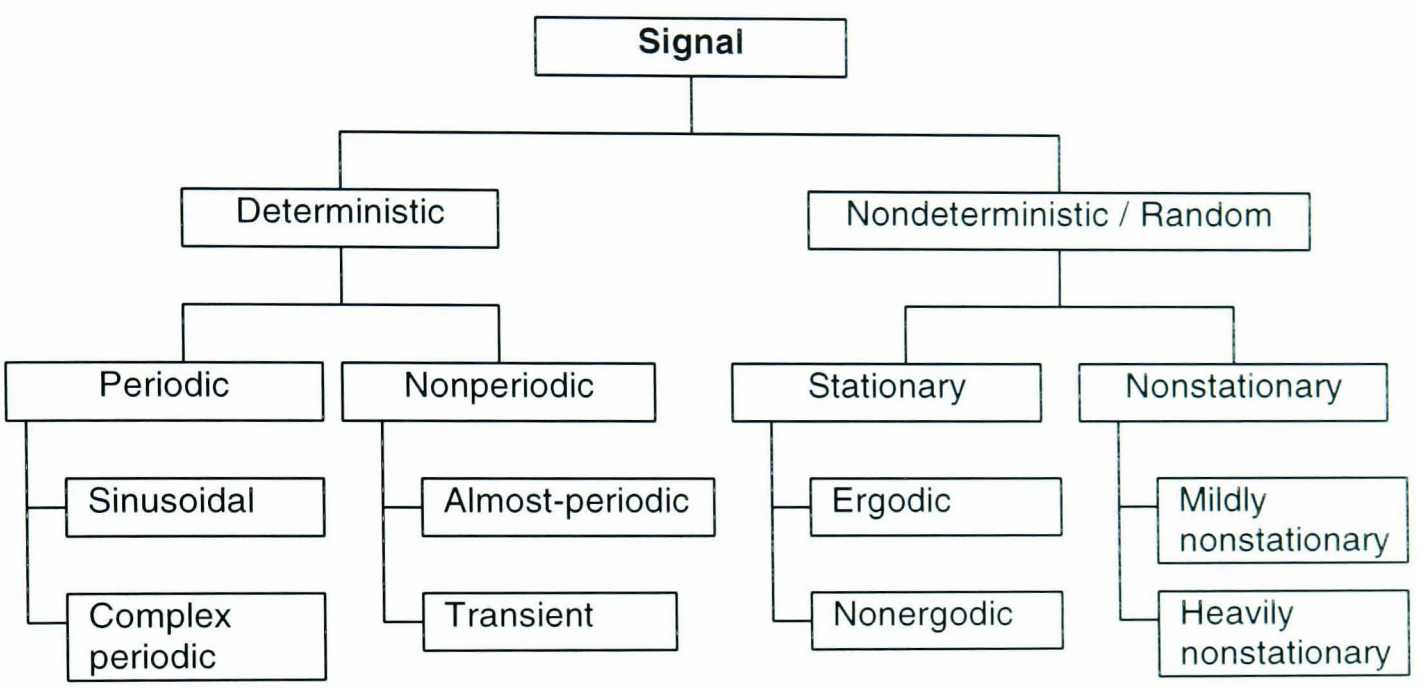

Figure 2.3: Classification of signals (Modified version of Bendat and Piersol 1986).

A deterministic signal can be described by a mathematical relationship between the value of the function and the value of time. It can be further characterised as being periodic or nonperiodic (Bendat and Piersol 1986). Periodic signals can further be divided into the categories of sinusoidal and complex periodic signals. A nonperiodic signal can be further categorised into almost-periodic and transient.

Sinusoidal signals are mathematically defined by the sinusoidal time-varying function:

$$x(t) = X \sin 2\pi f_0 t \tag{2.2}$$

where X is the amplitude, f_0 is the cyclic frequency and $x(t)$ is the instantaneous value at time t. A complex periodic signal is defined by a time-varying function whose waveform exactly repeats itself in a regular manner, i.e.

$$x(t) = x\left(t \pm nT_p\right) \qquad n = 1,2,3,\ldots \tag{2.3}$$

where n is number of discrete point and T_p is the period. A combination of two or more sine waves produces a signal which is mathematically defined as

$$x(t) = \sum_{n=1}^{\infty} X_n \sin(2\pi f_n t + \theta_n) \qquad n = 1,2,3,\ldots \tag{2.4}$$

where f_n is the cyclic frequency and θ_n is the phase angles. When all frequencies f_n are integer multiples of a single base frequency, the signal is defined as periodic. When some frequency components produce f_n/f_m which are not rational numbers (m = 1,2,3, ..., and $n \neq m$), thus the signal is defined as almost-periodic. A transient signal is defined (Bendat and Piersol 1986) as a nonperiodic signal with a finite time range. Example of the transient signal is an impulse loading.

Many signals in nature exhibit random or nondeterministic characteristics which provide a challenge to analysis using signal processing techniques (Tacer and Loughlin 1998). A signal representing a random physical phenomenon cannot be described in a point by point manner by means of a deterministic mathematical equation. A signal representing a random phenomenon can be characterised as either stationary or nonstationary.

A stationary signal is characterised by values of the global signal statistical parameters, such as the mean, variance and root-mean-square (refer to Section 2.1.2 for definition), which are unchanged across the signal length. Stationary random processes can further be categorised as being ergodic or nonergodic. If the random process is stationary, and the mean value and the autocorrelation function do not differ when computed over different sample segments measured for the process, the random process is defined as ergodic. For this case, the mean value $\mu_x(k)$ can be calculated as

$$\mu_x(k) = \lim(T \to \infty)\frac{1}{T}\int_0^T x_k(t)dt \tag{2.5}$$

and the autocorrelation function $R_x(\tau,k)$ for the k^{th} sample function is defined as

$$R_x(\tau,k) = \lim(T \to \infty)\frac{1}{T}\int_0^T x_k(t)x_k(t+\tau)dt \tag{2.6}$$

where τ is the time displacement and T is the period. In practice, random data representing stationary physical phenomena are generally ergodic, therefore, the properties of this type of signal can be measured easily (Bendat and Piersol 1986).

In the case of nonstationary signals the global signal statistical values are dependent on the time of measurement (Bendat and Piersol 1986). Nonstationary signals can be divided into two categories: mildly nonstationary and heavily nonstationary. A mildly nonstationary signal is defined as a random process with a stable mean, variance and root-mean-square values for most of the record, but with short periods of changed signal statistics due to the presence of transient behaviour (Giacomin *et al.* 1999). A heavily nonstationary signal is defined as being similar to a mildly nonstationary signal, but with the presence of transient events over a large interval of the time history (Giacomin *et al.* 1999). Examples of loadings exhibiting stationary and nonstationary characteristics are presented in Figure 2.4.

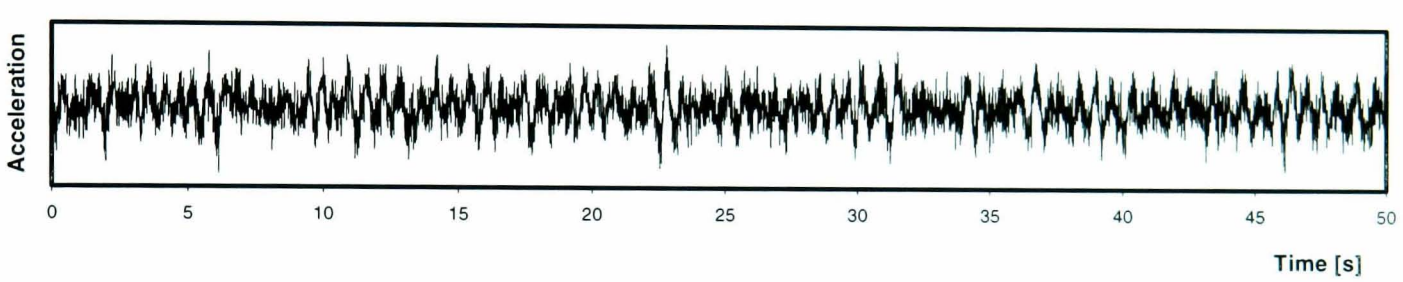

(a) Highway surface: kurtosis = 3.00, crest factor = 4.2

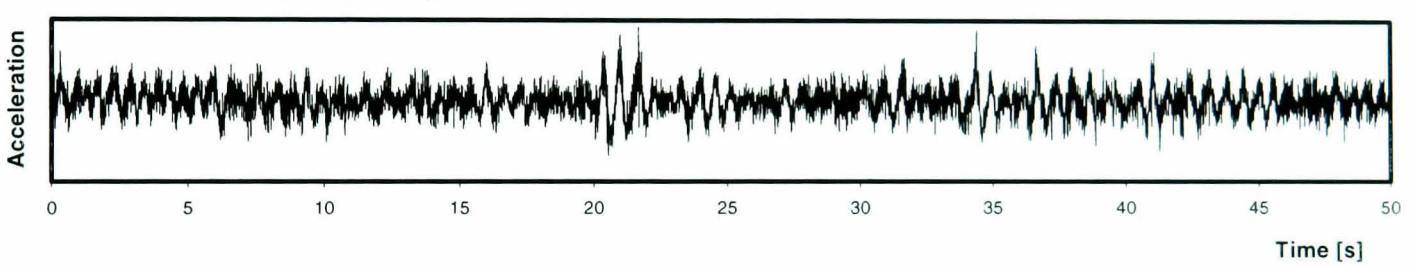

(b) Good road surface: kurtosis = 3.57, crest factor = 5.5

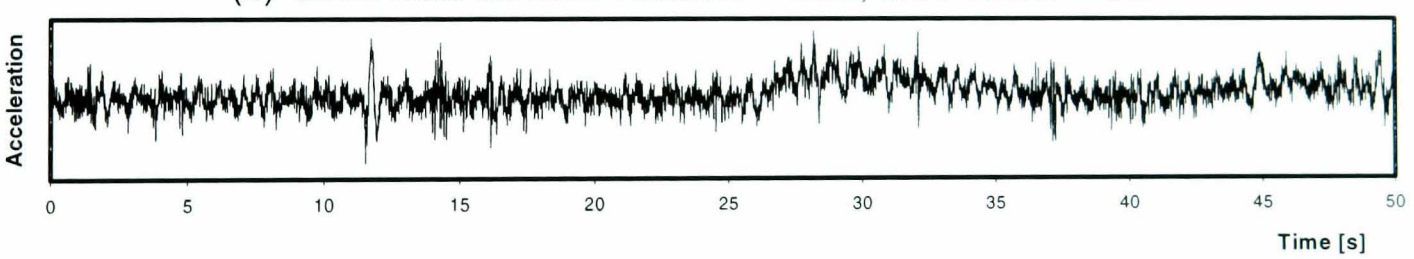

(c) Good road surface with a climb

Figure 2.4: Examples of stationary and nonstationary acceleration time histories measured on an automobile seat rail (Reproduced from Giacomin *et al.* 2000): (a) Stationary Gaussian, (b) Mildly nonstationary, (c) Heavily nonstationary.

Since nonstationary loadings are common in the case of fatigue analysis, signal modelling has often been used in the time domain due to its simplicity and efficiency for the purpose of loading simulation. Several studies which have used the time-varying signal analysis of fatigue damage can be found in the literature, such as in Matsuishi and Endo (1968), Ermer and Notohardjono (1984), Leser (1993), Raath and Van Waveren (1998) and others.

2.1.2 Signal Statistics

Global signal statistics are frequently used to classify random signals. The most commonly used statistical parameters are the mean value, the standard deviation value, the root-mean-square (r.m.s.) value, the skewness, the kurtosis and the crest factor (Hinton 1995). For a signal with a number *n* of data points in the sampled sequence *n*, the mean value $\bar{x}$, is given by

$$\bar{x} = \frac{1}{n}\sum_{j=1}^{n} x_j \tag{2.7}$$

The standard deviation (*SD*) is mathematically defined as

$$SD = \left\{\frac{1}{n}\sum_{j=1}^{n}\left(x_j - \bar{x}\right)^2\right\}^{1/2} \tag{2.8}$$

for the samples more than 30. If the samples less than 30, the standard deviation is defined as (Hinton 1995)

$$SD = \left\{\frac{1}{n-1}\sum_{j=1}^{n}\left(x_j - \bar{x}\right)^2\right\}^{1/2} \tag{2.9}$$

The standard deviation value measures the spread of the data about the mean value. The r.m.s. value, which is the 2nd statistical moment, is used to quantify the overall energy content of the signal. For discrete data sets the r.m.s. value is defined as

$$r.m.s. = \left\{\frac{1}{n}\sum_{j=1}^{n} x_j^{\,2}\right\}^{1/2} \tag{2.10}$$

For a zero-mean signal the r.m.s. value is equal to the *SD* value. The skewness, which is the signal 3rd statistical moment, is a measure of the symmetry of the distribution of the data points about the mean value. The skewness of a signal is given by

$$S = \frac{1}{n(r.m.s.)^3} \sum_{j=1}^{n} (x_j - \bar{x})^3 \tag{2.11}$$

The skewness for a symmetrical distribution such as a sinusoid or a Gaussian random signal is zero. Negative skewness values indicate probability distributions that are skewed to the left, while a positive skewness values indicate probability distributions that are skewed to the right, with respect to the mean value.

Kurtosis, which is the signal 4th statistical moment, is a global signal statistic which is highly sensitive to the spikiness of the data. For discrete data sets the kurtosis value is defined as

$$K = \frac{1}{n(r.m.s.)^4} \sum_{j=1}^{n} \left(x_j - \bar{x}\right)^4 \tag{2.12}$$

For a Gaussian distribution the kurtosis value is approximately 3.0. Higher kurtosis values indicate the presence of more extreme values than should be found in a Gaussian distribution. Kurtosis is used in engineering for detection of fault symptoms because of its sensitivity to high amplitude events (Qu and He 1986).

The crest factor, which is commonly encountered in engineering applications, is defined as the ratio between the maximum value in the time history and the r.m.s. value:

$$CF = \left| \frac{x_{j\max}}{r.m.s.} \right| \tag{2.13}$$

The crest factor value for sinusoidal time histories is 1.41 and the value approaches 4.00 in the case of a Gaussian random signal of infinite length.

2.2 Frequency Analysis

2.2.1 Fourier Transform

Frequency analysis is performed in order to convert a time domain signal into the frequency domain. The results of a frequency analysis are most commonly presented by means of graph having frequency on the *x*-axis and amplitude on the *y*-axis. The algorithm that is used to split the time history into its constituent sinusoidal components is the Fourier transform. This transform was first defined by the French mathematician and engineer Jean Baptiste Joseph Fourier who postulated that any periodic function could be expressed as the summation of sinusoidal waves of varying frequency, amplitude and phase. Smith (1999b) defines spectral analysis as understanding a signal by examining the amplitude, frequency and phase of its component sinusoids. For a periodic time function, *x(t)*, frequency analysis can be performed using the classical Fourier transform defined by the mathematical definition:

$$X(\omega) = \frac{1}{2\pi}\int_{-\infty}^{\infty} x(t)e^{-i\omega t}\,dt \qquad (2.14)$$

where $X(\omega)$ is the amplitude of Fourier transform in frequency distribution, ω is the angular frequency and $i = \sqrt{-1}$.

A commonly used form of Fourier transformation is the discrete Fourier transform (DFT). This algorithm transforms a time-domain sample sequence into a frequency-domain sequence which describes the spectral content of the signal (Stearns and David 1993). The DFT is defined as

$$X_k = \frac{1}{N}\sum_{t=0}^{N-1} x_j e^{-i(2\pi kt/N)} \qquad j,\ k = 0,\ 1,\ 2,\ 3,\ \ldots,\ (N\text{-}1) \qquad (2.15)$$

The frequency information obtained from the DFT can be reverted back into the time domain using the inverse discrete Fourier transform (IDFT) which is defined as

$$x_j = \sum_{k=0}^{N-1} X_k e^{i(2\pi kt/N)} \qquad k = 0,\ 1,\ 2,\ 3,\ \ldots,\ (N\text{-}1) \qquad (2.16)$$

The most common algorithm used for the Fourier transform is the fast Fourier transform (FFT) algorithm which was introduced in order to have a faster DFT calculation of the time series (Smith 1999b). Various FFT algorithms were developed. The algorithm introduced by Cooley and Tukey (1965) is the most commonly used because of its simplicity and fast computing time (Smith 1999b). This algorithm produced the N frequency spectra corresponding to the N data points of a time domain signal which is calculated using the log format or $\log_2 N$. For example, a 16-point signal (2^4) requires 4 stages, a 512-point signal (2^{10}) requires 10 stages and a-4096 point signal (2^{12}) requires 12 stages. The frequency information obtained from the FFT can also be reverted back into the time domain using the inverse fast Fourier transform (IFFT), which is a similar concept as the IDFT.

Many frequency analysis applications can be found in the literature and one of them is the generation of a power spectral density (PSD). A PSD is a normalised density plot describing the mean square amplitude of each sinusoidal wave with respect to its frequency. The PSD presents the vibrational energy distribution of the signal across the frequency domain as shown in Figure 2.5. Each frequency step value of the PSD is characterised by an amplitude, A_k, defined as

$$A_k = \sqrt{2\Delta f \cdot S(f_k)} \tag{2.17}$$

where $S(f_k)$ is the underlying PSD of the signal and f_k is the harmonic frequency.

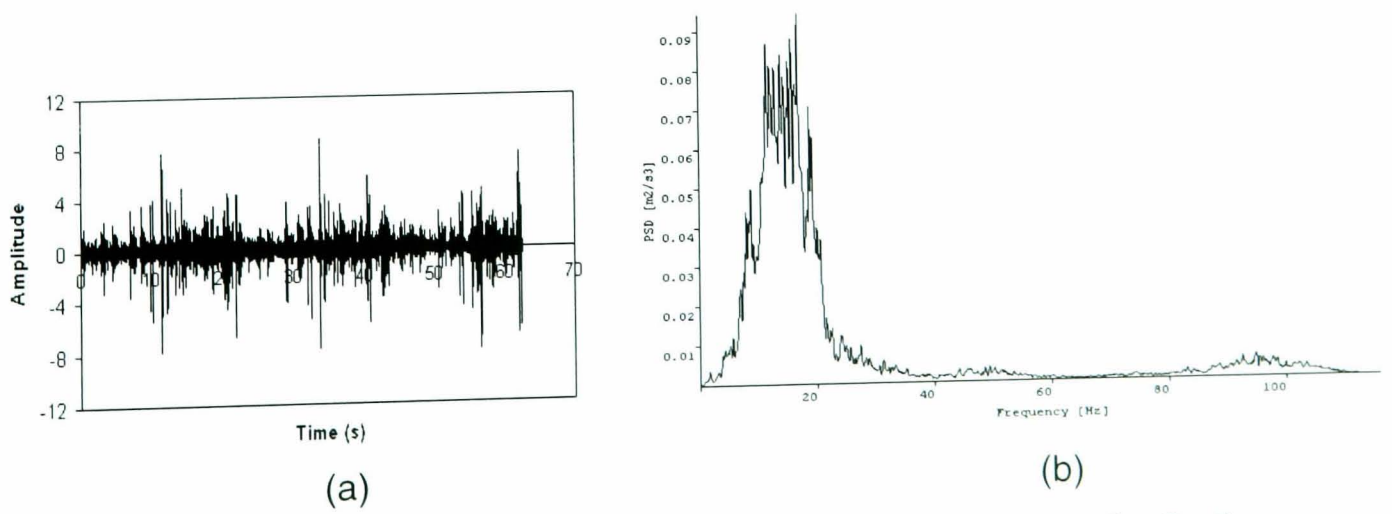

(a) (b)

Figure 2.5: (a) A variable amplitude loading, (b) Its PSD distribution.

The PSD can be as an input for generating a time-varying signal by performing the IDFT or IFFT. However, the time series which was generated from IFFT is not as accurate as the original signal, the PSD does not contain the original signal phase information. The assumptions of the signal phase content can be made in order to regenerate a statistically equivalent time history. For example, if the time history is taken from an ergodic stationary for Gaussian and random process, the phase is purely random between $-\pi$ and $+\pi$ radians (Halfpenny 1999; Li *et al.* 2001).

Following are several case examples of frequency domain analysis or the PSD approach in the field of fatigue study. The background of the fatigue analysis using PSD can be found in Halfpenny and Bishop (1997) and Halfpenny (1999).

Bishop and Sherratt (1989; 1990; 2000), Bishop and Cesario (1998) discussed the analysis of the offshore or oil rig structures, by converting the measured PSD caused by ocean wave and wind into the time domain fatigue stress. The signals were then used to predict fatigue damage of the structures.

In another application, Bishop *et al.* (1995) used the PSDs as the input information to predict the fatigue damage in automotive design by measuring the PSD at critical locations on the automotive component. The PSD was then converted into a time domain signal so as to predict fatigue damage.

In automotive research by Hu (1995), a PSD of a signal was used to predict the fatigue life using the r.m.s. value, suggesting material failure occurs at the largest r.m.s. value. Accordingly, r.m.s. is a function of the PSD of the input signal *G(f)* and the stress response function *H(f),* which is given as

$$r.m.s. = \sqrt{\int_0^\infty G(f)H^2(f)df} \tag{2.18}$$

In this study, the loading is Gaussian and the PSD of fatigue loading was distributed from 4.5 Hz to 250 Hz, as shown in Figure 2.6. The natural frequencies of the structure

were found to be at 62.1 Hz and 150.2 Hz. With this concept, the fatigue damage was subjectively measured across the frequency distribution with respect to the r.m.s. value.

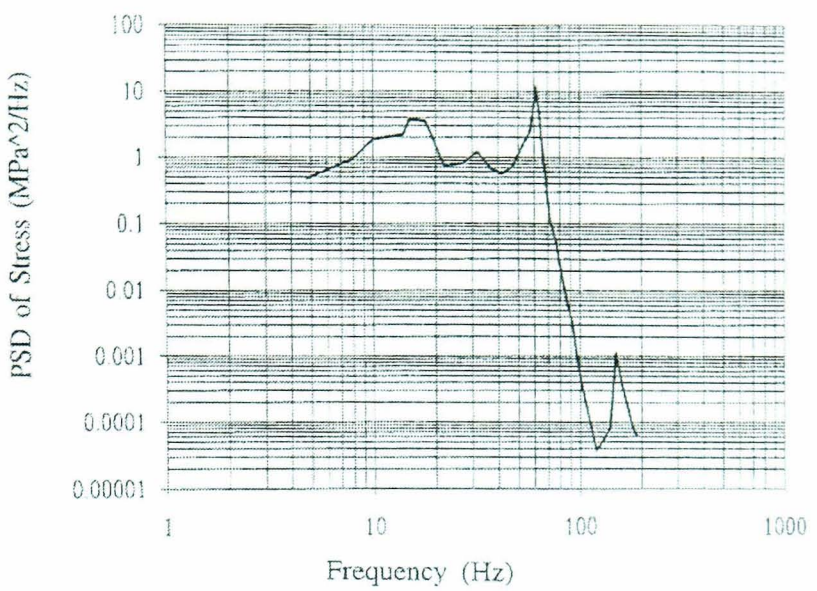

Figure 2.6: PSD distributed from 4.5 Hz to 250 Hz (Reproduced from Hu 1995).

2.2.2 Short-Time Fourier Transform (STFT)

Using the Fourier transform the frequency components of an entire signal can be analysed, but it is not possible to locate at what point in time that a frequency component occurred or its duration. This is not problematic when a stationary signal is analysed. However, Fourier analysis is not suitable for non-stationary signals. If there is a time localisation due to a particular feature in a signal such as impulse, this will only contribute to the overall mean valued frequency distribution and feature location on the time axis is lost (Newland 1993). To overcome this problem, the short-time Fourier transform (STFT) was developed.

STFT is a method of time-frequency analysis which aims to produce frequency information which has a localisation in time. It provides information about when and at what frequencies a signal event occurs (Matlab User's Guide 1998). The STFT approach assumes that if a time-varying signal is divided into several segments, each can be assumed stationary for analysis purposes. The Fourier transform is applied to

each of the segments using a window function, which is typically nonzero in the analysed segment and is set to zero outside (Patsias 2000). The most important parameter in the analysis is the window length, which is chosen so as to isolate the signal in time without any distortions.

The STFT was developed from the Fourier transform, and it is mathematically defined as

$$STFT = X(\tau, \omega) = \int_{-\infty}^{\infty} \omega(t-\tau) e^{-i\omega t} x(t) dt \qquad (2.19)$$

where the Fourier transform of the windowed signal is $x(t)e^{-i\omega t}$, ω is the frequency and τ is the time position of the window (Chui 1991). The result of this transformation is a number of spectra, each localised in a windowed segment.

The time-frequency resolution depends on the selection of the window length. The time window length is defined as Δt and the frequency bandwidth is $\Delta\omega$. The 'area' of the segment is given by the product $\Delta\omega$ and Δt. Considering the relationship between time and frequency, i.e.

$$\Delta\omega = {}^{1}\!/_{\Delta t} \qquad \text{or} \qquad \Delta\omega\Delta t = 1 \qquad (2.20)$$

it can be seen that a good time localisation (when Δt is small) or frequency localisation (when $\Delta\omega$ is small) can be obtained, but not both simultaneously. Therefore the time window length Δt and the frequency bandwidth $\Delta\omega$ are interrelated. The time-frequency resolution and its frequency bandwidth are shown in Figure 2.7.

While a useful tool, the STFT has a resolution problem, i.e. short windows provide good time resolution but poor frequency resolution. On the other hand, long windows provide good frequency resolution, but poor time resolution. The wavelet transform, which is described in the next section, is one of the most recent solutions to overcome the shortcomings of STFT (Grossman and Morlet 1984).

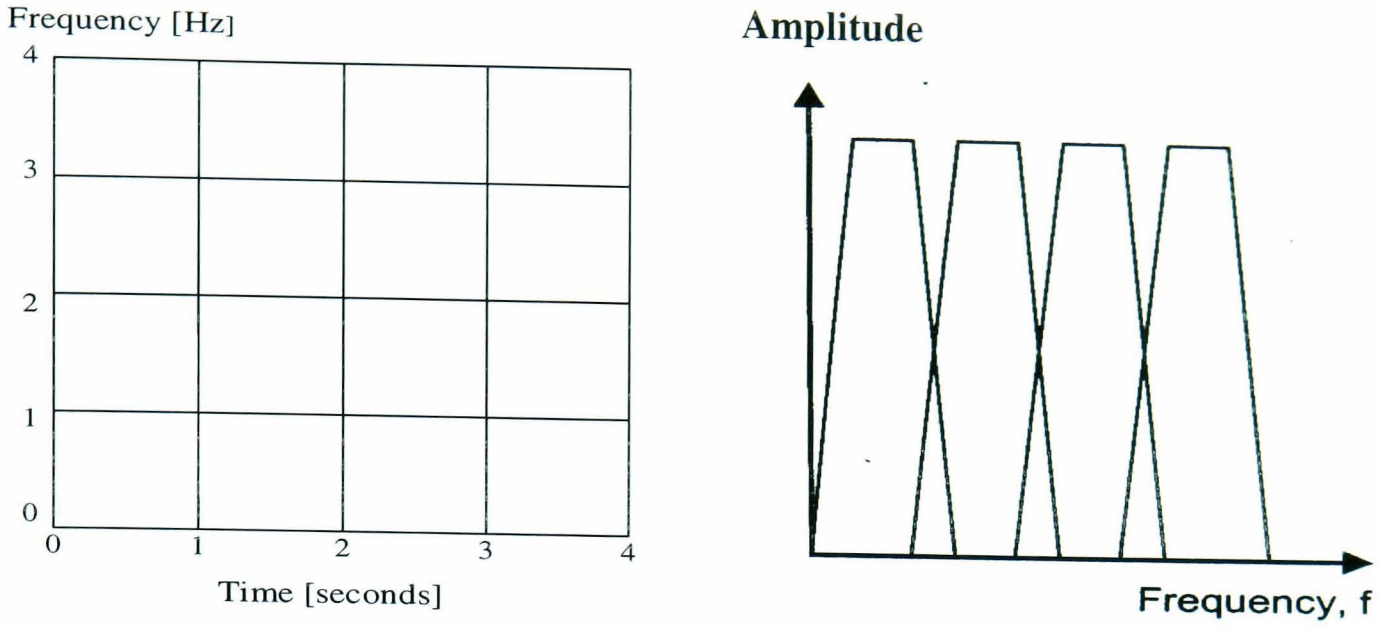

(a) (b)

Figure 2.7: Short-time frequency transform concept: (a) Time-frequency cell structure, (b) Bandwidth (Reproduced from Patsias 2000).

2.3 Time-Frequency Analysis

2.3.1 Introduction to Wavelet Analysis

A wavelet is a small wave with a signal energy concentrated in time (Burrus *et al.* 1998), on the condition of admissibility condition. An example is illustrated in Figure 2.8 alongside a sinusoidal wave of fixed amplitude. The wavelet transform is defined in the time-scale domain and is a significant tool for analysing time-localised features of a signal. It represents a windowing technique with variable-sized region. The harmonic form of the wavelet transform can be derived from the Fourier transform in the phase form, i.e.

$$X(\omega) = \int_{-\infty}^{\infty} x(t)\sin(2\pi ft - \phi(f))dt \tag{2.21}$$

Defining $a = 1/(2\pi f)$ and $b' = \phi_f/(2\pi f)$, then Eq. (2.20) can be rewritten as

$$X(\omega) = \int_{-\infty}^{\infty} x(t)\sin\left(\frac{t-b'}{a}\right)dt \tag{2.22}$$

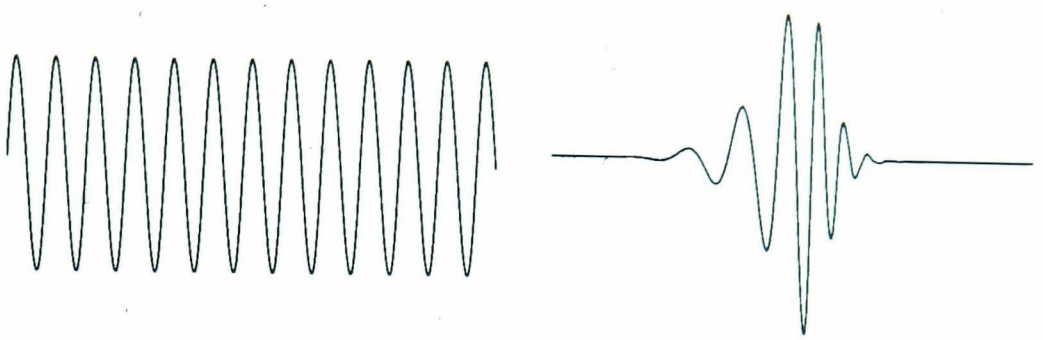

Figure 2.8: A sinusoidal wave and a wavelet (Reproduced from Burrus 1998).

where *a* is a scale parameter which controls the frequency by dilating or scaling the time *t*. The parameter *b'* translates the basic sine wave up and down the time axis and it is known as the translation parameter. By replacing the sine-wave with a localised oscillatory function, or wavelet ψ, the wavelet transform is obtained as

$$W_{\psi}(a,b') = \int_{-\infty}^{\infty} x(t)\psi\left(\frac{t-b'}{a}\right)\mathrm{d}t \qquad (2.23)$$

A wavelet transform can be classified as either a continuous wavelet transform (CWT) or a discrete wavelet transform (DWT) depending on the discretisation of the scale parameter of the analysing wavelet $\psi(t)$. The wavelet method solves the resolution problem because the window length is long for low frequencies and short for high frequencies. Therefore, the frequency resolution is good for low frequencies (at high scales) and the time resolution is good at high frequencies (at low scales). The time-frequency resolution of the wavelet transform is illustrated in Figure 2.9a and its frequency bandwidth is shown in Figure 2.9b. One of the earliest practical applications of wavelets came from the analysis of earthquake records by Goupillaud *et al.* (1984). Since then, wavelet analysis has been used in many applications in science and engineering.

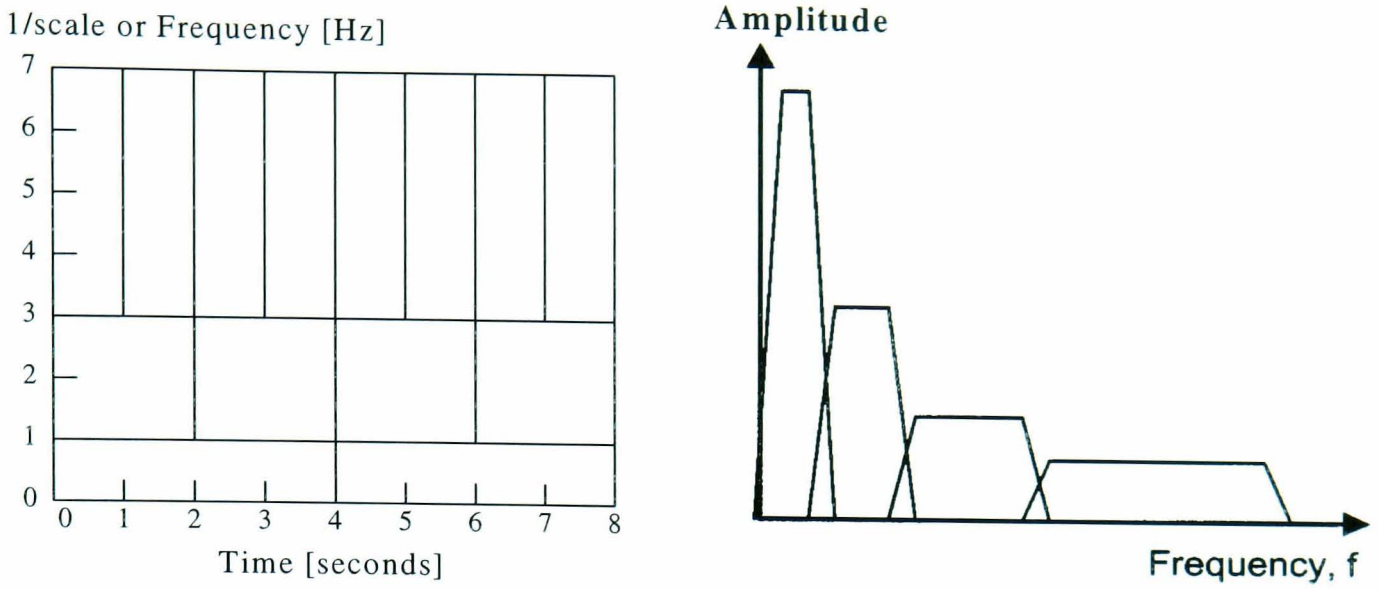

Figure 2.9: The wavelet transform concept: (a) Time-frequency cell structure, (b) Bandwidth (Reproduced from Patsias 2000).

2.3.2 Continuous Wavelet Transform (CWT)

Referring to Eq. (2.23), wavelets are analytical functions $\psi(t)$ which are used to decompose a signal $x(t)$ into scaled wavelet coefficients, $W_\psi(a,b')$. When the signal is infinite, and using $1/\sqrt{a}$ as energy normalisation constant to produce equal energy at all time scales, the mathematical definition of the wavelet transform becomes

$$W_\psi(a,b') = \frac{1}{\sqrt{a}} \int_{-\infty}^{\infty} x(t)\psi^* \left(\frac{t-b'}{a} \right) \mathrm{d}t \tag{2.24}$$

which gives the expression for the continuous wavelet transform (CWT) and ψ^* is the complex conjugate of ψ. The basis mother wavelet $\psi(t)$ can be any of a number of functions which satisfy a set of admissibility conditions. The admissibility conditions is mathematically defined as

$$\int_{-\infty}^{\infty} \frac{|\Psi(\omega)|^2}{|\omega|} d\omega = C_\psi < \infty \tag{2.25}$$

where $\Psi(\omega)$ is the Fourier transform of the mother wavelet. This condition is used for the inversion process of the wavelet transform. One of the families in the CWT category is the Morlet wavelet.

For an application example, a research performed by Staszewski (1998a) demonstrated the use of CWT to analyse the impact vibration response in a composite panel, as shown in Figure 2.10. It showed a two-dimensional contour plot of the CWT as well as the classical time and frequency domain representations. In this figure, an impulse was detected at the particular time interval from 0.7 seconds to 0.8 seconds and frequency interval from 0.6 Hz to 10.1 Hz (or from scale 2.9 to 4.2).

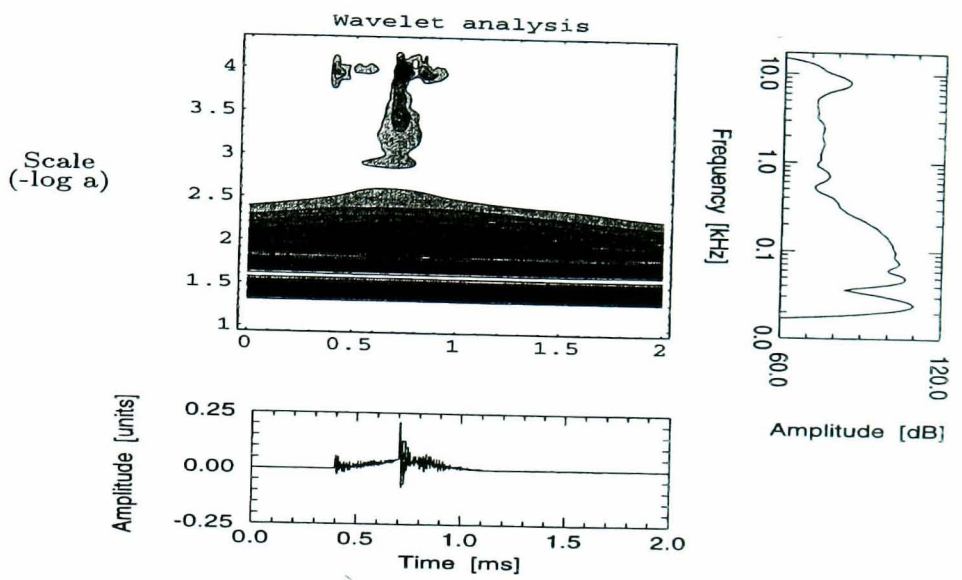

Figure 2.10: Wavelet analysis of a nonstationary signal using the CWT (Reproduced from Staszewski 1998a)

An example of the use of the CWT for the purpose of fatigue damage detection in the study of a gearbox system was performed by Boulahbal *et al.* (1999). In this study, the CWT wavelet function was used to analyse the cracking of a gear tooth that was caused by fatigue failure. Using the technique, the transient events that caused the damage of the geared system were detected and extracted from the acceleration input signal. Referring to the CWT wavelet map presented in Figure 2.11, the transient event was detected at the particular angular position (i.e. at interval from 80° to 180°) of the shaft, suggesting the efficiency of the CWT for detecting high amplitude events.

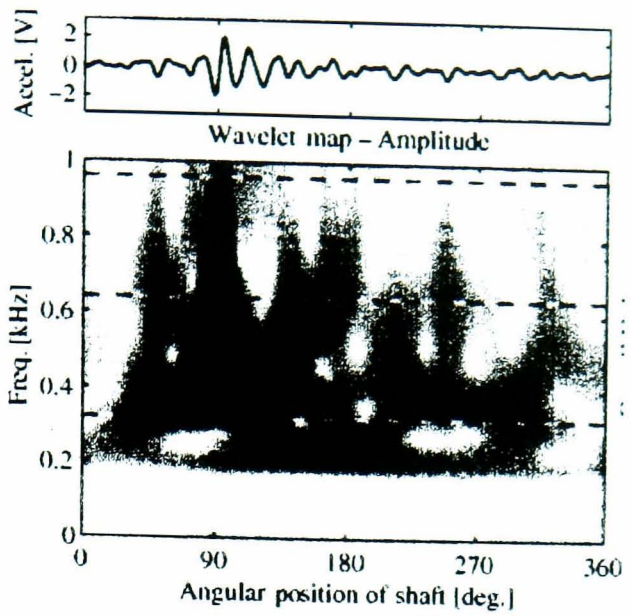

Figure 2.11: The map of CWT showing a transient affect caused by an impulse (Reproduced from Boulahbal *et al.* 1999).

2.3.3 Discrete Wavelet Transform (DWT)

Another wavelet transform approach is the discrete wavelet transform (DWT). With reference to Eq. (2.24), an extension of continuous analysis is the discretisation of time *b'* and scale *a* according to $a = a_0^{\ m}$, $b' = na_0^{\ n}b_0$ where *m* and *n* are integers, $b_0 \neq 0$ is the translation step. This implies the construction of a time-scale grid defined as (Chui 1991)

$$W_\psi(m,n) = \int_{-\infty}^{\infty} x(t) a_0^{\ -m/2} \psi^* \left(\frac{t - nb_0 a_0^{\ m}}{a_0^{\ m}} \right) \mathrm{d}t \qquad (2.26)$$

The discrete grid on the time-scale plane corresponds to a discrete set of continuous wavelet functions. When the wavelets $\psi_{m,n}(t)$ form a set of orthonormal functions, there is high efficiency because of the elimination of redundancy in the analysis. The DWT based on such wavelet functions is called the orthogonal wavelet transform (OWT).

Orthogonal wavelet transforms are normally applied for the compression and feature selection of signals. Wavelet types used in OWT analysis include the Haar wavelet which is the simplest type of wavelet (Walker 1999), and the Daubechies wavelet (Daubechies 1992) which is a more complex wavelet (Walker 1999; Graps 1995). The

Daubechies wavelet, which was developed by Ingrid Daubechies (Daubechies 1992), has orthogonal basis functions based on iteration procedure. Daubechies wavelets are commonly used for damage detection (Staszewski 1998a; 1998b; Li *et al.* 1999; Lin and Zuo 2003) and fatigue damage analysis (Oh 2001; Abdullah *et al.* 2004).

When performing the Daubechies wavelet decomposition process, an appropriate wavelet order needs to be determined. The order is defined as a scalar value that specifies the order number for the wavelet. Lower orders of Daubechies wavelet are suitable for more compactly supported, or less smooth wavelet functions. Compactly supported wavelet is defined that a wavelet function is vanished outside of a finite interval (Graps 1995). Therefore, these wavelet functions are suitable for analysing nonstationary signals with discontinuities. Higher orders of Daubechies wavelet are used when analysing less compactly supported, or more smooth wavelet functions. For this case, higher orders Daubechies wavelet functions are suitable to be used in analysing stationary signals (Daubechies 1992; Staszewski 1998b)

A case study comparing lower and higher orders of Daubechies wavelet functions was performed by Staszewski (1998b). For this case, a 4^{th} and 20^{th} order Daubechies wavelet and FFT were used to analyse three types of signal, i.e. periodic or stationary data, nonstationary data and transient data. The Daubechies wavelet functions and FFT were then compared by means of the normalised Mean Square Error (MSE) value, defined as the average mean squared deviation of the estimator from the true value (Kay 1993). The results of this analysis are presented in Figure 2.12. For the periodic or the stationary signals (Figure 2.12a), the MSE values of the FFT give the smaller error compared to wavelet functions. This suggests the suitability of the FFT method for analysing stationary signals. The MSE values of 20^{th} order Daubechies wavelet are relatively smaller than 4^{th} order Daubechies wavelet, suggesting the suitability of the 20^{th} order Daubechies wavelet for periodic or stationary signals. In Figure 2.12b, the 4^{th} order Daubechies wavelet produced the smallest error, suggesting the suitability of this wavelet function for nonstationary signals. Finally, in Figure 2.12c for a transient signal, both the 4^{th} and 20^{th} order Daubechies wavelet produced similar results. Figure 2.13

shows the irregular pattern of both orders of Daubechies wavelet. From this analysis, it was concluded that nonstationary signals are best analysed using lower orders of Daubechies wavelet functions.

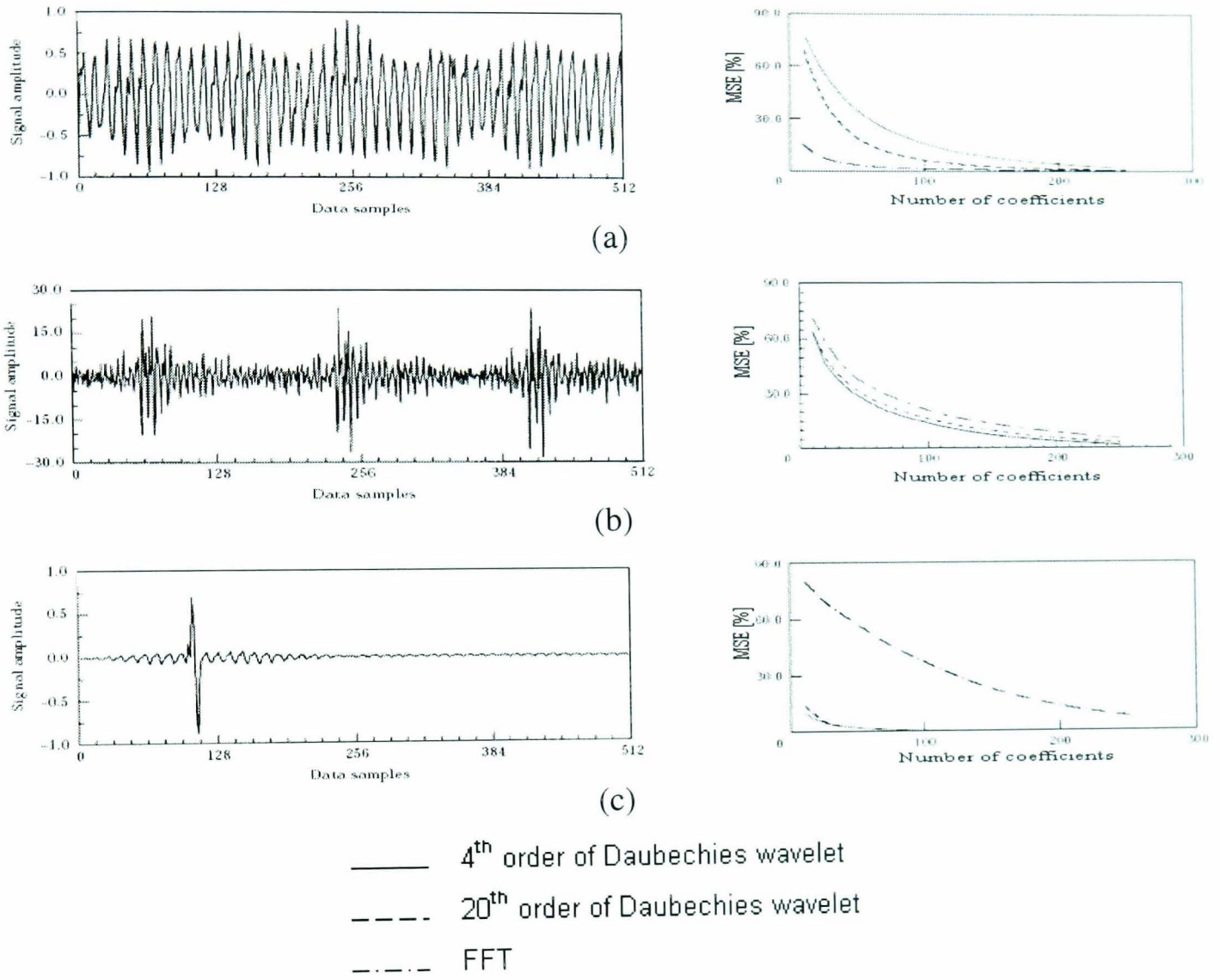

Figure 2.12: The Mean Square Error comparison to determine the performance analysis between 4th and 20th order Daubechies wavelets and FFT using (Reproduced from Staszewski 1998b): (a) Periodic or stationary data, (b) Nonstationary data, (c) Transient data.

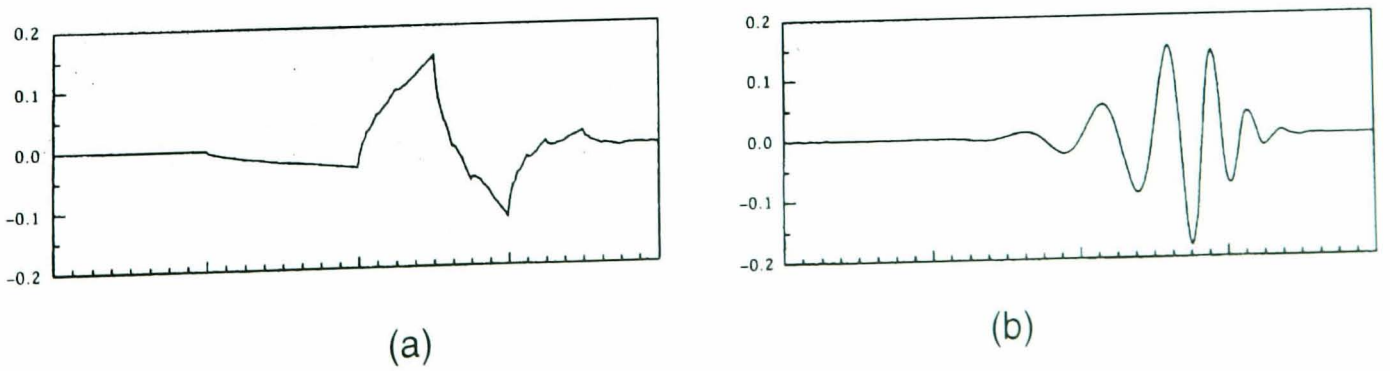

Figure 2.13: Examples of Daubechies wavelet functions: (a) 4th order, (b) 20th order.

The discrete wavelet transform allows the decomposition of an input signal into frequency bands. The decomposed parts of the signal can also be reconstructed in order to reform the original signal. The schematic diagram of decomposition-reconstruction process is shown in Figure 2.14. In the left-hand side of this figure, the original signal is decomposed into the wavelet levels. For the reconstruction analysis, shown on the right-hand side of Figure 2.14, the information of each frequency band is added together for producing a signal which has the same data points as the original signal.

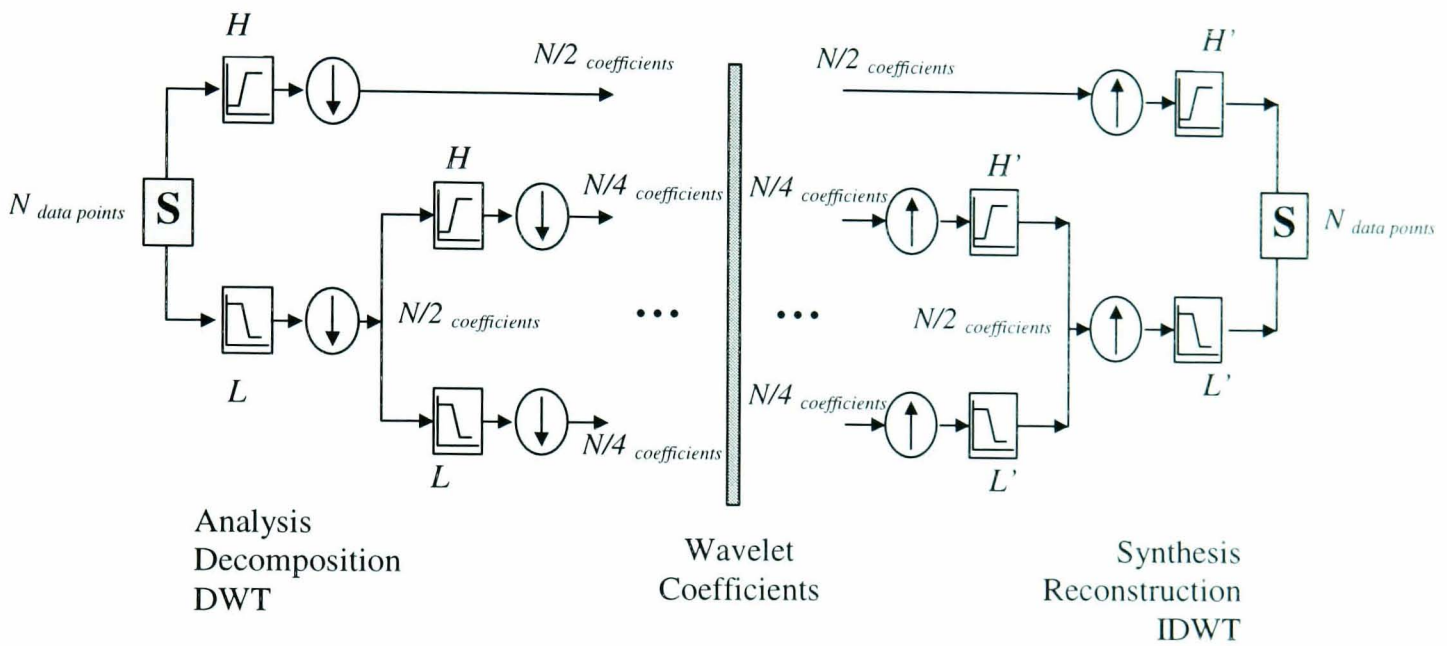

Figure 2.14: Schematic representation of the multi-step wavelet transform decomposition-reconstruction process.

In order to illustrate the Daubechies wavelet decomposition procedure, Figure 2.15a shows the decomposition of a signal into its constitutive components (Staszewski 1998b). This acceleration signal was measured on an automotive gearbox and it was decomposed into eight wavelet components. Each component is called a wavelet level, which is a part of the signal which is in a specific frequency band. When the wavelet levels are added together, the original signal is regained. Figure 2.15b shows the power spectra associated with the respective wavelet levels. The number of discrete points (N) in the signal sequence determines how many wavelet levels there are. When $N = 2^n$

there are n + 1 generated wavelet levels are generated. A detailed of the wavelet decomposition process can be found in Newland (1993) and in Staszewski (1998b).

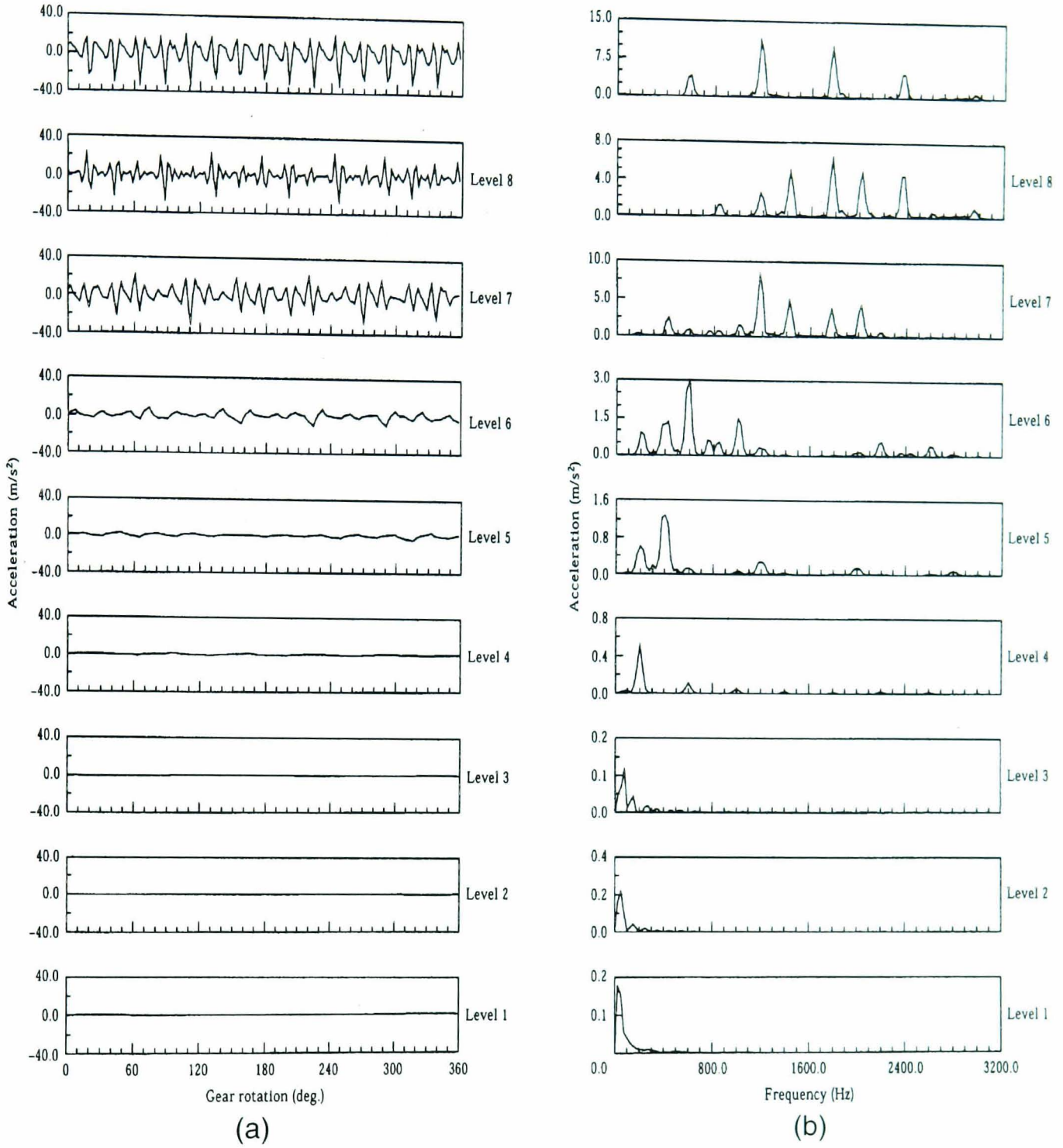

Figure 2.15: Example of the wavelet decomposition of a gearbox acceleration signal (Reproduced from Staszewski 1998b):

(a) Series of wavelet coefficients,

(b) Corresponding power spectral densities.

Among the many applications of the wavelet transform, Lin and Zuo (2003) analysed a gearbox which had a fatigue crack on one gear tooth. In this study, a nonstationary

signal (Figure 2.16a) was decomposed into six wavelet levels using 4th order of Daubechies wavelets in order to detect the impulse which caused the fatigue crack on the gear tooth. Impulses were not clearly observed in the original signal, but were detected in a wavelet level at particular time interval of 0.1–0.2 seconds, 0.3-0.4 seconds and 0.6-0.7 seconds. In Figure 2.16b, the presence of high amplitude impulses are observed in the time interval of 0.1-0.2 seconds and 0.6-0.7 seconds of the levels 2^2 and 2^4. This study demonstrated the suitability of 4th order of Daubechies wavelets for analysing random vibration signals which caused the fatigue cracks.

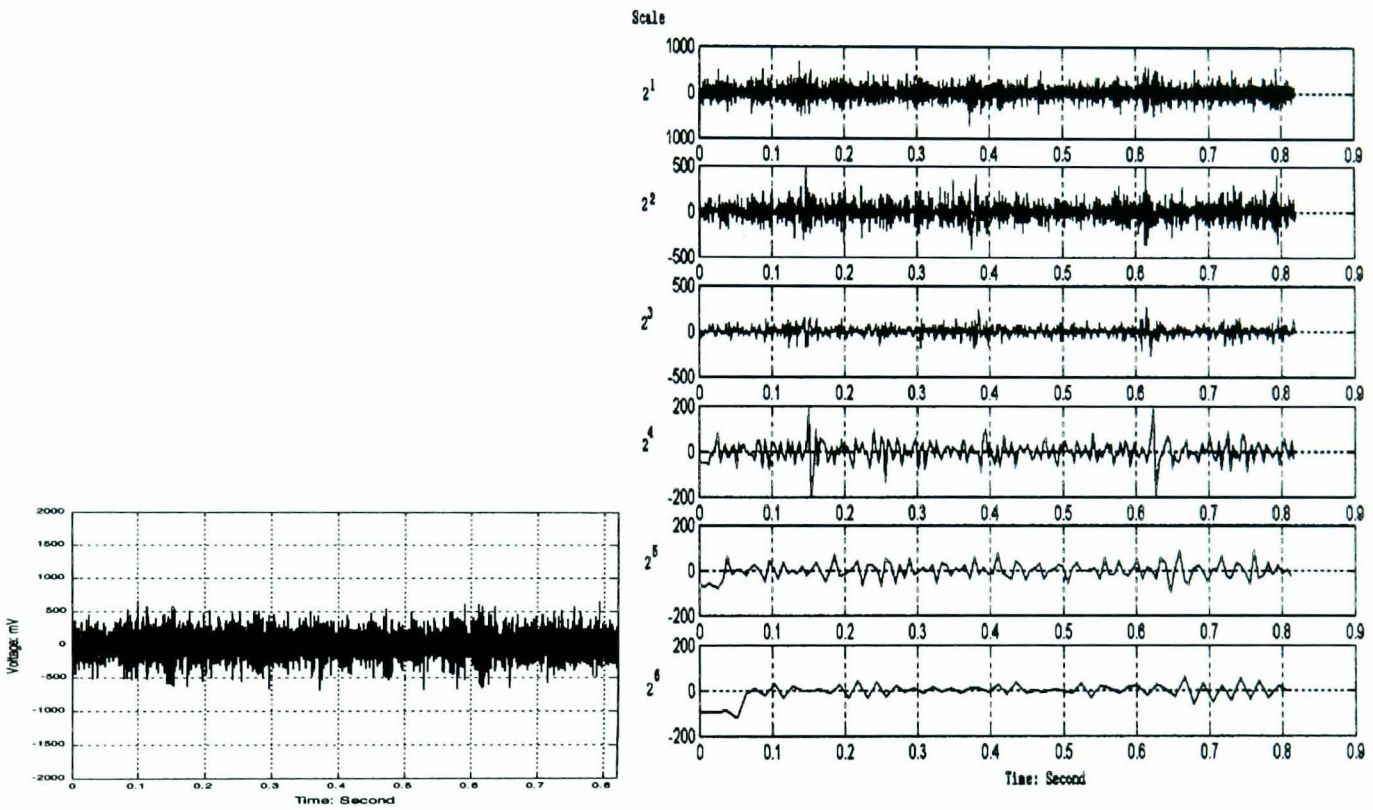

Figure 2.16: Example of a wavelet decomposition to detect vibration impulses:
(a) Original signal, (b) Wavelet levels
(Reproduced from Lin and Zuo 2003)

Another application of the orthogonal wavelet transform in the field of fatigue research was performed by Oh (2001) for the case of fatigue data editing. In this study, Oh (2001) applied Daubechies' wavelets to de-noise a noisy signal and to remove spikes. Recent fatigue damage research using the Daubechies wavelet was performed by Abdullah *et al.* (2004), who applied the MNMS algorithm to the analysis of the variable amplitude (VA) fatigue loadings of an automobile component.

2.4 Types of Fatigue Loadings

2.4.1 Constant Amplitude (CA) Loading

Two types of loading are traditionally defined in the fatigue analysis literature. The first is called a constant amplitude (CA) loading. It is a cyclic load which oscillates between fixed minimum and maximum stress amplitudes (Dowling 1999). In practice, CA loading fatigue tests are performed in order to determine the cyclic mechanical properties of the test materials. An example of a CA loading is a sinusoidal wave as shown in Figure 2.17a. Figure 2.17b shows the peak-valley (PV) reversals that are used to determine the minimum and maximum stress levels. A peak is defined to be associated with change in the slope from positive to negative, while a valley is associated with a change in the slope from negative to positive. In this figure, the notation used is σ_a for the stress amplitude, σ_{max} for the maximum stress, σ_{min} for the minimum stress and $\Delta\sigma$ for the stress range. Another parameter is the mean stress σ_m, which is zero for the signal in Figure 2.17, but which is generally defined as

$$\sigma_m = \frac{\sigma_{\max} + \sigma_{\min}}{2} \tag{2.27}$$

while the stress amplitude, σ_a, is defined as

$$\sigma_a = \frac{\sigma_{\max} - \sigma_{\min}}{2} \tag{2.28}$$

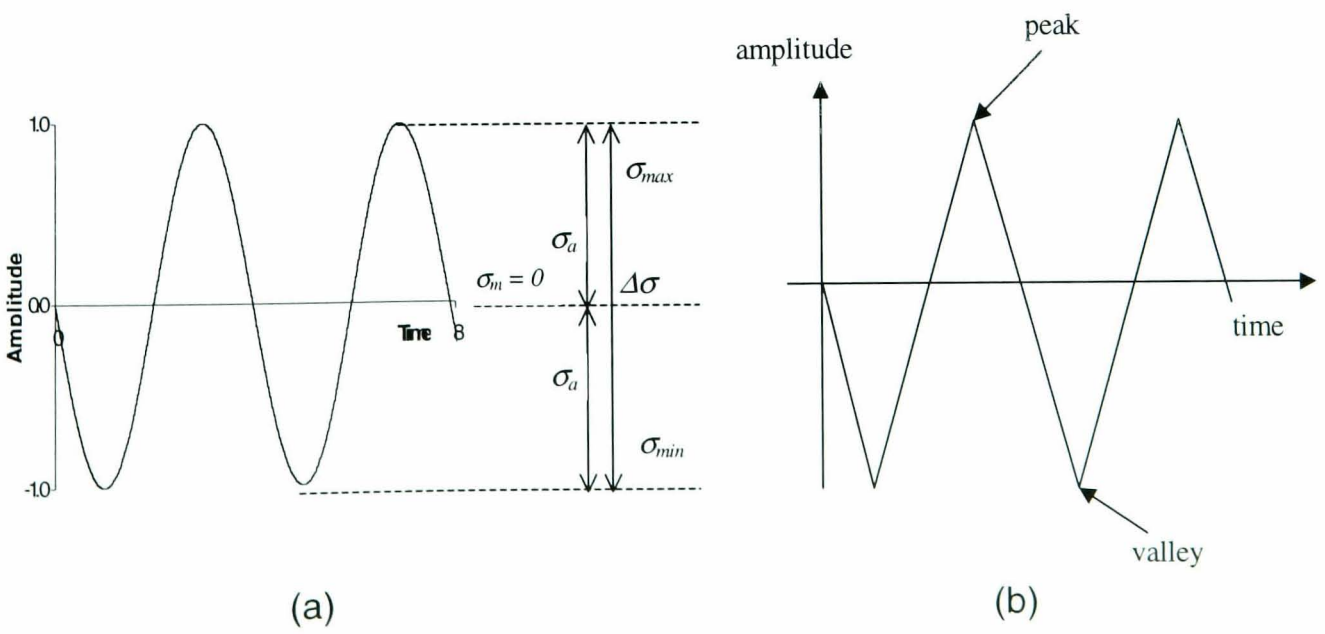

Figure 2.17: Constant amplitude loadings: (a) time history, (b) peak-valley reversals.

2.4.2 Variable Amplitude (VA) Loading

The second type of fatigue loading is the variable amplitude (VA) loading. VA loadings are more complex because the stress or strain values are not constant, but vary instead across the data set. Although CA loadings are commonly used to determine the fatigue life properties of materials, many structures and components will actually experience VA loadings in practice. The simplest type of VA loading is the occurrence of a small number of high peak loads in the background of what would otherwise be considered a CA loading, as shown in Figure 2.18.

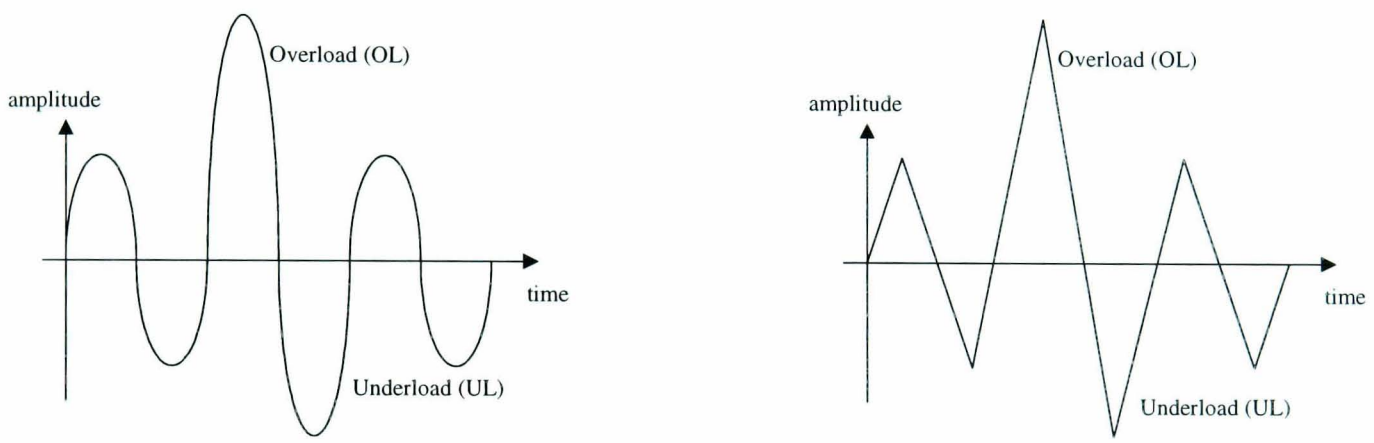

Figure 2.18: Variable amplitude loading: (a) time history, (b) peak-valley reversals.

Three types of load sequence can occur in a VA loading: tensile overload (OL), compressive underload (UL) and overload followed by underload (OL/UL). The interaction between OL, UL and OL/UL make VA loadings more complex than CA loadings (Taheri *et al.* 2003). Therefore, the fatigue life obtained from a VA loading is difficult to predict (Fatemi and Yang 1998). A section from a complete VA loading is known as a block loading, and each block is often called a mission or a duty cycle (Bolotin 1999). A block corresponds to a multiply repeated stage in the service of a structure or machine. An example of a fatigue loading for an aircraft structure is shown in Figure 2.19 (Fowler and Watanabe 1989). An aircraft loading normally includes duty cycles produced by ground motions, take-off, landing, climb, cruise and flight (Waisman

1959). Figure 2.20 shows a compound peak-valley reversal that has a repetitive block loading based on the repetition of one duty cycle.

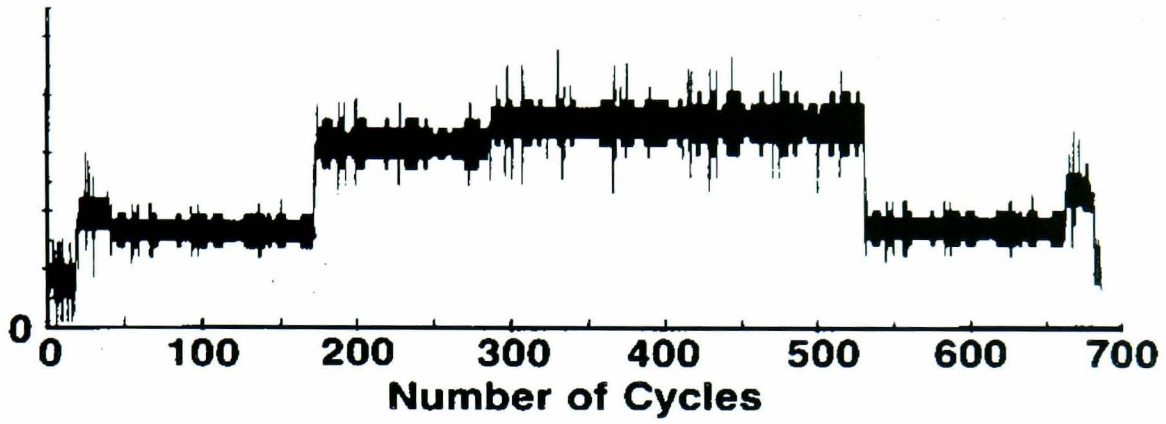

Figure 2.19: Component loading measured during one flight of an aircraft (Reproduced from Fowler and Watanabe 1989).

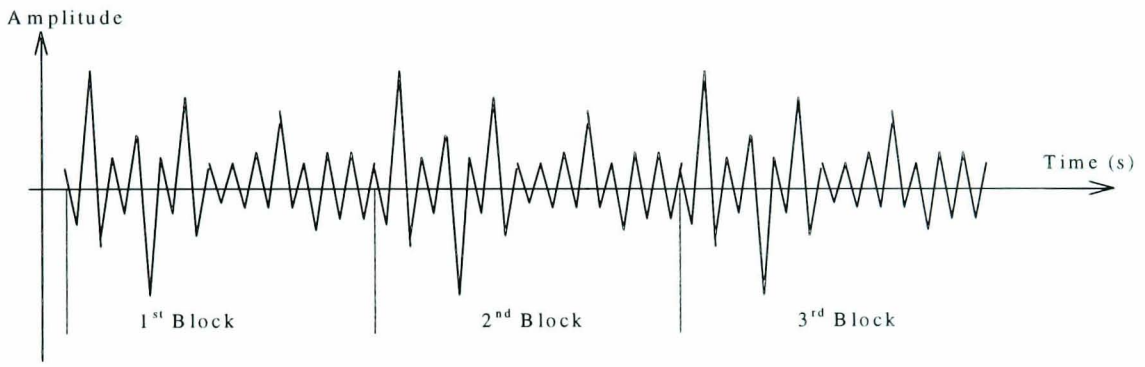

Figure 2.20: Example of a variable amplitude history obtained by multiple repetitions of a single duty cycle.

2.5 Fatigue Life Prediction

2.5.1 Fatigue Life Behaviour of Materials

In engineering practice the service loads measured on the components of machines, vehicles, and structures are analysed for fatigue life using crack growth approaches. This approach is suitable for high capital value machines such as large aircraft, the space shuttle, pressure vessels and oil rigs. The ability to inspect for cracks and monitor their growth until a maximum allowable defect size is reached enables the useful life to be extended beyond the original design safe life. However, it is not generally feasible to

apply the crack inspection process for inexpensive components that are made in large numbers. Performing periodic inspections on these components would generally increase the cost of the item. Examples of components which fall into this category are automobile engine, steering and suspension parts. For these components it is important to predict crack initiation in order to avoid fatigue failure by removing the part from service at the appropriate time. A fatigue life estimate determined by means of the stress-life approach and the strain-life approach is usually used in these cases (Dowling 1999).

For the stress-life approach, methods for characterising fatigue life are based on work performed by Wöhler (1860). In order to determine the fatigue life parameters of the stress-life approach, smooth specimens with cylindrical gauge length were normally tested under CA loading conditions with in-plane bending, rotational bending, uniaxial compression-tension or tension-tension cyclic loading. The results of the cyclic tests, which were performed at various stress levels, were plotted to obtain a stress-life curve known as the *S-N* curve (*S* denotes stress amplitude while *N* denotes the number of cycles to failure), as shown in Figure 2.21. The *S-N* curve exhibits a plateau level after 10^6 cycles. This plateau stress amplitude is known as the fatigue limit or endurance limit (S_e). The fatigue limit for a smooth specimen of a material is defined as (Suresh 1991):

$$S_e = 0.5 S_u \tag{2.29}$$

where S_u is the ultimate strength.

In general, the fatigue limit for a notched specimen is lower than the fatigue limit of a smooth specimen, as illustrated in Figure 2.22. For notched specimens, the fatigue life can be expressed in terms of the fatigue notch factor K_f by the expression

$$S_{e(notched)} = \frac{S_{e(smooth)}}{K_f} \tag{2.30}$$

where the fatigue notch factor K_f is determined from the stress concentration factor K_t and the notch sensitivity q.

$$K_f = 1 + q(K_t - 1) \tag{2.31}$$

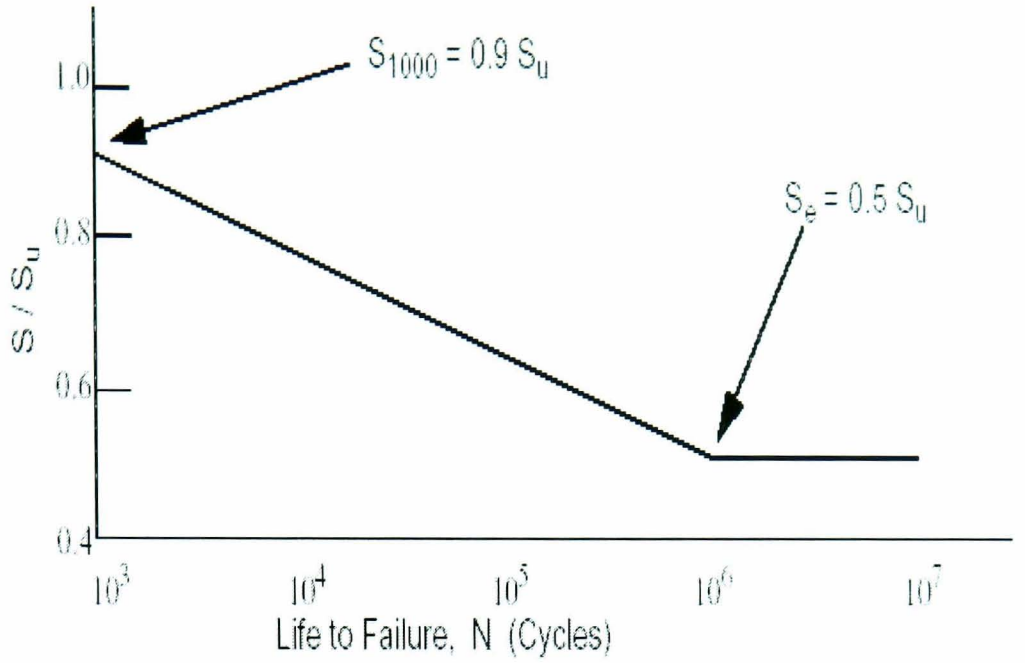

Figure 2.21: A *S-N* curve for a smooth specimen of a steel (Reproduced from nSoft® User Manual 2001).

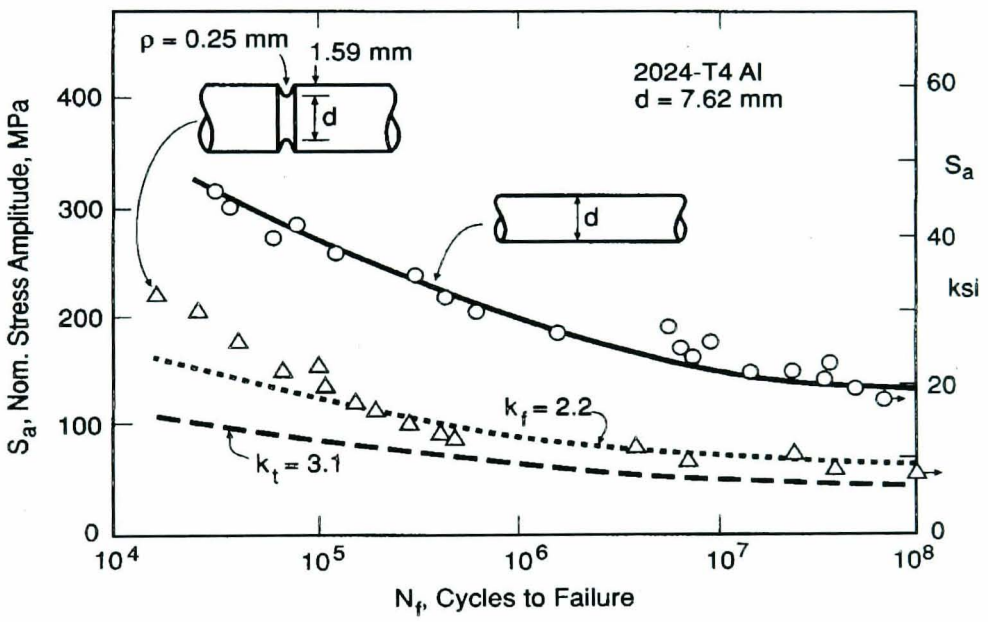

Figure 2.22: Effect of a notch on the rotational bending *S-N* curve of an aluminium alloy (Reproduced from Dowling 1999).

The value of K_t is determined based on specimen geometry and the location of the notch on the specimen. The material constant q is determined using a graph or empirical equation (Peterson 1959; 1974; Neuber 1958). Peterson (1959; 1974) proposed that the q value can be obtained using the expression

$$q = \frac{1}{1 + \alpha'/\rho} \tag{2.32}$$

where α' is a material constant having dimensions of length, and ρ is the notch tip radius. Neuber (1958) has proposed another expression for calculating the *q* value

$$q = \frac{1}{1 + \sqrt{\beta' / \rho}} \tag{2.33}$$

where β' is the material constant, which is different from α'. Detail of the derivation of the two expressions can be found in Dowling (1999). In the case of a notch that is relatively deep and sharp, it can be assumed that the notch is already cracked and the fatigue life can be predicted using the fracture mechanics approach (Taylor and Wang 2000; Ciavarella and Meneghetti 2004).

When no experimental data is available to produce an *S-N* curve, estimates of the fatigue limit can be made by estimating the entire *S-N* curve. The curve estimation is influenced by various factors such as specimen surface, specimen geometry, type of load applied and the presence or absence of notches on the specimen. One commonly used estimation method was introduced by Juvinall and Marshek (1991) for use with a variety of engineering metals. A similar approach for use with only steel was introduced by Shigley and Mischke (1989). Of the two approaches, the Juvinall's approach has been found to be more accurate, as it incorporates nonferrous metals (Dowling 1999).

The strain-life approach considers the plastic deformation that occurs in the localised region where fatigue cracks begin under the influence of a mean stress. This approach is often used for ductile materials at relatively short fatigue lives. This approach is also used where there is little plasticity at long fatigue lives. Therefore, this is a comprehensive approach that can be used in place of the stress-based approach. Consequently, it is common that the service loadings caused by machines and vehicles is evaluated using a strain-life fatigue damage approach (Tucker and Bussa 1977; Downing and Socie 1982; Conle and Landgraf 1983; Conle and Chu 1997; Chu 1998; Dowling 1999).

Completely reversed CA loading fatigue tests are used to provide information for developing a strain-life curve. Completely reversed CA is defined as the loading with zero mean amplitude, for which the ratio of the minimum and the maximum amplitude of this loading is –1. The procedure to construct strain-life curves can be found in ASTM E739-91 (1998) and in Williams *et al.* (2003). The procedure involves testing smooth specimens under uniaxial loading at different strain amplitudes for a particular number of cycles to failure or N_f. The results from the test are used to produce strain-life curves, such as the one shown in Figure 2.23.

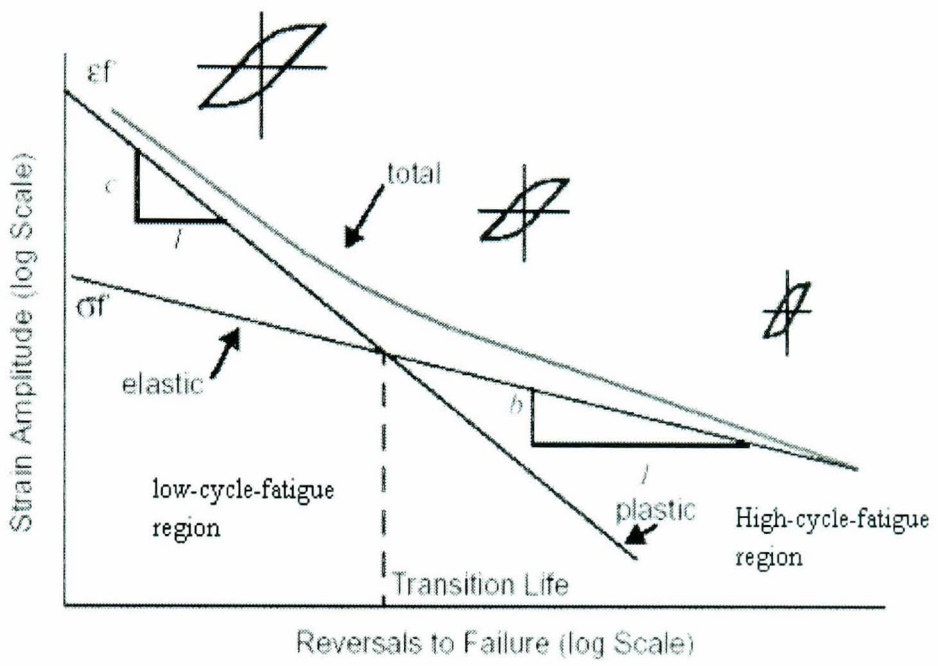

Figure 2.23: Strain-life curve (Reproduced from nSoft® User Manual 2001).

According to the strain-life plot in Figure 2.23, the total strain amplitude, ε_a is produced by the combination of elastic and plastic amplitudes

$$\varepsilon_a = \varepsilon_{ea} + \varepsilon_{pa} \tag{2.34}$$

where ε_{ea} is the elastic strain amplitude and ε_{pa} is the plastic strain amplitude. The elastic strain amplitude is defined by

$$\varepsilon_{ea} = \frac{\sigma_a}{E} = \frac{\sigma_f{}'}{E}\left(2N_f\right)^b \tag{2.35}$$

while the plastic strain amplitude is given as

$$\varepsilon_{pa} = \varepsilon_f'\left(2N_f\right)^c \tag{2.36}$$

where σ_a is the stress amplitude, N_f is the number of cycles to failure, σ'_f is the fatigue strength coefficient, b is the fatigue strength exponent, ε'_f is the fatigue ductility coefficient, c is the fatigue ductility component and E is the modulus of elasticity. A combination of Eq. (2.35) and Eq.(2.36) gives the Coffin-Manson relationship, which is the foundation of the strain-life approach. The relationship arose from the works by Coffin (1954) and Manson (1965) and it is mathematically defined as

$$\varepsilon_a = \frac{\sigma_f'}{E}(2N_f)^b + \varepsilon_f'(2N_f)^c \tag{2.37}$$

For situations producing long operating lives, the elastic strain is dominant and the plastic strains are relatively small. This situation is called High-Cycle-Fatigue (HCF) region, as shown in Figure 2.23. The inverse is true for short lives, where plastic strains are large compared to the elastic strains. This is called Low-Cycle-Fatigue (LCF) region, as again shown in Figure 2.23. At intermediate lives, there is a point where the elastic and plastic strains have similar strain amplitude.

2.5.2 Mean Stress Effects

The majority of material fatigue data is collected in the laboratory by means of testing procedures which employ fully reversed loadings. However, some of the realistic service situations involve non-zero mean stresses. Therefore, it is extremely important to know the influence of the mean stress, so that the fully reversed laboratory data can be usefully employed in the assessment of real situations. Two mean stress effect models are commonly used, i.e. the Morrow and Smith-Watson-Topper (SWT) strain-life models.

Morrow (1968) was the first to propose a modification to the base-line strain-life curve which accounted for the effect of the mean stress by modifying the elastic part of the strain-life curve. Mathematically, the Morrow model is defined by

$$\varepsilon_a = \frac{\sigma_f'}{E}\left(1 - \frac{\sigma_m}{\sigma_f'}\right)(2N_f)^b + \varepsilon_f'(2N_f)^c \tag{2.38}$$

The SWT strain-life model, which was developed by Smith *et al.* (1970), is defined instead by

$$\sigma_{\max}\varepsilon_a = \frac{(\sigma_f')^2}{E}(2N_f)^{2b} + \sigma_f'\varepsilon_f'(2N_f)^{b+c} \tag{2.39}$$

For the SWT model, the damage parameter is taken to be the product of the maximum stress and the strain amplitude of a cycle.

For loading sequences that are predominantly tensile, the SWT approach is more conservative and therefore recommended. In a case of the loading being predominantly compressive, particularly for wholly compressive cycles, the Morrow model provides more realistic life estimates (nSoft® User Manual 2001; Dowling 1999).

2.5.3 Cycle Counting Methods

Cycle counting is performed in order to reduce a random service history into a simpler form of discrete events. Cycle counted data is used in many strain-life prediction models (Suresh 1991). Detailed descriptions of various cycle counting methods can be found in Dowling (1972) and Fuchs and Stephens (1980). Several cycle counting methods have been introduced for the purpose of fatigue life prediction (ASTM E1049-85 1997), such as the level crossing method, the peak counting method, the simple-range counting method and the rainflow counting method.

The level crossing counting method, illustrated in Figure 2.24, is considered the simplest approach. It involves counting the number of positive slope crossings at specific levels above the mean, and counting the negative slope crossings below the mean. Despite its simplicity, it is not recommended for the fatigue damage analysis as it does not maintain the original history sequence (Conle 1974).

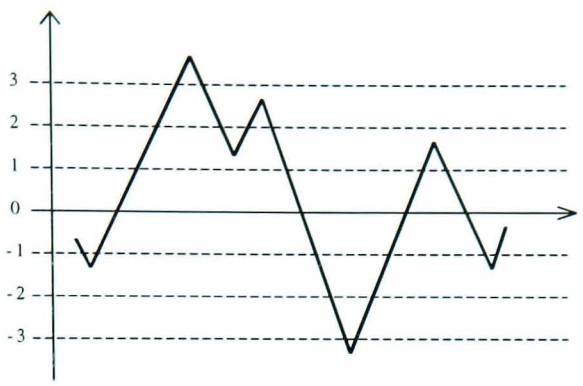

Level	Count
+3	1
+2	2
+1	2
0	2
-1	3
-2	1
-3	1

Figure 2.24: The level crossing counting method.

The peak counting method, illustrated in Figure 2.25, identifies the occurrence of a relative maximum or minimum load. The number of peaks above the reference load level are counted, as are the number of valleys below the reference load. To eliminate small amplitude loadings, mean-crossing peak counting is often used. Instead of counting all peaks and valleys, only the largest peak or valley between two successive mean crossings is counted (ASTM E1049-85 1997). This method is not recommended as it does not relate peaks to their corresponding valleys (Pompetzki 1993).

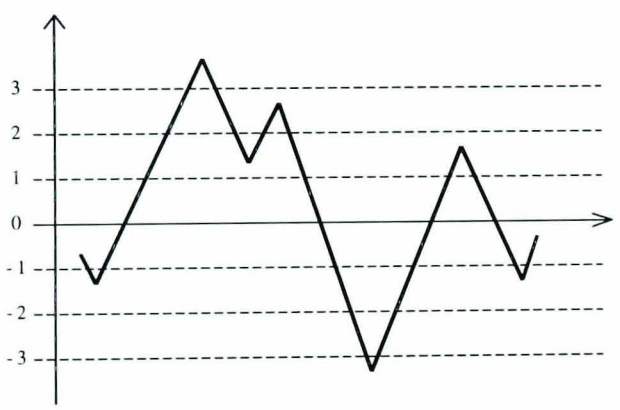

Level	Count
+3.5	1
+2.5	1
+1.5	2
+0.5	0
-0.5	0
-1.5	2
-2.5	0
-3.5	1

Figure 2.25: The peak counting method.

The simple-range method, illustrated in Figure 2.26, is defined as a difference between two successive reversals. The range is positive when a valley is followed by a peak, and negative when a valley follows a peak. If only positive and negative ranges are counted, then each is counted as one cycle. If both positive and negative ranges are counted, then each is counted as one-half cycle. This method is not recommended as it may omit large overall cycles (Fuchs *et al.* 1977).

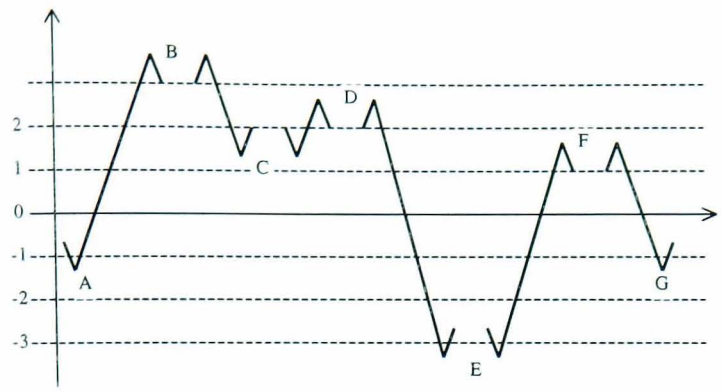

Range (Unit)	Count	Events
6	0.5	D-E
5	1	A-B, E-F
4	0	
3	0.5	F-G
2	0.5	B-C
1	0.5	C-D

Figure 2.26: The simple range cycle counting method.

The most commonly used cycle-counting method is the rainflow counting method, which was developed by Matsuishi and Endo (1968). This method is regarded as the best procedure to identify fatigue cycles in a VA loading (Fuchs and Stephens 1980; Anthes 1997). The rainflow counting method is based on the counting of the ranges and the means of the closed hysteresis loops present in the loading. A closed hysteresis loop is defined as one cycle of the corresponding CA loading. An example of a hysteresis loop can be seen in Figure 2.27 for a particular section of peak-valley reversals. In this figure, the local stress-strain response to the nominal strain time record shows a signal with four amplitude cycles, i.e. B-C-B, E-F-E, G-H-G and A-D-A. The main idea of this method is to treat small cycles as interruptions to larger cycles.

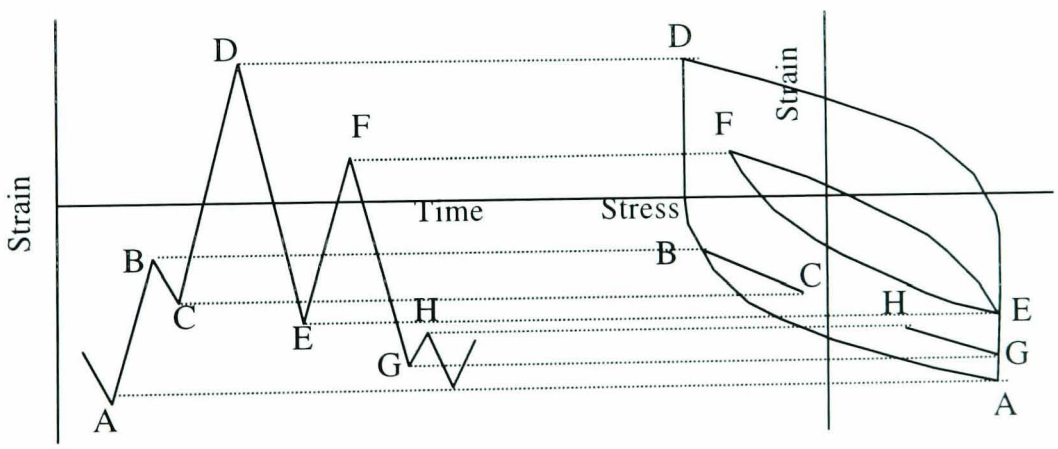

Figure 2.27: Illustration of the rainflow cycle counting.

Figure 2.28 presents an example of the rainflow counting performed for a loading history. In order to apply this counting method for the whole time history, the load must be rearranged from the maximum peak (minimum valley) as the beginning of the history

and to the maximum peak (minimum valley) as the end of the history, as illustrated in Figure 2.28b. Small cycles (Figure 2.28c,d) are extracted in the beginning of the rainflow counting process, leaving larger cycles (Figure 2.28e,f) to be extracted at the end of the process. In practice, several algorithms are available to perform this type of rainflow cycle counting which require the entire uniaxial load history be known before the counting process begins (Wetzel 1971; Downing *et al.* 1977; Socie 1977; Downing and Socie 1982; Hong 1991; Anthes 1997).

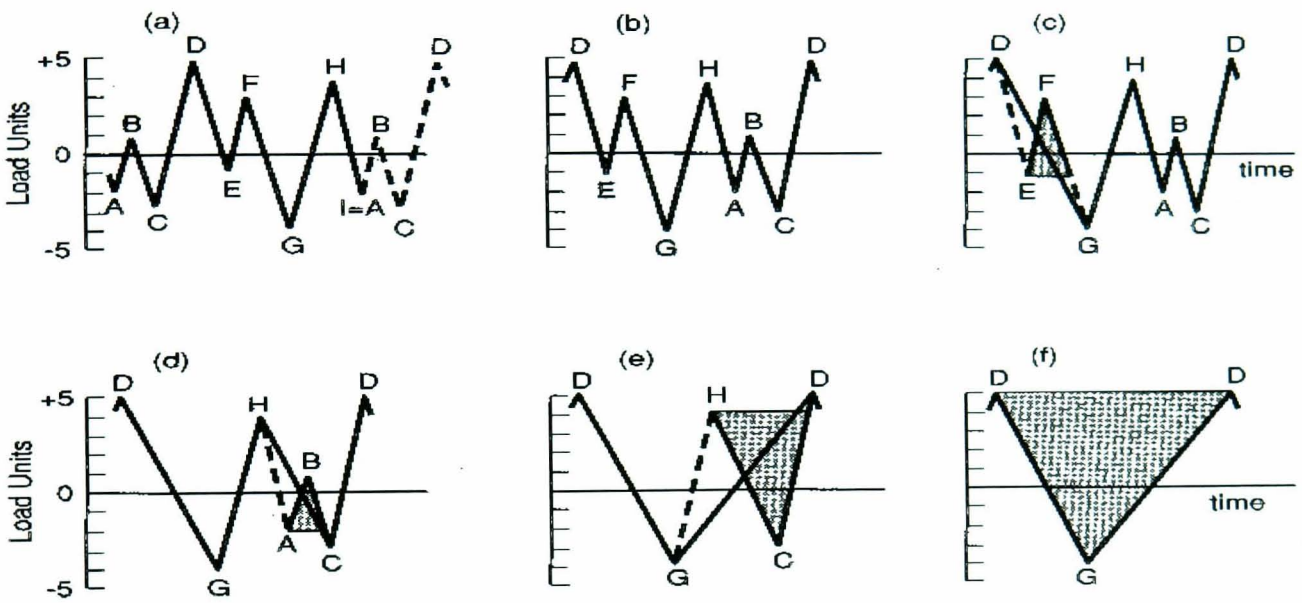

Cycle	Range	Mean
E-F	4.0	1.0
A-B	3.0	-0.5
H-C	7.0	0.5
D-G	9.0	0.5

Figure 2.28: Schematic diagram of the rainflow cycle counting method (Reproduced from Dowling 1999).

As an improvement to the earliest rainflow algorithms which operated only complete load histories, several optimised algorithms have been developed for use in real-time cycle counting. Two different algorithms were developed (Downing and Socie 1982; Clormann and Seeger 1986) for the purpose of analysing short uniaxial load histories. In the paper by Downing and Socie (1982), two simple rainflow counting algorithms for processing field data were discussed. One required the complete time history while the other was appropriate for on-board real-time cycle counting. Both methods produced identical results, but real-time cycle counting was found to offer the advantage that

counting can begin before the entire history is known. Another real-time rainflow counting algorithm was developed by Glinka and Kam (1987) for the use in the case of long uniaxial stress histories.

While rainflow counting has been widely and successfully applied to uniaxial loadings, no commonly accepted approach has been found to describe multiaxial loadings. This is because closed hysteresis loops are not readily defined for multiaxial loadings. For an example of applying the cycle counting using these loadings, Wang and Brown (1993; 1996) introduced a counting method to estimate the damage of a planar structure. This method counts cycles of relative equivalent strain, whereby a cycle is defined by a zero-to-maximum increase in the relative equivalent strain.

A detailed explanation of the cycle counting procedure and its schematic diagram can be found in most of the fatigue cycle counting documents and textbooks, including Fuchs and Stephens (1980), Downing and Socie (1982), ASTM E1049-85 (1997) and Dowling (1999).

2.5.4 The Palmgren-Miner Linear Damage Rule

With respect to the relationship between damage and cycle, the damage for one cycle, D_i, can be calculated as

$$D_i = \frac{1}{N_{fi}} \tag{2.40}$$

where N_{fi} is the number of constant amplitude cycles to failure. To calculate the fatigue damage for a block of VA loading, a linear cumulative damage approach has been defined by Palmgren (1927) and Miner (1945). The technique, known as the Palmgren-Miner (PM) linear damage rule, is defined as

$$D = \sum_{i=1}^{n} \frac{N_i}{N_{fi}} \tag{2.41}$$

where n is the number of loading blocks, N_i is the number of applied cycles and N_{fi} is the number of constant amplitude cycles to failure. Using this equation, component failure occurs when $D \geq 1$. Figure 2.29 presents the notation used in the application of the Palmgren-Miner linear damage rule. The damage calculation using the load in Figure 2.29 can be performed using Eq. (2.42). For three loading blocks, the values of N_{f1}, N_{f2} and N_{f3} are determined from the corresponding stress-life curve at the respective stress of σ_1, σ_2 and σ_3.

$$D = \frac{N_1}{N_{f1}} + \frac{N_2}{N_{f2}} + \frac{N_3}{N_{f3}} \tag{2.42}$$

Several limitations are found while implementing the Palmgren-Miner linear damage rule. The fatigue damage is accurately calculated for CA loadings, but it may lead to the erroneous prediction for VA loadings. This is because the Palmgren-Miner linear damage rule does not consider load sequence effects and lacks load interaction accountability. In order to prove this, two-step loading tests were performed by Bilir (1991) who showed that the damage accumulation values were less than unity when the load changed from low cycle fatigue to high cycle fatigue. The change of loading from high cycle fatigue to low cycle fatigue gave damage greater than unity. An example of the diagram used for this loading sequence is shown in Figure 2.30.

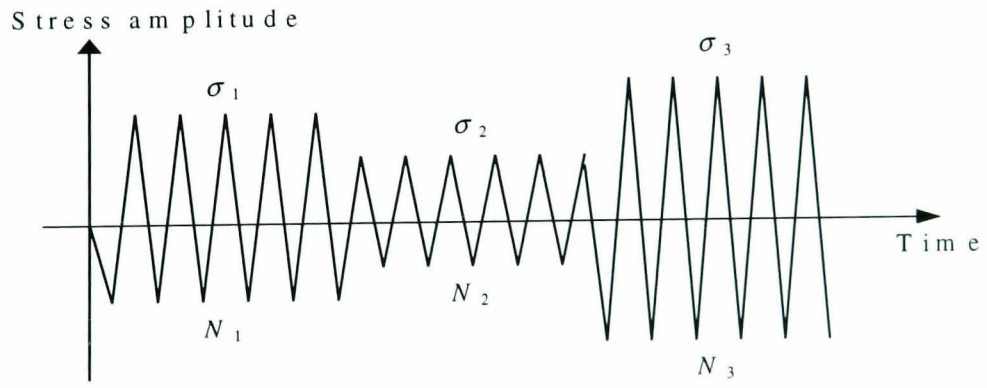

Figure 2.29: Block loading sequences for the Palmgren-Miner rule application.

In spite of the weaknesses of the Palmgren-Miner linear damage rule, it is widely used for the purpose of fatigue life prediction (Kliman 1985; Zheng 2001; Oh 2001; Memon *et al.* 2002). Often, the analytical fatigue life determined using the rule is found to be

acceptable compared to the experimental outcomes (Fatemi and Yang 1998). The majority of fatigue life predictions performed using commercial software packages today use material data obtained from CA loadings and the Palmgren-Miner rule.

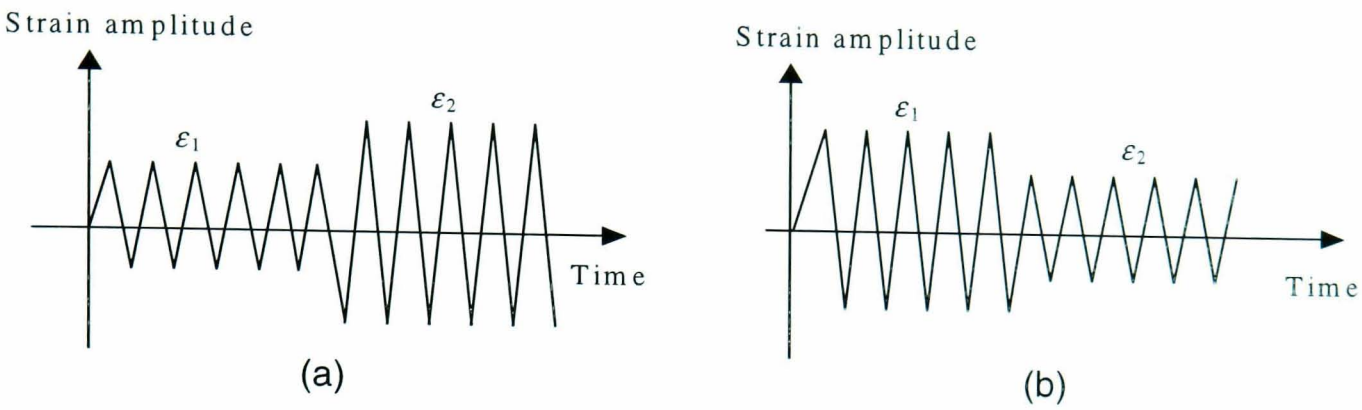

Figure 2.30: Different loading sequences: (a) low-high order, (b) high-low order.

2.5.5 Influence of the Sequence Effects

The situation where the order of loading affects the fatigue life is called a sequence effect. Sequence effects exist both in the early stage (crack initiation) and in the later stage (crack propagation) of fatigue.

An example of a cycle sequence effect is shown in Figure 2.31 (Mitchell 1996). Both load histories seem to have cycles with the same strain range, but in a different order. The first history (Figure 2.31a) has tensile leading edge as an initial transient, and the second history (Figure 2.31b) has a compressive leading edge as an initial transient. In the hysteresis loops of History A, the small cycles have the tensile mean, while in hysteresis loops of History B the small cycles have a compressive mean. In this case History A produces more damage than History B.

Sequence effects can also occur in cases involving overloads (OL) and underloads (UL). For example, when tensile or compressive OLs are inserted into a small cycle history, or below the material fatigue limit, the small cycles following the OL events contribute significantly to the damage accumulation. Extensive studies of the effect of OL and UL on the fatigue of the metal components have been performed by Pompetzki

et al. (1990a; 1990b), Jurcevic *et al.* (1990), DuQuesnay *et al.* (1993), Changqing *et al.* (1996), Hawkyard *et al.* (1996) and Bonnen and Topper (1999).

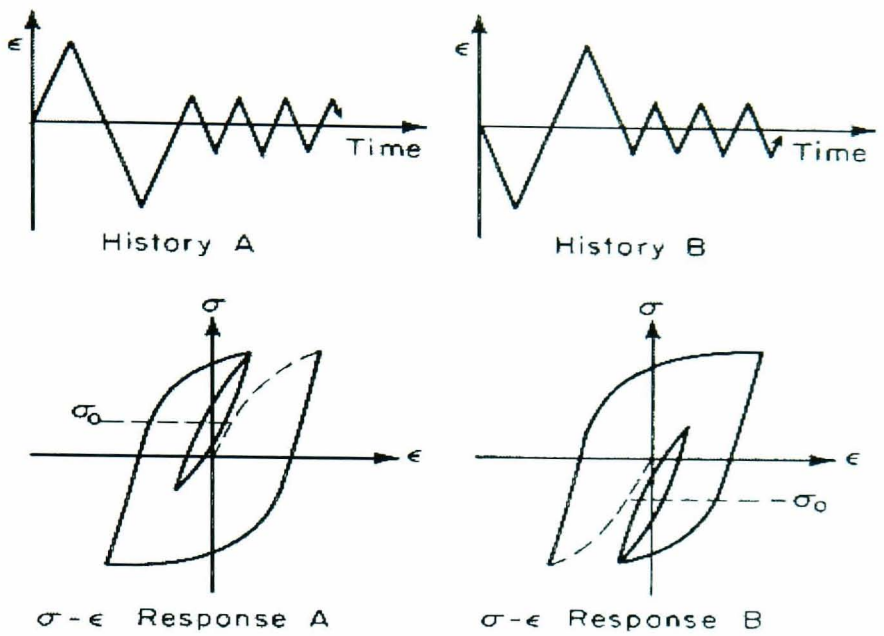

Figure 2.31: Two loading histories having similar strain ranges but different leading edge loadings (Reproduced from Mitchell 1996).

Considering the importance of sequence effects, and limitations of the Palmgren-Miner linear damage rule when handling VA loadings, a suitable approach needs to be defines for calculating the fatigue damage caused by these loadings. The approach should be capable to solve fatigue life predictions using various VA loadings. The next section describes one such approach.

2.5.6 Fatigue Damage Model for Variable Amplitude Loadings

The problem of performing fatigue life predictions for uniaxial and multiaxial VA fatigue loadings has been discussed by Fatemi and Yang (1998) and Banvillet *et al.* (2004), respectively. Previously, the fatigue strength of metals has conventionally been measured using CA fatigue tests for determining the strain-life or the stress-life curve of the material. However, it has been noted that the experimental fatigue lives of components subjected to VA loadings can be well below the fatigue life predicted using CA fatigue tests (Heuler and Seeger 1986; Dowling 1988; Yan *et al.* 1992). The reason

for these fatigue life differences is that a VA loading contains a mixture of large and small amplitude cycles which contribute to the cycle sequence effects. In addition, the large load cycles in a VA loading affect the increment of the effective stress for the subsequent smaller cycles. Hence, the crack growth rate for the smaller cycles is increased, and even small cycles below the CA fatigue limit can cause a significant amount of fatigue damage (Vormwald and Seeger 1991; DuQuesnay *et al.* 1995; Topper and Lam 1997).

Several investigators have proposed methods for improving the fatigue life prediction for components subjected to VA loadings. Models have been derived using random vibration theory (Liou *et al.* 1999), using non-linear damage summation (Marco and Starkey 1954; Plumtree and Shen 1990; Shang and Yao 1999), and by adopting a fracture mechanics approach (Wheeler 1972; Willenborg *et al.* 1971; Veers *et al.* 1989; Taheri *et al.* 2003). Methods of modifying the stress-life and strain-life approaches have been suggested in order to predict the fatigue life of the metal structures and automobile components exposed to VA loadings (Conle and Topper 1980; Yan *et al.* 1992). However, fatigue life prediction using these methods is generally specific to a specific material.

Although such models have provided improved fatigue life predictions under VA loadings compared to the CA linear damage methods under specific conditions, they have proved difficult to incorporate in fatigue life prediction programmes for general use (DuQuesnay *et al.* 1993). Considering the limitations observed in the fatigue life predictions determined for VA loadings, the use of a simple linear damage model such as the Palmgren-Miner rule has been found to be unsuitable. Therefore, a fatigue damage model for use with VA strain loadings was developed by DuQuesnay *et al.* (1993), called the Effective Strain Damage (ESD) strain-life model. This model is based on crack growth and crack closure mechanisms. It has been shown to work well for a wide range of materials, load spectra, component geometries, strain magnitudes and mean-strain effects (DuQuesnay *et al.* 1992a; 1992b; 1993; Topper and Lam 1997; DuQuesnay 2002).

The ESD strain-life model was developed for the purpose of life to crack detection, which is based on the use of the effective strain range as the damage parameter. Using this model, the fatigue damage can be analysed based on the assumption of short crack growth, since the crack length at failure is usually less than a few millimetres. The ESD strain-life model is defined as

$$E\Delta\varepsilon^{*} = A(N_f)^{B} \tag{2.43}$$

where E is the elastic modulus of the material, $\Delta\varepsilon^{*}$ is the net effective strain range for a closed hysteresis loop which is related to fatigue crack growth, A and B are material constants, and N_f is the number of cycles to failure. The study by DuQuesnay *et al.* (1993) determined the curves shown in Figure 2.32 of ESD strain-life for SAE 1045 steel and aluminium alloy.

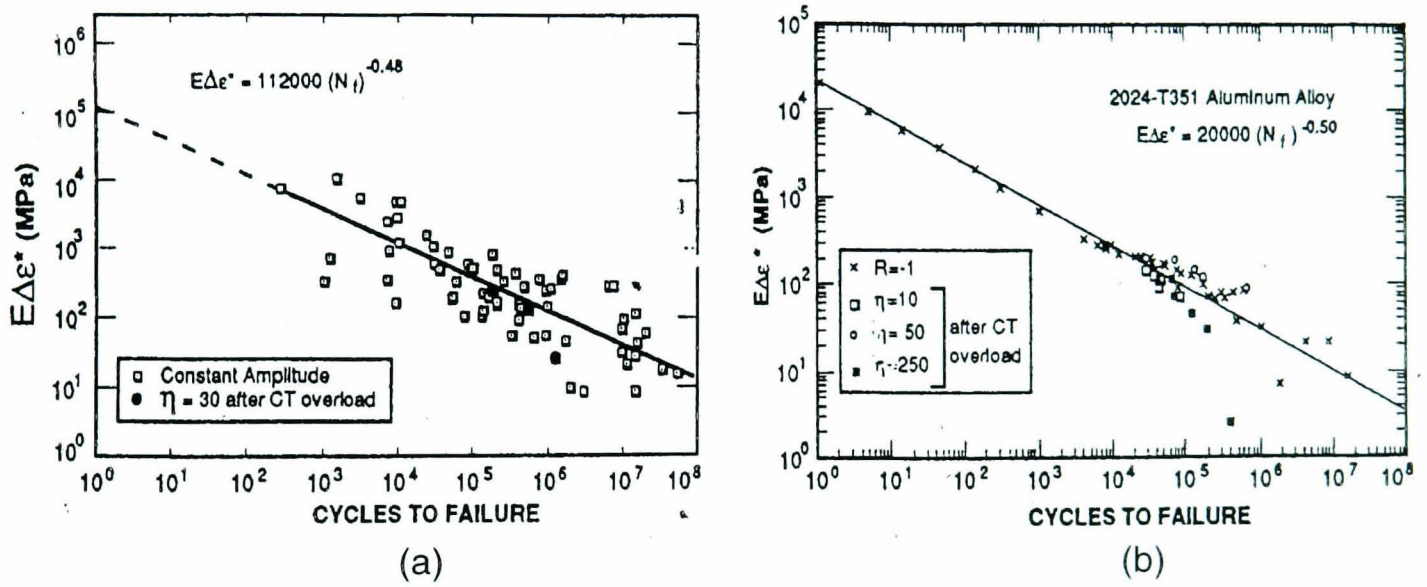

Figure 2.32: Curve of effective strain range ($E\Delta\varepsilon^{*}$) versus number of cycles to failure (N_f) for: (a) SAE 1045 steel, (b) 2024-T351 aluminium alloy. (Reproduced from DuQuesnay *et al.* 1993).

The magnitude of $E\Delta\varepsilon^{*}$ for a given cycle is a function of the crack-opening stress (S_{op}) and is dependant on the prior stress and strain magnitudes in the loading history. Studies by Topper *et al.* 1991 and DuQuesnay *et al.* 1992 have shown that the parameter $E\Delta\varepsilon^{*}$ sufficiently accounts for the mean stress effect of the CA loading. The left side of Eq. (2.43) can be expanded to the form

$$E\Delta\varepsilon^{*} = E(\varepsilon_{\max} - \varepsilon_{op}) - E\varepsilon_{i} \tag{2.44}$$

where

$$\Delta\varepsilon_{eff} = \varepsilon_{\max} - \varepsilon_{op} \tag{2.45}$$

In both equations, ε_{max} and ε_{op} are the maximum strain and the crack-opening strain of the particular cycle, respectively. If ε_{op} is smaller than the minimum strain (ε_{min}) for a particular cycle, then ε_{op} is equal to ε_{min}. Another parameter is ε_i, which is the intrinsic fatigue limit strain range under the VA loading. The difference of ε_{max} and ε_{op} is known as the effective strain range ($\Delta\varepsilon_{eff}$). It is the strain range which opens a fatigue crack.

The measurement of steady crack opening levels, or S_{op}, is difficult, time consuming and requires equipment which is not available in many laboratories (Topper and Lam 1997). As a result, several analytical and experimental studies have been performed to determine the crack opening stress, S_{op}, which leads to the crack opening strain, ε_{op}.

In order to consider the cycle sequence effects in the fatigue life calculation, a decay parameter is used to define the change in a crack-opening stress between two adjacent cycles (Dabayeh and Topper 1995; Khalil *et al.* 2002, Khalil and Topper 2003). The formula of the change in crack opening or ΔS_{op} was first proposed by Vormwald and Seeger (1991) i.e.

$$\Delta S_{op} = m(S_{ss} - S_{cu}) \tag{2.46}$$

where m is a material constant, S_{cu} is the current opening stress and S_{ss} is the steady-state opening stress. The m value is determined by means of a curve fitting method performed using a graph of crack opening stress versus number of cycles to failure (see Figure 2.33 for the SAE 1045 steel). The graph in Figure 2.33 shows a value of 0.002 gave a good fit for the measured crack opening stress using SAE 1045 steel (Khalil and Topper 2003).

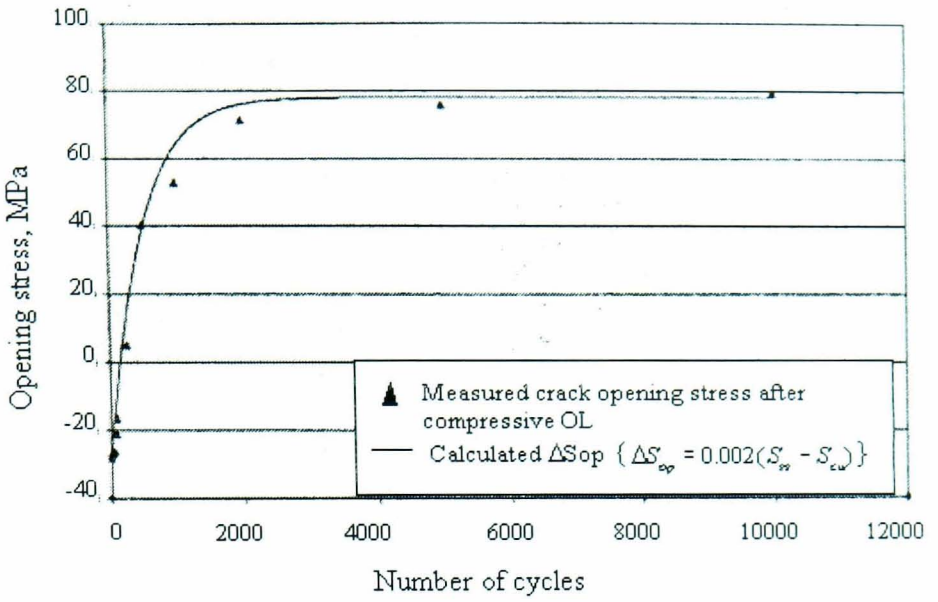

Figure 2.33: Curve fitting for the crack-opening stress build-up data for SAE 1045 steel (Reproduced from Khalil and Topper 2003).

In Eq. (2.46), the current opening stress, S_{cu}, is determined from the previous value of crack opening stress or S_{op}. The value of steady-state opening stress S_{ss} is calculated using the following expression

$$S_{ss} = \alpha S_{\max}\left(1-\left(\frac{S_{\max}}{S_{cy}}\right)^2\right)+\beta S_{\min} \tag{2.47}$$

where α and β are material constants which are obtained from a curve fitting procedure performed using a graph of the measured crack opening stress versus the maximum stress (DuQuesnay *et al.* 1992a; 1992b; Topper and Lam 1997) as shown in Figure 2.34. S_{max} is the maximum stress of the previous largest cycle in the time history, S_{min} is the minimum stress of the previous largest cycle and S_{cy} is the cyclic yield stress.

For the application of the ESD model, the loading spectrum needs to be rainflow counted (Matsuishi and Endo 1968) to determine the fatigue life for each cycle. This fatigue life can be determined from Eq. (2.41), which can be rearranged to the form

$$N_f = \left(E\Delta\varepsilon^*/A\right)^{1/B} \tag{2.48}$$

Using the ESD model to predict the fatigue life of metal components has been shown to provide better results than the Palmgren-Miner linear damage rule.

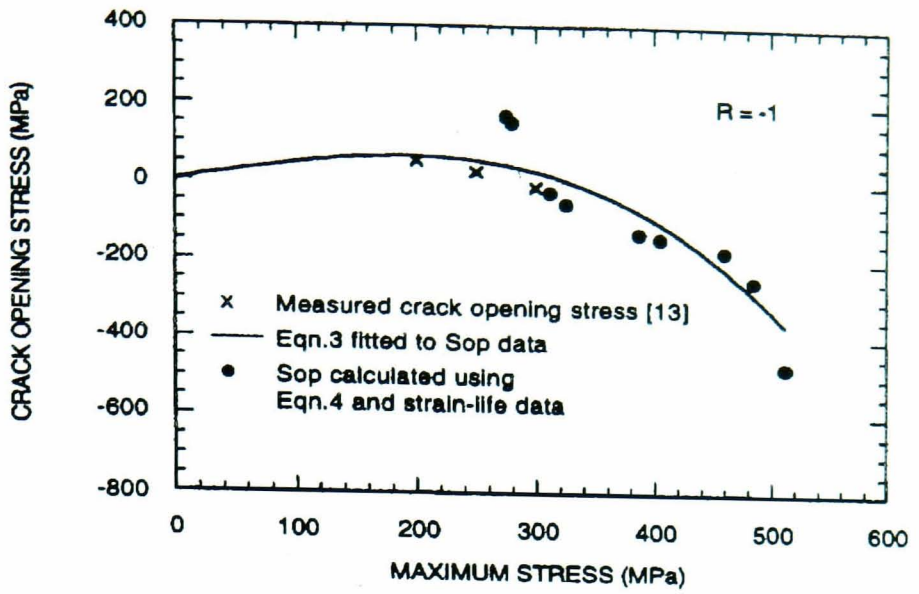

Figure 2.34: Curve fitting of the experimental data using Eq. (2.47) in order to find the α and β values, performed by Topper and Lam (1997).

Research by DuQuesnay *et al.* (1993) and by Topper and Lam (1997), for which the results are presented in Figure 2.35, showed the comparison between the fatigue lives predicted using the ESD model and Smith-Watson-Topper (SWT) model, and the experimentally determined fatigue lives. Smooth specimens of the SAE 1045 steel and 2024-T351 aluminium alloys were used under two types of VA fatigue loadings. In this figure for steel and aluminium alloy, the ESD model produced the fatigue life predictions that follow the trend of the experimental data. However, the predictions using CA strain-life data by means of the SWT model significantly overestimate the fatigue lives when comparing to the experimental data. The main finding of the study DuQuesnay *et al.* (1993) and by Topper and Lam (1997) confirmed that the accuracy of the ESD model in predicting fatigue lives of VA loadings for different types of materials.

In a study by Choi (2004), uniaxial fatigue tests using eleven VA loadings were performed using smooth specimens of BS 080A42 steel. The loadings were measured from the lower suspension arm of a road vehicle travelling over a pavé test track surface. The experimental fatigue damage were compared to the prediction results obtained using four strain-life models, i.e. Coffin-Manson, Morrow, SWT and ESD. Referring to Figure 2.36, the ESD model produced the closest correspondence between prediction and experiment, with an average difference of only 5%. From this study (Choi

2004), it is concluded that the ESD model is a suitable approach for predicting fatigue lives or fatigue damage using metal components.

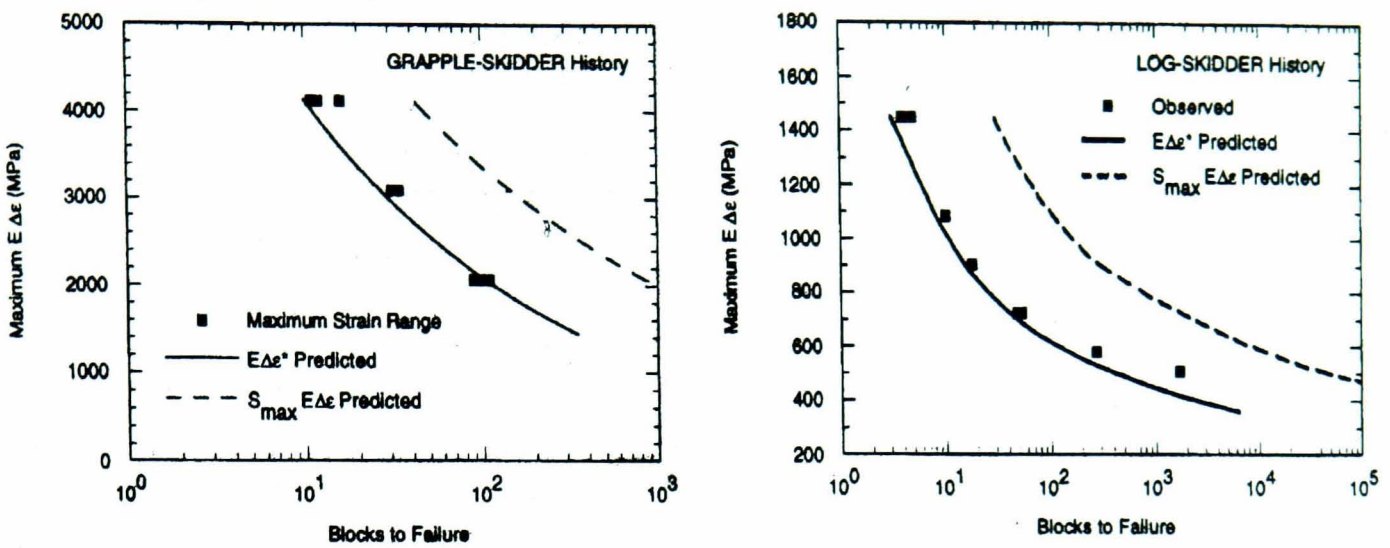

(a) (b)

Figure 2.35: Comparison between the experimental and predicted fatigue lives for:

(a) SAE 1045 steel tested using the grapple-skidder history,

(b) 2024-T351 aluminium alloy using the log-skidder history.

(Reproduced from Topper and Lam 1997)

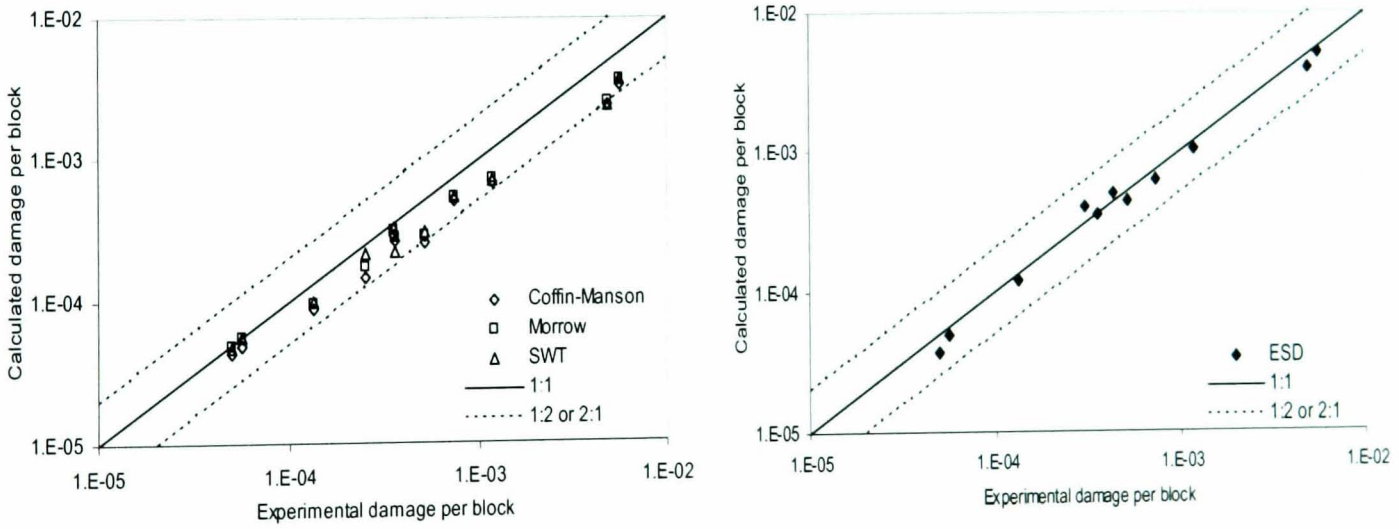

(a) (b)

Figure 2.36: Fatigue damage correlation between the prediction and experiment for BS 080A42 steel (Choi 2004): (a) The Coffin-Manson, Morrow and SWT strain-life models, (b) The ESD strain-life model.

2.6 Fatigue Data Editing Techniques

Fatigue data editing is a technique to remove small amplitude cycles that lead to minimal fatigue damage (Frost *et al.* 1974). In this approach, large amplitude events which produced the majority of damage are retained, so as to produce a shortened loading for accelerated fatigue tests (Conle and Topper 1979; Conle *et al.* 1997).

Section 2.6.1 to Section 2.6.4 contain overview of the currently available fatigue data editing techniques which are used for summarising long records of variable amplitude fatigue loadings. Section 2.6.5 discusses instead the application of the wavelet transform as an approach for performing fatigue data editing.

2.6.1 Editing in the Time Domain

Time series data is the most general format data, containing all the information of relevance to fatigue analysis. Time domain editing techniques have been developed to remove time segments, for an example, using the method called Time Correlated Fatigue Damage (TCFD) analysis. TCFD, as implemented in the nSoft® software package, is used to remove non-damaging sections of the time history on the basis of time correlated fatigue damage windows of the input signal.

Using the time domain editing approach, the damage signal is divided into a number of time segments. Fatigue damage is then calculated for each time-window containing a short segment of time history. Windows having minimal damage are removed, so as to retain the windows containing the majority of the fatigue damage. These windows are assembled together in order to produce a shortened signal for the purpose of the durability analysis. Using this approach, both the percentages of damage retention and the required acceleration factors, or one of them, could be set as editing targets (nSoft User Manual 2001). This technique is recommended as it maintains the phase and amplitude of the original signal (El-Ratal *et al.* 2002).

2.6.2 Editing in the Frequency Domain

In the frequency domain, fatigue loading time histories are often low-pass filtered in order to reduce small amplitudes located in the high frequency region of PSD distribution (Morrow and Vold 1997). The idea behind the method is that small amplitude events do not cause much fatigue damage. Unfortunately, the low pass filter does not reduce the length of the signal, but almost certainly reduces the fatigue damage. Therefore, the frequency domain editing technique is not recommended, as the time series regenerated from a frequency spectrum does not produce the same fatigue life.

2.6.3 Editing in the Peak-Valley Domain

The peak-valley (PV) editing technique reduces the number of points of the original loading. This technique can be used when the signal frequency content is not important for the fatigue damage analysis. However, the time information of the original time history is lost when using this fatigue data editing technique. An example of the PV editing technique is presented in Figure 2.37, showing the removal of small PV pairs using a range omission (Mercer *et al.* 2003).

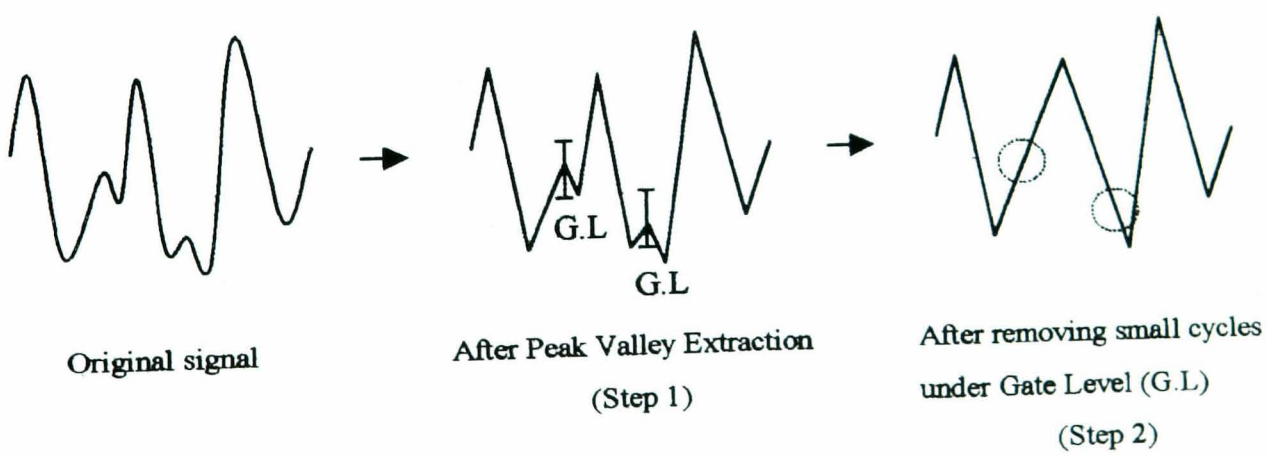

Figure 2.37: Peak-Valley extraction procedure.

2.6.4 Editing in the Cycle Domain

The rainflow cycle counting method (Matsuishi and Endo 1968) is used as the basis for the cycle domain fatigue data editing technique. A time history is rainflow cycle counted in order to extract the fatigue cycles and also to produce a range-mean histogram. An example of the range-mean histogram produced from a variable amplitude fatigue loading measured from a road vehicle lower suspension arm is presented in Figure 2.38. From this histogram, the identified small cycles having minimal damage are removed, and the damaging cycles are retained in the edited loading.

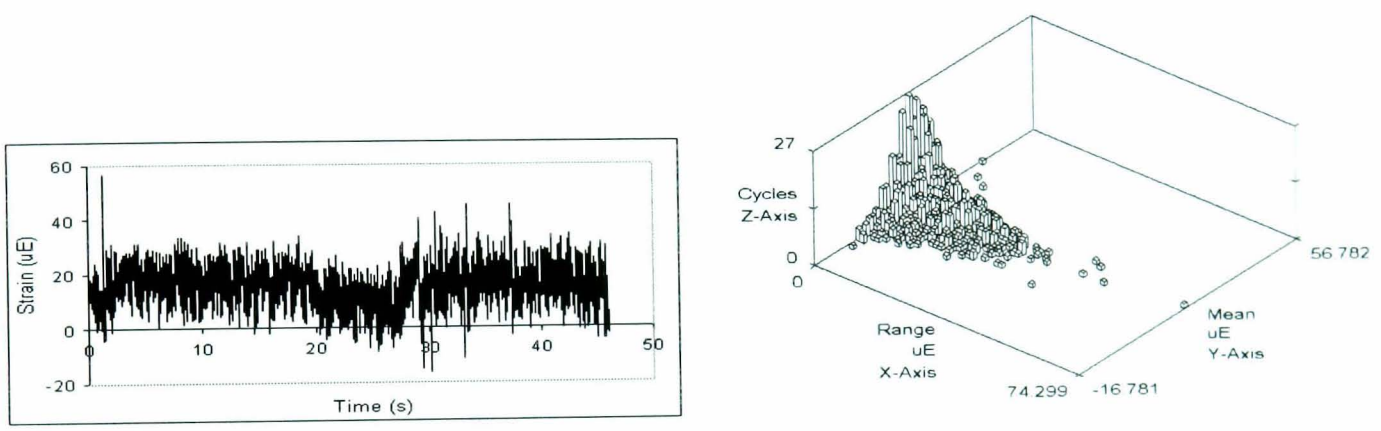

Figure 2.38: Example of a variable amplitude fatigue loading time history and its fatigue range-mean histogram.

2.6.5 Editing in the Time-Frequency Domain

For editing in the time-frequency domain by means of the wavelet-based fatigue data editing, only two research studies have been found in literature. They are a study conducted by Oh (2001) using a VA loading measured on light railway train component and by Abdullah *et al.* (2004) using a VA loading measured on automobile component. The wavelet-based fatigue data editing using the vibration and comfort mission synthesis algorithm, which was performed by Abdullah *et al.* (2004), is discussed in Section 2.7.

In a research by Oh (2001), the wavelet transform was identified as an approach for editing VA fatigue loadings. A 30th order Daubechies wavelet at the decomposition level 3 was used to perform the fatigue data editing by means of denoising, spike removal and signal compression. The wavelet order and level were chosen based on a correlation coefficient which was calculated between the original signal and the denoised signal. A VA loading measured from a light railway train component travelling over a test rail at the maximum speed of 80 km/h, having 103,700 data points (28,390 PV reversals), was used for the analysis. Using the 30th order Daubechies wavelet function at decomposition level 3, the background noise and spikes of the original signal were removed. As a result, the original signal was compressed into 8,349 PV reversals. At this shortened signal length, approximately 80% of the original loading fatigue damage was retained with the reduction of 71% in the original record length. In this case, the fatigue damage was calculated using the Palmgren-Miner linear damage rule with the SWT mean stress correction effect which does not account for load sequence effects.

2.7 Mildly Nonstationary Mission Synthesis (MNMS) Algorithm

2.7.1 The MNMS Method

The Mildly Nonstationary Mission Synthesis (MNMS) algorithm was initially developed by Giacomin *et al.* (1999) for defining vibration mission signals for vehicle components. MNMS represents a method of summarising mildly non-stationary vibration records to obtain short mission signals that can be used for experimentation or numerical testing. MNMS was conceived by recognising that mildly non-stationary behaviour could be simulated by inserting the characteristic high peaks from a road record into a synthesised background signal equivalent to the underlying random Gaussian vibration of the original process. It is based on signal processing algorithms (Discrete Fourier transform and orthogonal wavelet transform) and the use of simple peak selection techniques. The output mission signals replicate the vibration characteristics of the input

data in terms of the global statistical values of root-mean-square, skewness, kurtosis, crest factor and power spectral density (PSD). Three main stages were found in MNMS:

- Application of the discrete Fourier transform to the original signal to determine the background power spectral density of the input signal;
- Application of the orthogonal wavelet transform to the original signal for the purpose of subdividing the signal into frequency bands (wavelet groups);
- Identification of bumps in the wavelet groups, and the reinsertion of these bumps into the artificial background signal so as to 'correct' it. In MNMS, a bump is defined as an oscillatory transient characterised by a monotonic decay envelope either side of the peak value.

In MNMS a reinsertion procedure is used to reinsert bumps into the Fourier background signal. Two bump reinsertion procedures are defined. In proportional reinsertion bumps are chosen by moving down the list of sorted bumps in descending steps equal to the compression ratio. In maximal reinsertion, all the bumps that can be fit into the Fourier signal are reinserted starting from the first event and continuing until there is no further space in the signal.

When reinserting bump events coming from different wavelet groups, three synchronisation procedures are, i.e. Nonsynchronised (Figure 2.39a), Synchronisation 1 (Figure 2.39b) and Synchronisation 2 (Figure 2.39c).

The nonsynchronised procedure treats each wavelet group independently, assuming that a bump which occurs in one wavelet group has no relation to bumps in any other wavelet group. The bumps were reinserted independently into the respective wavelet groups of the Fourier signal.

The synchronisation 1 procedure reinserts group of bumps from different wavelet groups which occur simultaneously in time. The wavelet group associated with the lowest frequency band is used as the basis for the synchronisation check. All bumps from

Wavelet Groups 2 and above which were found to occur at the same time of a bump in Wavelet Group 1 were clustered together. The clustered bumps were reinserted into Wavelet Group 1 of the Fourier signal. Then, the remaining independent bumps were fitted in the remaining unoccupied space in each of the Fourier wavelet groups.

Synchronisation 2 involves reinserting whole segments of the original loading into the Fourier signal. If a bump is found in any of the wavelet groups, a block of data covering the time extent of the bump is taken from the original data set and substituted into the Fourier signal. This is the most conservative of the bump reinsertion strategies since it retains all of the original amplitude and phase relationships of the original signal.

Detailed descriptions of the MNMS algorithm for performing vibrational comfort mission synthesis are found in Giacomin *et al.* (1999; 2000; 2001), Grainger (2001) and Steinwolf *et al.* (2002).

2.7.2 MNMS as the Fatigue Data Editing Technique

MNMS was customised for the purpose of performing fatigue mission synthesis by Abdullah *et al.* (2004). The aim of the research described in the paper was to investigate the effectiveness of the MNMS algorithm in the fatigue analysis application and to develop new modules based on the fatigue damage properties of the individual bump events. Several experimental road load data sets were used to analyse the fatigue life properties of vehicle components under transient loadings such as potholes and curb strikes. Using MNMS, the extraction and reinsertion of these bumps retains important information which is often lost by conventional strain-life fatigue analysis tools which ignore the load cycle sequence. Consideration of the fatigue damage potential of each individual bump during the operations leading to the shortened mission signal was expected to produce shorter and more accurate sequences.

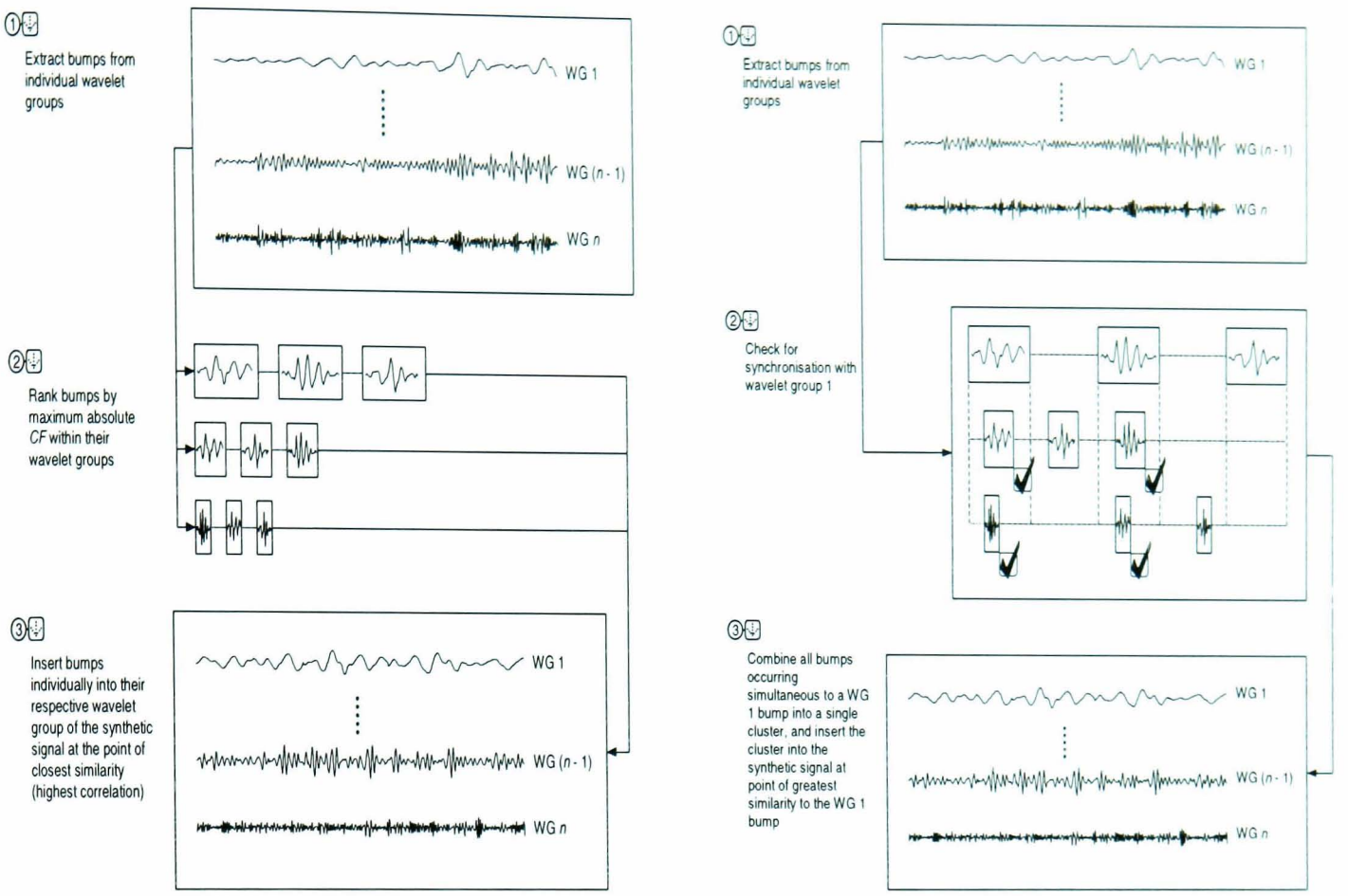

Figure 2.39: Operational diagrams of the MNMS bump reinsertion processes: (a) Nonsynchronised, (b) Synchronisation 1, (c) Synchronisation 2.

In order to develop and validate the needed procedures, a fatigue analysis case study was performed using two sets of experimental data measured on the lower suspension arm of a vehicle travelling over a pavé surface at 34 km/h. These VA loadings, as shown in Figure 2.40, have different amplitudes of mean strain, i.e. a loading with tensile (above zero strain level) mean strain and a loading with compressive (below zero strain level) mean strain. Using the MNMS algorithm, mission signals were produced by shortening the originals by a factor of up to 10. The fatigue damage of these signals was then calculated using the Palmgren-Miner linear damage rule, adopting both the Morrow and SWT mean stress correction models.

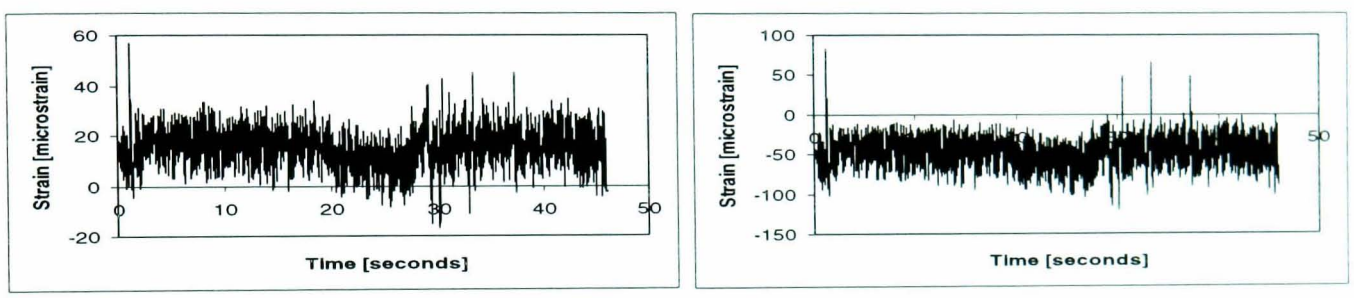

(a) (b)

Figure 2.40: Variable amplitude fatigue loading used for the purpose of fatigue data editing by means of the MNMS algorithm (Reproduced from Abdullah *et al.* 2004):

(a) A loading having tensile mean strain,

(b) A loading having compressive mean strain.

Figure 2.41 presents one of the results presented in Abdullah *et al.* (2004). The values of fatigue damage obtained for the tensile mean strain loading using the Palmgren-Miner linear damage rule with the Morrow and SWT mean stress correction effects are shown plotted against the compression ratio of the mission signal with respect to the original data. In this figure, target is defined as the fatigue damage level that should be achieved by the mission signals at all compression ratios. For the case of maximum reinsertion (Figure 2.41a), the target damage of the original signal is a straight line at all compression ratios. In an ideal scenario the concept of maximum reinsertion might permit the damage to remain constant when most of the bumps are reinserted into the

synthetic Fourier signal. For all three synchronisation procedures, however, the fatigue damage at all compression ratios decreased as the compression ratio increased. For the case of proportional reinsertion (Figure 2.41b), the fatigue damage values at all synchronisation procedures and the fatigue damage target line decreased in proportion to the compression ratio.

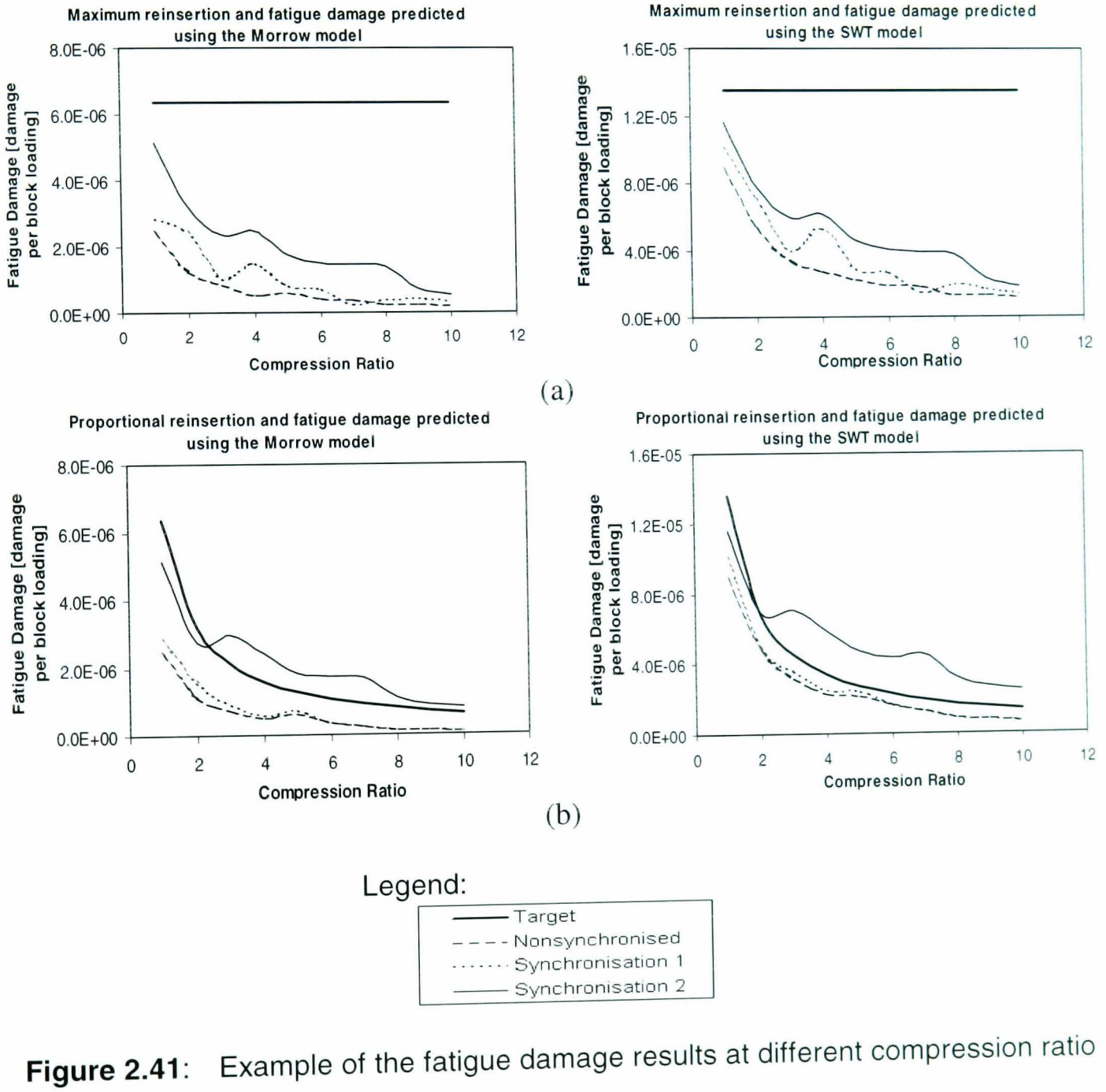

Figure 2.41: Example of the fatigue damage results at different compression ratio values using the VA loading having tensile mean strain loading for: (a) Maximum reinsertion, (b) Proportional reinsertion.

From the results in Figure 2.41, the decrement of fatigue damage using all synchronisation procedures when the compression ratio values increased, was due to not all the fatigue damaging events being reinserted into the Fourier signal. This is the

main disadvantage of the MNMS algorithm when used for fatigue data editing. In an ideal approach to fatigue data editing, high amplitude events must be retained to produce a shortened signal with equivalent fatigue damage to the original signal. Comparing the fatigue damage values for both reinsertion processes, the Synchronisation 2 procedure produced higher fatigue damage compared to other synchronisation procedures, as the mission signals preserved the original phase and amplitude relationships. Finally, the results obtained by Abdullah *et al.* (2004) also suggested that the trigger level values are important parameters requiring further investigation.

2.8 Summary

This chapter has discussed the concepts and approaches which form the basis of the research. Relevant signal analysis, signal processing, fatigue life prediction and fatigue data editing techniques have all been defined. Many experimental signals exhibit time-varying, or nonstationary characteristics, which provide a challenge in signal analysis. Using the Fourier transform the frequency components of an entire signal can be analysed, but it is not possible to locate at what point in time that a frequency component occurred or its duration. To overcome this problem, the wavelet is a significant tool for analysing time-localised features of a signal, and it is defined in the time-scale domain. Thus, wavelet transform gives a separation of components of a signal that overlap in both time and frequency and it gives a more accurate local description of the signal characteristics.

Several aspects have been discussed in the field of fatigue background such as fatigue loadings, fatigue life behaviour, fatigue life prediction and fatigue data editing technique. It is common that the service loads measured on relatively small components of machines, vehicles, and structures are analysed for fatigue life using crack growth approaches. For these components, it is important to predict crack initiation in order to avoid fatigue failure by removing the part from service at the appropriate time. A fatigue

life estimate based on the strain-life approach is usually used in these cases. The strain-life fatigue model relates the plastic deformation that occurs at a localised region where fatigue cracks begin to the durability of the structure.

In current practice, the fatigue damage calculations are based on the Palmgren-Miner linear damage rule, but this rule has limitations in analysing VA loadings since it does not account for load interaction or cycle sequence effects. Considering these limitations, the use of a fatigue damage model which was developed by DuQuesnay *et al.* (1993) is suitable for VA strain loadings. This model is called Effective Strain Damage (ESD). This model is based on crack growth and crack closure mechanisms and works well for a wide range of materials, load spectra, component geometries, strain magnitudes and mean-strain effects (DuQuesnay *et al.* 1992a; 1993; Topper and Lam 1997; DuQuesnay 2002).

Background of available fatigue data editing techniques was also discussed, including a wavelet-based technique, known as the MNMS algorithm. The evaluation of MNMS for fatigue data editing was performed by Abdullah *et al.* (2004), exposing the limitations in shortening fatigue signals for the purpose of accelerated fatigue tests. Apart from MNMS, only one study used the wavelet transform for fatigue data editing has been found in literature. This study which was performed by Oh (2001) with the signal denoising process and spike removal as the stages implemented in fatigue data editing method of a signal measured on a light railway component. Realising that the wavelet transform is new to the fatigue research of the road vehicles and its suitability to analyse nonstationary signals, therefore, it has been chosen as a method for developing a new fatigue data editing algorithm.

CHAPTER 3

3. Development of the Wavelet-Based Fatigue Data Editing Algorithm

Referring to Chapter 1 and Chapter 2, three keywords were identified for the new wavelet-based fatigue data editing algorithm. These are *wavelet* (a signal processing element to analyse nonstationary signals), *bump* (a high amplitude which causes the majority of the fatigue damage) and *extraction* (a procedure to extract fatigue damaging events from original loading). The combination of these three keywords was expected to produce a highly effective fatigue data editing algorithm, and is thus the main subject of this thesis. The algorithm, called Wavelet Bump Extraction (WBE), is a computational method which was developed in the Fortran programming language by means of the Salford ClearWin+® compiler.

3.1 Flowchart of the Wavelet Bump Extraction (WBE) Algorithm

A flowchart describing the Wavelet Bump Extraction (WBE) processing is shown in Figure 3.1 and Figure 3.2. Three main stages can be observed: application of the

orthogonal wavelet transform (OWT); identification of fatigue damaging events; and production of a shortened or mission signal.

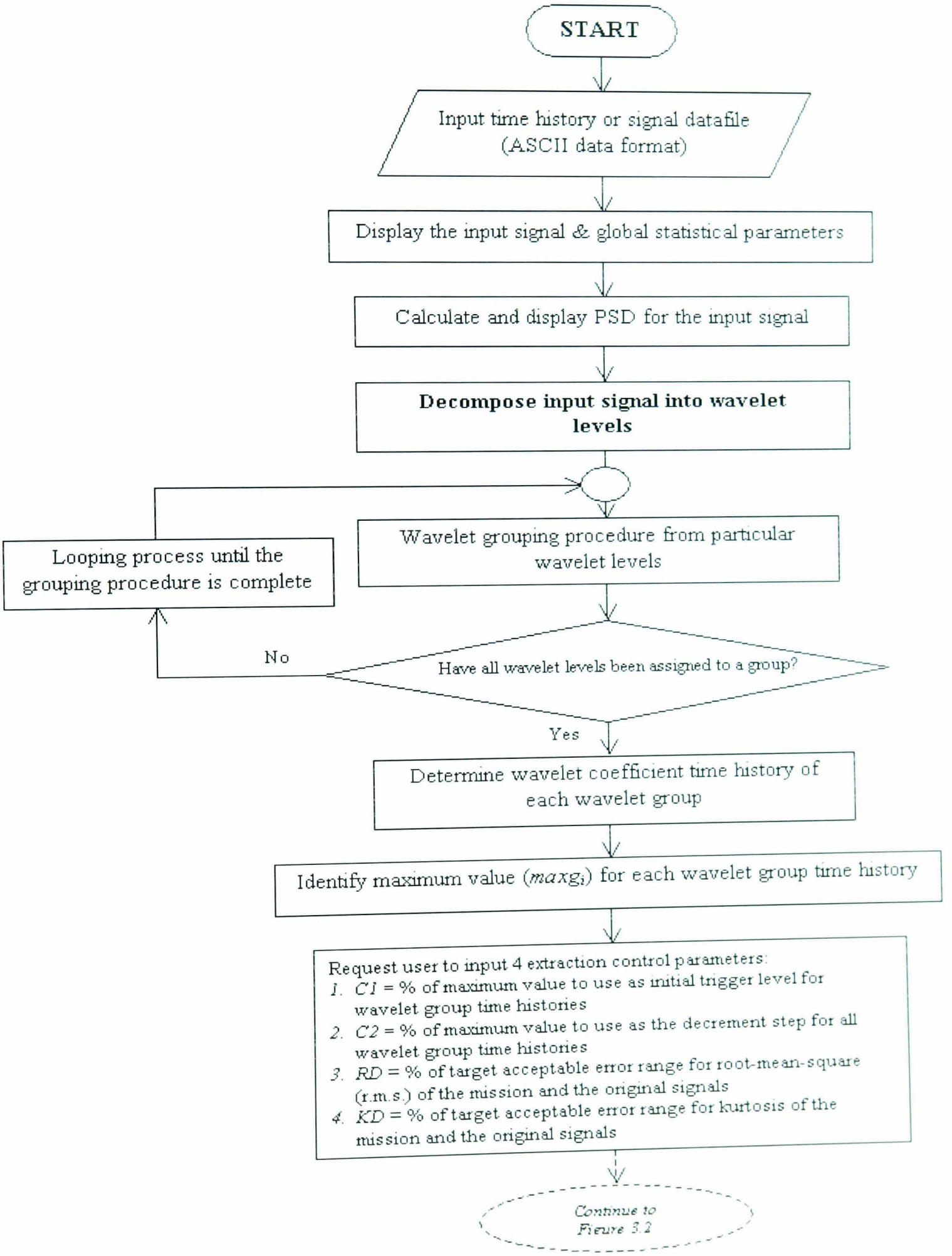

Figure 3.1: The WBE algorithm flowchart – Part 1: Wavelet decomposition and grouping stages.

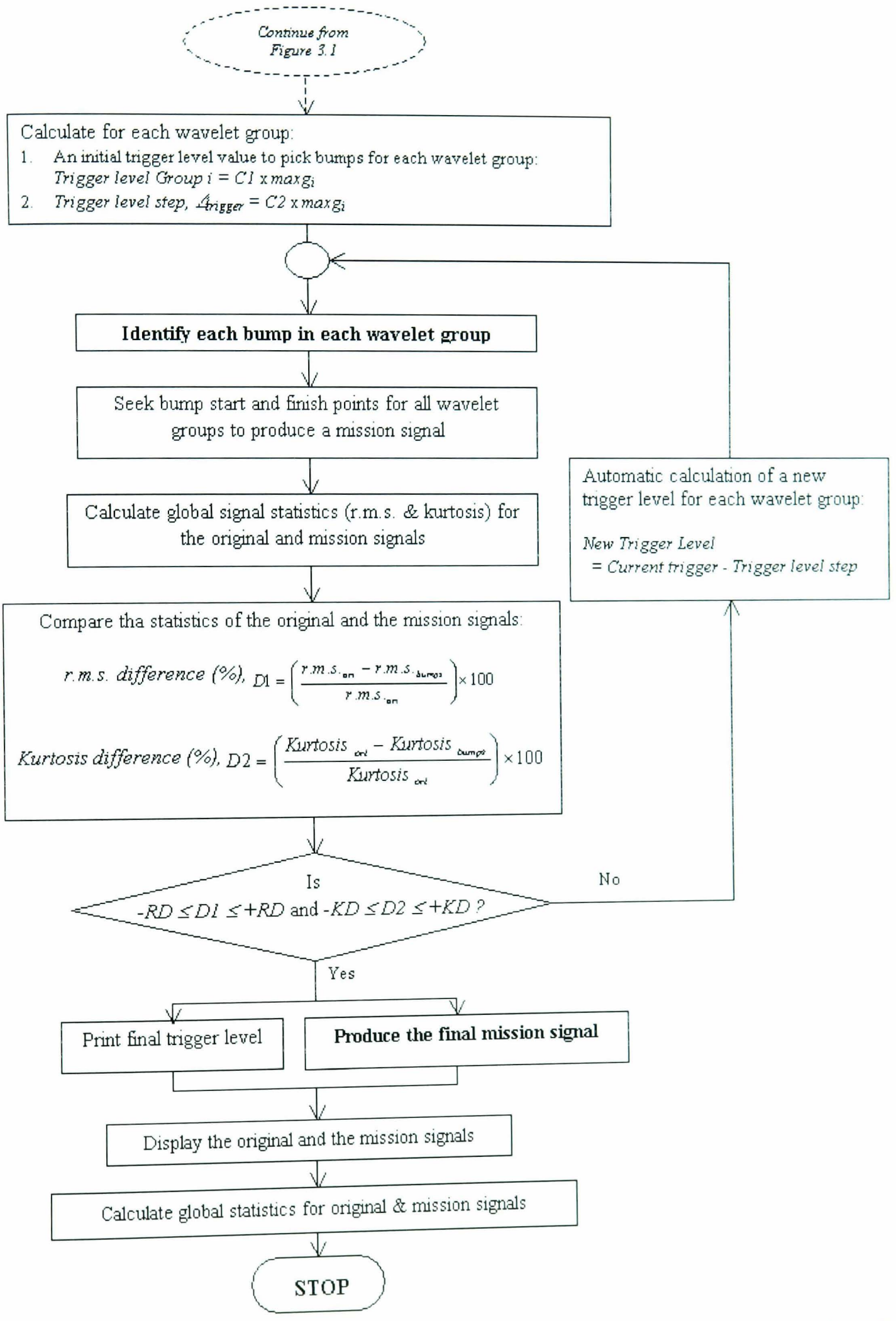

Figure 3.2: The WBE algorithm flowchart – Part 2: Identification and extraction of fatigue damaging events, and production of the mission signal.

The first stage of the WBE algorithm, being the application of the OWT, was adapted from the methodologies applied in the MNMS algorithm (Giacomin *et al.* 1999; 2000; 2001). On the other hand, the second and third stages have been developed in this thesis specifically to identify and extract fatigue damaging events from the original time history.

3.2 Application of the Orthogonal Wavelet Transform

3.2.1 Wavelet Decomposition

In the WBE algorithm the orthogonal wavelet transform (OWT) is used to decompose the original time history into wavelet levels. For this purpose, the Daubechies wavelet function was selected since it has been proven useful in many engineering applications, especially in the field of signal reconstruction such as in the mechanical damage detection research (Staszewski 1998a; 1998b; Li *et al.* 1999; Lin and Zuo 2003) and fatigue damage analysis (Oh 2001; Abdullah *et al.* 2004). For Daubechies wavelet it has been suggested that lower order, such as 4^{th} order, are suitable for nonstationary signals, while higher order, such as 20^{th} order, are suitable for stationary signals. For some nonstationary signals which contains transient events, however, both 4^{th} and 20^{th} order of Daubechies wavelet have been shown to provide similar results (Staszewski 1998b).

For the algorithm development, the 12^{th} order of Daubechies wavelet was chosen due to its successful application in several previous studies involving automotive road data (Giacomin *et al.* 1999; 2000; 2001; Grainger 2001; Steinwolf *et al.* 2002; Abdullah *et al.* 2004). Since Daubechies wavelets of order *N* provides $\frac{N}{2}$ vanishing moments (Daubechies 1992; Burrus *et al.* 1998), a 12^{th} order of Daubechies wavelet can be considered adequate for the WBE application, since greater than two vanishing moments are rarely required when compressing complex signals, such as speech or

video (Hubbard 1996). A vanishing moment is defined as the wavelets ability to represent polynomial behaviour of a signal. For example, 2nd order Daubechies wavelet which has one moment encodes polynomials of one coefficient, i.e. constant signal components. 4th order Daubechies wavelet encodes polynomials of two coefficients, i.e. constant and linear signal components (Matlab User's Guide 1998).

In the WBE algorithm the wavelet decomposition is used to produce a series of wavelet level time histories that cover subbands of the frequency domain. This is equivalent to using the wavelet transform as a multiple band-pass filter bank, dividing the vibrational energy of the original signal amongst the wavelet levels. For VA fatigue loadings exhibiting nonstationary characteristics such as the example of Figure 3.3, most bump events are not immediately obvious. This is one of the difficulties observed in the bump identification process. Therefore, it is useful to manually separate the signal into a number of components, each of which is related to certain physical phenomenon that occur during vehicle motion, e.g. the rigid-body resonance of the vehicle, the torsional and flexural flexible-body resonances of the vehicle, the tire resonances, etc. When this has been done and each of the constituent vibration components is considered separately, bumps caused by one physical phenomenon will not be covered by background vibration related to another.

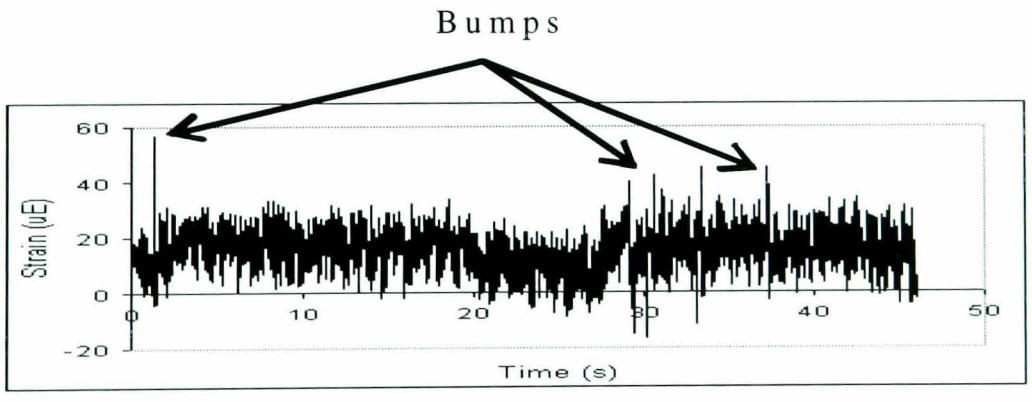

Figure 3.3: A fatigue road load time history indicating several clear bumps.

For the WBE algorithm the important choice was made to use wavelet decomposition rather than more traditional techniques such as digital filtering. Frequency separation is

often performed by means of band-pass digital filters, but since every point in the filtered output is influenced by its neighbours, the filtering process affects the time history by smoothing the peaks. If a number of band-pass outputs from the same input process are summarised, the result will not exactly duplicate the original time history. The rigorous signal reconstruction achievable by means of the orthogonal wavelet transform and Daubechies wavelets was considered necessary to maintain accuracy in WBE.

3.2.2 Wavelet Grouping

A wavelet grouping procedure is used to group wavelet levels into a specific frequency intervals. Each wavelet group is defined by the user so as to cover specific frequency regions, such as high energy peaks caused by a subsystem resonance. The joining of the wavelet levels into wavelet groups permits analysis to be performed for each frequency region of interest. Wavelet group time histories are then formed by the summation of their constituent wavelet level time histories. A schematic diagram of the wavelet decomposition and wavelet grouping procedures is shown in Figure 3.4. The programme code for these operations was first developed for use in the MNMS (Giacomin *et al.* 1999; 2000; 2001), and was later implemented for the same purposes in the WBE algorithm.

As an example, Figure 3.5 presents the case of an acceleration signal measured in the vertical direction at the rail of the driver's seat. In this case, an automobile was driven over a smooth asphalt road surface. The frequency range up to 3 Hz contains the rigid body resonances of the chassis on the suspensions (Giacomin *et al.* 1999; 2000). Similarly, higher frequency bands containing predominantly suspension modes, chassis modes or tyre modes can be defined by grouping those wavelet levels covering the relevant resonant frequencies. The procedure of grouping wavelet levels into specific bands in this way is helpful, as it becomes less likely that vibrational energy from one subsystem resonance conceals the energy of other subsystem resonances.

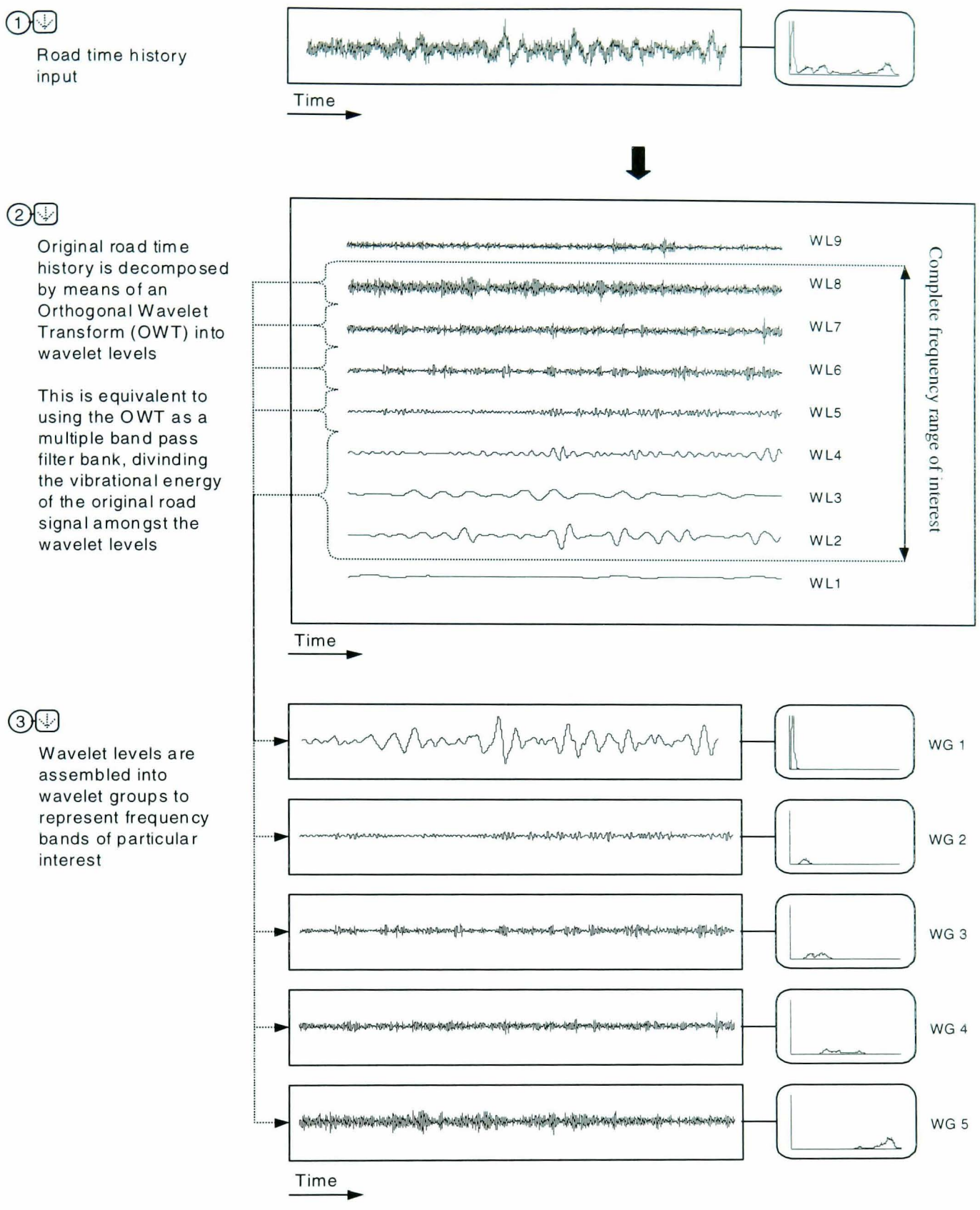

Figure 3.4: Schematic diagram of the wavelet decomposition and grouping procedures, where WL and WG denoted as wavelet level and wavelet group, respectively (Reproduced from Giacomin *et al.* 2000).

In Figure 3.5, six clear peaks can be observed in the PSD plot, having centre frequencies of 1.5, 10, 18, 25, 37 and 53 Hz. The meaning of these peaks and the

vibrational energy which spread within the peaks are described as follows (Giacomin *et al.* 2000; Grainger 2001):

- The lowest frequency peak occupying the region from 0.5 to 3 Hz (Wavelet Group 1) is associated with the rigid body dynamics of the car;
- The second peak, spreading across the range from 6 to 13 Hz (Wavelet Group 2) is related to the resonant frequencies of the suspension and the rigid body motion of the engine/gearbox;
- The third peak, distributed within the region between 14 and 21 Hz (Wavelet Group 3) mainly reflects the first flexible body resonance of the chassis;
- Finally, two smaller peaks and a larger peak are found in the frequency range 23 to 57 Hz (Wavelet Group 4 and Wavelet Group 5). These are higher chassis resonances and resonant frequencies of the tyres.

Each of the wavelet levels correspond to a certain frequency range which contains time domain features such as transient events. In WBE, the wavelet levels are grouped in such a way that each group isolates a single, physiological, frequency band of the whole PSD. Following this logic, some groups will combine several wavelet levels while others may consist of only one individual wavelet level.

The usefulness of wavelet decomposition and grouping for the identification of bump events is illustrated in Figure 3.6. A bump event is observed in the higher frequency wavelet group (Figure 3.6a). At the same time there are no bump events present in the low frequency wavelet group (Figure 3.6b). In Figure 3.6c, the bump is concealed in the overall road signal. This would not have been apparent without first decomposing the overall signal and assembling wavelet groups.

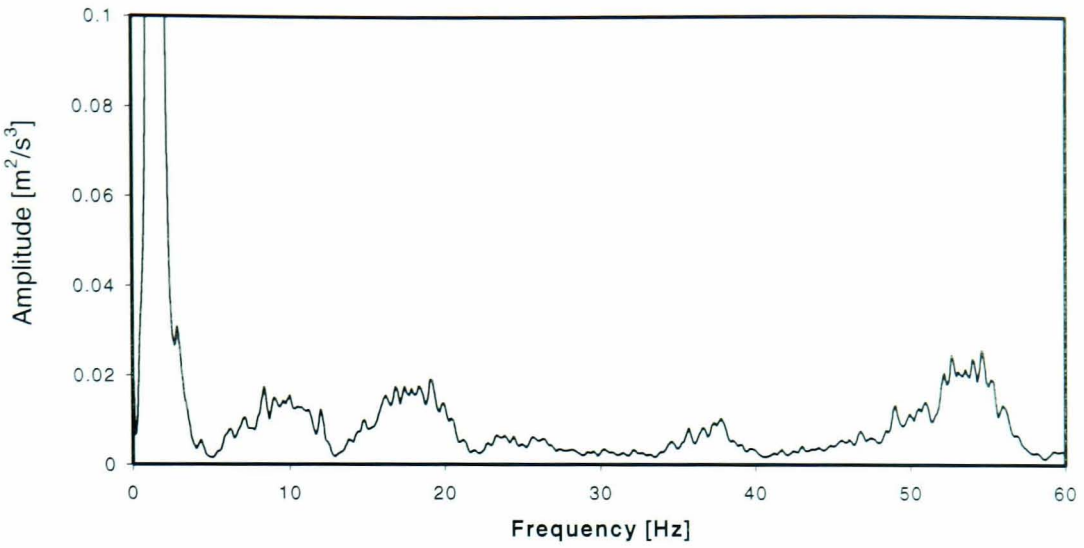

(a)

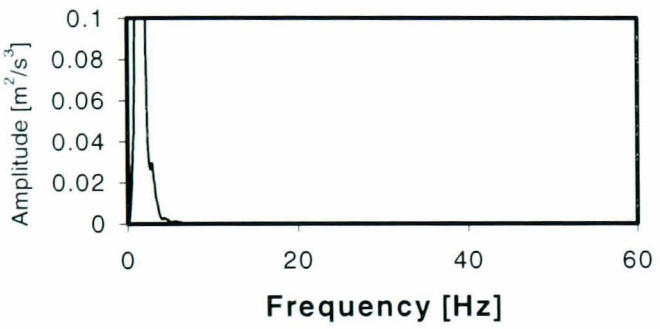

(b)

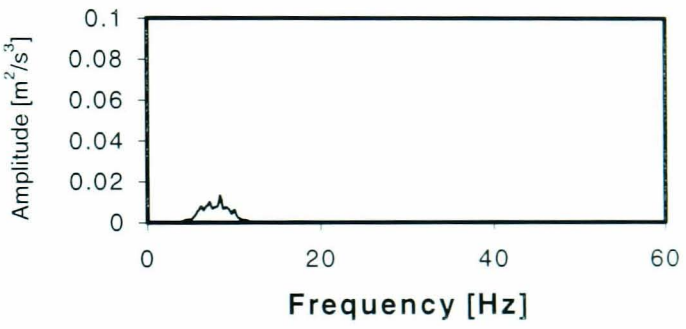

(c)

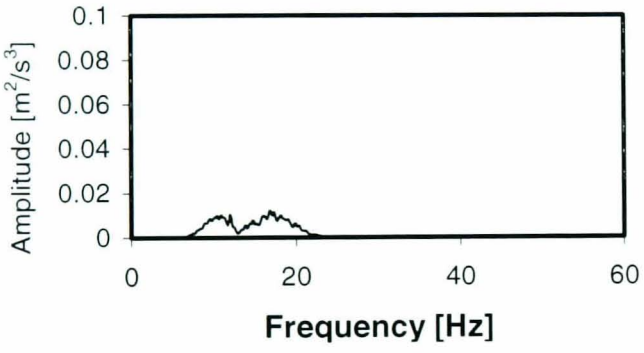

(d)

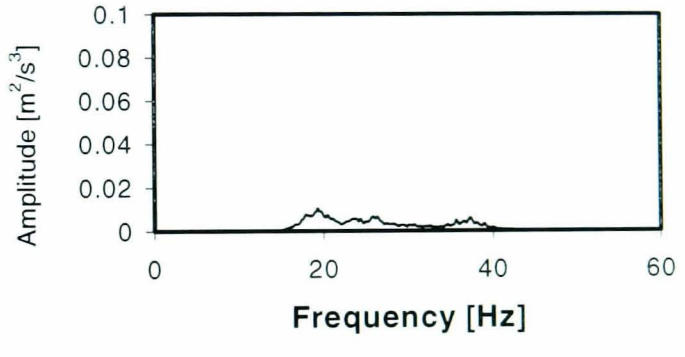

(e)

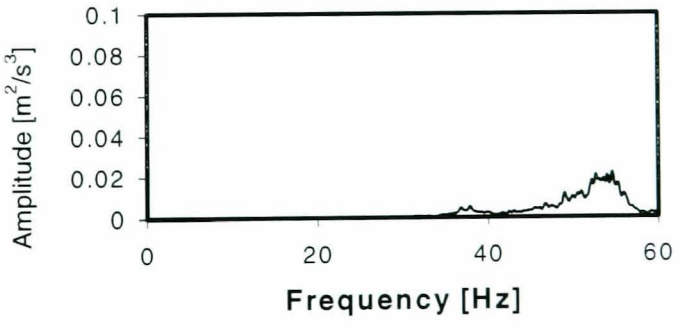

(f)

Figure 3.5: Overall power spectral density of the vertical direction seat rail acceleration and the individual wavelet groups into which the signal was divided (Reproduced from Giacomin *et al.* 2000): (a) PSD of the original signal, (b) PSD of Wavelet Group 1, (c) PSD of Wavelet Group 2, (d) PSD of Wavelet Group 3, (e) PSD of Wavelet Group 4, (f) PSD of Wavelet Group 5.

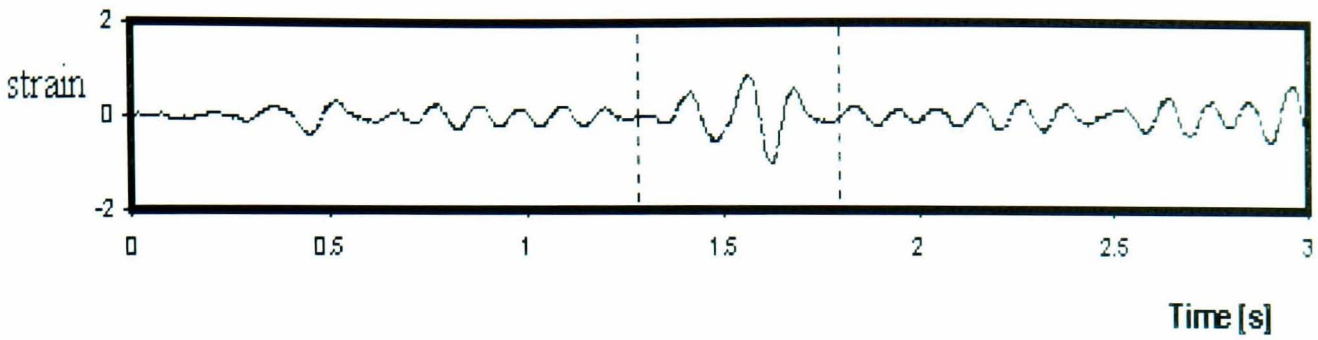

(a)

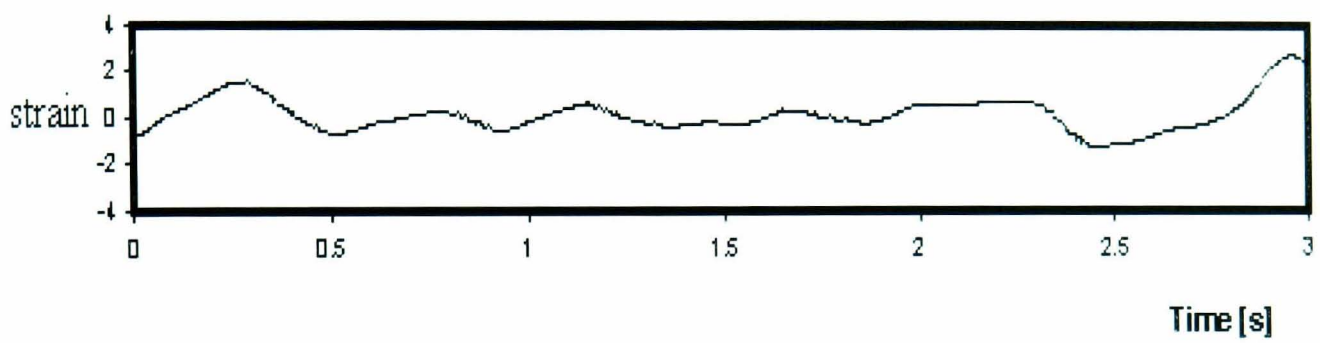

(b)

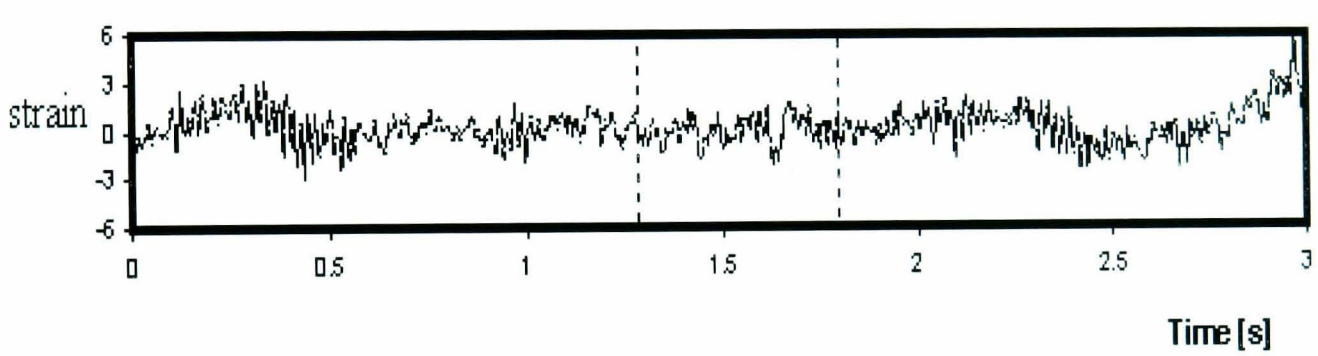

(c)

Figure 3.6: Example of a time history where a bump event is concealed in the overall background of the signal:

(a) Higher frequency wavelet group: bump presents,

(b) Lower frequency wavelet groups: no bumps,

(c) Complete road signal: bump is concealed.

3.3 Bump Identification in Wavelet Groups

After the wavelet grouping process, the peak of each wavelet group time history is determined by the algorithm. The peak is used to determine the initial trigger level for the bump identification process. Bump identification is achieved in each wavelet group time history by means of an automatic trigger level value specific to the wavelet group.

At the program launch, the user is asked to specify initial trigger level values for each wavelet group. Trigger level determination is performed by specifying the percentage value of the peak for the wavelet group, which is denoted as *C1*. The user is also asked to specify the trigger step, which is denoted as *C2,* which is a percentage value which can be applied to the peak of each wavelet group. In addition, the user is asked to specify an acceptable percentage difference between the r.m.s. and the kurtosis of the mission signal and the original signal (denoted as *RD* and *KD,* respectively). Both statistical parameters are used in order to retain a certain amount of the signal vibrational energy and range characteristics, leading to the retention of the original fatigue damage (Hu 1995; Qu and He 1986) in the mission signal.

The trigger level for each wavelet group is automatically determined to achieve the requested statistics (simultaneous analysis for both *RD* and *KD*) for each wavelet group. Referring to the flowchart of Figure 3.2, other parameters used in the WBE algorithm are *D1* and *D2.* Both parameters are defined as the calculated difference of r.m.s. (for *D1*) and kurtosis (for *D2*) between a current iteration of the mission signal and the original signal. For this case, the approach of producing the final mission signal, which is discussed in Section 3.4 and 3.5, is used to produce the current iteration of the mission signal at specific trigger level values.

In the algorithm computational analysis to determine the trigger level value for each wavelet group, the simultaneous comparison between the values of *D1* with *RD* and the values of *D2* with *KD* are required. If the values of *D1* and *D2* are not to be found in the ranges of $\pm RD$ (or $-RD < D1 < +RD$) and $\pm KD$ (or $-KD < D2 < +KD$), respectively, then the algorithm will compute the trigger level step (*C2*) for a new trigger level value. This process is iterated until *D1* and *D2* meet the user-defined value of both *RD* and *KD,* thus the final trigger levels can then be finalised.

Since the WBE algorithm tends to retain signal energy and signal amplitude range, the use of ±10% difference in r.m.s. and kurtosis of the mission and the original signal is suitable for analysing experimental road load data sets. The percentage value of ±10%

is chosen for the bump determination process of the WBE algorithm in order to produce a shortened mission signal which has close global statistical parameter (PSD, r.m.s. and kurtosis) values to those of the original signal. Related studies of the difference in the global signal statistical values between the mission and the original signals can be found in Giacomin *et al.* (2001), Grainger (2001) and Abdullah *et al.* (2004), with the application of the MNMS algorithm using various road load data sets.

Figure 3.7 presents a set of possible trigger levels for an individual wavelet group to determine a bump labelled as -4 to 4. Once a bump exceeding a specified trigger level has been identified, its time duration must be defined. In WBE, bumps were defined to be rapid transients that oscillated for two or more cycles before becoming lost in background vibration. The determination of the bump temporal time extent was performed by means of searching the points at which the signal envelope inverts from a decaying shape. The schematic definition of the bump time extent defined for use in WBE is shown in Figure 3.8.

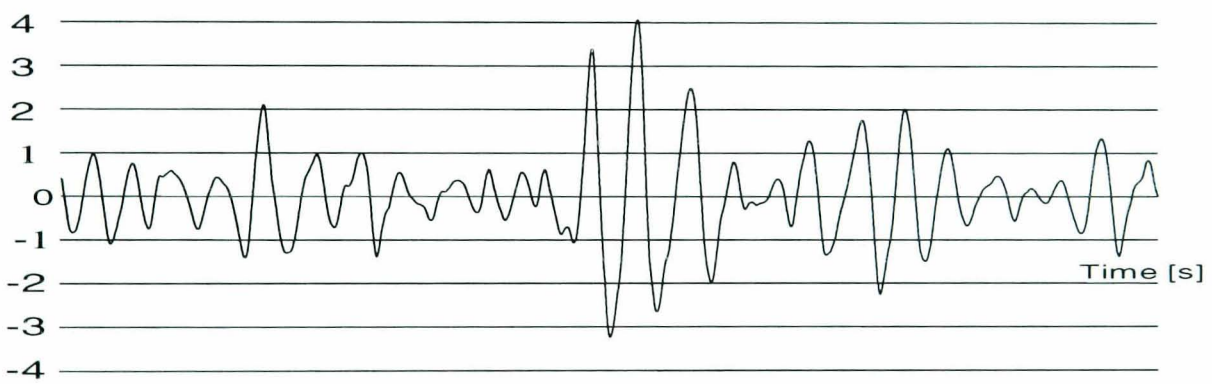

Figure 3.7: Bump identification using trigger levels.

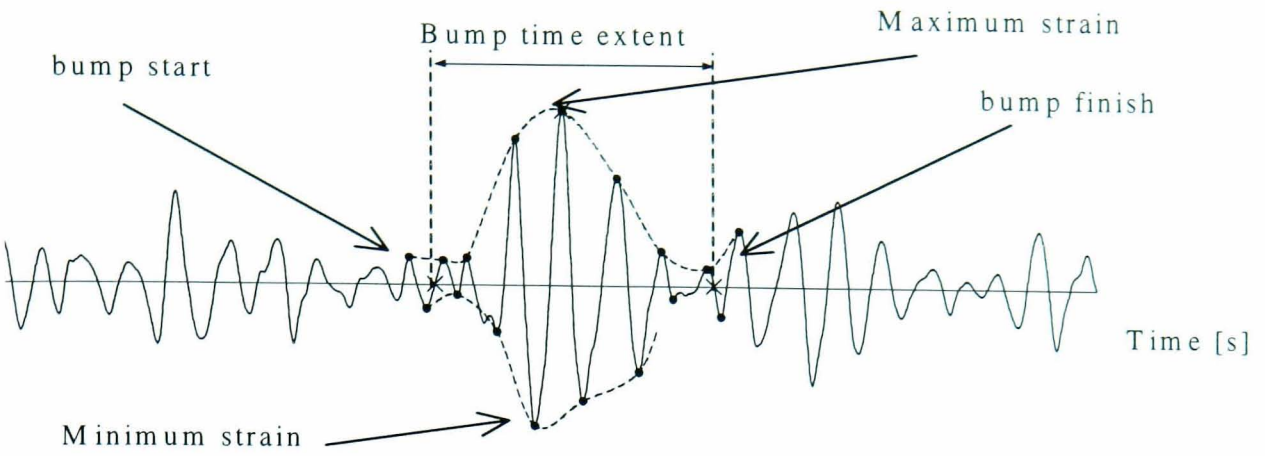

Figure 3.8: Determination of the time extent of a bump in WBE.

3.4 Extraction of Bump Segments from the Original Signal

After all bumps are identified in each wavelet group, a search of the time extent of the bump is performed, as shown in Figure 3.9. If a bump event is found in any of the wavelet groups, a block of data covering the time frame of the bump is taken from the original time history. The blocks are then compared, and any temporally overlapping sections are eliminated so as to avoid redundancy in the final mission signal.

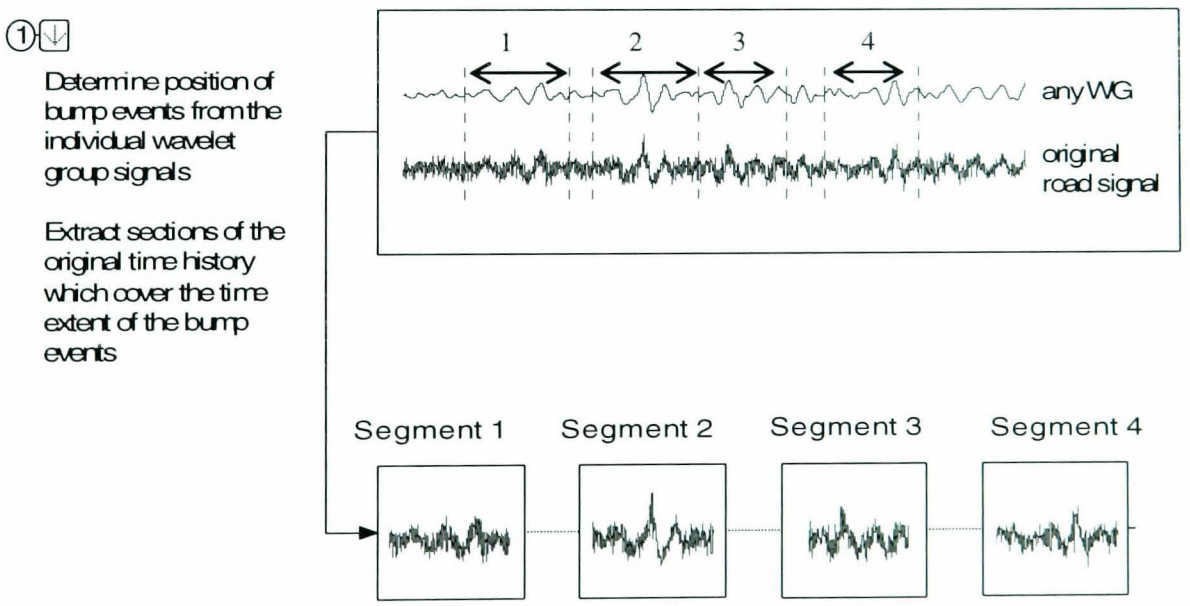

Figure 3.9: Bump extraction and section elimination processes of the WBE algorithm.

This extraction strategy retains the amplitude and phase relationships of the original signal. Using this strategy to identify bump segments, the load sequence of VA fatigue

loadings can be retained within the bump segments. Therefore, the extracted bump segments can be used in the study of cycle sequence effects.

3.5 Construction of the WBE Mission Signal

Once all bump segments have been identified from the input fatigue time history, they are sorted based on the severity of the expected fatigue damage. The parameters obtained from four strain-life fatigue damage model can be used to determine the sorting criteria. They are the Coffin-Manson relationship (Eq. (2.37)), the Morrow (Eq. (2.38)) and Smith-Watson-Topper (Eq. (2.39)) mean stress correction model, consisting of mainly the constants at the left hand side of their respective equations. Another strain-life model is the Effective Strain Damage (Eq. (2.43)), which consists of experimental variables to determine the parameters in the equation.

However, by using the Smith-Watson-Topper (SWT) fatigue damage model the left hand side of Eq. (2.39) can be seen to consist of more constants compared to the fatigue damage models of Eq. (2.37) and Eq. (2.38), thus suggesting that the relative expected fatigue damage of the bump segment can be quantified in the WBE algorithm by means of the product of the modulus of elasticity of the material E, maximum strain σ_{max} and the strain amplitude ε_a, as in the following expressions

$$\sigma_{\max}\varepsilon_a \approx E\varepsilon_{\max}\varepsilon_a \tag{3.1}$$

$$E\varepsilon_{\max}\varepsilon_a = E\varepsilon_{\max}\left(\frac{\varepsilon_{\max}-\varepsilon_{\min}}{2}\right) \tag{3.2}$$

where ε_{max} and ε_{min} is the maximum and the minimum strain of a particular bump segment extracted from WBE.

In its current form, the WBE algorithm provides three bump segment sequences: the original order sequence of the bump segments; from the highest expected fatigue damage to the lowest and from the lowest expected fatigue damage to the highest.

Figure 3.10 presents an example of the process of mission signal generation in which the highest-to-lowest ordering is used.

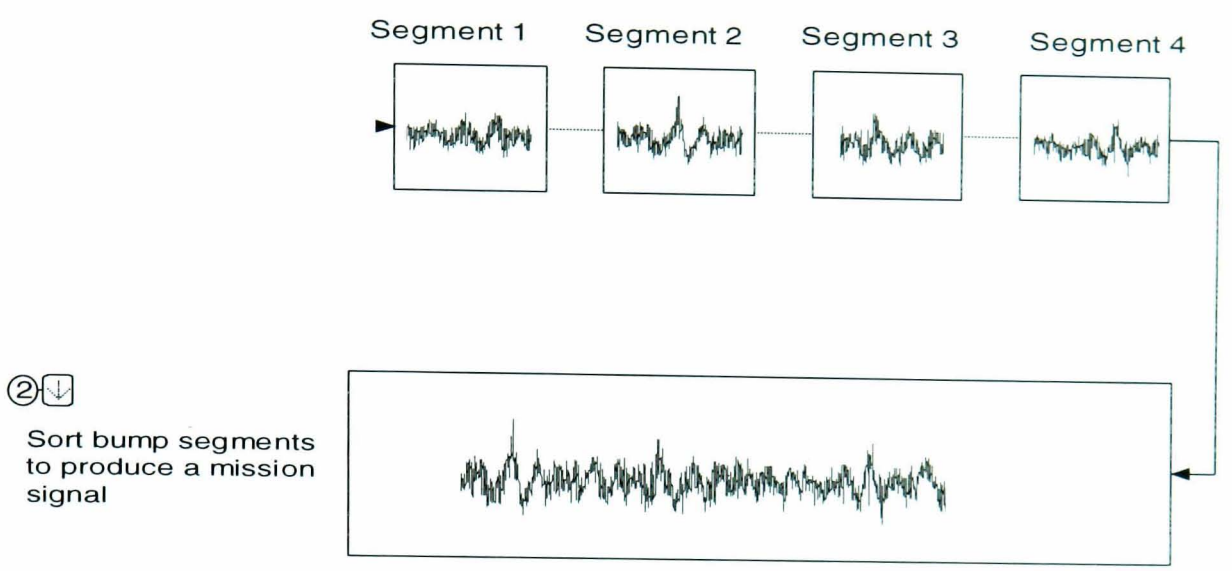

Figure 3.10: Mission definition using the highest-to-lowest damage sequence ordering.

3.6 Summary

This chapter has discussed the Wavelet Bump Extraction (WBE) algorithm which was developed as a part of the Ph.D. research described in this thesis. WBE was developed in the Fortran programming language using the Salford ClearWin+® compiler. The algorithm is able to identify and extract fatigue damaging events from variable amplitude fatigue loadings, so as to produce a shortened mission signal which preserves the original load sequences. The WBE algorithm is the first fatigue data editing technique that has been developed using the orthogonal wavelet transform. In this research, the 12^{th} order Daubechies wavelet was chosen due to its successful application in previous studies involving automotive road data.

The key concept adopted in WBE is that a fatigue damaging event, or bump, is defined as an oscillatory transient which has a monotonic decay envelope either side of the peak value. Bumps are identified based on an automatic trigger level specific to each wavelet group into which the signal is decomposed. The trigger level of each wavelet

group is automatically determined to achieve the user defined global signal statistical parameters (r.m.s. and kurtosis) difference, with the comparison of the calculated values of r.m.s. and kurtosis of the mission and original signals. If the comparison values are within the range of the user defined global signal statistics differences, the final trigger level values for the particular road load data set are finally determined. Then, a method of searching the bump start and finish points from the original time history was developed in order to produce the bump data segments. By saving only the bump data segments most small amplitude events which produce minimal fatigue damage are removed.

The bump segments are assembled in order to produce a mission signal that has a shorter time length compared to the original signal. The mission signal contains the original load sequences, amplitude and phase relationships, thus is suitable for the simulation or experimental testing of any structures or materials where cycle sequence effects may play a prominent role in the overall fatigue life. WBE is thus also an appropriate algorithm for use when accelerated (time shortened) fatigue tests are desired.

CHAPTER 4

4. Application of the Wavelet-Based Fatigue Data Editing Algorithm

4.1 Signals for the Validation of the Wavelet Bump Extraction (WBE) Algorithm

The main objective of developing the Wavelet Bump Extraction (WBE) algorithm was to provide a procedure for summarising variable amplitude (VA) fatigue loadings, whilst retaining the original load sequences. In order to verify the ability of WBE to compress VA fatigue signals, six test signals containing a range of possible behaviours were created. These signals are divided into two categories: Synthetic Signals (T1 and T2) and Experimental Signals (T3 – T6). The signal time histories and vibrational energy distribution (in PSD) are shown in Figure 4.1 for the Synthetic Signals and in Figure 4.2 for the Experimental Signals.

4.1.1 Synthetic Signals

The first category consists of two artificial signals which were defined so as to test several possible failure modes of the WBE algorithm. The basic statistical properties of these two signals are summarised in Table 4.1, while the time history and the power spectral density (PSD) plots are shown in Figure 4.1.

Table 4.1: Statistical properties of the Synthetic Signals.

Signal Name	Global Statistical Parameters						
	No. of data points	Signal length [s]	Mean [$\mu\varepsilon$]	r.m.s. [$\mu\varepsilon$]	Skewness	Kurtosis	Crest factor
T1	16,000	40.0	0.0	1.5	0.1	7.4	3.9
T2	16,000	40.0	0.4	2.9	0.0	4.4	7.1

The T1 signal, as illustrated in Figure 4.1a, was defined to have 16,000 data points which are sampled at 400 Hz. The logic of producing T1 was to verify the WBE ability in dealing with any signal containing large transients in an otherwise small amplitude background. T1 consists of a combination of sinusoidal and random segments of different amplitude or frequency. The signal was intentionally defined to be a mixture of both high amplitude bump events and low amplitude harmonic backgrounds.

T2, as illustrated in Figure 4.1b, was defined to have 16,000 data points which are sampled at 400 Hz. The logic of creating T2 was to verify the WBE performance in analysing a signal containing a low frequency background. T2 was produced by summing together an actual random road load time history which contained several shocks and a low frequency sinusoidal signal.

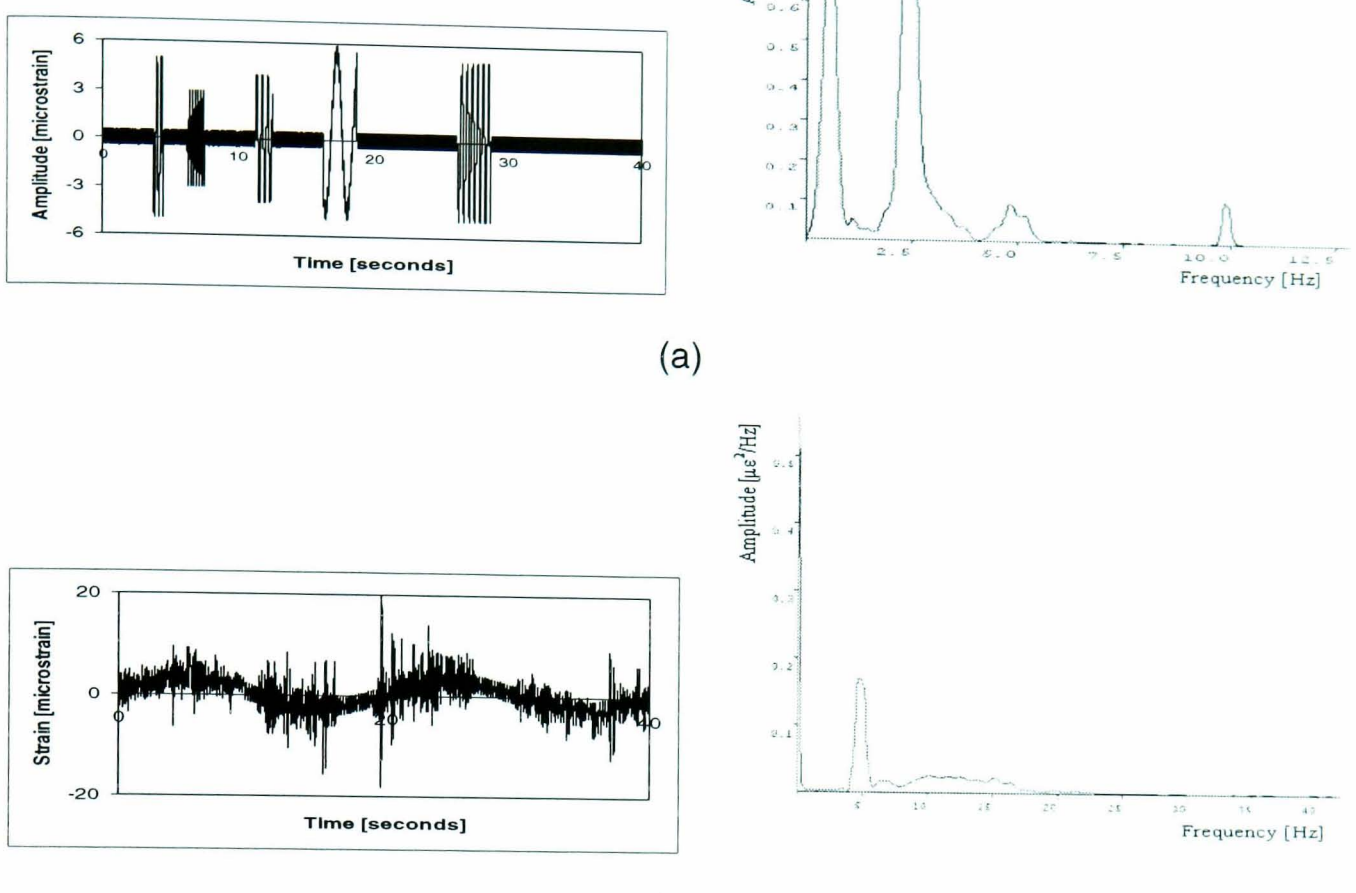

Figure 4.1: Time histories and power spectral densities of the synthetic signals: (a) T1, (b) T2.

4.1.2 Experimental Signals

The second contains road loading time histories measured on the suspension components of road vehicles. The global statistical properties of the signals are presented in Table 4.2, while both the time histories themselves and the associated PSDs are presented in Figure 4.2.

The T3 signal, as illustrated in Figure 4.2a, is a variable amplitude (VA) loading sampled at 200 Hz for 45,000 data points. The signal was measured on the front left lower suspension arm of an automobile which was travelling on public road surface (mixture of smooth and irregular asphalt) in North Wales, United Kingdom. This 225-second signal was provided by Leyland Technical Centre (United Kingdom). T3 was used to validate

the ability of the WBE algorithm in selecting an appropriate number of bumps when attempting to summarise a long time history.

Table 4.2: Statistical properties of the Experimental Signals.

Signal Name	Global Statistical Parameters						
	No. of data points	Signal length [s]	Mean [$\mu\varepsilon$]	r.m.s. [$\mu\varepsilon$]	Skewness	Kurtosis	Crest factor
T3	45,000	225.0	0.8	4.6	-1.1	8.0	5.4
T4	23,000	46.0	15.0	16.7	-0.1	3.4	3.4
T5	23,000	46.0	-48.1	51.6	0.1	3.7	1.6
T6	12,500	61.0	205.5	235.5	0.5	2.6	2.5

Signals T4 (Figure 4.2b) and T5 (Figure 4.2c) are strain signals which were measured on a lower suspension arm of a van travelling at 34 km/h over a pavé test track. Both signals were sampled at 500 Hz for a total of 23,000 data points, producing a record length of 46 seconds. The different between these two signals are that T4 has a tensile mean loading, while T5 has a compressive mean loading. Figure 4.3a shows a section of the pavé test track at Leyland Technical Centre (United Kingdom) which was used for measuring both signals. Figure 4.3b presents a diagram which indicates the location of the strain gauges on the lower suspension arm during the test.

The final signal for the WBE validation, T6, is illustrated in Figure 4.2d. T6 contains 12,500 discrete points and was sampled at 204.8 Hz, producing a total record length of 61 seconds. It was measured on an automobile (not the same as T3) front suspension component while travelling over a proving ground manoeuvres, containing rough road surface. T6 exhibits a low frequency background which contains occasional shocks. For this reason, it was used to observe the effectiveness of WBE when processing a signal with low frequency content. This signal was taken from the database of Society of Automotive Engineers Fatigue Design Evaluation (SAEFDE) committee and has previously been analysed by Leser *et al.* (1998) as part of a study of fatigue loading reconstruction using the Auto Regressive Moving Average (ARMA) approach.

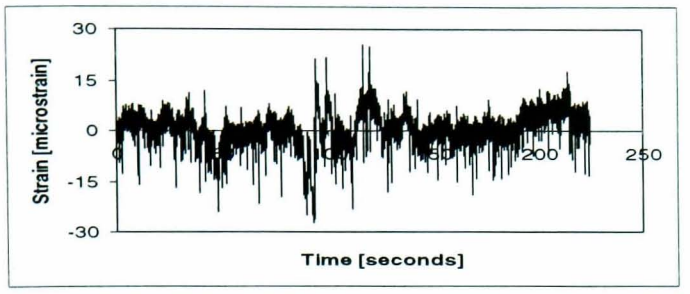

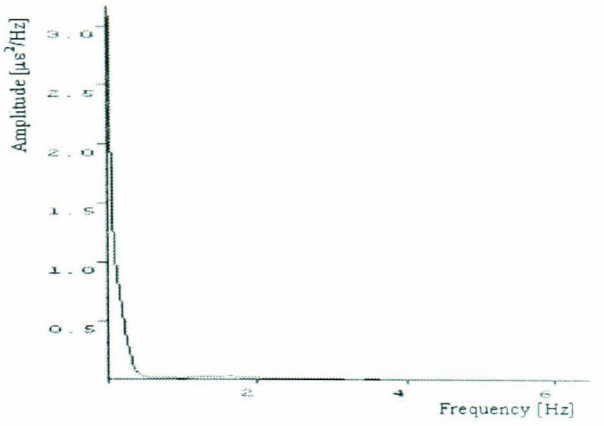

(a)

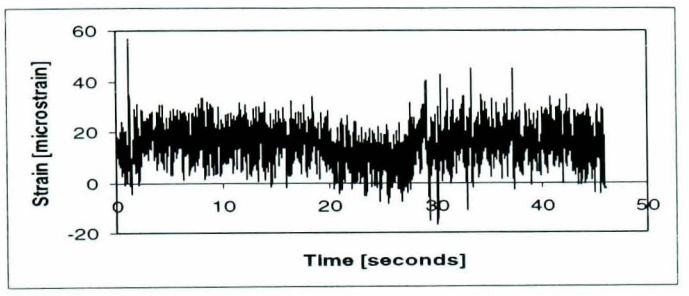

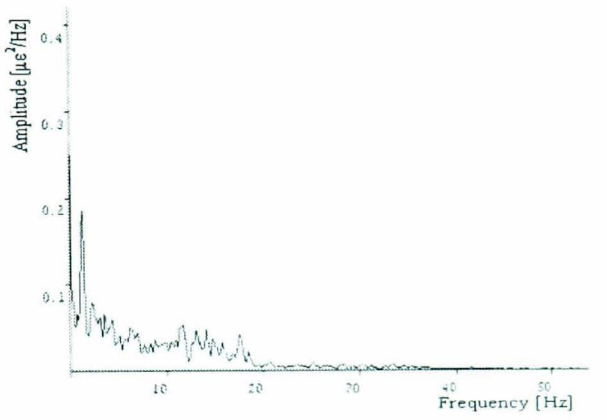

(b)

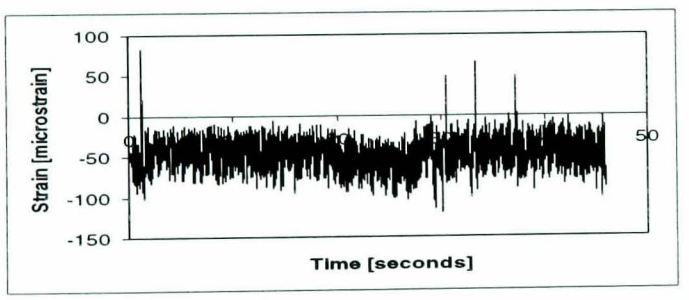

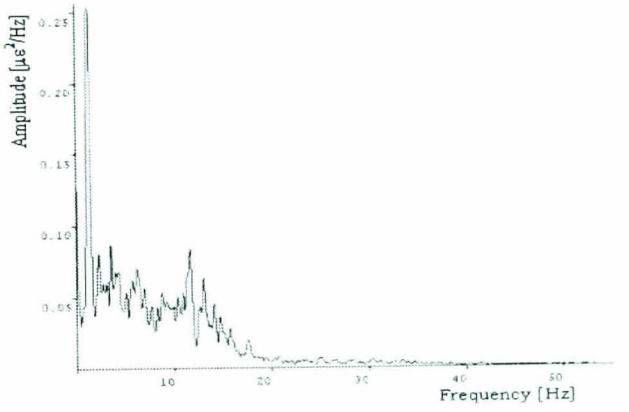

(c)

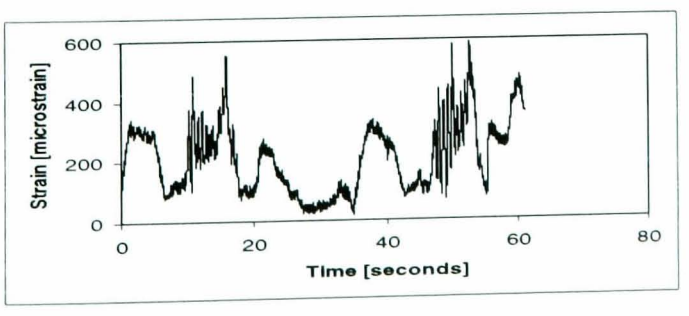

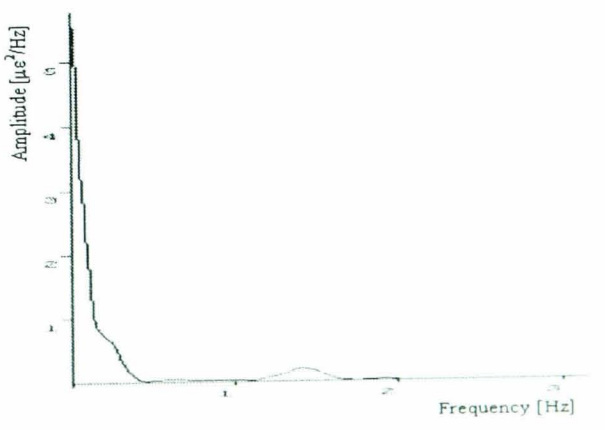

(d)

Figure 4.2: Time histories and power spectral densities of the experimental signals: (a) T3, (b) T4, (c) T5, (d) T6.

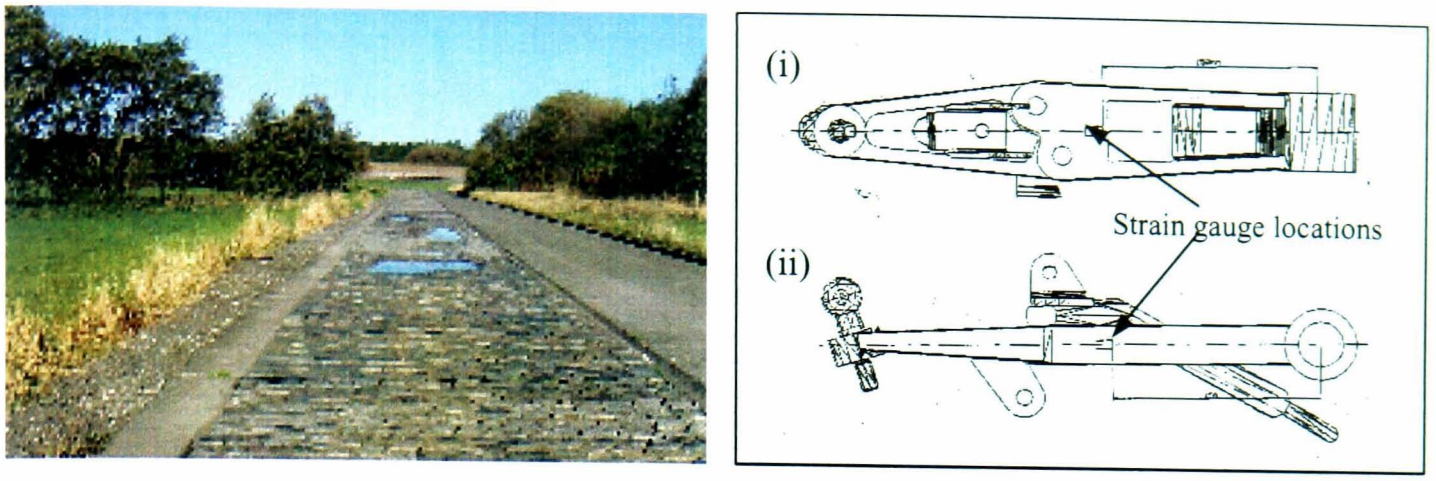

(a) (b)

Figure 4.3: Road surface and a lower suspension arm for signal measurements:

(a) Pavé test track used for the test,

(b) Strain gauge positions on a lower suspension arm for measuring T4 - refer to top figure or (i), and T5 – refer to bottom figure or (ii).

(With permission from Leyland Technical Centre, United Kingdom)

4.1.3 Selected Signals to the WBE Validation

The WBE algorithm was run using a range of control parameters (*C1, C2, RD* and *KD*) for each of the six test signals (T1 to T6). The algorithm was found to behave robustly under a range of parameter combinations, and the validation testing was used to make small improvements to the WBE programme code so as to eliminate small problems associated with the use of floating point values and with space limitations associated with bump memory allocation. In order to illustrate the robustness of the WBE programme code, the next sections will present examples of the WBE processing obtained for test signals T1, T2 and T4.

The reason for selecting T1 is to illustrate the ability of WBE to identify and extract appropriate bumps from an original time history. T2 was selected due to the low frequency components which challenges the ability of WBE when determining the length of the extracted bump segments. Finally, T4 was chosen as it is an experimental signal which contains a wide variety of signal components at various frequencies and

amplitudes, and can thus be considered typical of actual road vehicle fatigue testing results.

4.2 Input of the WBE Algorithm

The first menu of WBE is shown in Figure 4.4, which requests four user inputs about the data that is to be analysed. The first and second inputs are the fatigue history filename and number of data points. For these, the fatigue loading data file must be a time series in ASCII format (.txt, .asc, .dat). The data file must have a single column for the specified number of discrete data points. The third input is the sampling frequency, which is used to generate the PSD used in the frequency analysis and wavelet decomposition process. Finally, the frequency upper limit value is the maximum frequency of the PSD. The maximum value of the frequency upper limit allowed is at the Nyquist frequency, which is half of the sampling frequency.

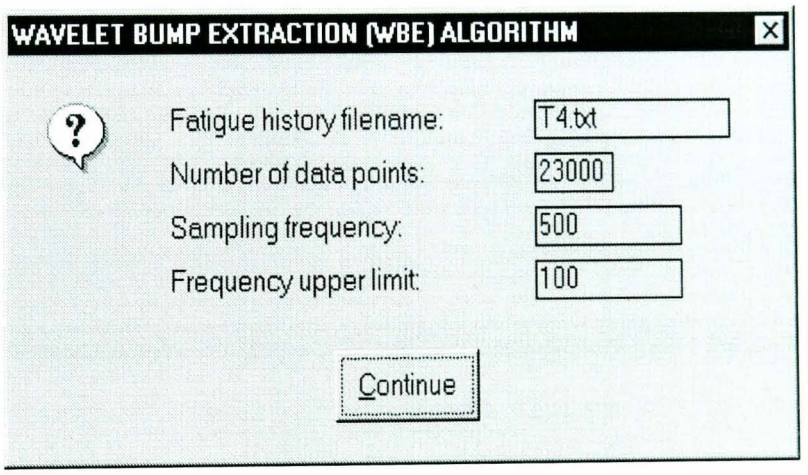

Figure 4.4: First menu of the WBE algorithm.

4.3 Wavelet Decomposition of the Original Signal

T1 was decomposed into 14 wavelet levels. Referring to the PSD plot of T1 (Figure 4.1a), four peaks were found in the frequency domain at 0.59 Hz, 2.54 Hz, 4.9 Hz and 10.0 Hz. The wavelet levels were grouped into four wavelet groups. The wavelet group time histories are shown along with their respective PSDs in Figure 4.5.

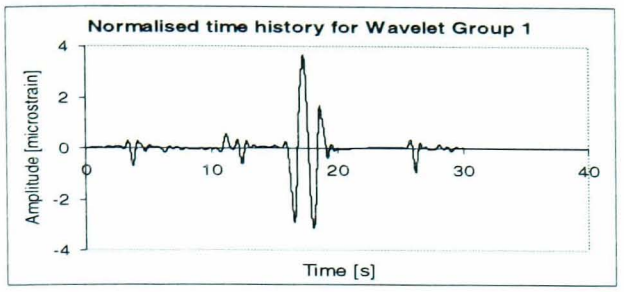

(a)

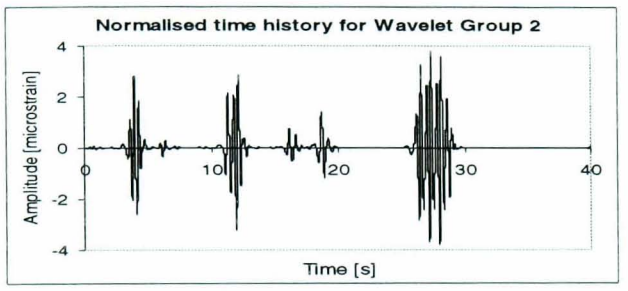

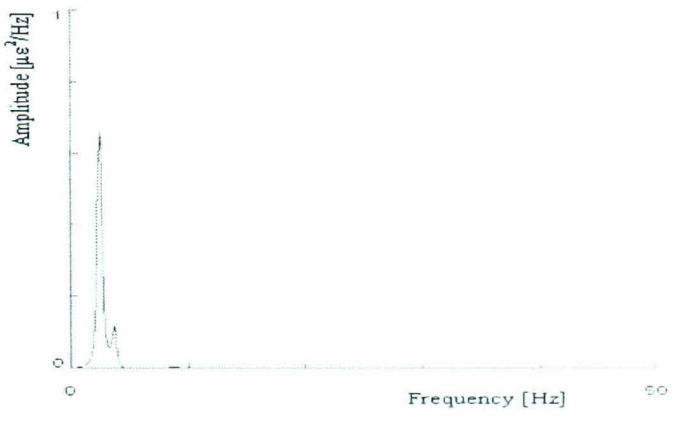

(b)

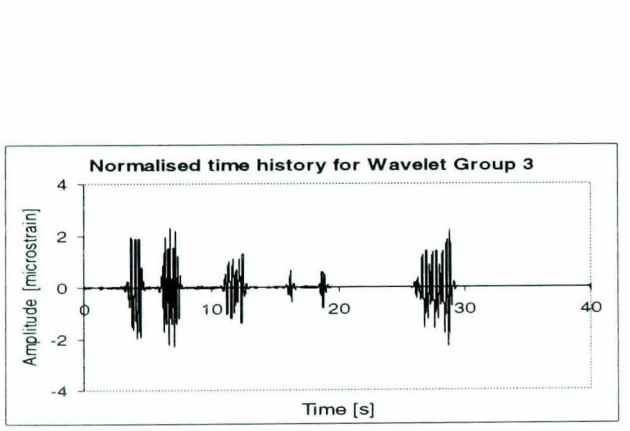

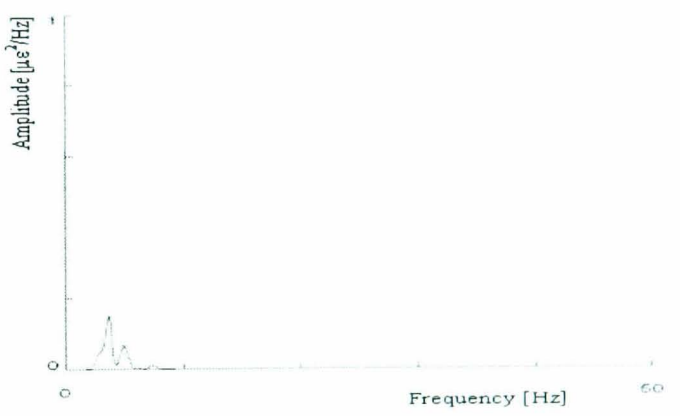

(c)

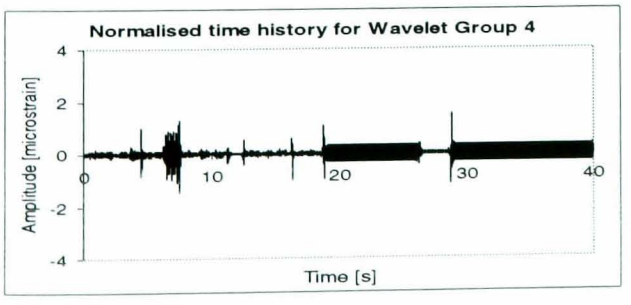

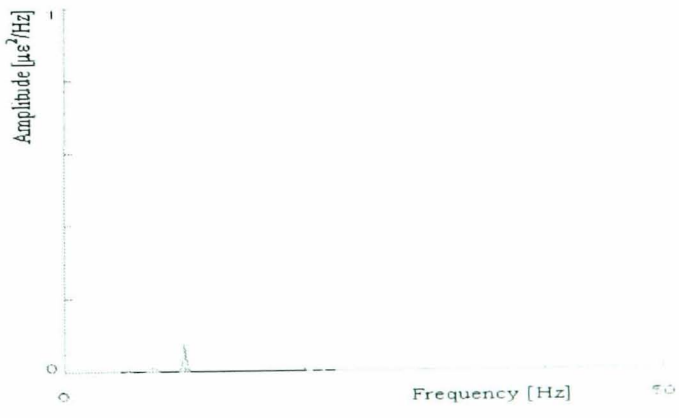

(d)

Figure 4.5: The wavelet group time histories and the PSD plots for T1: (a) Wavelet Group 1, (b) Wavelet Group 2, (c) Wavelet Group 3, (d) Wavelet Group 4.

T2 was decomposed into 14 wavelet levels and three peaks were found in the PSD plot, as shown in Figure 4.1b. Three wavelet groups were formed with their peaks at 0.00 Hz for Wavelet Group 1, 5.27 Hz for Wavelet Group 2 and 7.23 Hz for Wavelet Group 3. The wavelet group time history and their respective PSD are shown in Figure 4.6.

T3 was decomposed into 16 wavelet levels and three peaks were found in the PSD plot (Figure 4.2a). Resonance peaks were found at three frequencies, i.e. 0.1 Hz, 1.8 Hz and 98.8 Hz, suggesting there were three wavelet groups, as shown in Figure 4.7.

T4 was decomposed into 15 wavelet levels and referring to the T4 PSD plot (Figure 4.2b), resonance peaks were found at four frequencies, i.e. 1.4 Hz, 2.7 Hz, 11.7 Hz and 35.9 Hz. The signal was divided into four wavelet groups, as shown in Figure 4.8.

T5 was decomposed into 15 wavelet levels and resonance peaks were found at four frequencies as shown in the PSD plot (Figure 4.2c), i.e. 1.5 Hz, 3.7 Hz, 11.7 Hz and 17.8 Hz. It is showed that the T5 signals can be divided into four wavelet groups, as shown in Figure 4.9.

Finally, T6 was decomposed into 14 wavelet levels and referring to the PSD plot (Figure 4.2d), resonance peaks were found at two frequencies, i.e. 0.1 Hz and 1.4 Hz. The signal was later divided into two wavelet groups, as shown in Figure 4.9.

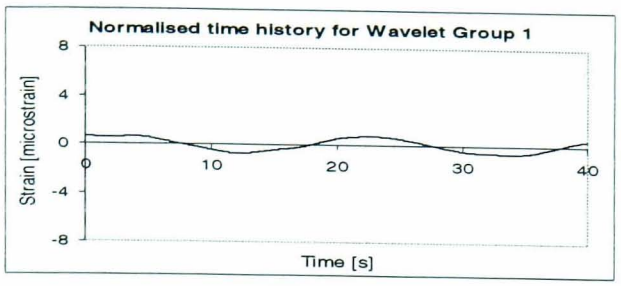

(a)

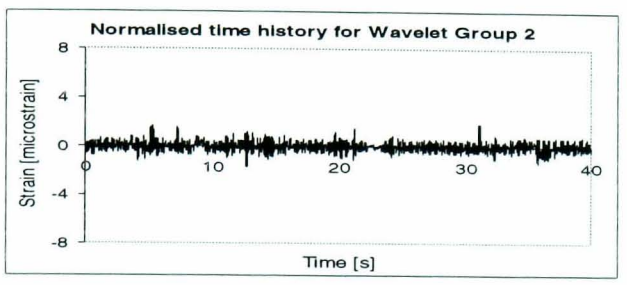

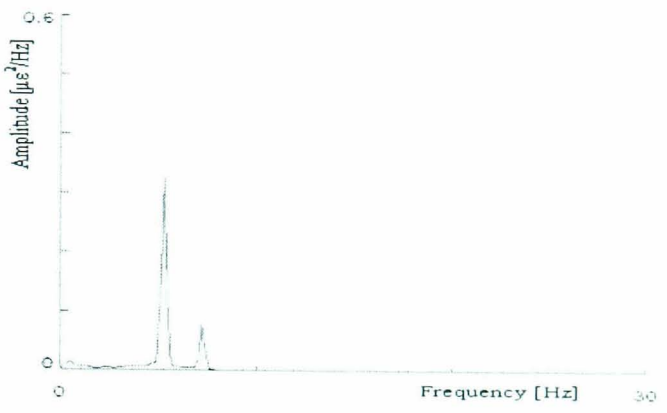

(b)

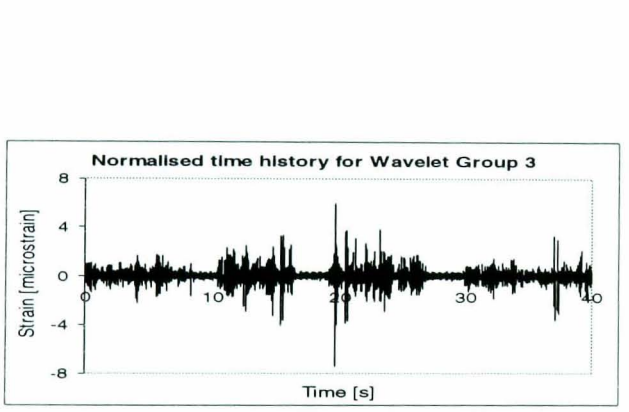

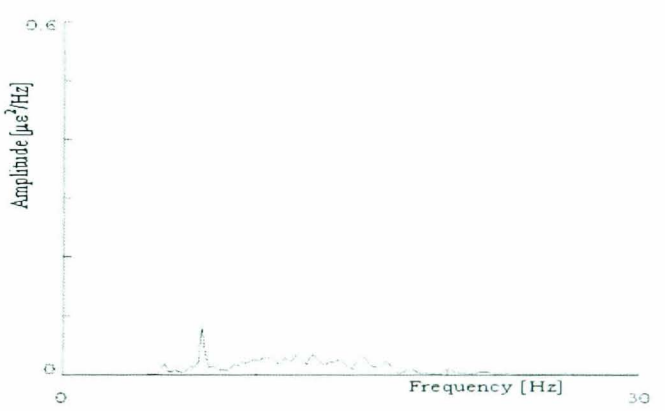

(c)

Figure 4.6: The wavelet group time histories and the PSD plots for T2:

(a) Wavelet Group 1, (b) Wavelet Group 2, (c) Wavelet Group 3.

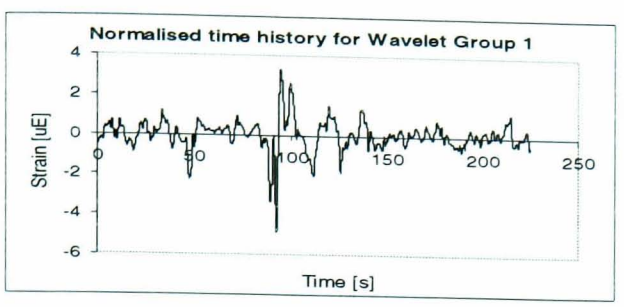

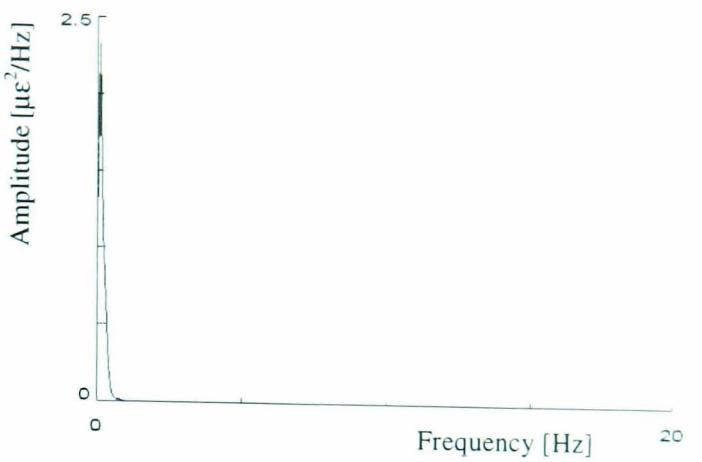

(a)

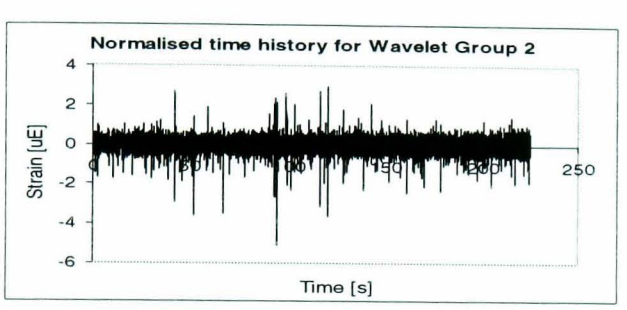

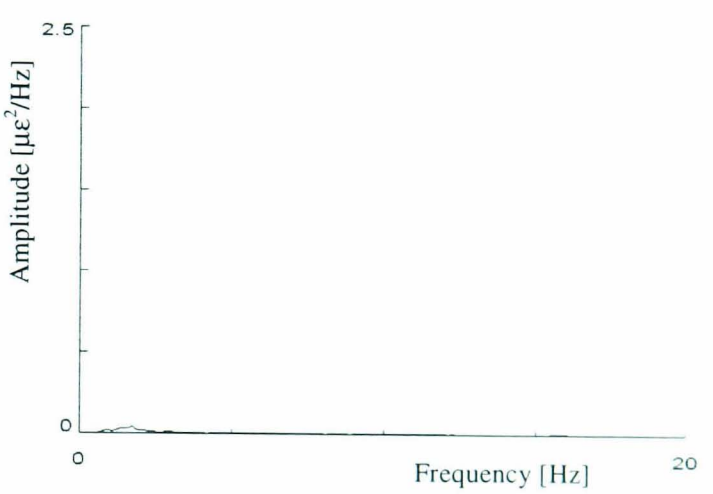

(b)

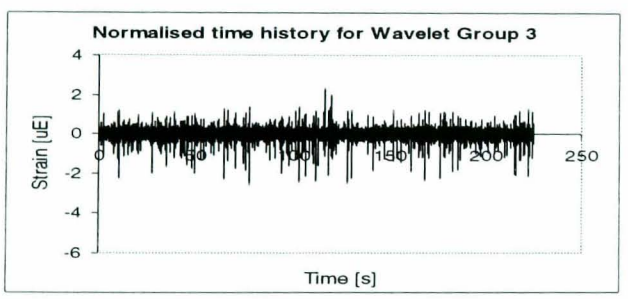

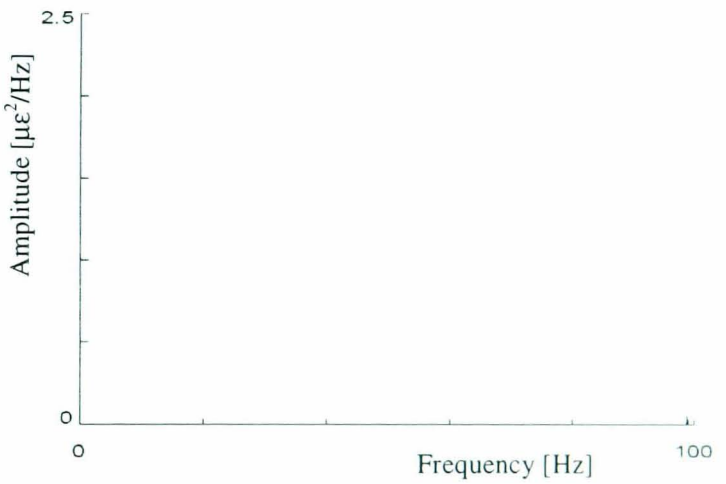

(c)

Figure 4.7: The wavelet group time histories and the PSD plots for T3:

(a) Wavelet Group 1, (b) Wavelet Group 2, (c) Wavelet Group 3.

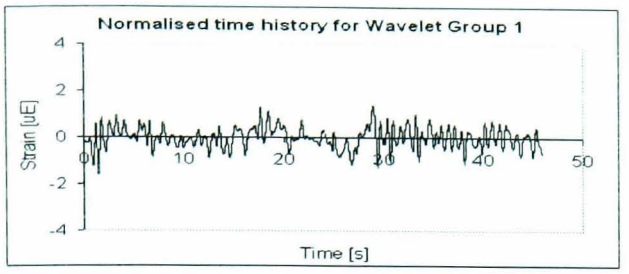

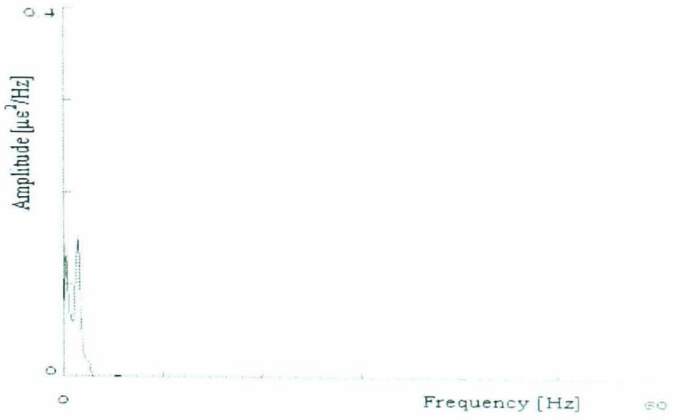

(a)

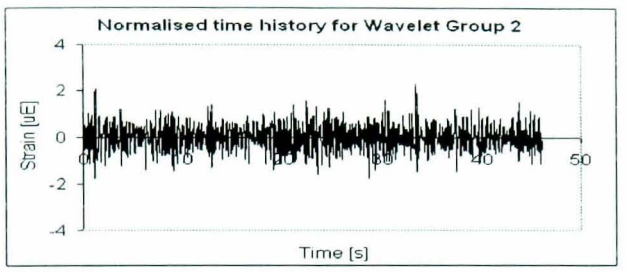

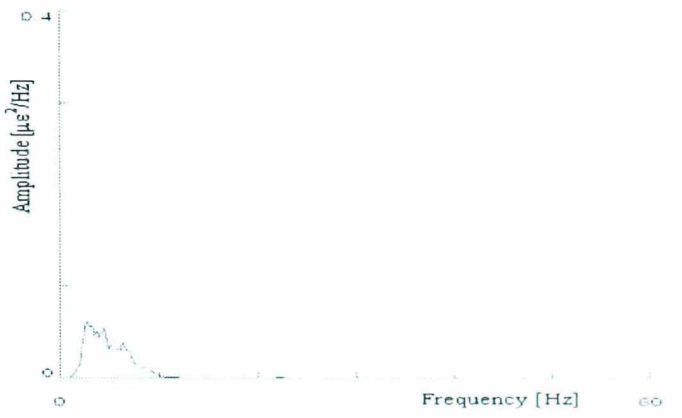

(b)

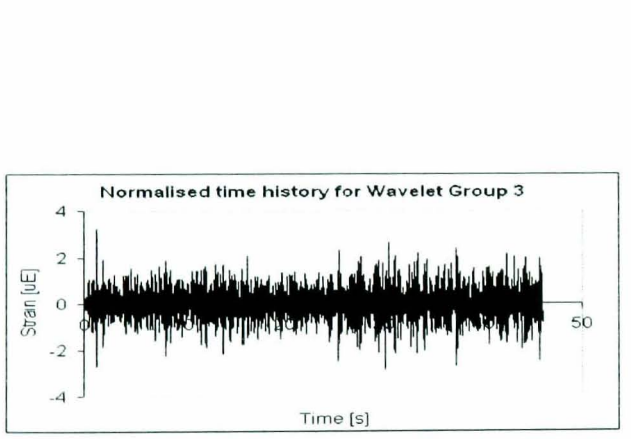

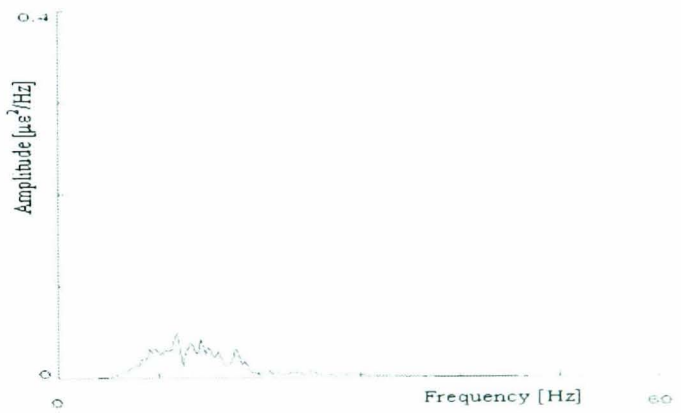

(c)

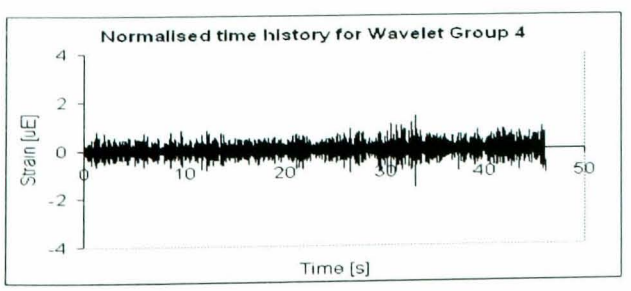

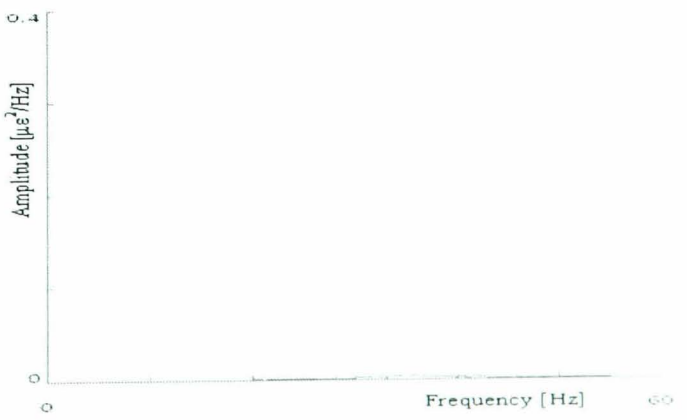

(d)

Figure 4.8: The wavelet group time histories and the PSD plots for T4:

(a) Wavelet Group 1, (b) Wavelet Group 2, (c) Wavelet Group 3,

(d) Wavelet Group 4.

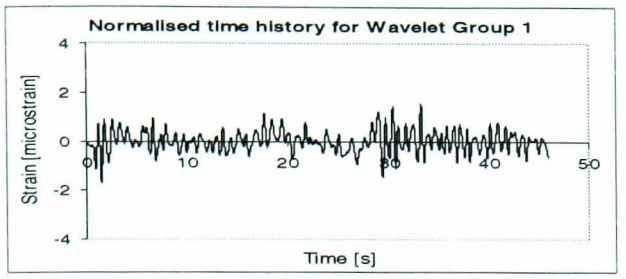

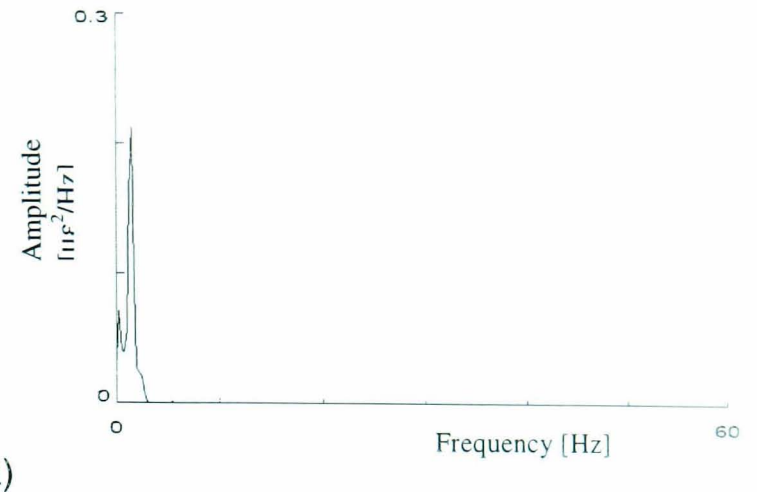

(a)

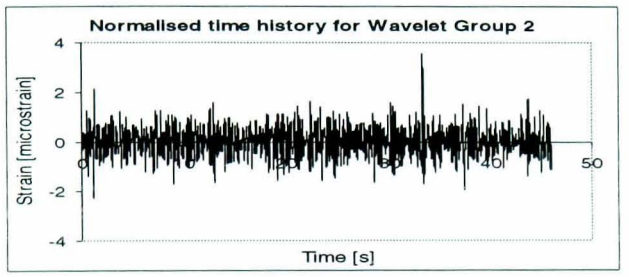

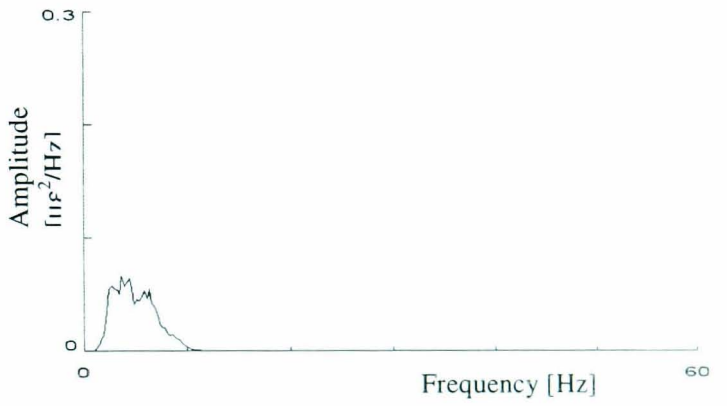

(b)

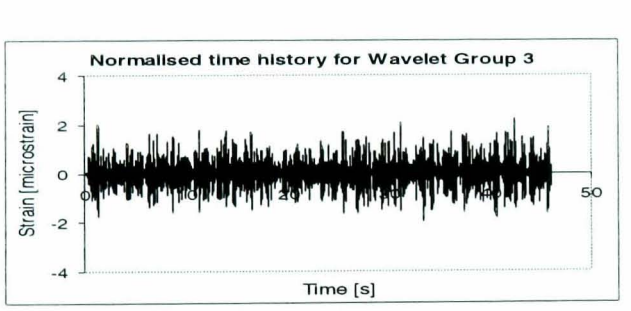

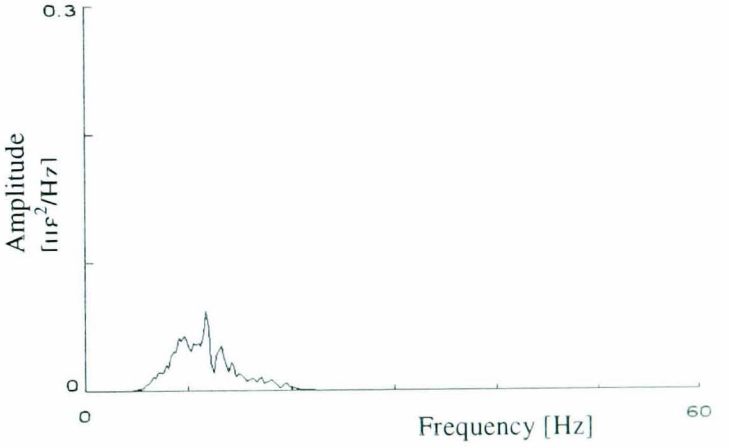

(c)

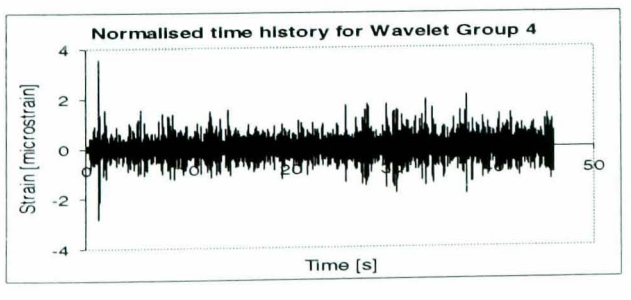

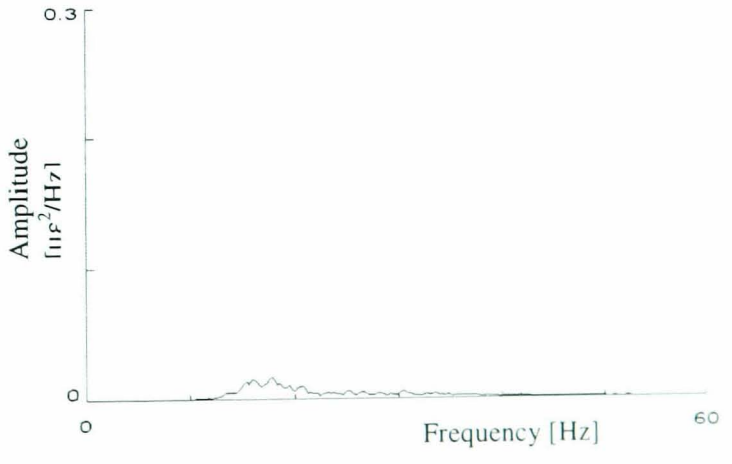

(d)

Figure 4.9: The wavelet group time histories and the PSD plots for T5:

(a) Wavelet Group 1, (b) Wavelet Group 2.

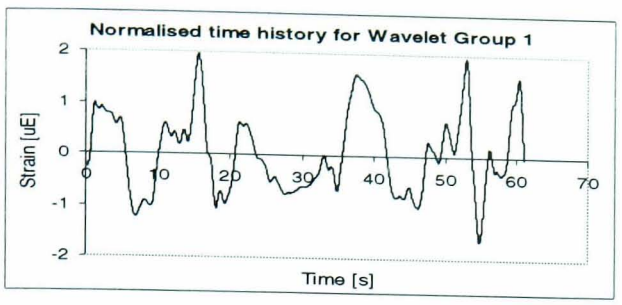

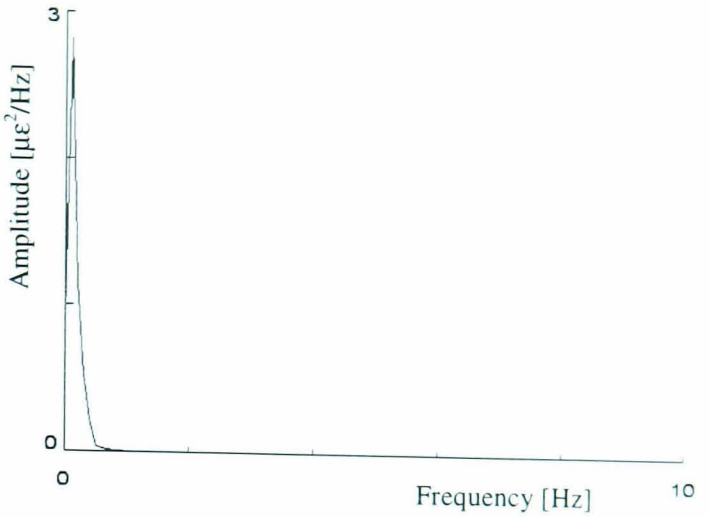

(a)

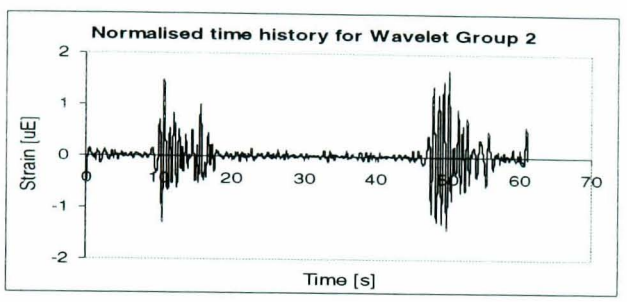

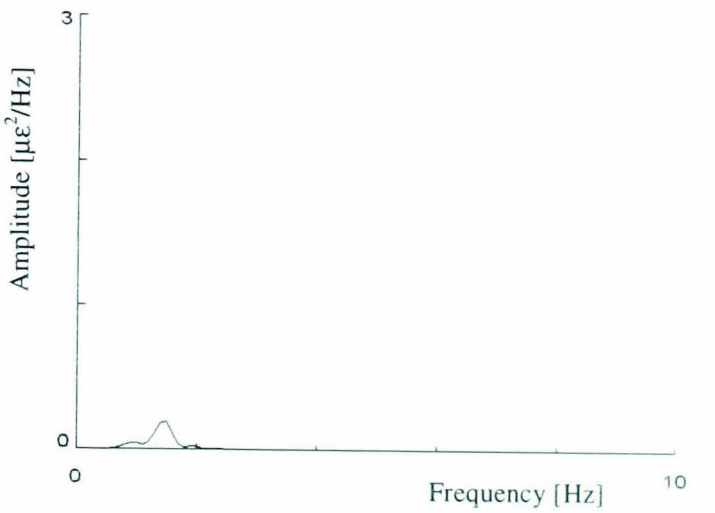

(b)

Figure 4.10: The wavelet group time histories and the PSD plots for T6: (a) Wavelet Group 1, (b) Wavelet Group 2.

4.4 Identification and Extraction of Bumps

4.4.1 Trigger Level Determination

In order to identify the bumps, trigger level values were set based on the root-mean-square (r.m.s.) and kurtosis difference between the original and mission signals. For this case, the use of ±10% difference in r.m.s. and kurtosis of the mission and the original signal is used for analysing experimental road load data sets in order to retain the signal energy and amplitude ranges (Abdullah *et al.* 2004). Therefore, the shortened mission

signal produced using the WBE algorithm has approximately the same global statistical values (PSD, r.m.s. and kurtosis) to those of the original signal.

As shown in Figure 4.11, the software requires the user to input four values. The first parameter, *C1*, is the percentage of the signal maximum value to use as a preliminary trigger level value in each wavelet group. The second parameter, *C2*, is the percentage value used to determine the trigger level step. The third and the fourth parameters are the r.m.s. and kurtosis difference values between the original signal and the WBE mission signal (*RD* and *KD*, respectively). If the user defined differences are not met, the trigger level is reduced in WBE by a step size of *C2*. The newly determined initial trigger levels are then presented to the user on screen as shown in Figure 4.12 as it appears when analysing signal T4.

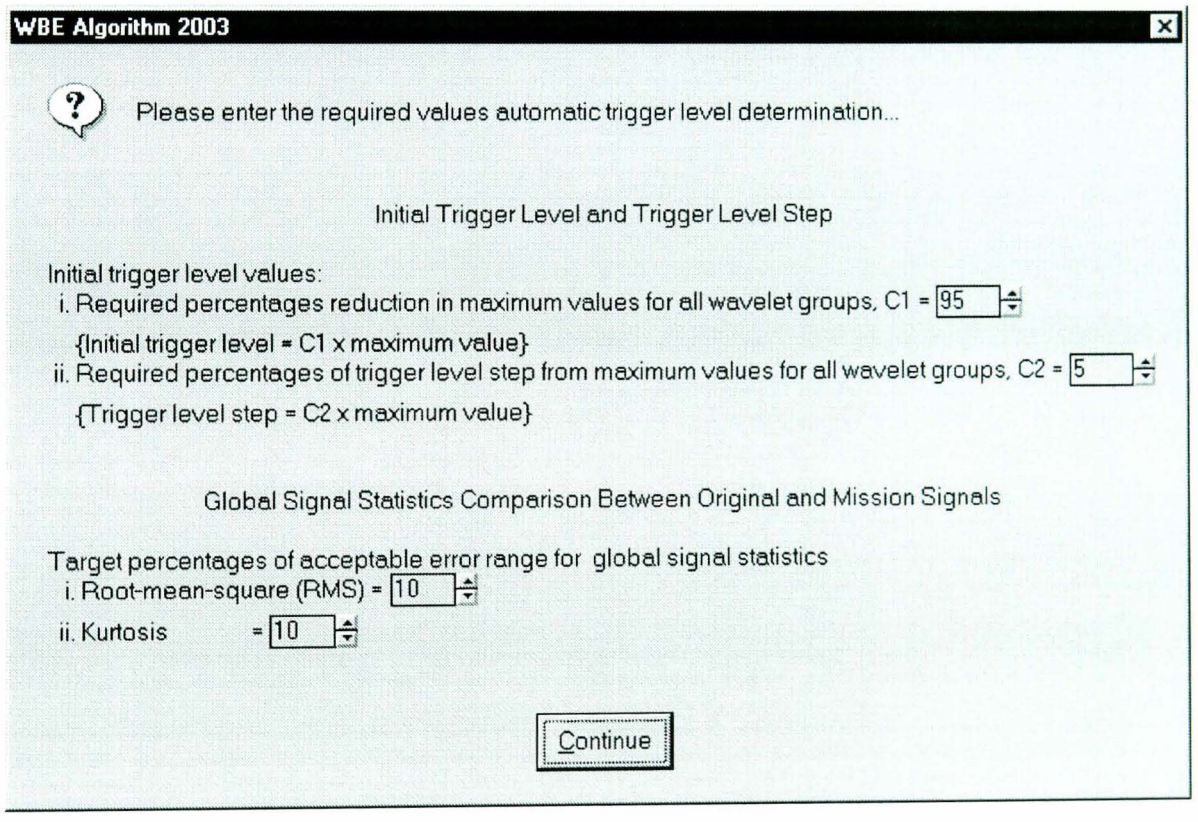

Figure 4.11: Input menu for the trigger level values.

In WBE the trigger level iteration process is terminated when the difference of the mission and original signals achieves the target statistical values. The final statistical differences between the mission and the original signals is presented on screen to the

user as shown in Figure 4.13 for which the target difference in r.m.s. and kurtosis was set to ±10%.

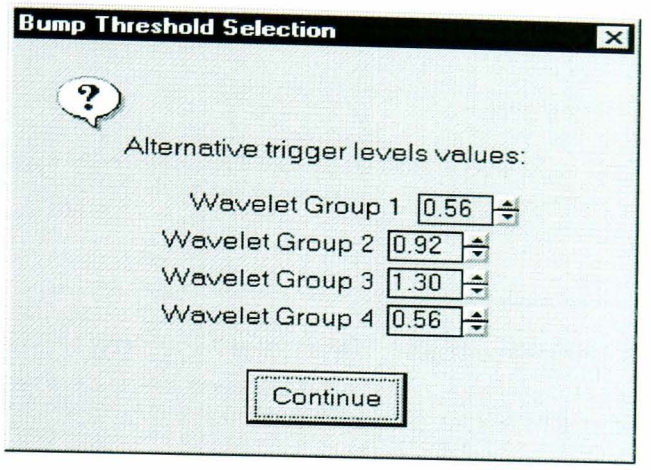

Figure 4.12: Alternative trigger level values for all wavelet groups as presented for signal T4.

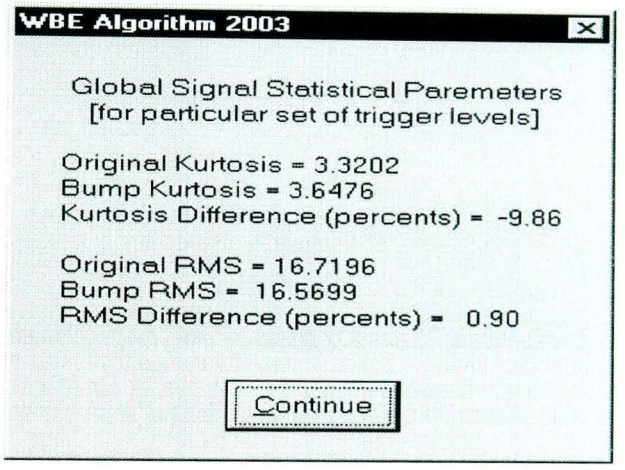

Figure 4.13: Final r.m.s. and kurtosis values for the T4 mission and for the original T4 signal.

4.4.2 Bumps Identification in Wavelet Groups

Figure 4.14 presents the identified bumps in each wavelet group of the test signal T1. The bumps were extracted using a ±75% difference in r.m.s. and kurtosis between the original and the mission signals. A large difference in r.m.s. and kurtosis values was required in the case of signal T1 as approximately 75% of the original signal contained low amplitude cycles, which significantly contributed to the r.m.s. and kurtosis calculations. The bump patterns were found to be different in each wavelet group,

especially between the lowest and highest frequency wavelet groups. In Wavelet Group 1 (Figure 4.14a), the bump exhibits a clear decay shape and it has longer time extent compared to bumps in other wavelet groups. It is due to the low frequency effects in Wavelet Group 1, hence contributing to the determination of the bump segment time length. In a higher frequency wavelet group or Wavelet Group 4 (Figure 4.14d) as an example, it is difficult to observe the decay shape of the bumps because of their short time extent.

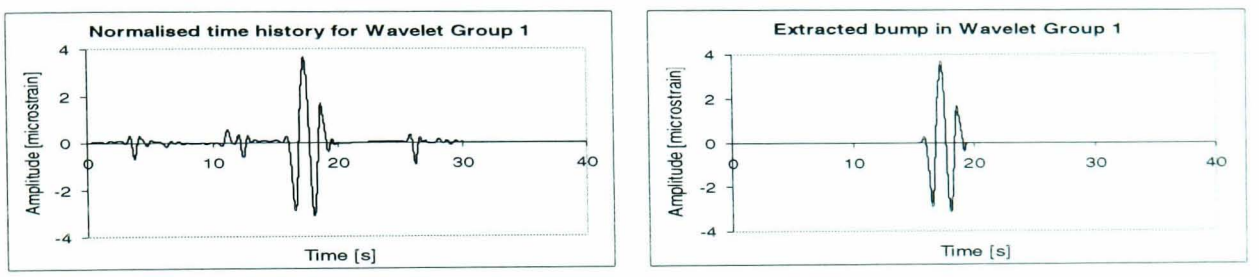

(a)

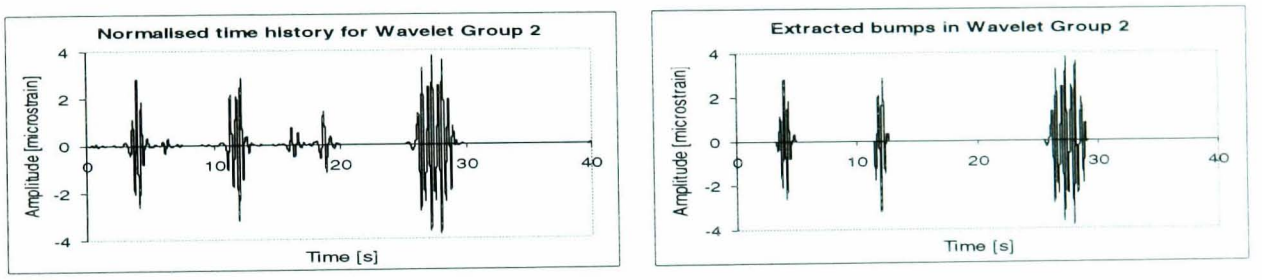

(b)

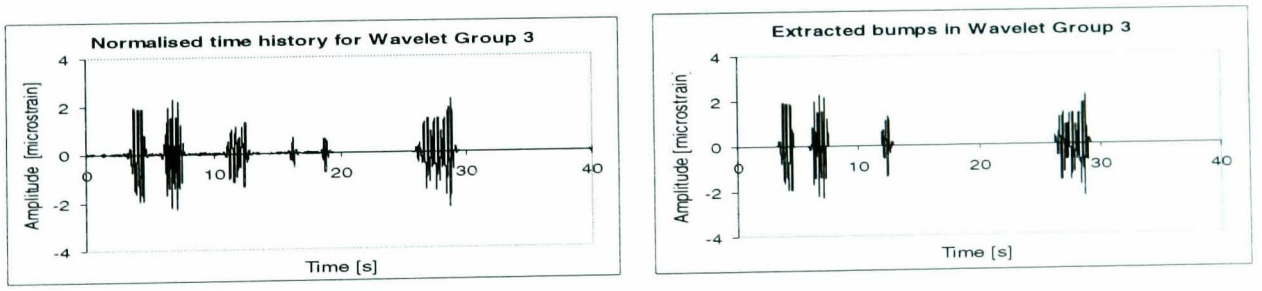

(c)

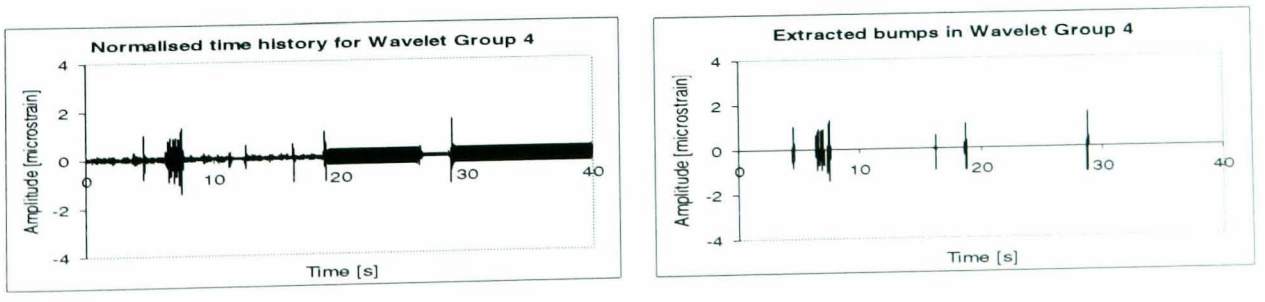

(d)

Figure 4.14: Time history plots and bumps identified in the wavelet groups for T1: (a) Wavelet Group 1, (b) Wavelet Group 2, (c) Wavelet Group 3, (d) Wavelet Group 4.

Figure 4.15 presents the bump extraction results for test signal T2. Since T2 was formed using random signals which contained with shocks, the bumps were easily identified at ±10% r.m.s. and kurtosis difference between the mission and the original signals. From Figure 4.15 it can be seen that the number of bump events varies greatly across the different wavelet groups. Finally, test signal T2 illustrates how a bump in the lowest frequency wavelet group can in practice determine the total time length of the mission signal.

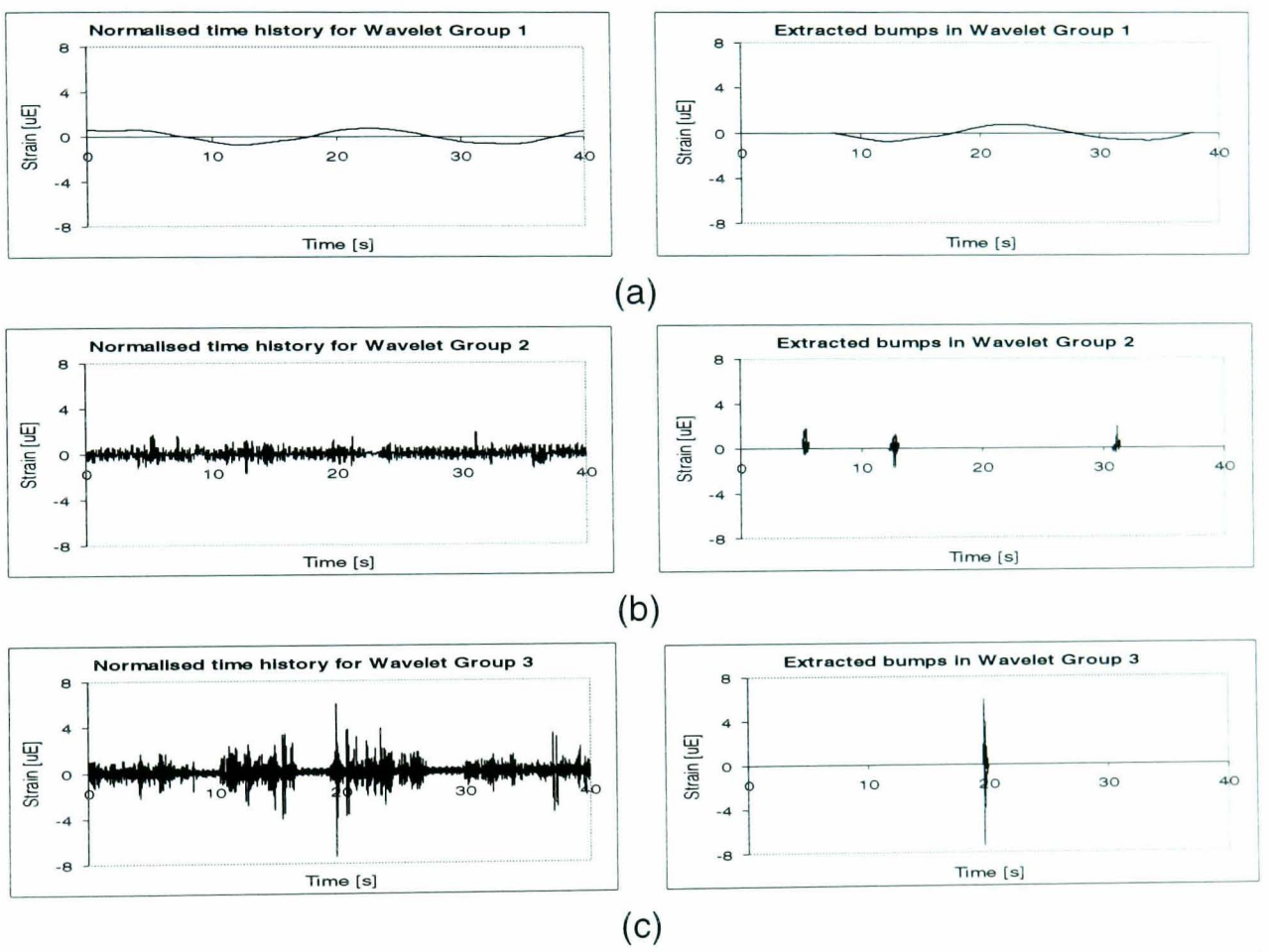

Figure 4.15: Time history plots and bumps identified in the wavelet group for T2: (a) Wavelet Group 1, (b) Wavelet Group 2, (c) Wavelet Group 3.

Figure 4.16 presents the bump extraction results for test signal T3 and the bumps were identified and extracted at ±10% r.m.s. and kurtosis difference between the mission and the original signals. From Figure 4.16 it can be seen that the number of bump events varies greatly across the different wavelet groups. This signal illustrates the shape of bumps which can be found when the automobile was driven over the public road surface.

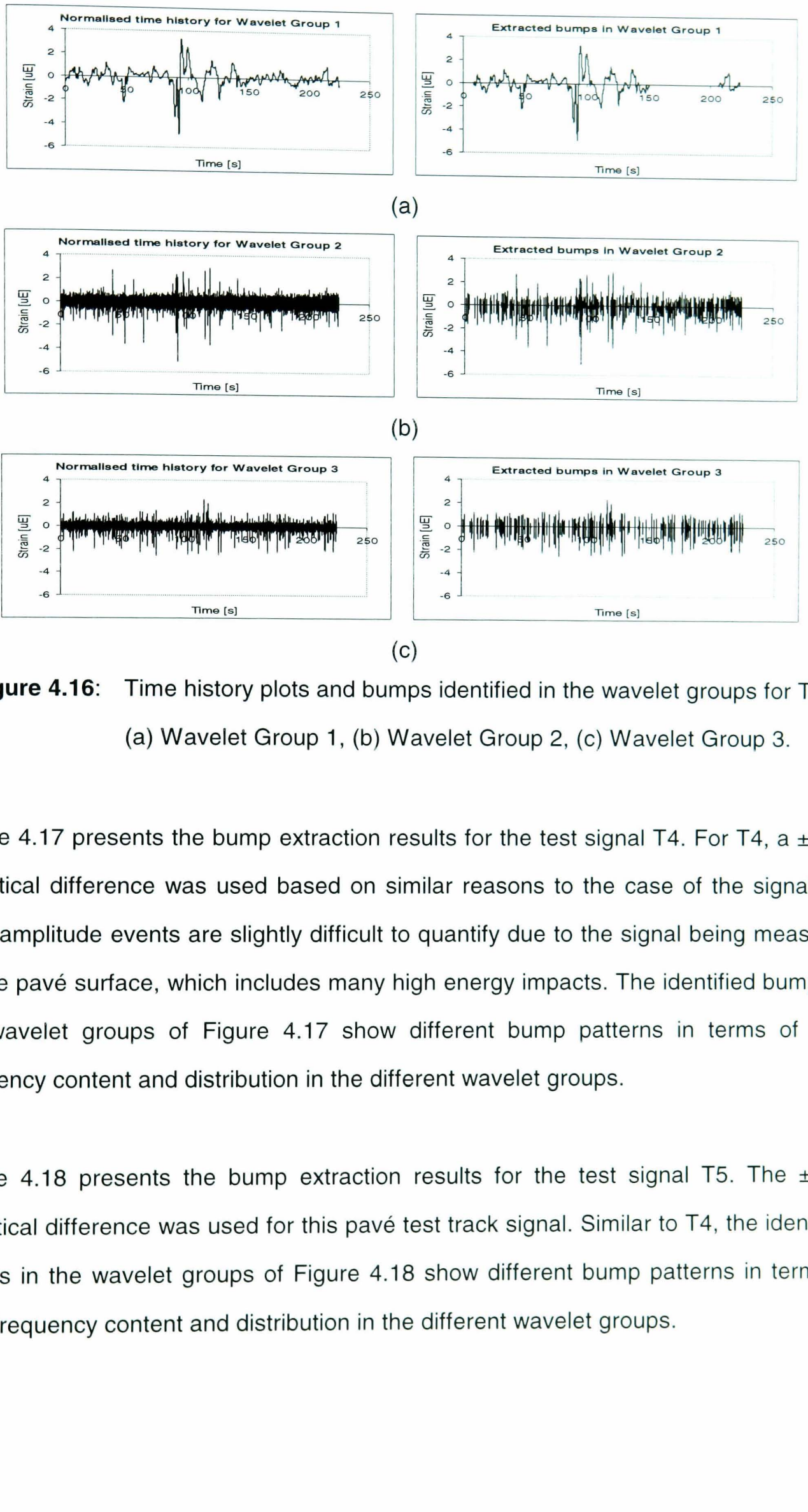

Figure 4.16: Time history plots and bumps identified in the wavelet groups for T3: (a) Wavelet Group 1, (b) Wavelet Group 2, (c) Wavelet Group 3.

Figure 4.17 presents the bump extraction results for the test signal T4. For T4, a ±10% statistical difference was used based on similar reasons to the case of the signal T2. High amplitude events are slightly difficult to quantify due to the signal being measured on the pavé surface, which includes many high energy impacts. The identified bumps in the wavelet groups of Figure 4.17 show different bump patterns in terms of their frequency content and distribution in the different wavelet groups.

Figure 4.18 presents the bump extraction results for the test signal T5. The ±10% statistical difference was used for this pavé test track signal. Similar to T4, the identified bumps in the wavelet groups of Figure 4.18 show different bump patterns in terms of their frequency content and distribution in the different wavelet groups.

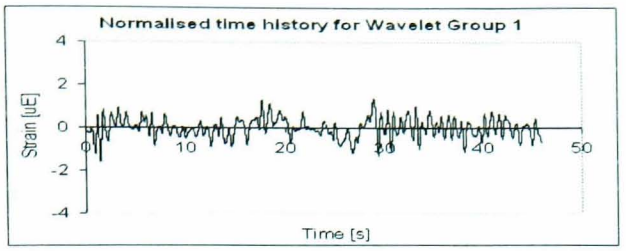

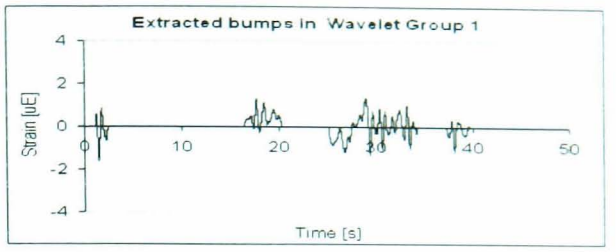

(a)

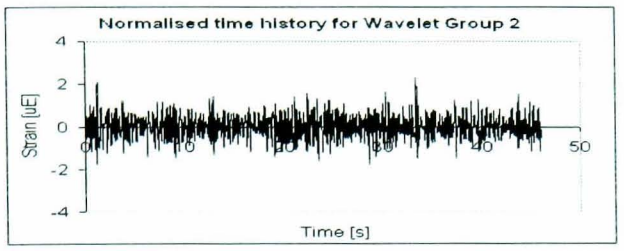

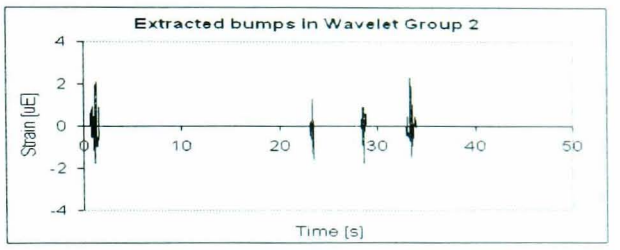

(b)

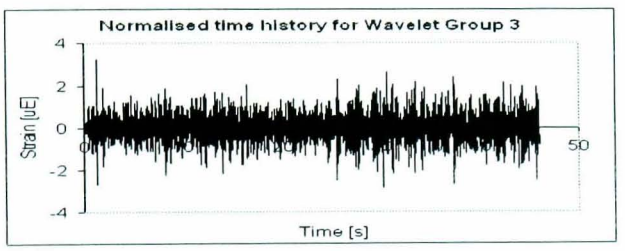

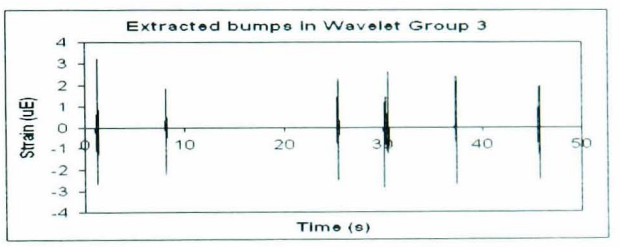

(c)

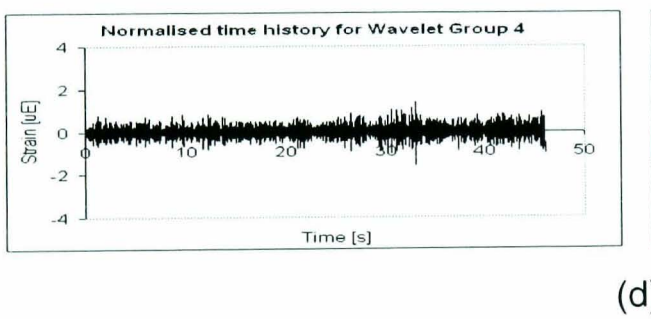

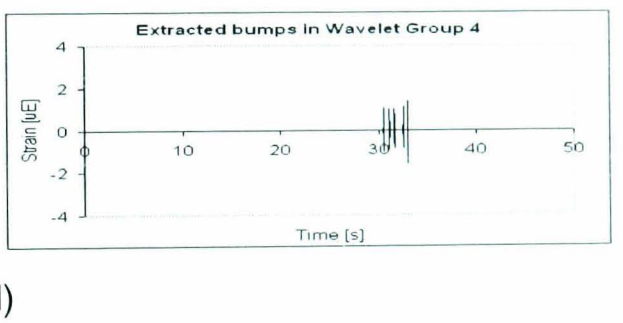

(d)

Figure 4.17: Time history plots and bumps identified in the wavelet group for T4: (a) Wavelet Group 1, (b) Wavelet Group 2, (c) Wavelet Group 3, (d) Wavelet Group 4.

For T6, finally, Figure 4.19 shows the bump extraction results using the ±10% r.m.s. and kurtosis difference between the mission and the original signals. Similar condition of this signal with T2, the T6 signal exhibits how a bump in the lowest frequency wavelet group can in practice determine the total time length of the mission signal.

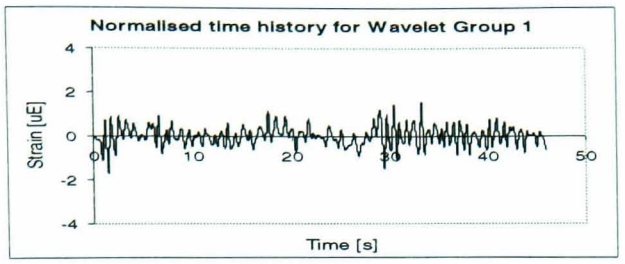

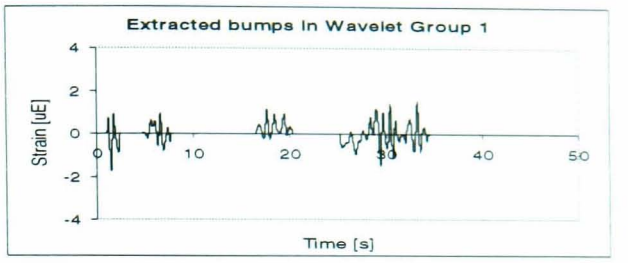

(a)

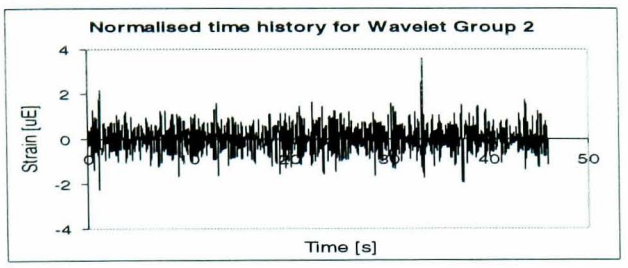

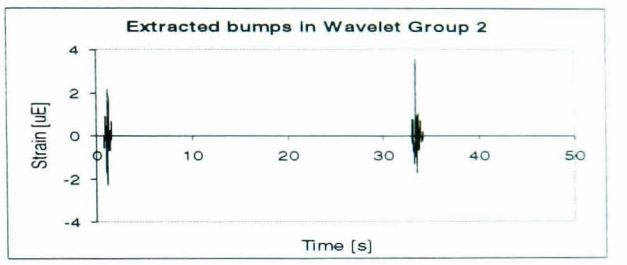

(b)

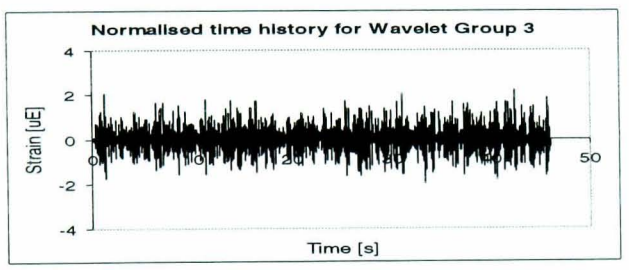

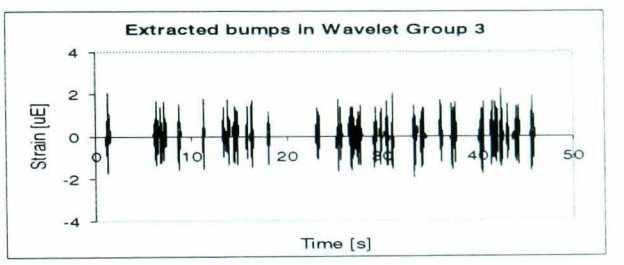

(c)

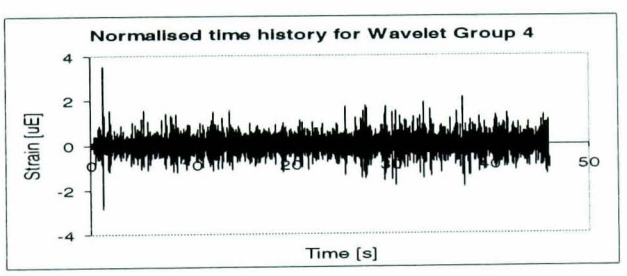

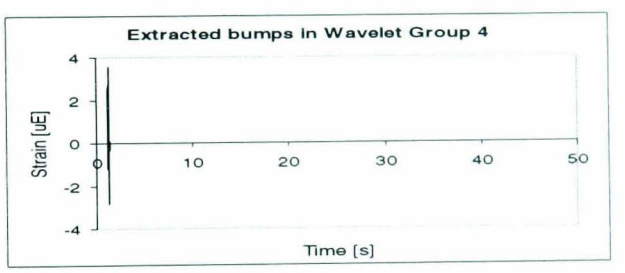

(d)

Figure 4.18: Time history plots and bumps identified in the wavelet groups for T5: (a) Wavelet Group 1, (b) Wavelet Group 2, (c) Wavelet Group 3, (d) Wavelet Group 4.

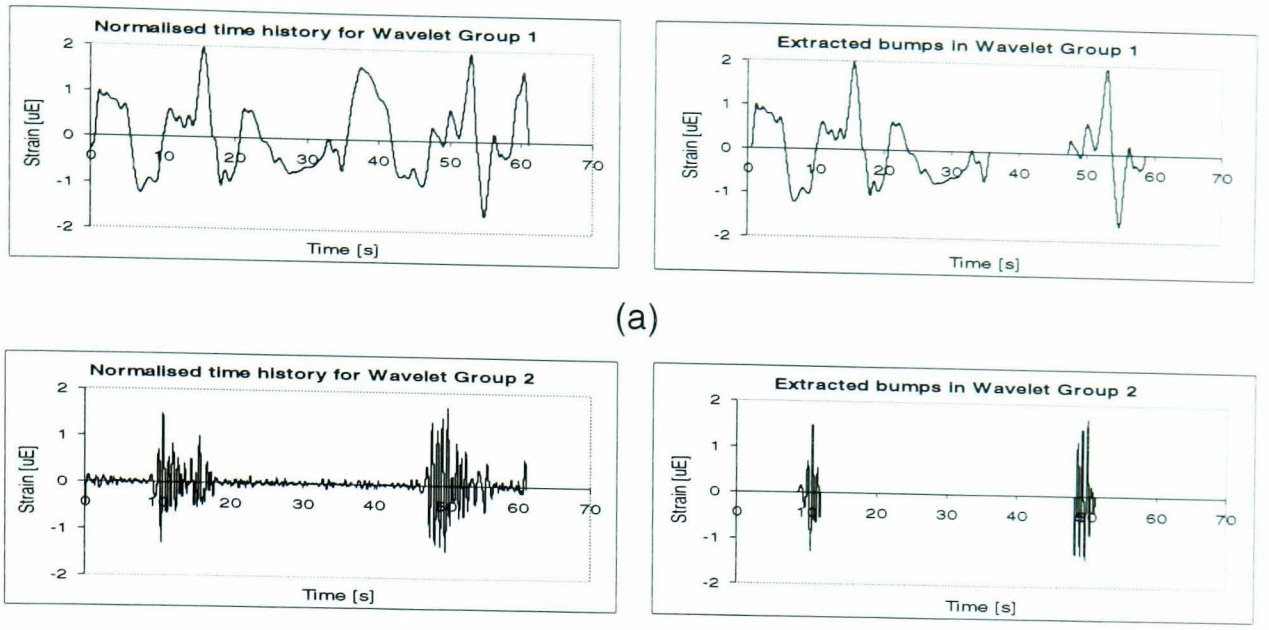

Figure 4.19: Time history plots and bumps identified in the wavelet groups for T6: Wavelet Group 1, (b) Wavelet Group 2.

4.4.3 Bump Segments Extraction from the Original Signal

When all bumps had been identified in the wavelet groups, the start and finish points need to be determined in order to identify high amplitude segments, later known as bump segments, of the original signal. The identified bump segments are shown at the real-time positions in Figure 4.20 to Figure 4.25 for T1 to T6.

All major bump events of signal T1 were identified and extracted by WBE. Only two bump segments were extracted from T2, indicating a major influence of the low frequency content to the determination of the bump segment length. In the T3 signals, 103 bump segments were identified and extracted. A large number of bump segments were expected since T3 is the longest signal (225 seconds) compared to the other signals. For T4, nine bump segments were identified and extracted for producing the mission signal. Using T5 with the WBE algorithm, 30 bump segments were extracted in order to produce the mission signal. Finally, two bump segments were extracted from the original T6 signal, showing the influence of low frequency content of the signal.

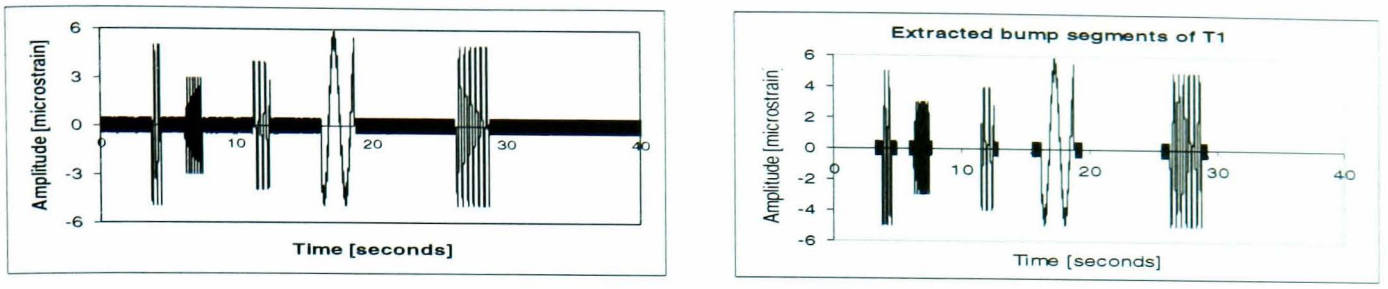

(a) (b)

Figure 4.20: T1 - (a) The original signal, (b) The bump segments.

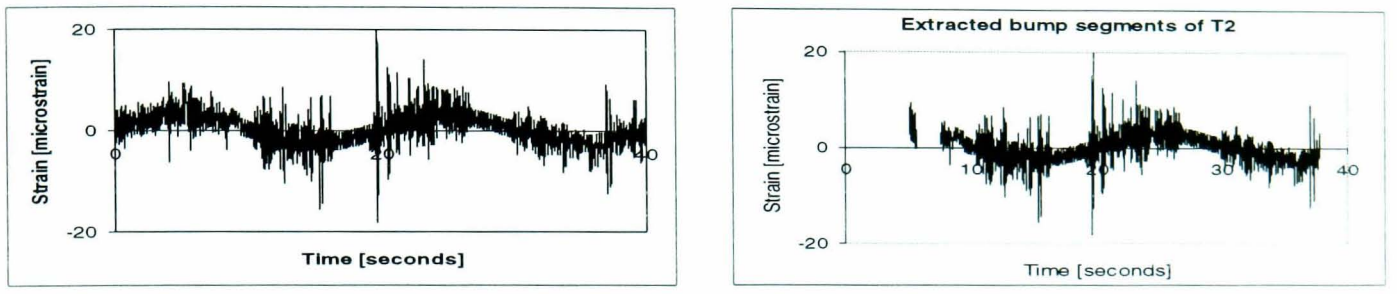

(a) (b)

Figure 4.21: T2 - (a) The original signal, (b) The bump segments.

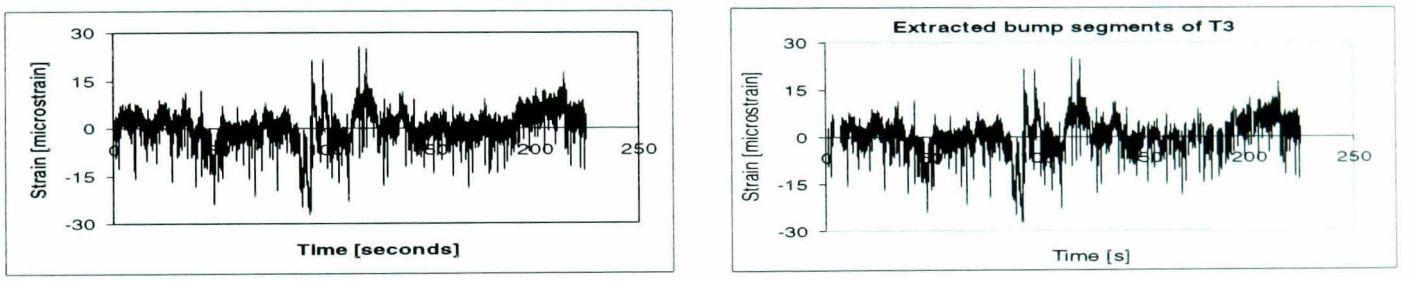

(a) (b)

Figure 4.22: T3 - (a) The original signal, (b) The bump segments.

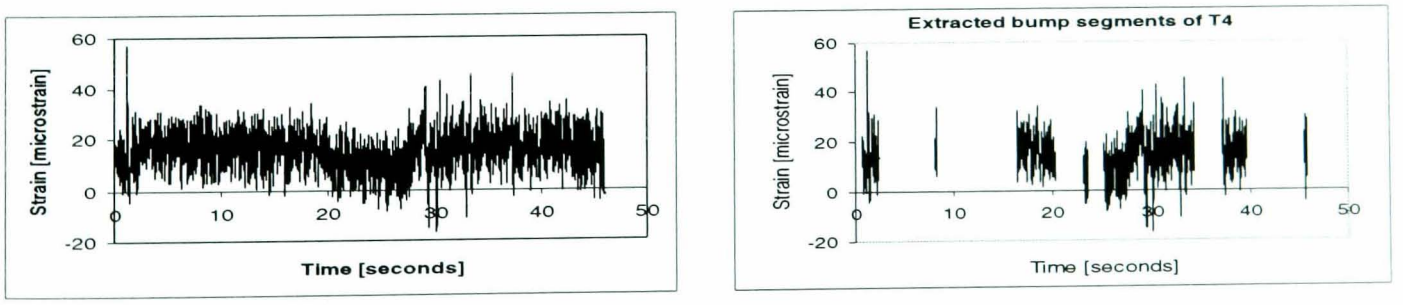

(a) (b)

Figure 4.23: T4 - (a) The original signal, (b) The bump segments.

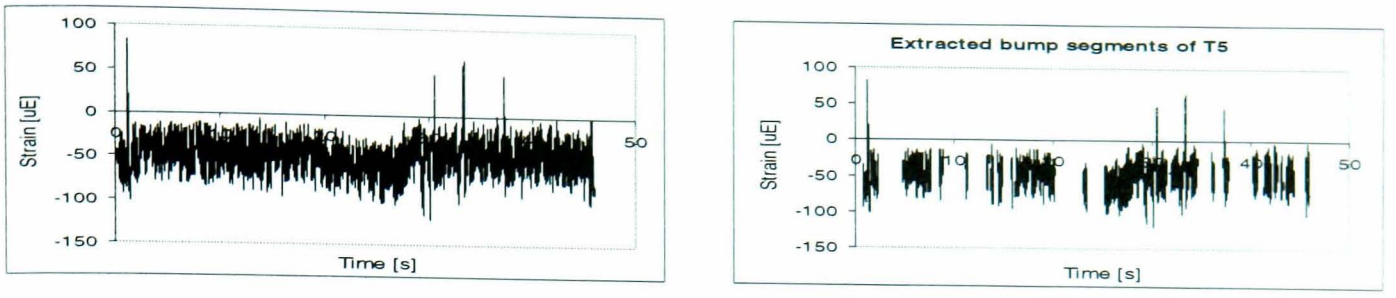

(a) (b)

Figure 4.24: T5 - (a) The original signal, (b) The bump segments.

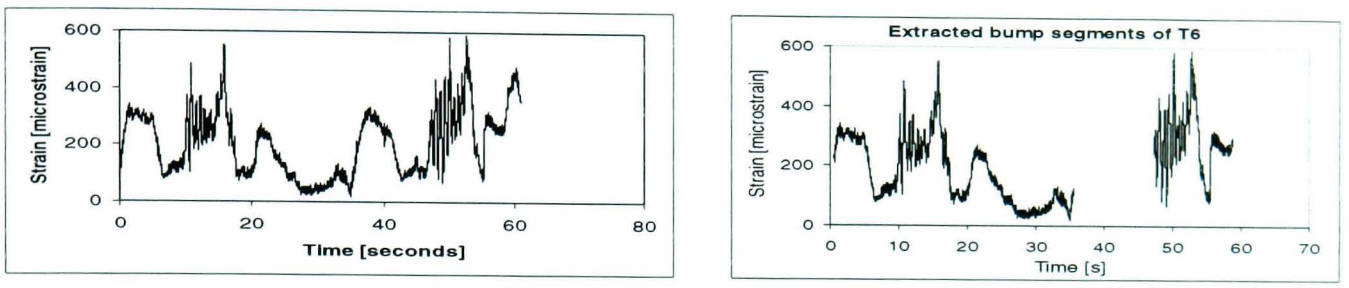

(a) (b)

Figure 4.25: T6 - (a) The original signal, (b) The bump segments.

4.5 Construction of the Mission Signals

When defining mission signals, the WBE algorithm orders the bumps in three different ways: the original order sequence of the bump segments (denoted as BS1), from the highest expected fatigue damage to the lowest (denotes as BS2) and from the lowest expected fatigue damage to the highest (denotes as BS3). The mission signals with different bump segment sequences will later be used for the analysis of bump segment sequence effects (discussed in Chapter 7). Using WBE, the mission signals produced from six test signals are shown in Figure 4.26 to Figure 4.31. In addition, characteristics of signal compression are tabulated in Table 4.3. For T3, T5 and T6, similar WBE processing procedures as T1, T2 and T4 were implemented in order to produce the mission signals.

As shown in Figure 4.26, all T1 mission signals were at the length of 12.5 seconds or 31.3% of the original signal after removal of the majority of small amplitudes. Some of the small amplitudes were found in the mission signals and these amplitudes were generated from a bump decaying shape in the wavelet groups. With reference to the

comparison of the global signal statistics, as tabulated in Table 4.3, the difference between the mission and original signals was 73.3% for r.m.s. and 66.2% for kurtosis. The significant differences illustrates the difficulties of performing fatigue data editing analysis based on global signal statistics alone.

The length of the T2 mission signals was 30.7 seconds or 76.7% of the original signal, as illustrated in Figure 4.27. Analysis of the bump segment pattern showed that low frequency content contributed to the determination of the mission signal length, as a lengthy bump was found in the lower frequency wavelet group. Since only two bump segments were extracted from the original signal, therefore, T2BS1 and T2BS3 exhibit similar mission signals. In another observation according to the information in Figure 4.21, the length of the T2 mission signal was also caused by a single bump segment in the low frequency wavelet group. Thus, it is not easy to heavily compress VA loadings with a substantially low frequency content.

Using T3, the ±10% difference in r.m.s. and kurtosis was applied for the bump identification process. At this difference value, the time length of the mission signals (Figure 4.28) was 181.9 seconds or 83.4% of the original signal. Referring to the global statistics comparison in Table 4.3, the difference between the mission and original signals were 6.5% for r.m.s. and 7.5% for kurtosis. For this signal, the pattern of the bump segment sequences are clearly observed in the mission signals.

For T4, the length of the mission signals was 18.8 seconds or 40.9% of the original signal, as illustrated in Figure 4.29. At this length, 9,129 data points were extracted to produce the mission signals. With reference to Table 4.3, the r.m.s. and kurtosis difference between the mission and the original signals were 0.6% and 9.1%, respectively. The comparison in the time length and global signal statistics between the mission and original signals showed that higher signal compression was obtained when the majority of high amplitude events were extracted.

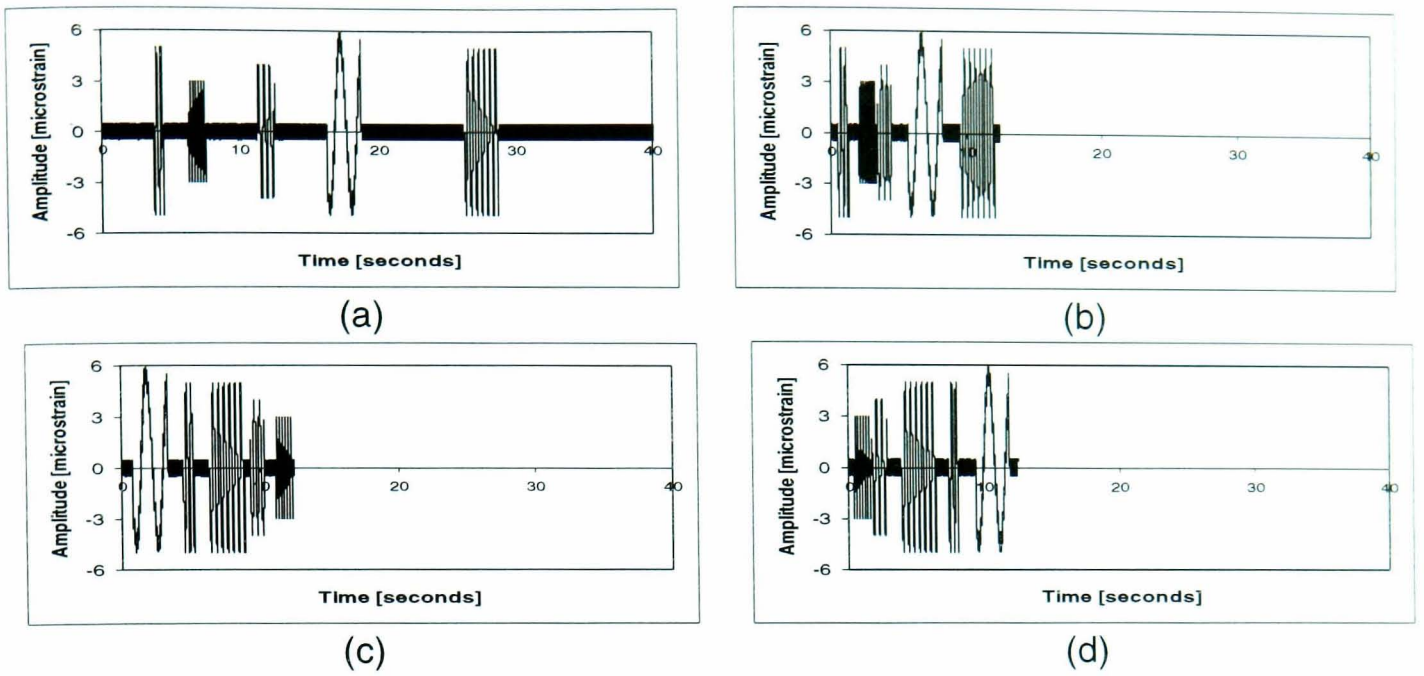

Figure 4.26: Different bump segment sequences in the mission signals for T1:

(a) T1 - the original signal,

(b) T1BS1 - the original order sequence of the bump segments,

(c) T1BS2 - from the highest expected fatigue damage to the lowest,

(d) T1BS3 - from the lowest expected fatigue damage to the highest.

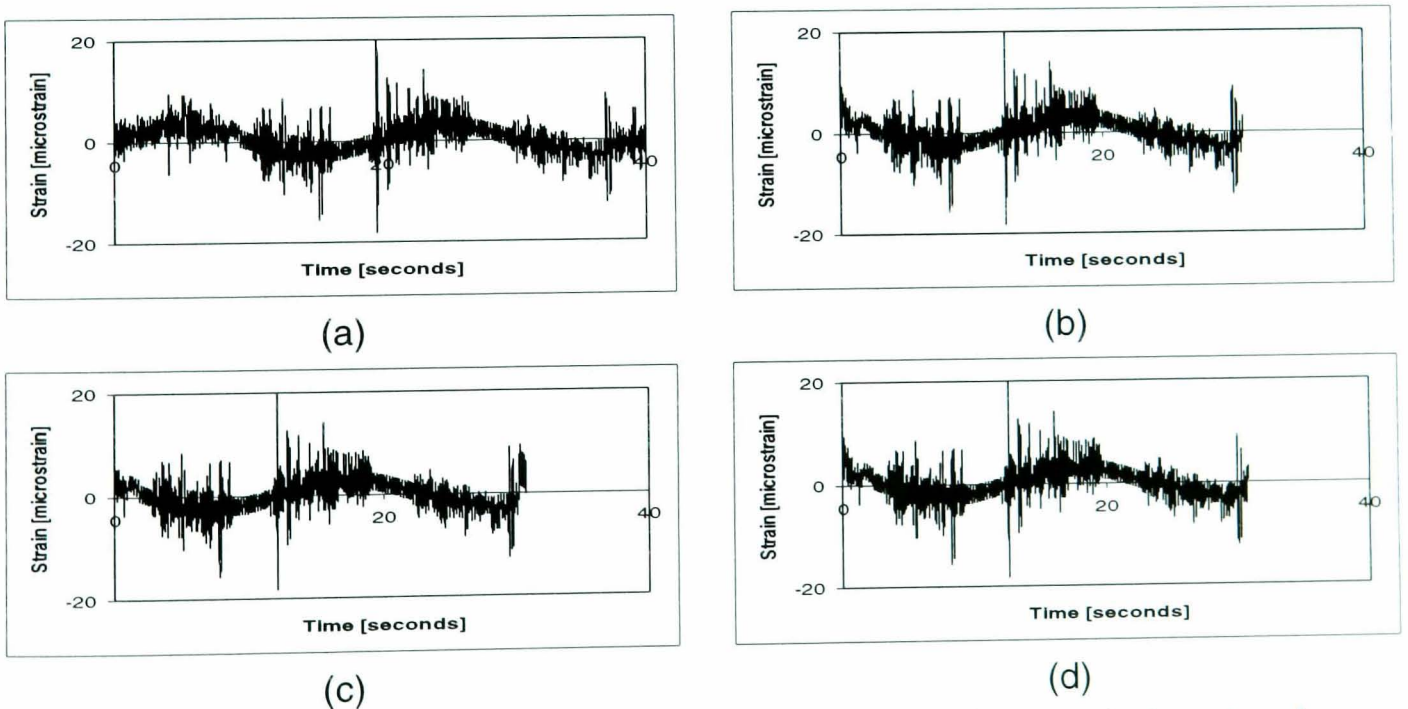

Figure 4.27: Different bump segment sequences in the T2 mission signals:

(a) T2, (b) T2BS1, (c) T2BS2, (d) T2BS3.

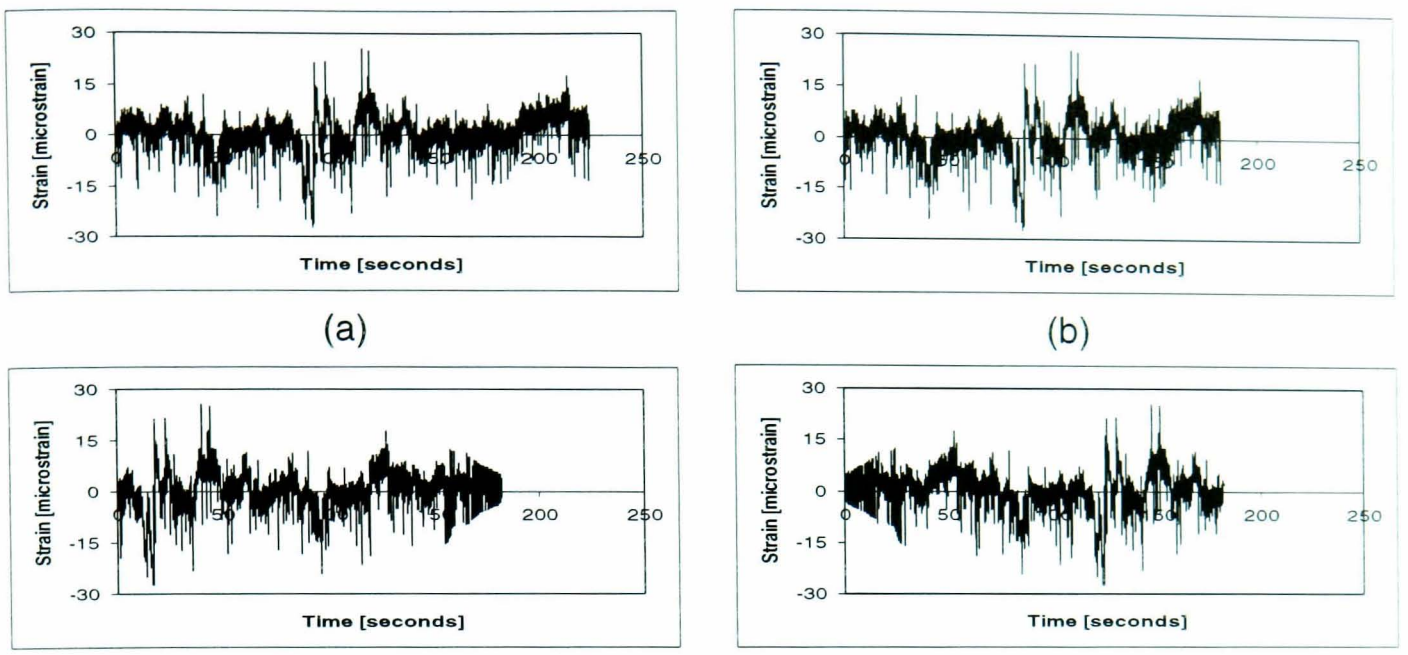

Figure 4.28: Different bump segment sequences in the T3 mission signals: (a) T3, (b) T3BS1, (c) T3BS2, (d) T3BS3.

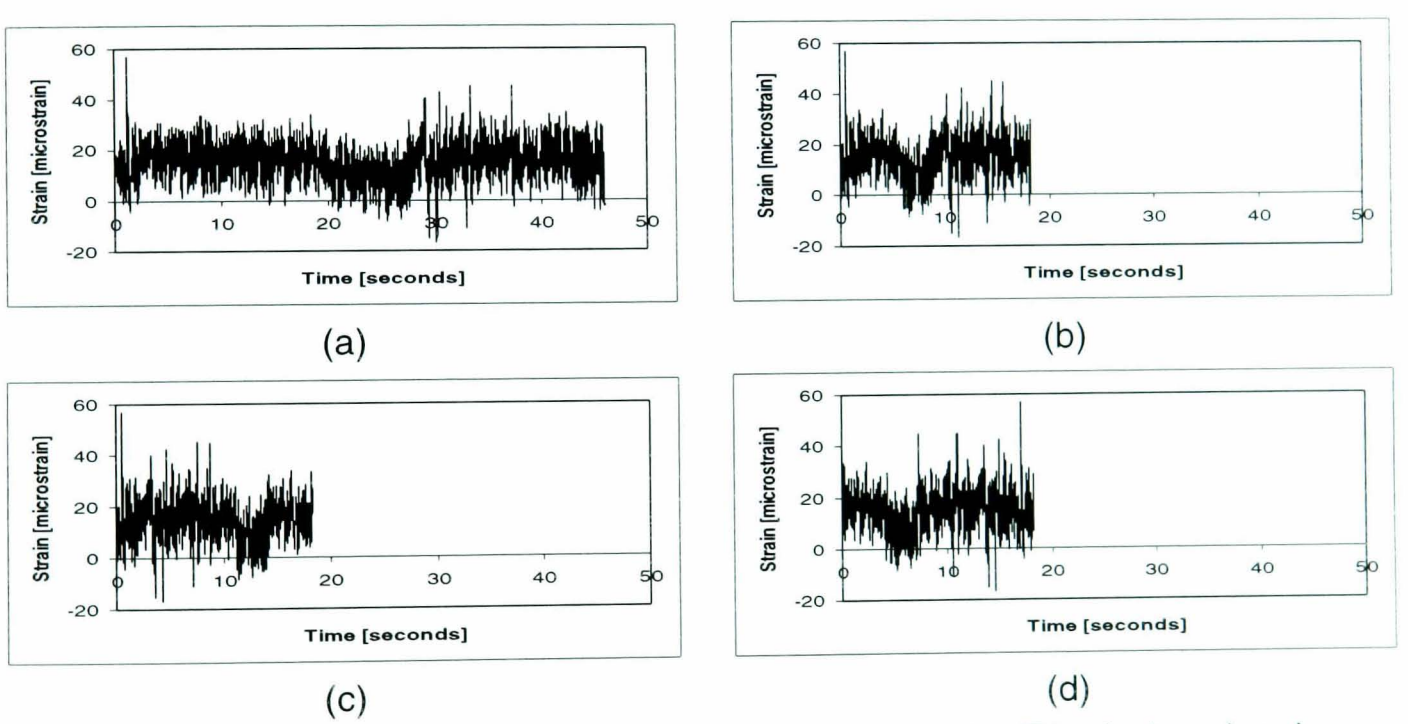

Figure 4.29: Different bump segment sequences in the T4 mission signals: (a) T4, (b) T4BS1, (c) T4BS2, (d) T4BS3.

The T5 mission signals have the time length of 24.8 seconds or 53.9% of the original signal, as illustrated in Figure 4.30. This time length was obtained when the r.m.s. and kurtosis difference of the mission signal was within ±10% of the original signal. Similar to T4, it shows that higher signal compression can be obtained from the signal measured on the pavé test track surface.

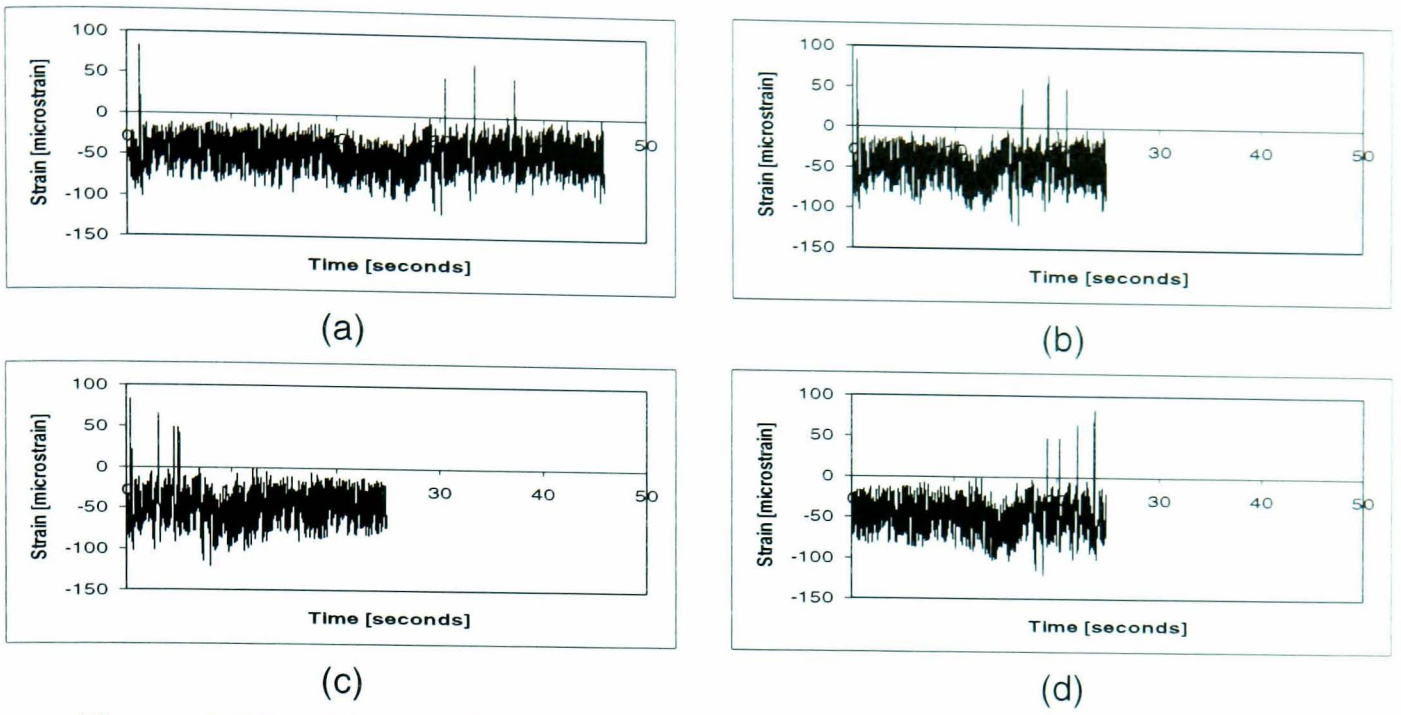

Figure 4.30: Different bump segment sequences in the T5 mission signals: (a) T5, (b) T5BS1, (c) T5BS2, (d) T5BS3.

Finally, the time length of the T6 mission signals were 46.4 seconds or 76.1% of the original signal, as illustrated in Figure 4.31. Referring to Table 4.3, the global signal statistical differences of 2.0% for r.m.s. and 3.8% for kurtosis were found between the mission and original signals. Since only two bump segments were extracted from the original signal, therefore, T6BS1 and T6BS3 exhibit similar mission signals. By comparing the pattern of the T6 bump segments (Figure 4.25b) and the T6 mission signals (Figure 4.31), it is shown that the low frequency content signal gave a significant contribution to the determination of the length of bump segments and mission signals. Similar to T2, the T6 signal demonstrated difficulty in producing a substantially shortened mission signal using this type of signal.

Figure 4.32 to Figure 4.37 show the PSD of the test signals and their WBE mission signals, showing the preservation of the original frequency content and signal energy in the mission signal. For T1, the difference of PSD amplitude can be observed at 10 Hz, indicating the removal of low amplitude cycles which were located at higher frequency region of the PSD. In all figures (Figure 4.32 to Figure 4.37), the overlapping pattern of PSD between the mission and the original signals can be observed. It is due to the technique of bump identification in the individual frequency band or wavelet group.

Therefore, the frequency information was accounted for in the bump segments extraction and the mission signals construction.

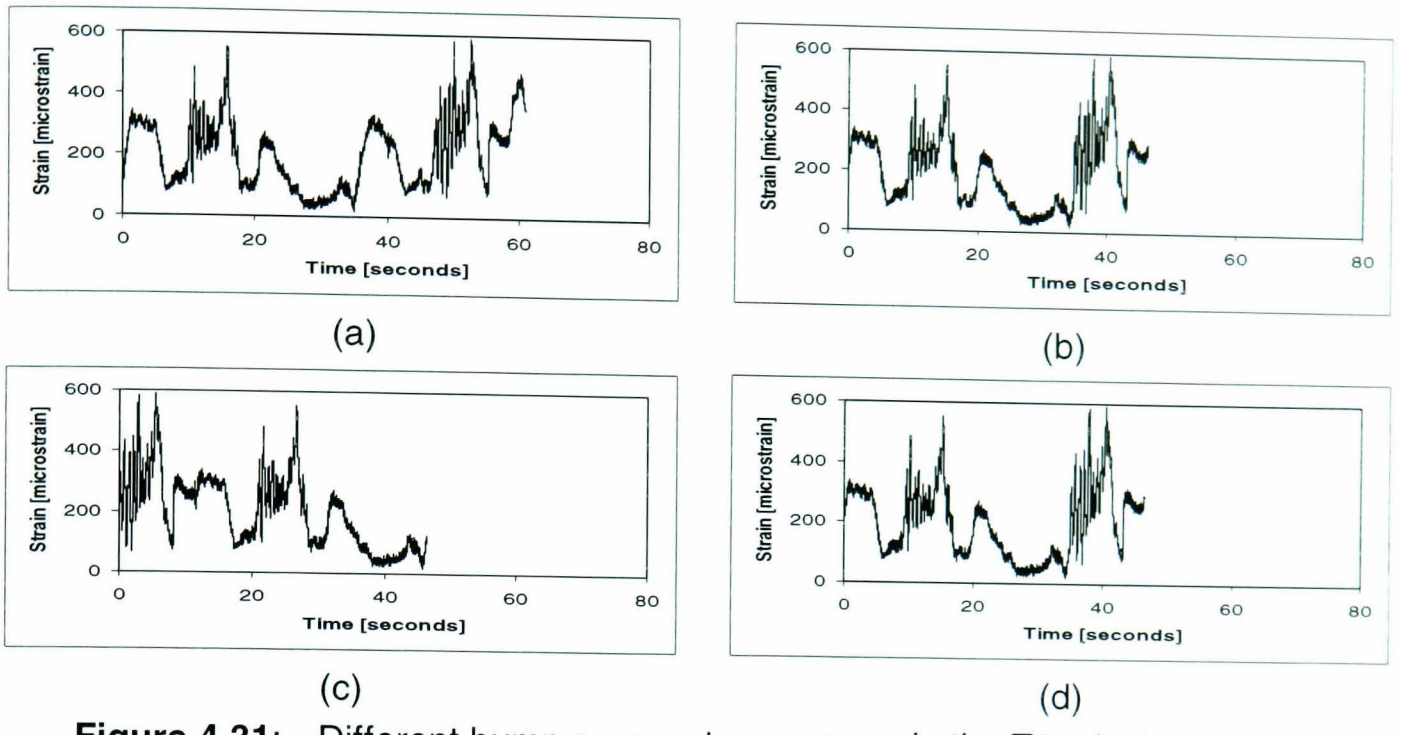

Figure 4.31: Different bump segment sequences in the T6 mission signals: (a) T6, (b) T6BS1, (c) T6BS2, (d) T6BS3.

Table 4.3: The compression characteristics of signal length and global signal statistics between the original and mission signals.

Signal Name		Signal Statistical Properties						
		Signal length [seconds]	Time ratio [%]	r.m.s. [$\mu\varepsilon$]	Kurtosis	r.m.s. difference [%]	Kurtosis difference [%]	Difference required [%]
T1	Original	40.0	31.3	1.5	7.4	73.3	66.2	±75.0
	Mission	12.5		2.6	2.5			
T2	Original	40.0	76.7	2.9	4.4	3.4	6.8	±10.0
	Mission	30.7		3.0	4.7			
T3	Original	225.0	83.4	4.6	8.0	6.5	7.5	±10.0
	Mission	181.9		4.9	7.4			
T4	Original	46.0	40.9	16.7	3.3	0.6	9.1	±10.0
	Mission	18.8		16.6	3.6			
T5	Original	46.0	53.9	51.6	3.7	1.6	8.1	±10.0
	Mission	24.8		52.4	4.0			
T6	Original	61.0	76.1	235.5	2.6	2.0	3.8	±10.0
	Mission	46.4		230.7	2.7			

Note: *Time ratio (%)* = $(t_{mission} / t_{original})$ x 100%,

Statistical difference = $\left| (statistics_{mission} - statistics_{original})/statistics_{original} \right|$ x 100%

Absolute values were taken for the statistical difference

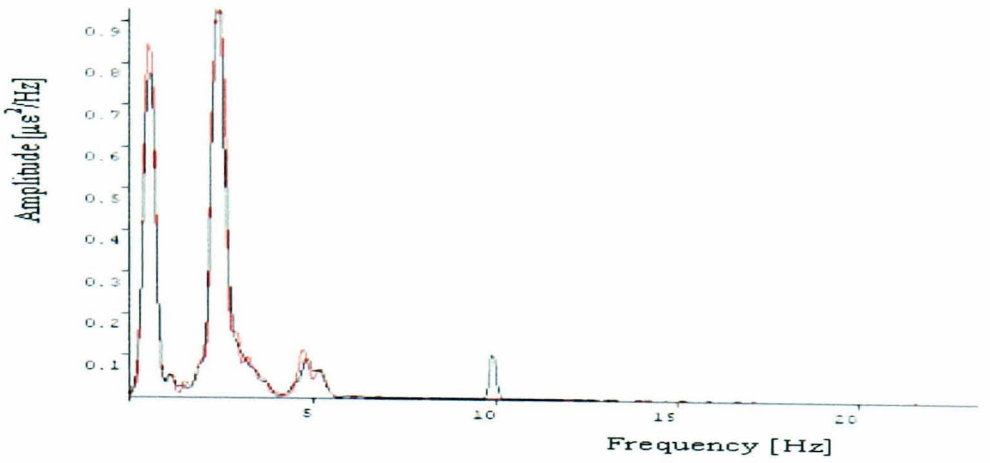

Figure 4.32: PSD comparison between the T1 original signal (black colour) and its equivalent WBE mission signal (red colour).

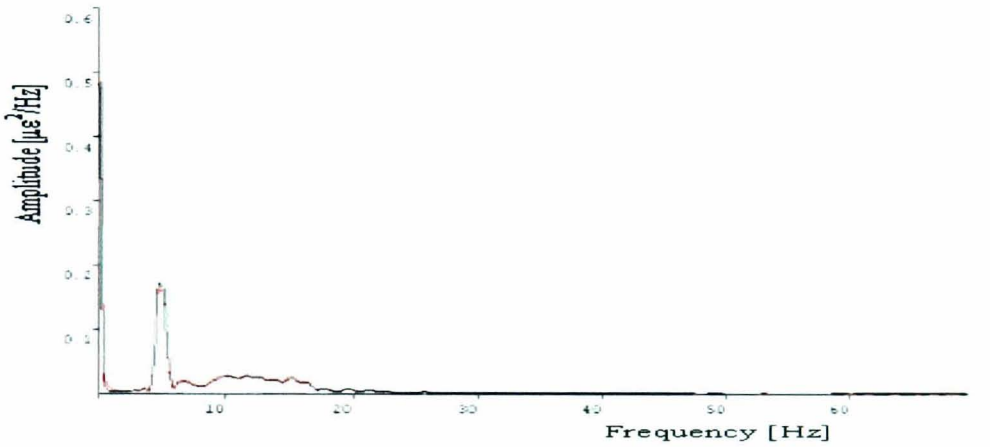

Figure 4.33: PSD comparison between the T2 original signal (black colour) and its equivalent WBE mission signal (red colour).

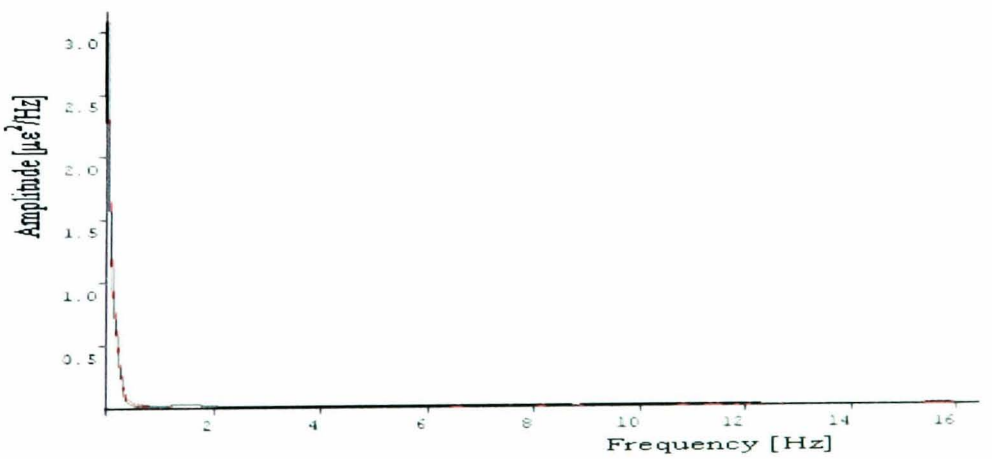

Figure 4.34: PSD comparison between the T3 original signal (black colour) and its equivalent WBE mission signal (red colour).

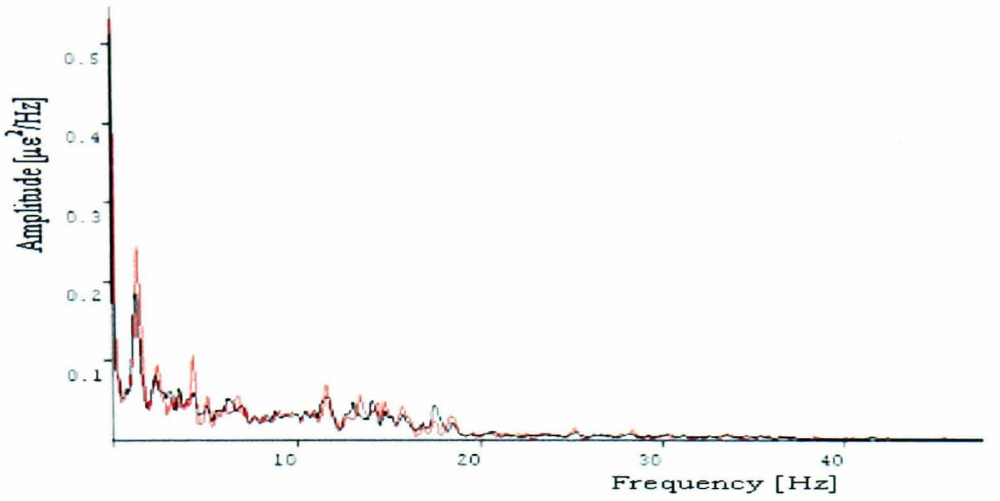

Figure 4.35: PSD comparison between the T4 original signal (black colour) and its equivalent WBE mission signal (red colour).

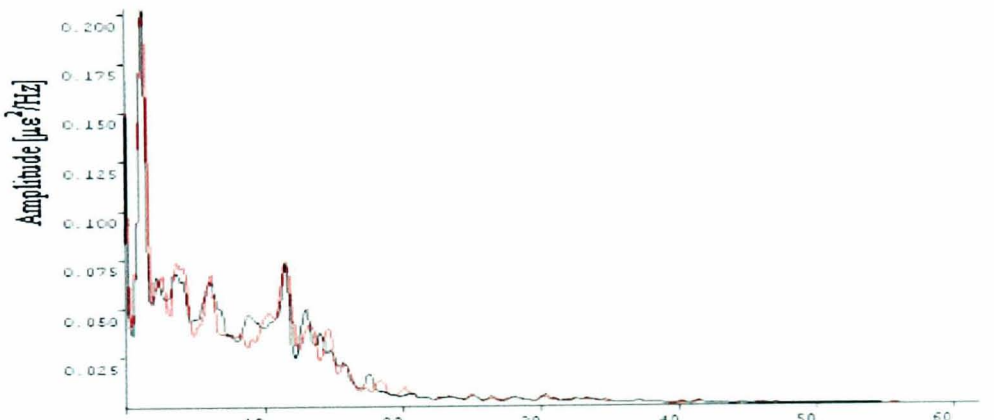

Figure 4.36: PSD comparison between the T5 original signal (black colour) and its equivalent WBE mission signal (red colour).

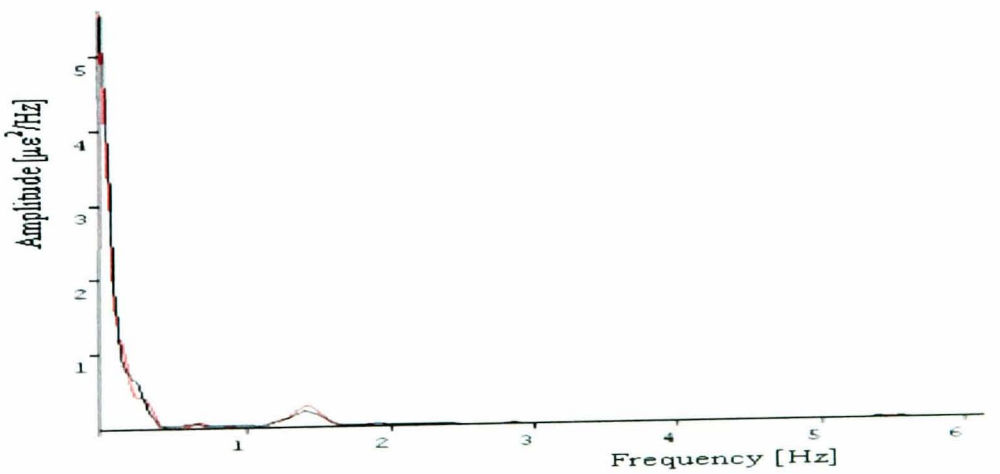

Figure 4.37: PSD comparison between the T6 original signal (black colour) and its equivalent WBE mission signal (red colour).

4.6 Summary

This chapter has discussed the WBE processing using six test signals, which were categorised into two groups: Synthetic Signals and Experimental Signals. Three test signals were chosen for the WBE detail analysis, i.e. T1 - the signal with a mixture of high transients in small amplitude backgrounds; T2 - the signal with the influence of low frequency content; and T4 - the signal which was experimentally measured on the lower suspension arm of a van travelling over the pavé test track.

Using the WBE algorithm, a signal was decomposed into the wavelet levels which were then grouped to form wavelet groups. By applying the automatic determined trigger level values, the bumps were identified in each wavelet groups. The trigger level values were set based on the user defined differences of r.m.s. and kurtosis between the mission and original signals. The r.m.s. and kurtosis difference of ±10% was used as the maximum loss of 10% in signal energy can be considered to be an acceptable value for automotive applications. This ±10% difference could not be applied for T1 (applying ±75%), illustrating the difficulties of performing fatigue mission synthesis based only on the global signal statistics.

It is observed that a signal low frequency content is important in determining the length of the bump segments, contributing to the length of the mission signal. Therefore, it is not easy to heavily compress VA loadings with a substantial low frequency content (such as T2 and T6), as the length of mission signal is caused by a single bump from the low frequency wavelet group.

Three orders of bump segment sequences were used to produce the mission signals. These mission signals have similar global statistical values, but may have different fatigue damage due to the bump segment sequence effects. According to the information in Table 4.3, the WBE algorithm which produced the shortened mission signals can be proposed for the use in accelerated fatigue tests.

CHAPTER 5

5. Experimental Stages

5.1 Purpose of the Experiments

The ability of the WBE algorithm to perform efficient fatigue data editing was evaluated by means of experimental tests. Analytically estimated, and experimentally measured fatigue lives were compared using the T4 bump segments. For this purpose, the T4 signal was used because it is the experimental signal with the highest time compression ratio as being analysed in Chapter 4 (refer to Table 4.3). In addition, this signal contains a wide variety of signal components at various frequencies and amplitudes, and can thus be considered typical of actual road vehicle fatigue testing results.

Several test were performed by the author using different bump sequence orders so as to check the possible effects of cycle sequence and bump sequence. Uniaxial variable amplitude (VA) loading fatigue tests using the T4 bump segments were performed by Choi (2004) using smooth specimens of BS 080A42 steel. In order to observe bump segment sequence effects in the mission signals, uniaxial VA loading fatigue tests were performed by the author of this thesis using three T4 mission signals, which each mission signal defined in such a way as to have a different order of bump segment sequence (refer to Figure 4.20 for the three mission signals of T4). The fatigue lives

obtained from this experiment were compared with the prediction fatigue lives using the available strain-life fatigue damage model.

5.2 Available Experimental Data (Choi 2004)

Choi (2004) discussed an experimental study performed using loadings extracted by means of the WBE algorithm. The bump segments of the T4 signal were used in the Choi's experiment. Uniaxial fatigue tests were performed for nine VA strain loadings using smooth specimens of BS 080A42 steel. For the material properties characterisation, a tensile test and uniaxial constant amplitude (CA) loading fatigue tests were conducted in order to obtain the monotonic mechanical properties and the cyclic mechanical properties, respectively. The cyclic properties were used to define the parameters of the Coffin-Manson relationship.

5.2.1 Tensile Test to Determine Monotonic Mechanical Properties

A tensile test was performed by Choi (2004) according to BS 10002-1 (2001) to define the monotonic properties of BS 080A42 steel. The results are presented in Figure 5.1 and Table 5.1. Although the nominal monotonic mechanical properties of BS 080A42 steel can be obtained from text books, such as in Woolman and Mottram (1969), this kind of test is necessary in order to guarantee the properties of the material that was actually supplied. Other BS 080A42 steels may slightly differ in mechanical properties due to varying preparation and production processes.

5.2.2 Uniaxial Constant Amplitude Fatigue Tests to Determine Cyclic Mechanical Properties

Seven uniaxial CA loading fatigue tests at different strain amplitudes were performed by Choi (2004) to determine the strain-life curve and cyclic mechanical properties of BS 080A42 steel. The test results are tabulated in Table 5.2. A strain-life curve of BS 080A42 was generated (ASTM E739-91 1998) as in Figure 5.2, and the parameters of the Coffin-Manson relationship are given in Table 5.3.

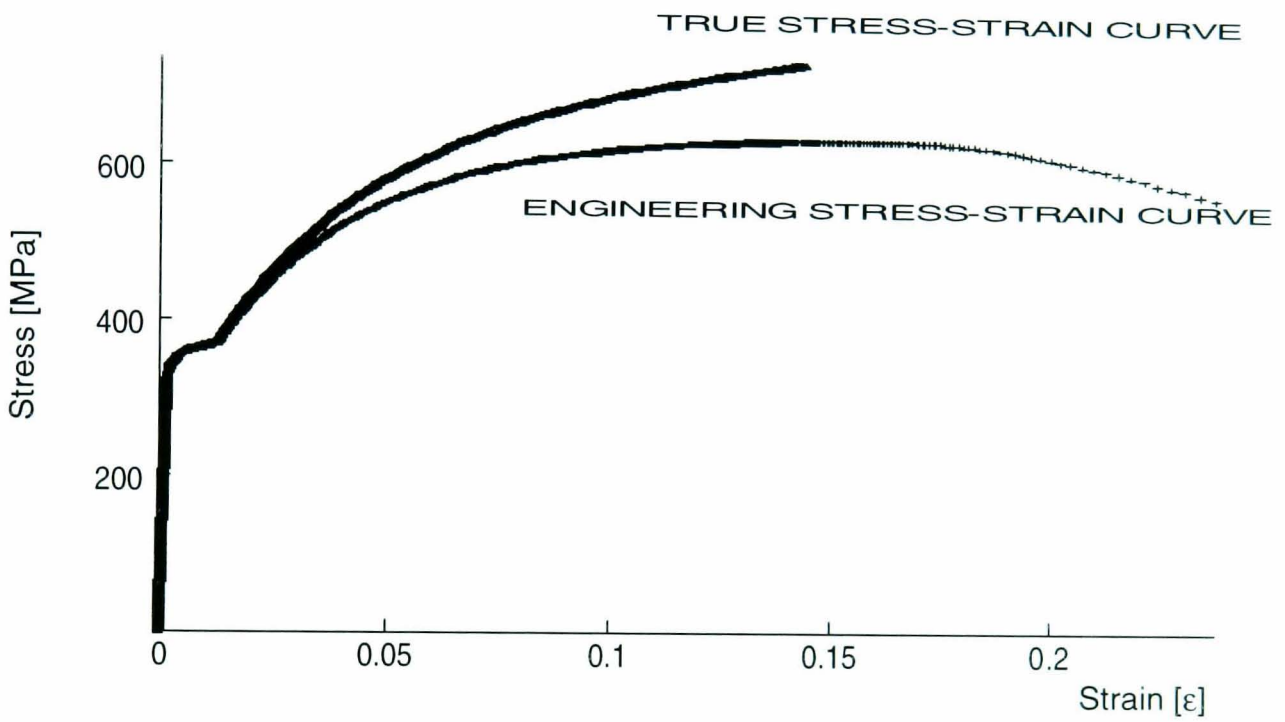

Figure 5.1: Monotonic stress-strain curve for BS 080A42 steel (Reproduced from Choi 2004).

Table 5.1: Monotonic mechanical properties of BS 080A42 steel (Choi 2004).

Monotonic Mechanical Properties	
Ultimate tensile strength, S_u (MPa)	624
Modulus of elasticity, E (MPa)	2.10×10^5
Static yield stress 0.2%, S_y (MPa)	342
Reduction in area, (%)	51.9
Elongation (%)	28.4

Table 5.2: Results of uniaxial constant amplitude loading fatigue tests (Choi (2004).

Stress amplitude [MPa]	Reversals to failure, N_f	Total strain amplitude, ε_a	Elastic amplitude, ε_{ae}	Plastic amplitude, ε_{ap}
415.0	2608	0.0084	0.0019	0.0064
366.2	8380	0.0054	0.0017	0.0037
369.0	8600	0.0054	0.0017	0.0037
339.7	26358	0.0036	0.0016	0.0020
321.7	27600	0.0036	0.0015	0.0021
294.3	66874	0.0028	0.0014	0.0015
266.8	169922	0.0022	0.0012	0.0010

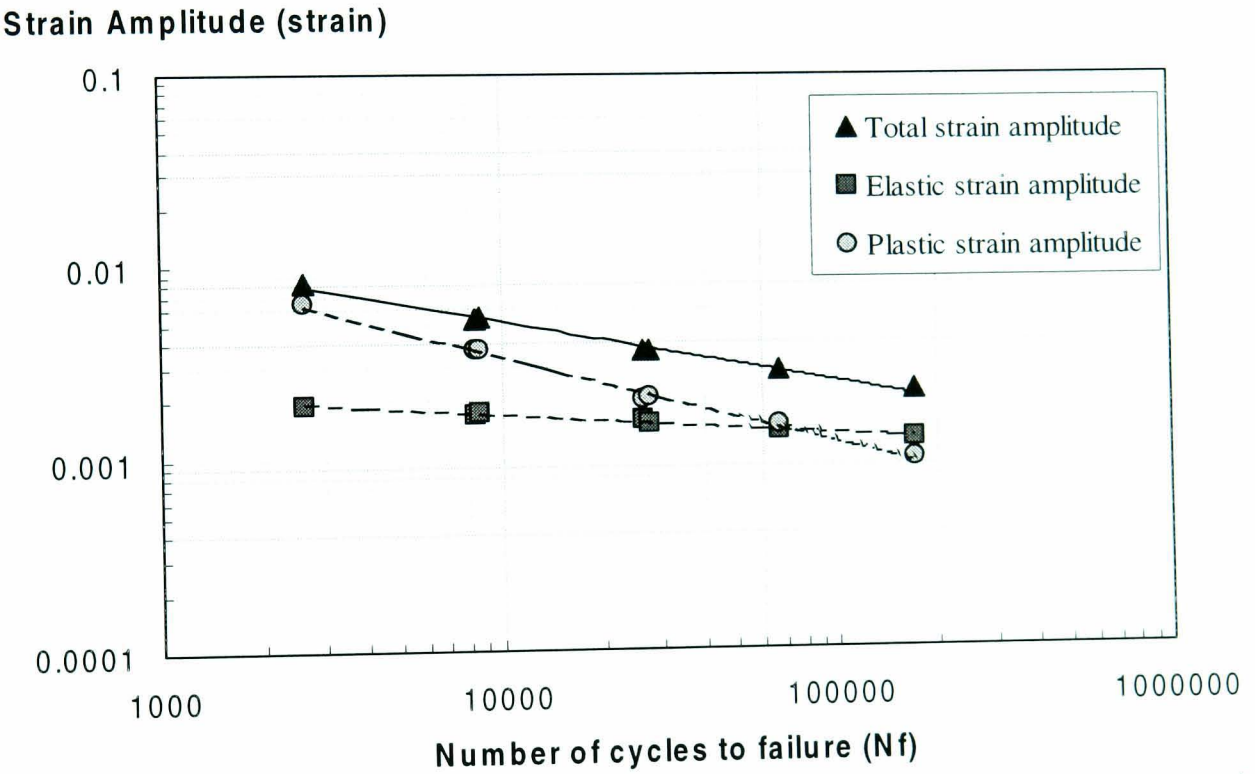

Figure 5.2: Constant amplitude strain-life curves obtained by Choi (2004).

Table 5.3: Cyclic properties of the BS 080A42 steel determined from constant amplitude fatigue tests (Choi 2004).

Coefficients of the Coffin-Manson equation	
Fatigue strength coefficient, σ'_f (MPa)	971
Fatigue strength exponent, b	-0.107
Fatigue ductility coefficient, ε'_f	0.233
Fatigue ductility exponent, c	-0.459

5.2.3 Fatigue Tests Using Bump Segments

Nine T4 bump segments, illustrated in Figure 5.3, were used in the uniaxial VA loading fatigue tests by Choi (2004). Referring to Table 5.4, B6 has the longest time length of 4.6 seconds with B2 having the shortest time length of 0.2 seconds. The uniaxial VA fatigue tests of the smooth specimens were performed under the displacement mode using the Instron 8501 servo-hydraulic machine. The experimental results obtained by Choi (2004) are tabulated in Table 5.4. The fatigue life of the specimen was determined when there is a 3-mm microcrack observed at the specimen gauge area.

Table 5.4: Identification of bump segments, experimental fatigue lives and fatigue damage of the bump segments (Choi 2004).

Signal Name	Signal length [seconds]	Location in original signal		Fatigue life, N_f [No. of blocks to failure]	Fatigue damage, $1/N_f$ [Damage per block]
		Start time [seconds]	End time [seconds]		
B1	1.7	0.68	2.39	2831	3.53×10^{-4}
B2	0.2	8.07	8.25	17880	5.59×10^{-5}
B3	3.9	16.32	20.21	3996	2.50×10^{-4}
B4	0.5	23.07	23.53	20084	4.98×10^{-5}
B5	2.4	25.14	27.50	2792	3.58×10^{-4}
B6	4.6	27.50	32.06	843	1.19×10^{-3}
B7	2.3	32.07	34.34	1366	7.32×10^{-4}
B8	2.5	37.14	39.65	1942	5.15×10^{-4}
B9	0.3	45.47	45.77	7500	1.33×10^{-4}
TOTAL FATIGUE DAMAGE					3.63×10^{-3}

* refer to Figure 5.3 for signal name

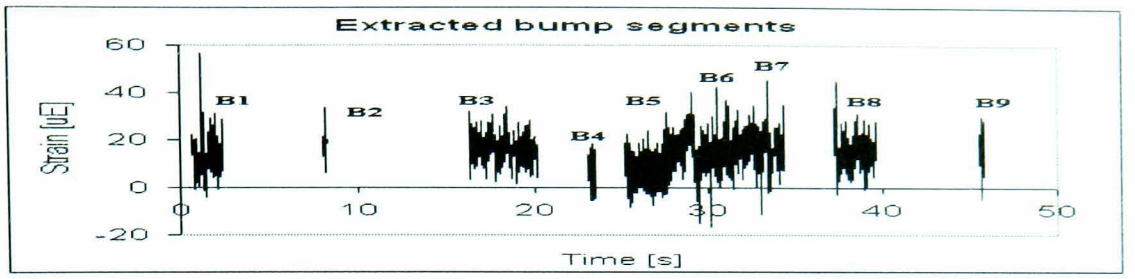

(a)

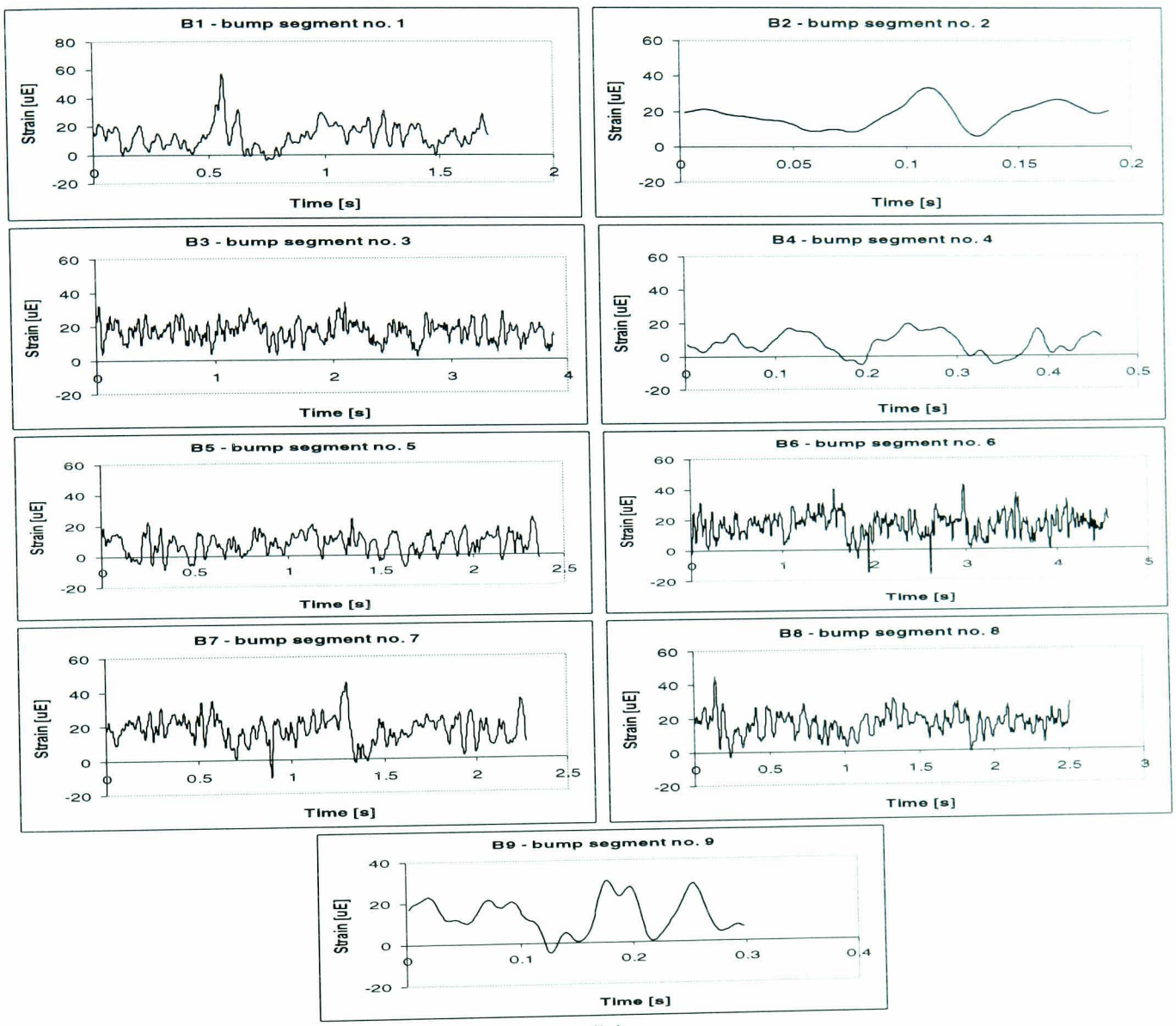

(b)

Figure 5.3: (a) Location of the bump segments in the original T4 time history, (b) Individual time histories of bump segments B1 to B9.

5.3 Experimental Procedure

Several factors should be considered before performing uniaxial fatigue tests; material, specimen geometry, loading range, frequency, and the characteristics of the fatigue testing machine. The actual material should be selected from the various materials used to fabricate a vehicle suspension. A test specimen must be designed in accordance with

the BS 7270 (1990) guideline. The geometry and dimensions of the test specimen need to be specified along with appropriate grips for a suitable fatigue test machine. Finally, the machine should be able to apply static loading for the tensile test, and uniaxial cyclic loading at various mean loads, load ranges and cycle frequencies for the VA loading tests.

5.3.1 Material Selection

The material chosen for the test samples was BS 080A42 steel, which is often used for the suspension components of cars. The United Kingdom coding system used for this type of steel can be found in BS 970-1 (1996) which uses a six-digit designation, for example 080A42. The first three digits of this designation denote the family of steels to which the alloy belongs. The fourth digit is a letter (A, H or M) denoting that the supplied steel should meet the appropriate material characteristics. The fifth and sixth digits represent 100 times the mean carbon content of the steel. Details of the designation procedure are listed in Table A.1 of Appendix A.

BS 080A42 is categorised as a medium carbon and carbon manganese steel. The fourth digit of the designation A, is a letter indicating that the steel will be supplied to close limits of chemical composition. The fifth and sixth digits represent 100 times the mean carbon content of the steel. For BS 080A42, the coding system defines this material as a medium carbon-manganese of 0.7 - 0.9% manganese and 0.4 – 0.45% carbon content. The nominal chemical composition of this type of steel is shown in Table A.2 (Appendix A) and the cast composition provided by the supplier is given in Table 5.5. The equivalent grades of this steel are shown in Table A.3 (Appendix A).

Table 5.5: Cast composition of BS 080A42 steel as provided by the supplier, Argent Steel Limited, United Kingdom.

Carbon	Silicone	Manganese	Sulphur	Phosphorus
0.42	0.178	0.75	0.025	0.011

5.3.2 Specimen Preparation

Two specimen types, a uniformly smooth gauge and a circular notched gauge, were prepared for the uniaxial fatigue tests. Both specimens were machined from the supplied BS 080A42 bar stock to have an hourglass round bar profile for tension-compression loading in compliance with BS 7270 (1990). Table 5.6 presents the dimensional requirements of the cylindrical uniform gauge of a smooth specimen. Figure 5.4 shows the geometry and dimensions of the smooth specimen, having a diameter of 6 mm at the gauge.

Table 5.6: British Standard dimensional requirements for smooth cylindrical test specimens (BS 7270 1990).

Dimension	Gauge diameter, *d*	Gauge length, *l*	Gauge radius, *r*
Requirement	5 – 10 mm	2d – 4d	≥2d
Specimens	6.0 mm	25.0 mm	24.0 mm

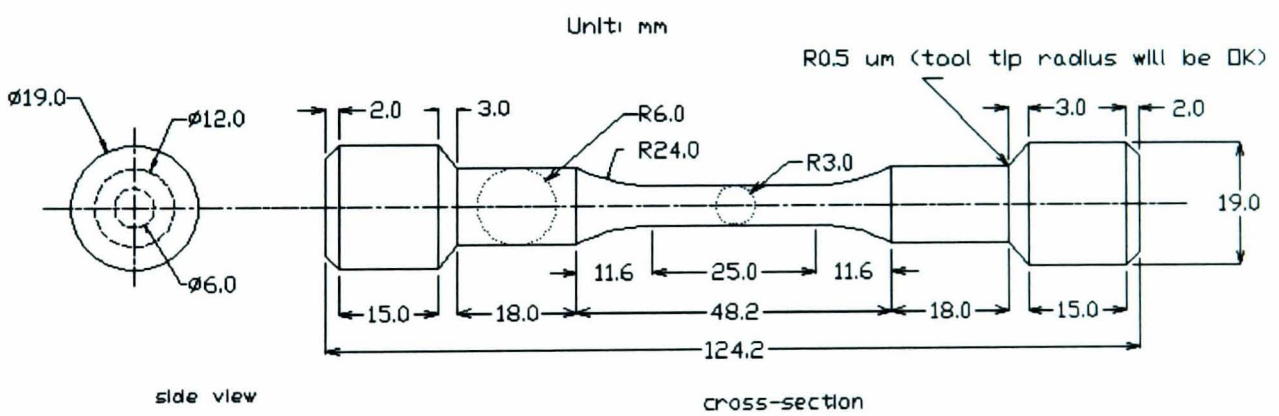

(a)

(b)

Figure 5.4: Smooth specimen: (a) The geometry and dimensions - in mm units unless otherwise specified, (b) Photograph.

For the notched specimens, a circumferential notch with a root radius of 3 mm was machined in the centre of the gauge length. The stress concentration factor K_t for the notch was found to be 1.3 when calculated using the approaches in Juvinall and Marshek (1991) and Shigley and Mischke (1989). This K_t value was then used to produce the fatigue notch factor K_f value of 1.28. Figure 5.5 shows the geometry and dimensions of the notched specimens.

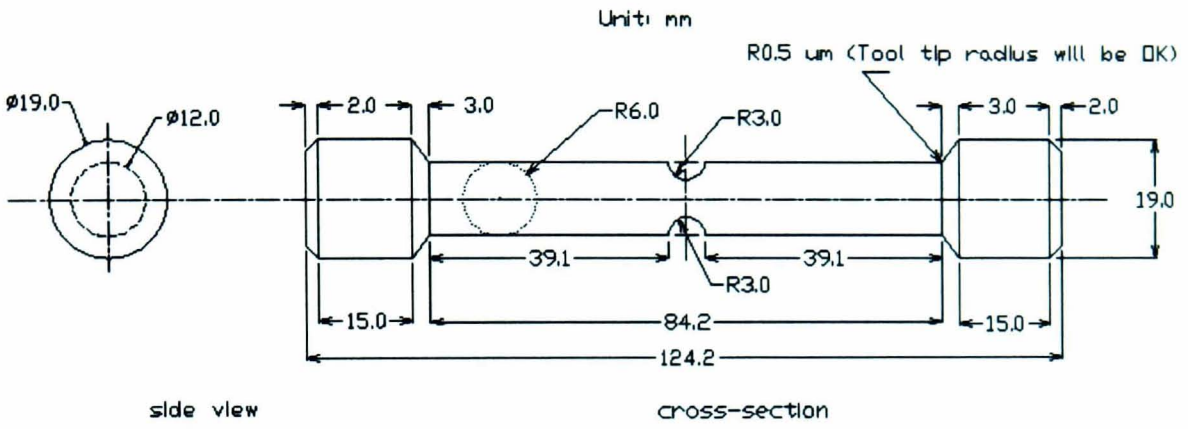

(a)

(b)

Figure 5.5: Notched specimen: (a) The geometry and dimensions - in mm units unless otherwise specified, (b) Photograph.

Both type of specimens were hand polished in order to remove machining scratches. For this process, grades 60 to 1000 silicone carbide abrasive paper were used, and final finishing was performed using 6-µm diamond compound.

5.3.3 Experimental Apparatus

Three main types of apparatus were used to perform the uniaxial fatigue tests: A servo-hydraulic machine test, extensometers and a data acquisition software. An Instron 8501 servo-hydraulic machine was used for the uniaxial fatigue tests, as shown in Figure 5.6.

The machine permitted the uniaxial fatigue tests to be performed under displacement mode, providing a load in the range ±100 kN, a displacement range of the ram position of ±75 mm and a maximum frequency of 100 Hz for cyclic tests.

The strain of the specimen was measured using a displacement extensometer clip gauge at ±2.5 mm calibration range, based on the intended displacement measurement. Two different lengths of extensometer clip gauge were used: a 25-mm extensometer (Figure 5.7a) for the smooth specimens and a 12.5-mm extensometer (Figure 5.7b) for the notched specimens. In Figure 5.7 both extensometers are shown attached to the respective smooth and notched specimens.

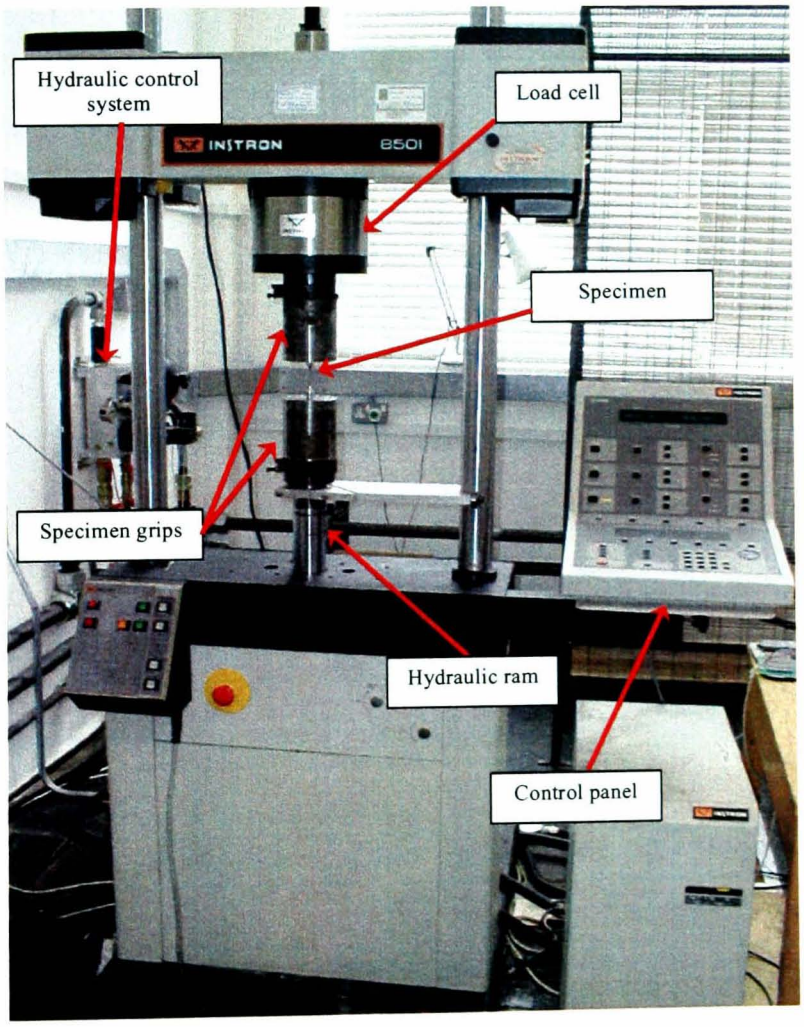

Figure 5.6: Instron 8501 servo-hydraulic machine.

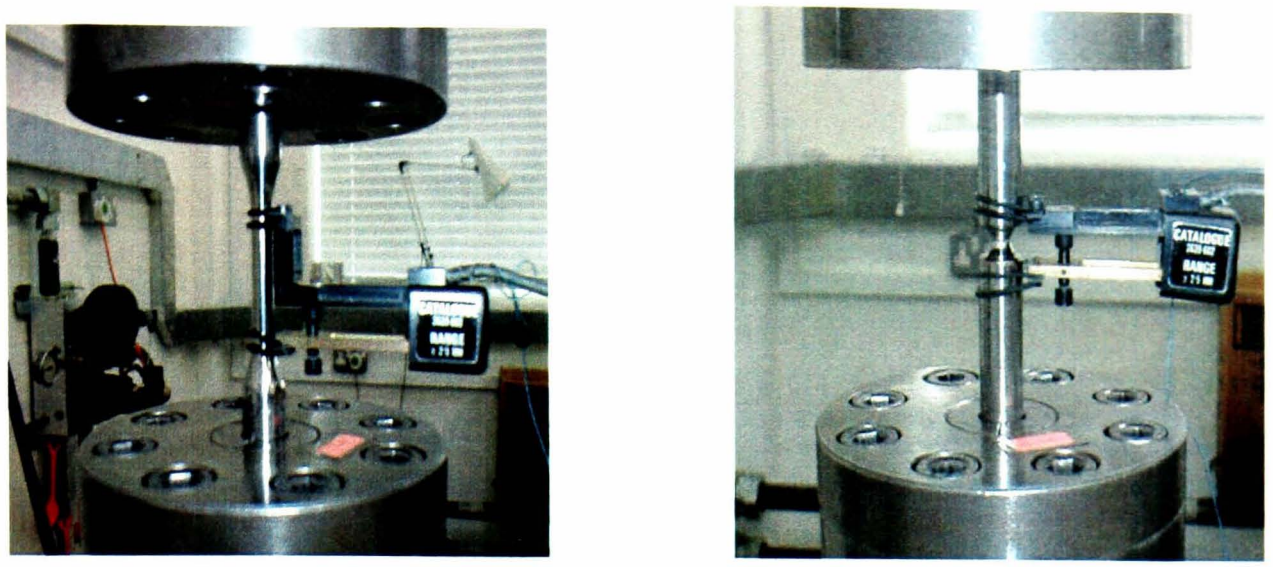

Figure 5.7: Specimens with extensometer: (a) A smooth specimen with 25-mm extensometer, (b) A notched specimen with 12.5-mm extensometer.

Finally, the Labtech® data acquisition software was used to provide the loading input to the Instron 8501 servo-hydraulic machine and to record the force and strain output data. The interface between the input signal for the fatigue tests, the Instron 8501 servo-hydraulic machine and the output signals is illustrated as a circuit diagram in Figure 5.8. In this figure, the icon 'POSITION(V)' represents the input loading, 'LOAD KN' represents the recorded output force from the test which this data being recorded as 'LOAD DATA' and 'STRAIN MM' is the recorded output strain displacement from the test and being recorded as 'STRAIN DATA'. By determining the time of the output data in 'TIME DATA', finally, a single output file (in ASCII format) which contain 'TIME DATA', 'LOAD DATA' and 'STRAIN DATA' was created.

5.3.4 Uniaxial Constant Amplitude Fatigue Tests

An addition to test performed by Choi (2004), two additional CA loading fatigue tests were performed by the author at different strain amplitudes in order to have more data points for the cyclic properties determination process. The tested strain amplitudes were set at 0.0060 m/m and 0.0022 m/m. The tests were performed using smooth specimens with the Instron 8501 servo hydraulic machine. Fatigue failure was taken to be when the output load decreased below 50% of the initial load level (ASTM E466-96 2000).

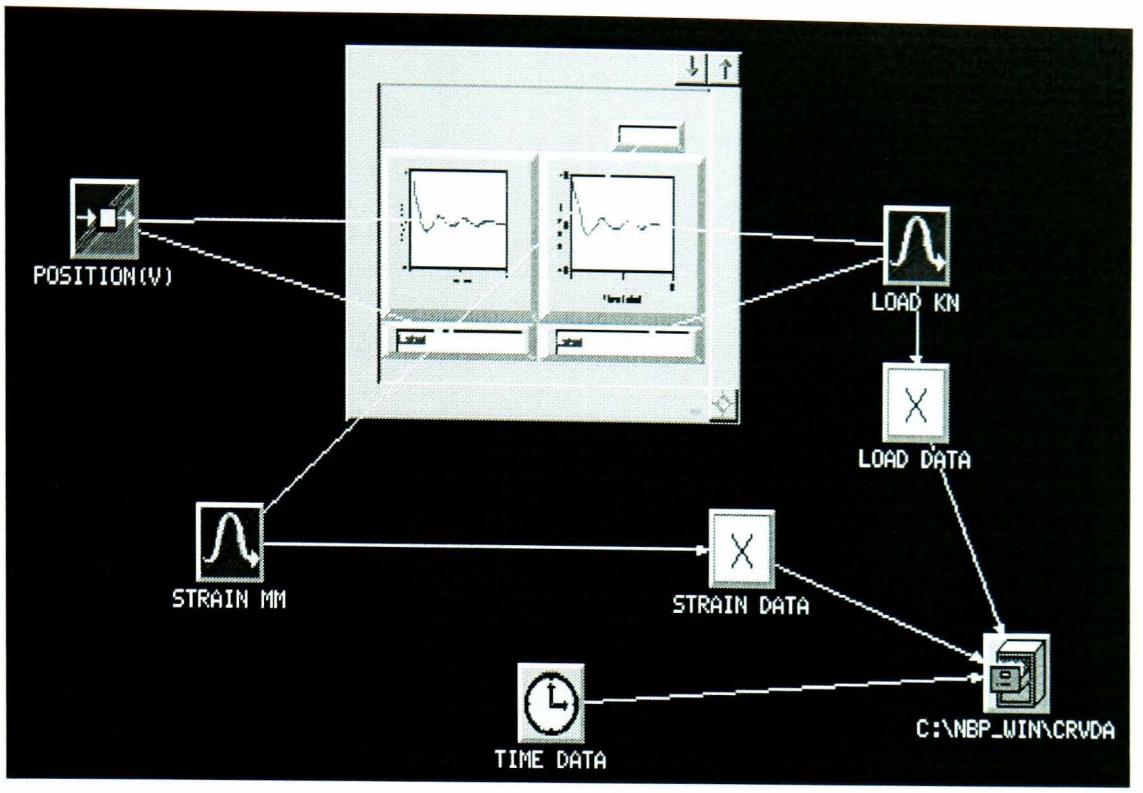

Figure 5.8: Uniaxial fatigue test circuit diagram in the Labtech® software.

5.3.5 Uniaxial Variable Amplitude Fatigue Tests

The second type of fatigue test performed for the purposes of the research described in this thesis was the determination of the fatigue life obtained from three different T4 mission signals. The purpose was to observe the fatigue damage potential of the bump segment sequence in a mission signal. The tests were also performed in order to determine the achieved fatigue test acceleration.

The original 46-second T4 signal and three 18.8-second T4 mission signals (with different order of bump segment sequences for each mission signal) were used. Each T4 mission signal has different bump order sequence, i.e. the mission signal with the original order sequence of bump segments or named as T4BS1 (Figure 4.29b), the mission signal with the bump segment sequence of the highest expected fatigue damage to the lowest or named as T4BS2 (Figure 4.29c) and the mission signal with the bump segment sequence of the lowest expected fatigue damage to the highest or named as T4BS3 (Figure 4.29d). As stated earlier in this chapter, the signal T4 was chosen for the uniaxial fatigue tests since T4 is an experimental signal which contains a

wide variety of signal components at various frequencies and amplitudes, and can thus be considered typical of actual road vehicle fatigue testing results.

The experimental equipment and procedure described in Sections 5.3.3 and 5.3.4 were used to test both smooth and notched specimens. Two experiment repetitions were performed for each signal. The fatigue life of the specimen was determined when there is a 3-mm microcrack observed at the specimen gauge area. The results obtained from the experiments were compared with analytical results obtained using the available strain-life models.

5.4 Summary

This chapter discussed the experimental procedures performed in order to validate the Wavelet Bump Extraction (WBE) algorithm. Uniaxial fatigue test specimens were manufactured from BS 080A42 steel, and were hand polished using several grades of abrasive paper and a 6-μm diamond compound. An Instron 8501 servo-hydraulic machine was used for the experimental tests, which were all performed in displacement mode.

Experimental data from previous tests performed by Choi (2004) were used to determine the mechanical properties of the BS 080A42 steel. The monotonic mechanical properties were obtained from a tensile test and the cyclic mechanical properties were obtained from uniaxial CA loading fatigue tests. The data obtained from the tensile and uniaxial fatigue tests were used to define the parameters of the strain-life fatigue damage models. An experiment using nine bump segments extracted using the WBE algorithm was also performed by Choi (2004) in order to observe the cycle sequence effects of VA loadings.

In addition to the experiments performed by Choi (2004), an extra two uniaxial CA loading fatigue tests were performed by the author in order to have more points for the

generation of a strain-life curve and strain-life properties. The second experimental scheme was to apply uniaxial VA loading fatigue tests using the mission and original signals. The mission signal, which has a shorter time length, was used for accelerated fatigue tests instead of the original signal. Apart from the accelerated fatigue tests, the purpose of this experiment is to observe the effects of bump segment sequences.

CHAPTER 6

6. Experimental Results and Analysis

This chapter discusses the results obtained in the experimental stages using constant amplitude (CA) and variable amplitude (VA) fatigue loadings. The analysis of the experimental results obtained by the author and by Choi (2004) is performed in order to validate the effectiveness of the Wavelet Bump Extraction (WBE) algorithm.

6.1 Experimental Results: Uniaxial CA Loading Fatigue Tests

The first experiment was performed in order to add more CA loading data points for use in determining the strain-life parameters of the Ramberg-Osgood relationship and the Effective Strain Damage (ESD) model. The results obtained from the uniaxial CA loading fatigue test are tabulated in Table 6.1. Referring to the CA strain-life curve of Figure 6.1, the fatigue lives of the new strain amplitudes were found to lie along the strain-life curve produced by Choi (2004) for BS 080A42 steel. The Coffin-Manson relationship parameters for the strain-life curve of Figure 6.1 are presented in Table 6.2.

Table 6.1: Results from the uniaxial constant amplitude loading fatigue tests.

Stress amplitude [MPa]	Number of cycles to failure, N_f	Total strain amplitude, ε_a	Elastic strain amplitude, ε_{ae}	Plastic strain amplitude, ε_{ap}
477.9	4972	0.0060	0.0022	0.0038
183.6	233530	0.0022	0.0009	0.0013

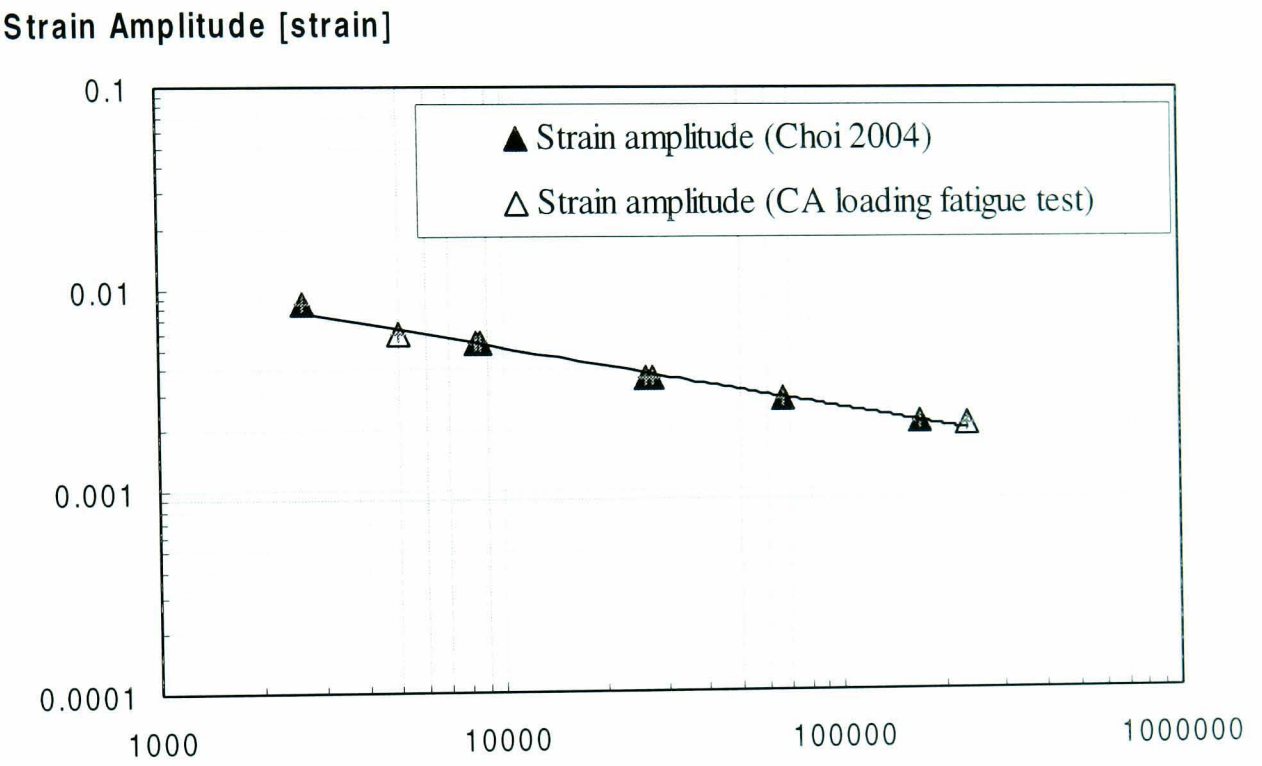

Figure 6.1: Constant amplitude strain-life curve generated from the combined results of Choi (2004) and the current study.

Table 6.2: Cyclic properties of BS 080A42 steel determined from the constant amplitude fatigue tests of Choi (2004) and the current study.

Coefficients of the Coffin-Manson equation	
Fatigue strength coefficient, σ'_f (MPa)	1505
Fatigue strength exponent, b	-0.144
Fatigue ductility coefficient, ε'_f	0.176
Fatigue ductility exponent, c	-0.400

6.2 Experimental Results: Uniaxial VA Loading Fatigue Tests Using Mission Signals

The second experiment was to perform accelerated laboratory fatigue tests using different bump segment sequences in the mission signals, therefore the bump segment sequence effects can be observed. The experimental results obtained using the original 46-second T4 signal and the three 18.8-second WBE mission signals are tabulated in Table 6.3 for the smooth test specimens and in Table 6.4 for the notched test specimens. Two experiment repetitions were performed for both specimen types, so that the variation of fatigue life for a particular signal can be observed.

Table 6.3: Experimental fatigue lives and fatigue damage obtained for the smooth specimens.

Signal Name	Experiment 1	Experiment 2
Fatigue life [Number of blocks to failure]		
T4	289	454
T4BS1	409	261
T4BS2	367	285
T4BS3	291	340
Fatigue Damage [Damage per block]		
T4	3.46×10^{-3}	2.20×10^{-3}
T4BS1	2.44×10^{-3}	3.83×10^{-3}
T4BS2	2.72×10^{-3}	3.51×10^{-3}
T4BS3	3.44×10^{-3}	2.94×10^{-3}

From Table 6.3 it can be seen that the fatigue lives of the T4BS3 mission signal was closer to the fatigue life of the T4 original signal. This results indicating the influencing of bump segment sequence effects in determining fatigue life of the mission signals. Table 6.4 exhibits the experimental fatigue lives and fatigue damage caused by the T4 mission signals using the notched specimens. The T4BS1 mission signal has a closer fatigue life of both experiments to the fatigue life of the original signal. Observing the difference in

fatigue lives in Table 6.3 and Table 6.4 between the mission signals and the original signal, it is suggested that there was an influence of bump segment sequence effects in the fatigue life prediction of the mission signals. Further analysis and discussion of these experimental results are presented in Chapter 7.

Table 6.4: Experimental fatigue lives and fatigue damage obtained for the notched specimens.

Signal Name	Experiment 1	Experiment 2
Fatigue life [Number of blocks to failure]		
T4	45	36
T4BS1	60	36
T4BS2	153	28
T4BS3	111	8
Fatigue Damage [Damage per block]		
T4	2.22×10^{-2}	2.78×10^{-2}
T4BS1	1.67×10^{-2}	2.78×10^{-2}
T4BS2	6.54×10^{-3}	3.57×10^{-2}
T4BS3	9.01×10^{-3}	1.25×10^{-1}

6.3 Analysis Using CA Loading Fatigue Data

6.3.1 Ramberg-Osgood Relationship

The cyclic stress-strain curve is represented by a Ramberg-Osgood relationship, i.e.

$$\varepsilon_a = \frac{\sigma}{E} + \left(\frac{\sigma}{H}\right)^{\frac{1}{n'}} \tag{6.1}$$

where H is a material constant and n' is the strain hardening exponent. The values of H and n' are determined using curve fitting techniques to fit one of the following expressions to the experimental data

$$\varepsilon_{pa} = \left(\frac{\sigma}{H}\right)^{\frac{1}{n'}} \tag{6.2}$$

or

$$\sigma = H\varepsilon_{pa}^{\ n'} \tag{6.3}$$

From the experimental strain amplitude information of Table 5.2 and Table 6.1, the graph was plotted (using double logarithmic axis) of the stress amplitude σ versus the plastic strain amplitude ε_{pa}, as shown in Figure 6.2. Applying the linear regression fitting technique (Hinton 1995) to the experimental data points by means of the Microsoft Excel® software package, where $y = log\ \sigma$ and $x = log\ \varepsilon_{pa}$, the value of H and n' were found to be 1318 MPa and 0.23, respectively. Substituting the value of the modulus of elasticity E = 210,000 MPa, H and n' into Eq. (6.1) provided the Ramberg-Osgood relationship for the total strain of BS 080A42 steel as following expression:

$$\varepsilon_a = \frac{\sigma}{210000} + \left(\frac{\sigma}{1318}\right)^{\frac{1}{0.23}} \tag{6.4}$$

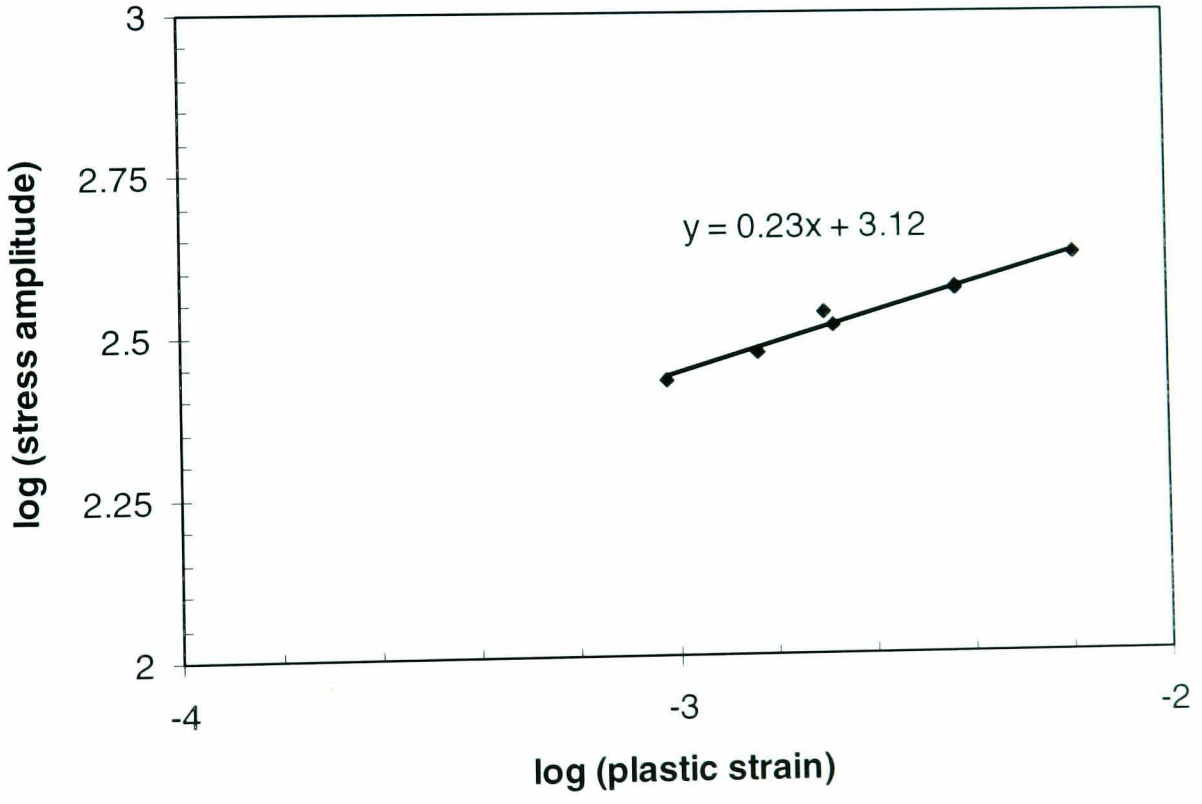

Figure 6.2: Relationship between stress amplitude and plastic strain amplitude for BS 080A42 steel.

Figure 6.3 presents the cyclic stress-strain curve of BS 080A42 steel defined by Eq. (6.4). In this plot, the total strain amplitudes and stress amplitudes were used. The

hysteresis data obtained from the uniaxial CA loading fatigue tests were also plotted with the cyclic stress-curve for comparison purposes. In this figure, a close correspondence is evident between the experimental results and the fitted curve. However, there were two outlier experimental points which can be observed in the Figure 6.3. It might be caused by these two CA loading fatigue test were performed in different period to the fatigue tests by Choi (2004). In addition, the specimens used by the author were come from the different batch to the specimens used by Choi (2004).

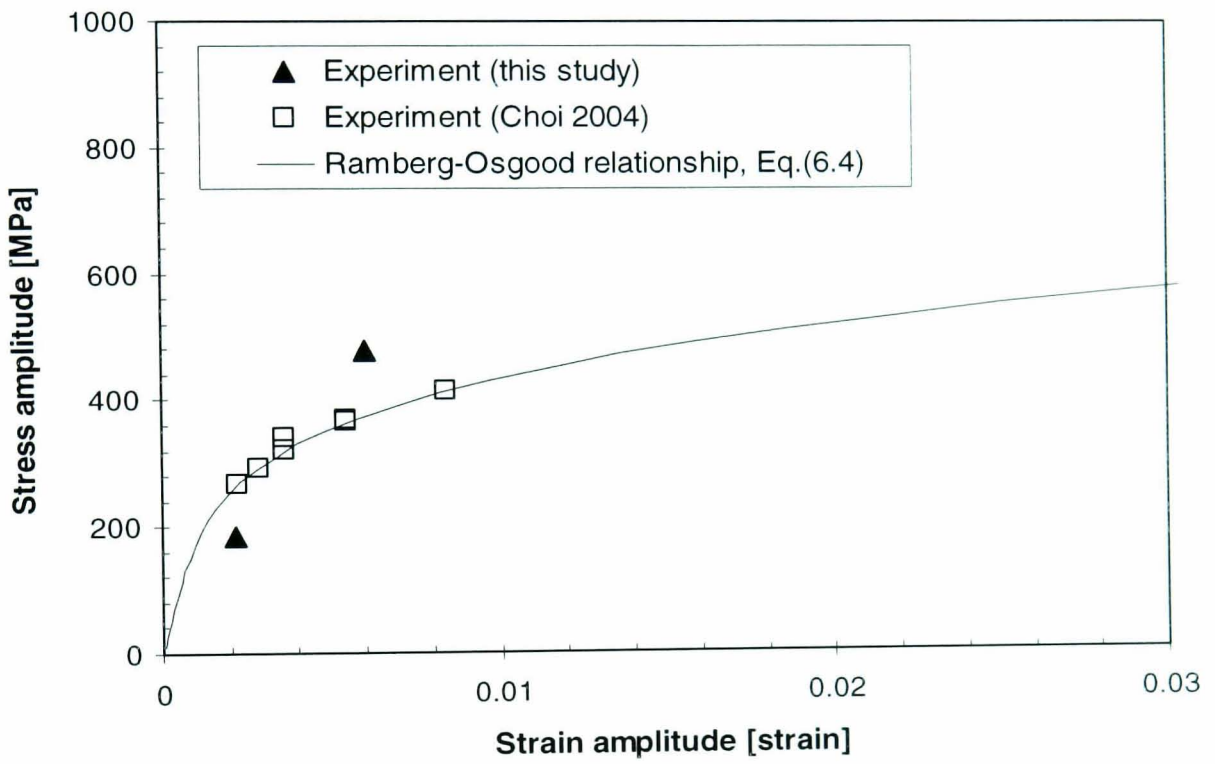

Figure 6.3: Constant amplitude loading cyclic stress-strain for BS 080A42 steel calculated using Eq. (6.4) and the experimental relationship.

6.3.2 Effective Strain Damage (ESD) Strain-Life Model

The values of the material constants *A* and *B* of the Effective Strain Damage (ESD) model of DuQuesnay *et al.* (1993), which has been presented in this thesis as Eq. (2.43), were determined from the CA loading fatigue test data. The approaches explained in Section 2.5.6 were used in order to find these values. The mechanical monotonic properties of Table 5.1 were used together with the CA loading fatigue test data of Table 5.2 and Table 6.1, for which a curve of damage stress range ($E\Delta\varepsilon^{*}$) versus cycles to failure (N_f) was plotted.

For the smooth specimens, the curve, which is plotted using double logarithmic scales, is shown in Figure 6.4. In this figure, y is the parameter for $E\Delta\varepsilon^*$ and x is the parameter for N_f. The material constants of A = 119,000 MPa and B = –0.5 were determined using the linear regression curve fitting technique (implemented in the Microsoft Excel® software) to the data. As a result, the final expression of Eq. (2.43) is defined as

$$210000\ (\Delta\varepsilon^*) = 119000\ (N_f)^{-0.5} \tag{6.5}$$

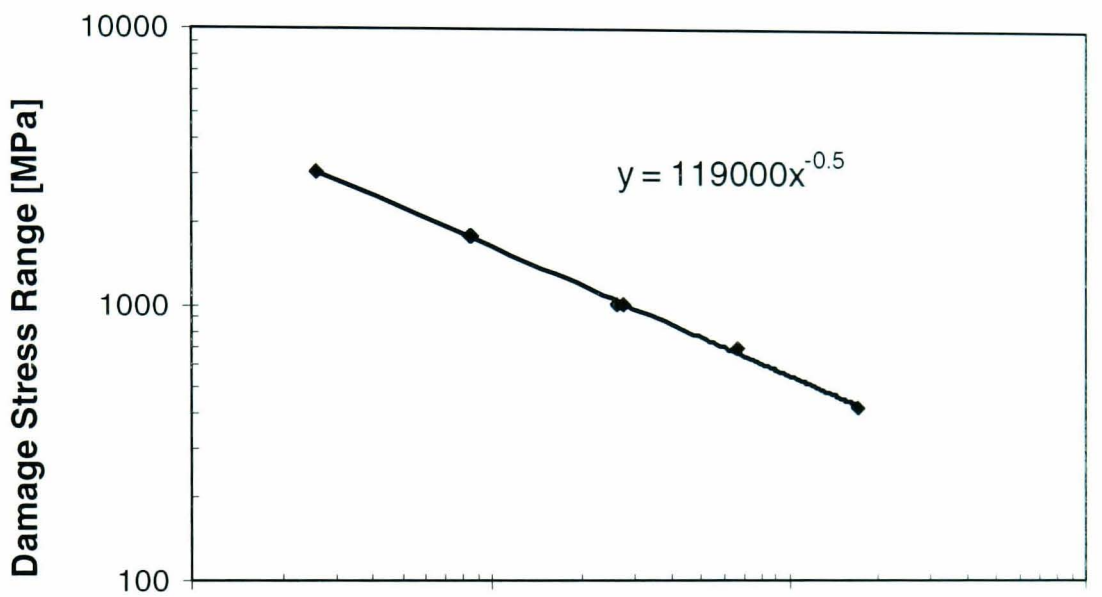

Figure 6.4: Damage stress range ($E\Delta\varepsilon^*$) versus fatigue life (N_f) for the smooth specimens of BS 080A42 steel.

For the notched specimens, the similar curve of damage stress range versus number of cycles to failure is shown in Figure 6.5. In this case the material constants A and B were found to be 85,000 MPa and –0.5, respectively. Therefore, the final expression of the ESD model for the notched specimens with K_t = 1.3 is

$$210000\ (\Delta\varepsilon^*) = 85000\ (N_f)^{-0.5} \tag{6.6}$$

The value of 85,000 in Eq. (6.6) for the notched specimen is close to the smooth specimen value of 119,000 in Eq. (6.5) divided by the K_t value of 1.3.

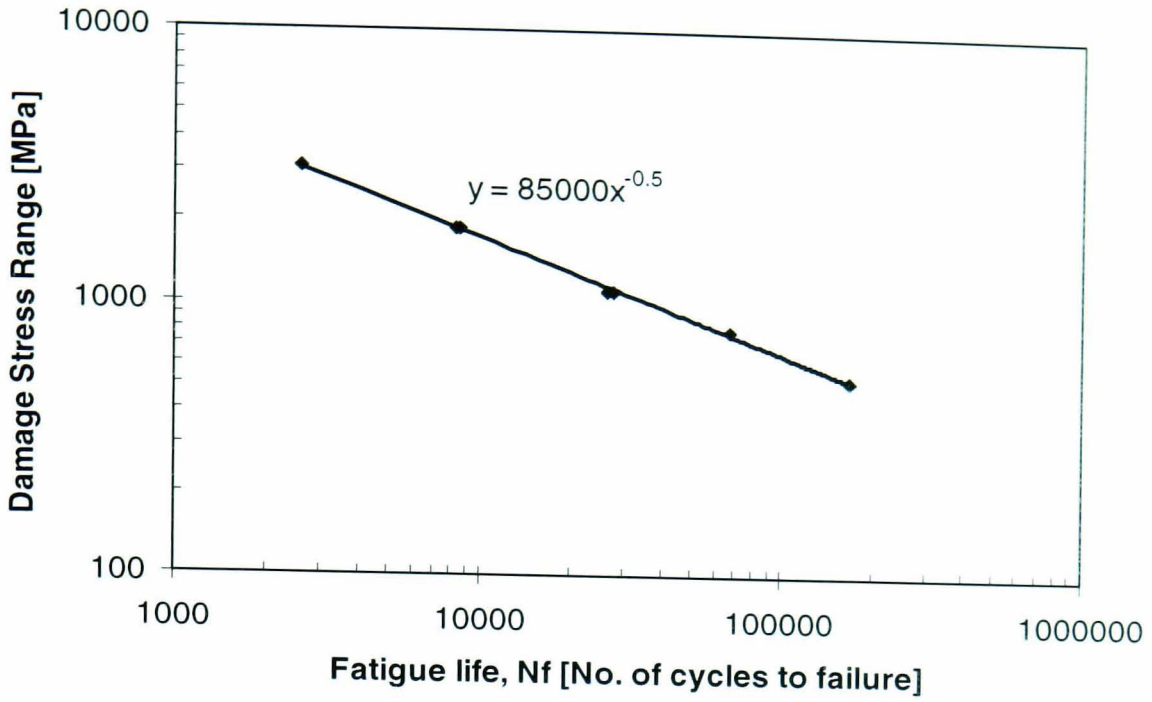

Figure 6.5: Damage stress range ($E\Delta\varepsilon^*$) versus fatigue life (N_f) for the notched specimens of BS 080A42 steel.

Eq. (6.5) and Eq. (6.6) were taken to be the expressions for the fatigue life prediction using VA loadings. In order to calculate the value of $\Delta\varepsilon^*$ in Eq. (2.43), related parameters of the expressions in Section 2.5.6 also need to be determined. Ideally, the value of the intrinsic fatigue limit S_i in Eq. (2.44), which is produced from $E\varepsilon_i$, and the parameter values of m in Eq. (2.46) and both α and β in Eq. (2.47), should be experimentally determined. When there is no experimental data to help determine the S_i value for VA loadings, it can be estimated using the graph in DuQuesnay (2002), which is shown in Figure 6.6. At E = 210 GPa, the S_i value is approximately 270 MPa.

According to Khalil and Topper (2003), the value of m can be determined by a curve fitting using the experimental data of crack opening stress against number of cycles. The value of α and β can be determined using the experimental data of the crack opening stress versus maximum stress (DuQuesnay *et al.* 1992b; Topper and Lam 1997). No experimental data were available which could be used in order to find these three parameter values. Since the main purpose of the research was, however, to develop the fatigue data editing algorithm associated with cycle sequence effects, the measurement of crack opening stress under VA loadings was not undertaken. The

values of m, α and β values were therefore assumed based on the results of related studies on other carbon steels.

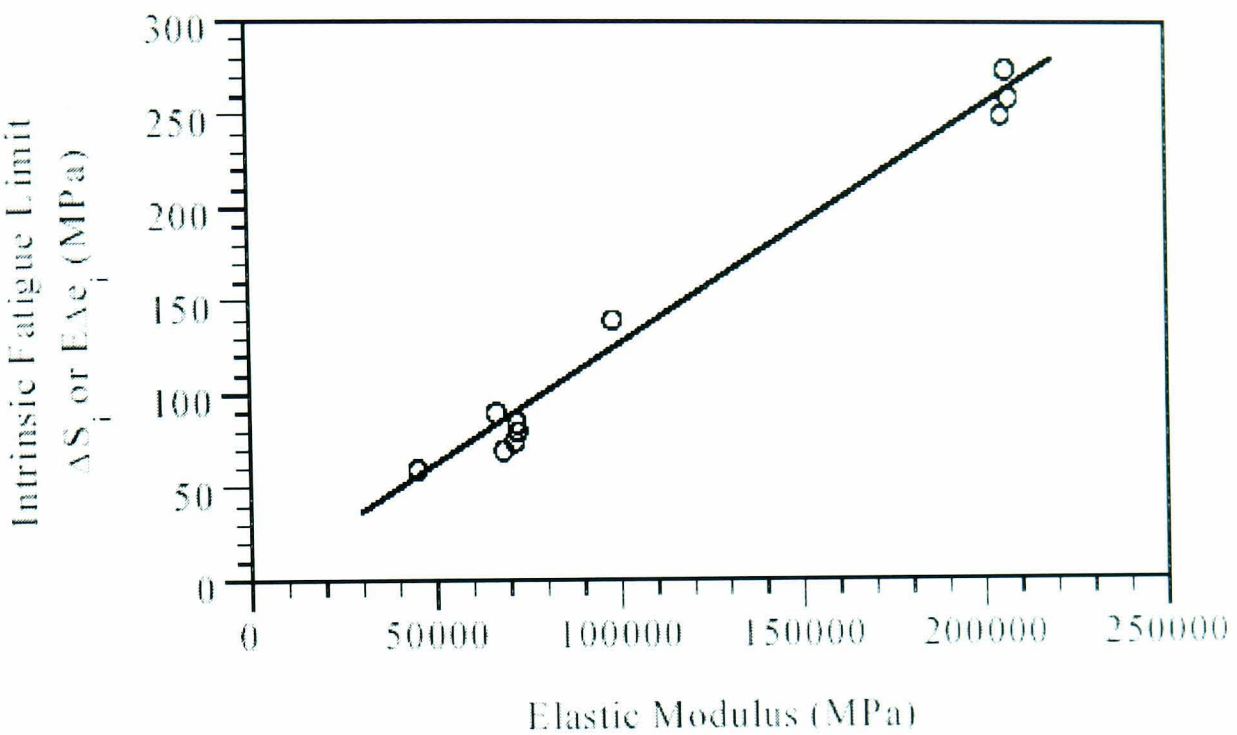

Figure 6.6: Relationship between intrinsic fatigue limit S_i and the modulus of elasticity E (Reproduced from DuQuesnay 2002).

Previous research treating steels and aluminium alloys (Vormwald and Seeger 1991; DuQuesnay *et al.* 1992b; 1993; Topper and Lam 1997; DuQuesnay 2002; Khalil *et al.* 2002; Khalil and Topper 2003), showed that different values of m, α and β had a minimal effect on the fatigue life prediction of the component under VA loading. From the latest research of this model by Khalil and Topper (2003) using SAE 1045, which is a carbon steel, the values of m, α and β were 0.002, 0.55 and 0.23, respectively. Since BS 080A42 is also a carbon steel, the m, α and β values of SAE 1045 steel were used in the research described in this thesis.

The flowchart describing the fatigue life calculation of VA loadings using the ESD model is shown in Figure 6.7 and 6.8. Using the procedure in this flowchart, the automatic calculation of fatigue life under VA strain loadings was developed by the author using the Fortran computer programming language. To begin the fatigue life calculation using this model, an ASCII format VA time history or fatigue loading is required. Then, this VA

loading is used to produce PV reversals and fatigue cycles. Then, the fatigue life for each fatigue cycle is calculated. Finally, the final fatigue life of VA fatigue loadings can be calculated at the end of the procedure.

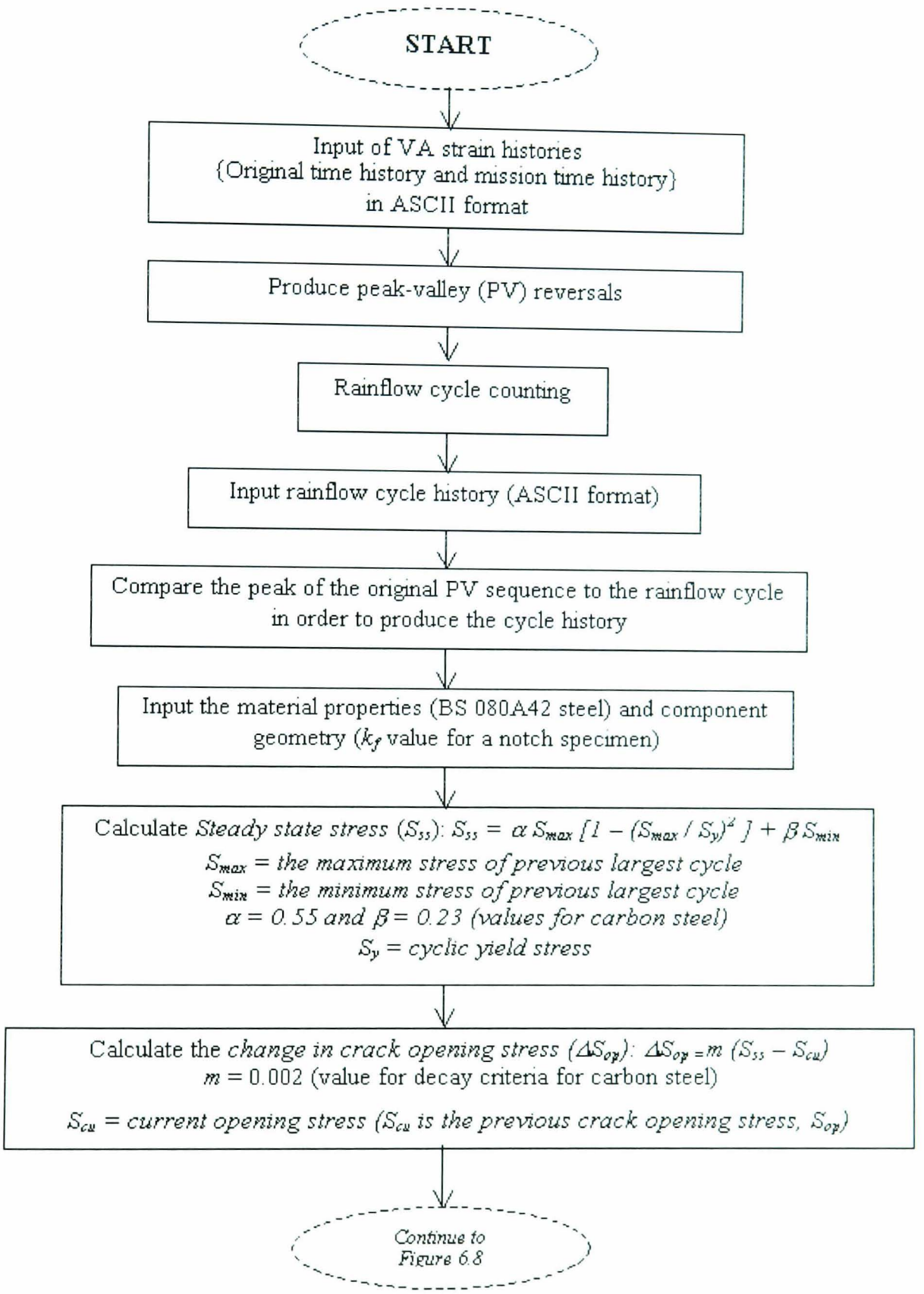

Figure 6.7: Flowchart of the ESD strain-life model – Part 1.

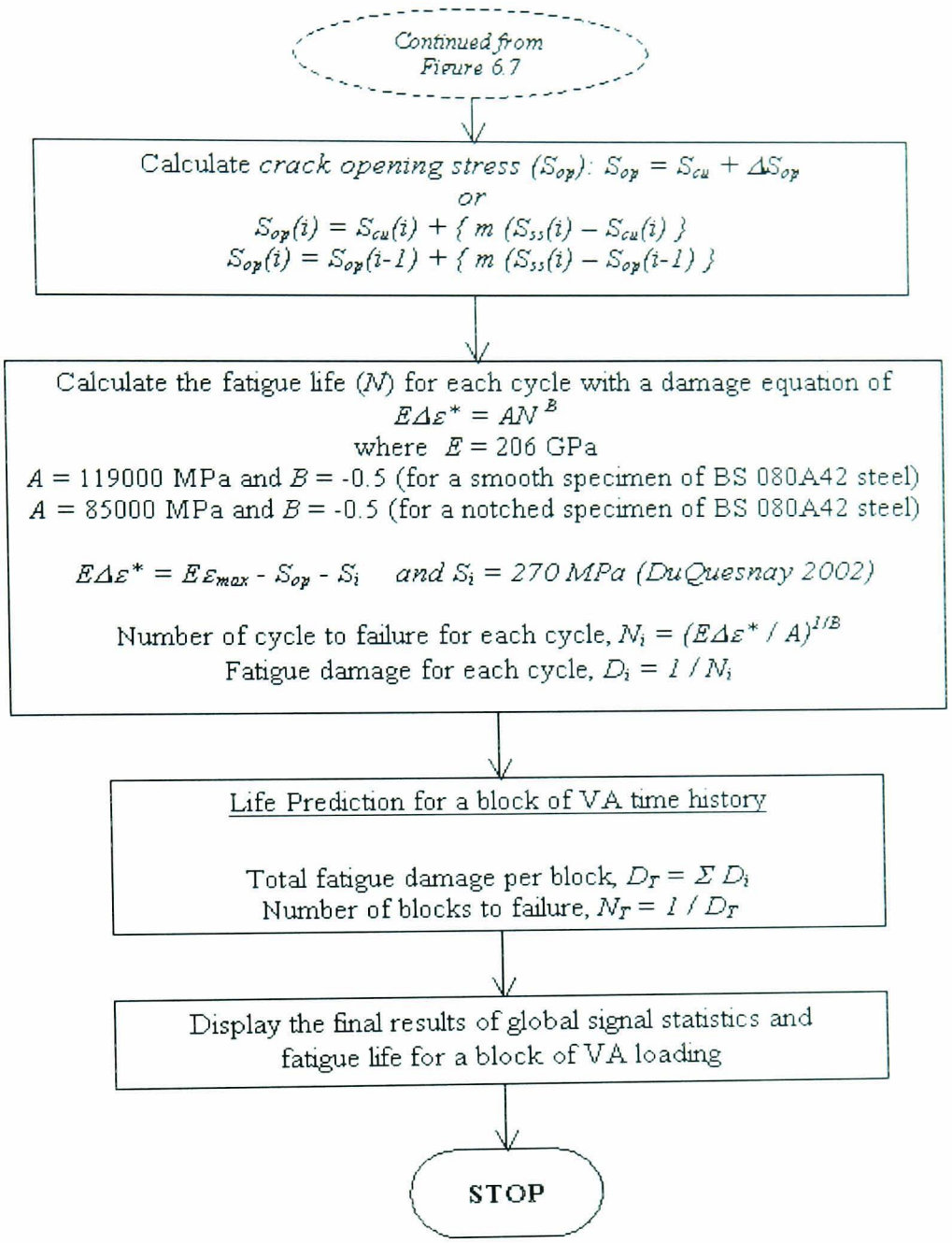

Figure 6.8: Flowchart of the ESD strain-life model – Part 2.

6.4 Validation of the ESD Model Using CA Fatigue Tests Data

In order to demonstrate the suitability of the ESD model for fatigue life prediction, its CA strain-life curve was compared with the strain-life curve generated from the Coffin-Manson relationship and the experimental strain-life data. The Coffin-Manson relationship of Eq. (2.37) was chosen since CA loadings with zero mean stress were used for the fatigue tests. Using the material properties values of Table 5.1 and Table 6.2, the Coffin-Manson relationship for BS 080A42 steel is

$$\varepsilon_a = \frac{1505}{210000}\left(2N_f\right)^{-0.144} + 0.176\left(2N_f\right)^{-0.400} \qquad (6.7)$$

The comparison between the strain-life curves and the experimental data points is presented in Figure 6.9 and in Table 6.5.

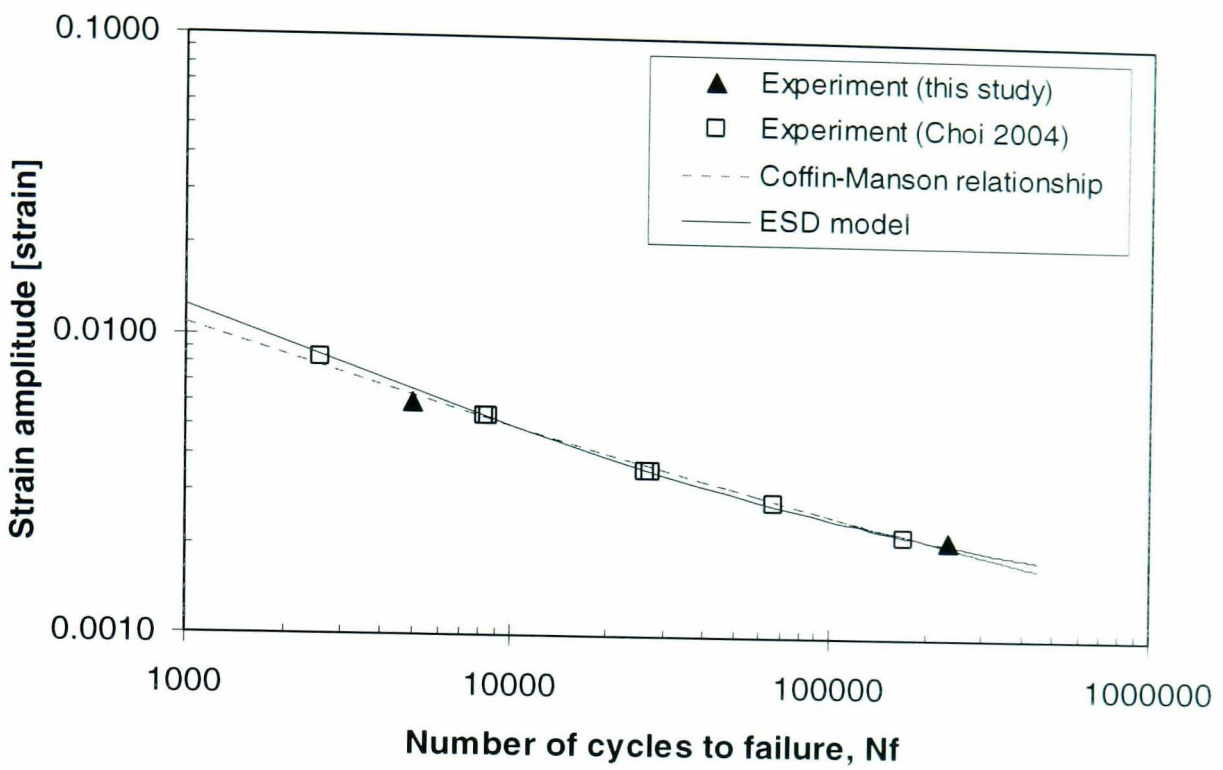

Figure 6.9: Comparison between the ESD model, the Coffin-Manson relationship and the experimental strain-life points.

Table 6.5: Comparison between the ESD model, the Coffin-Manson relationship and the experimental strain-life points.

Fatigue Life [No. of cycles to failure	Strain Amplitude [strain]			Experiment and ESD difference [%]	Coffin-Manson and experiment difference [%]
	ESD	Coffin-Manson	Experiment		
2608	0.0084	0.0078	0.0084	-0.8	6.4
4972	0.0065	0.0063	0.0060	-9.1	-5.6
8380	0.0054	0.0054	0.0054	0.3	0.9
8600	0.0053	0.0053	0.0054	1.7	2.1
26358	0.0037	0.0038	0.0036	-1.7	-5.0
27600	0.0036	0.0037	0.0036	-0.2	-3.6
66874	0.0028	0.0029	0.0028	2.0	-1.3
169922	0.0022	0.0022	0.0022	-0.7	-0.9
233530	0.0021	0.0020	0.0021	3.3	4.8
			Average Difference* [%]	3.3	3.4

* For the case of negative difference between the experiment and prediction strain amplitude, the absolute value was used to calculate the 'Average Difference [%]'.

Figure 6.9 shows that both the ESD and the Coffin-Manson strain-life curves have a close correspondence to the experimental data. The difference between the ESD prediction and the experimental result was, on average, 3.3%, while the difference for the Coffin-Manson relationship was, on average, 3.4%. From this comparison, it was concluded that the ESD strain-life model was also suitable for performing fatigue life estimations. Since the ESD model was originally developed by DuQuesnay *et al.* (1993) for solving the fatigue life prediction of VA strain loadings and a consideration of a decay in crack opening stress by Khalil and Topper (2003), thus the use of ESD model in fatigue life prediction of cyclic loadings can produce better results.

6.5 Fatigue Cycles Reconstruction

In order to predict fatigue life using the ESD model for a VA loading history, the fatigue cycles should be reconstructed based on the original position in the time history. This reconstruction procedure is required in order to retain the original load cycle sequences present in the original VA loading. Cycle reconstruction is not required for CA loadings, since the cycle sequences are not affected in the fatigue life prediction using this type of loading.

The process of fatigue cycle reconstruction consists of converting a time history into a series of peak-valley (PV) reversals. The PV history is then rainflow counted (Matsuishi and Endo 1968; Downing and Socie 1982) in order to extract fatigue cycles. The cycles were then sorted based on the PV history in order to produce a similar pattern to the original load sequences. For example, a reconstructed cycle history is shown in Figure 6.10 for the first bump segment (B1) of T4.

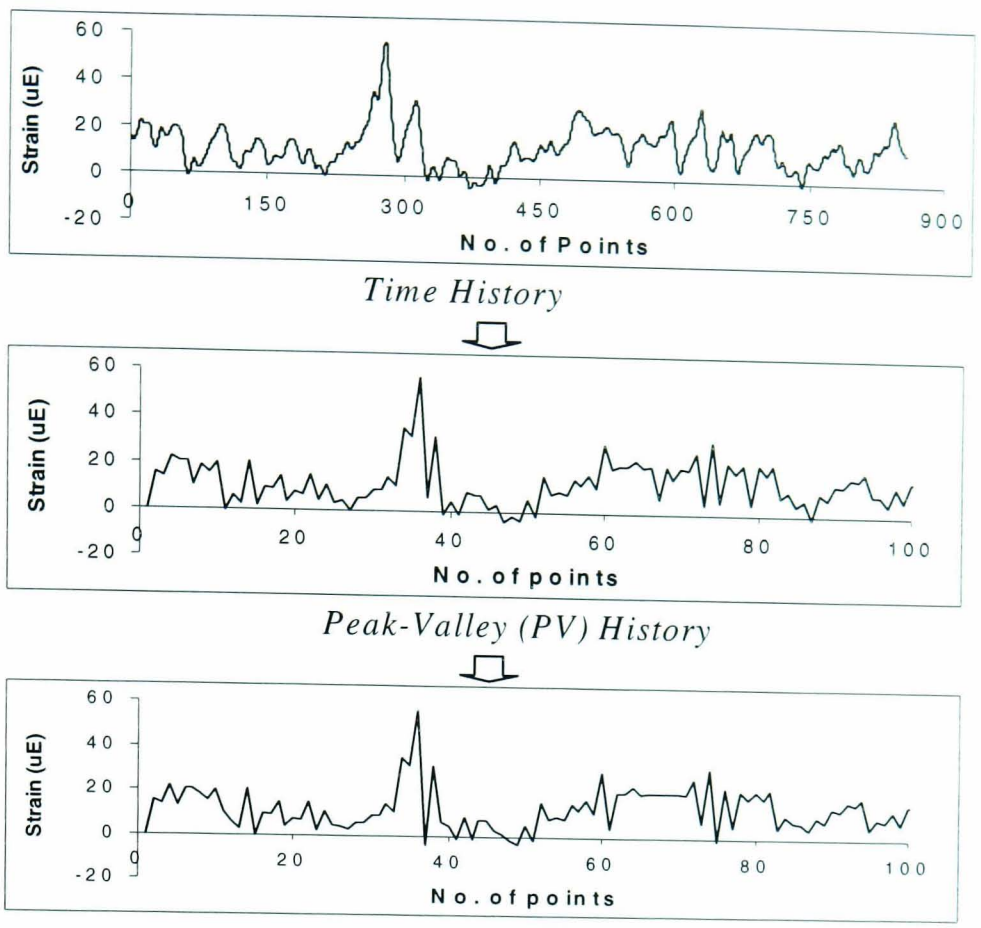

Figure 6.10: Time history reconstruction for the first T4 bump segment (B1).

6.6 Summary

In this chapter the results obtained from the experimental tests using constant amplitude (CA) and variable amplitude (VA) fatigue loadings were presented. The first experiment using CA loading was performed in order to obtain more CA data points for the stress-strain relationship and related strain-life model, i.e. the Ramberg-Osgood relationship and the effective strain damage (ESD) strain-life model. Two CA loading fatigue tests using smooth test specimen of BS 080A42 steel were performed at strain amplitudes of 0.0060 m/m and 0.0022 m/m. These two data points were added to the available CA loading fatigue test data points obtained by (Choi 2004).

The second experiment involved obtaining the fatigue lives of the BS 080A42 samples by means of accelerated fatigue tests consisting of three different WBE mission signals. Two types of specimen were used, i.e. smooth and notched specimens. The experimental results are presented in the form of mean and standard deviation values

which can be seen in Tables 6.3 and 6.4. From these tables, the mean fatigue lives of the mission signal with the original bump segment sequences were found close to that of the original loading signal, indicating its suitability for accelerated fatigue tests.

Using the results of the CA loading fatigue tests, the Ramberg-Osgood relationship was obtained for BS 080A42 steel, showing that a close correspondence was found between the experimental data and the fitted curve. The CA loading fatigue test results were then used to define the parameters of the ESD model for the smooth and the notched specimens. For both specimen types, the ESD model and the Coffin-Manson relationship produced nearly identical results to the experiment, leading to the conclusion that the ESD model can be used to accurately predict fatigue life.

CHAPTER 7

7. Discussion

7.1 A Suitable Strain-Life Model for the WBE Algorithm

In this section the results of a fatigue damage analyses of the variable amplitude (VA) loadings performed by means of strain-life models are compared with the experimental data. For this case, the bump segments extracted from the T4 signal using the Wavelet Bump Extraction (WBE) algorithm are used. The experimental results are taken from the study performed by Choi (2004). The purpose of conducting this analysis is to discuss the suitability of the strain-life fatigue damage model that was, at the end of the current research, adopted for use with the WBE algorithm.

7.1.1 Why Use a Strain-Life Approach for the WBE Algorithm?

The service loads of components of machines, vehicles, and structures are typically analysed for fatigue life using crack growth approaches. This approach is suitable for high capital value items such as large aircraft, the space shuttle, pressure vessels and oil rigs (Dowling 1999). The ability to inspect for cracks and monitor their growth until a maximum allowable defect size is reached, normally enables the useful life to be extended beyond the original design safe life. However, it is not generally feasible to perform crack inspection for inexpensive components that are made in large numbers.

Periodic inspections on these components would generally increase the cost of the item beyond the value accepted by the international market. Examples of components which fall in this category are automobile engines, steering components and suspension parts. For these components, it is important to predict crack initiation so as to avoid fatigue failure by removing the part from service at the appropriate time. A fatigue life estimate is usually made in such cases by means of a strain-based approach (Collins 1981; Dowling 1999; Wu *et al.* 1997).

The strain-life fatigue models relate the plastic deformation that occurs at a localised region where fatigue cracks begin to the durability of the structure. This model is often used for ductile materials at relatively short fatigue lives. This approach is also used where a little plasticity is acceptable at long fatigue lives. Therefore, strain-based approaches are comprehensive and can be used in place of stress-based approaches. Consequently, it is common that the service loadings of machines and vehicles is evaluated using a strain-life fatigue damage approach (Tucker and Bussa 1977; Conle and Landgraf 1983; Conle and Chu 1997).

Four strain-life models are discussed in this section. They are the Coffin-Manson relationship (Coffin 1954; Manson 1965), Morrow (Morrow 1968) and Smith-Watson-Topper (Smith *et al.* 1970) mean stress correction equations, and the Effective Strain Damage model (DuQuesnay *et al.* 1993). The first three are suitable for the conventional analysis with the constant amplitude (CA) loading (Dowling 1999). These models are not suitable, however, for analysing variable amplitude (VA) loadings (Fatemi and Yang 1998) as the load or cycle interaction effects are not accounted for. Despite this, they are often used for VA problems in practise. To properly treat VA loading histories, the Effective Strain Damage (ESD) strain-life model has been developed by DuQuesnay *et al.* (1993) to perform life-to-crack detection. In the ESD model the damage parameter that is treated is the effective strain range. The fatigue damage is analysed based on short crack growth concepts to incorporate retardation by changing crack closure levels.

The main reason for developing the WBE algorithm was the production of shortened mission loadings with the retention of original load cycle sequences. Based on the theoretical background in the previous paragraph and the literature review in Section 2.5, it appears that the ESD model is suitable for this kind of analysis. However, this statement can only be verified based on the analysis of fatigue damage performed using a range of strain-life fatigue damage models. From such comparison, a suitable strain-life model can be obtained for WBE.

7.1.2 Fatigue Life Prediction

In order to choose a suitable strain-life fatigue damage model to be used with the WBE algorithm, the experimental data which was obtained from the research work performed by Choi (2004) was used. In his work, Choi (2004) used nine VA fatigue loadings which were the WBE extracted bump segments of the signal measured on a pavé test track. This is the T4 signal, as illustrated in Figure 4.2b for the plot of the time history. The experimentally determined fatigue lives are presented in Table 5.4. These are compared with those calculated using four strain-life models, i.e. Coffin-Manson, Morrow, Smith-Watson-Topper (SWT) and ESD.

The fatigue life predictions based on the Coffin-Manson, Morrow and SWT strain-life models were performed using the nSoft® software package. The monotonic properties and strain-life parameters of BS 080A42 steel in Table 5.1 and Table 6.2, respectively, were used. The fatigue life prediction based on the ESD model was performed according to the routine shown in Figure 6.7 and Figure 6.8. Finally, Table 7.1 shows the predictions of the fatigue lives and fatigue damage. In this table, the total fatigue damage was calculated by linear summation of all bump segments.

Table 7.1: Fatigue life and fatigue damage values of the T4 bump segments calculated using four strain-life models and determined from the experiments.

Signal Name	Strain-life models				Experiment (Choi 2004)
	Coffin-Manson	Morrow	SWT	ESD	
Fatigue Life, N_f [Number of blocks to failure]					
B1	6214	5964	10462	1968	2831
B2	107000	97000	114000	19523	17880
B3	15199	14008	17720	2400	3996
B4	101000	96400	163000	25586	20084
B5	14287	13708	24566	2714	2792
B6	3569	3428	6070	927	843
B7	6512	6216	10409	1536	1366
B8	9890	9370	14783	2206	1942
B9	37811	35667	55200	8181	7500
T4	665	642	1194	191	178
T4-mission	1092	1057	2013	319	204
Fatigue Damage = $1/N_f$ [Damage per block]					
B1	1.61×10^{-4}	1.68×10^{-4}	9.56×10^{-5}	5.08×10^{-4}	3.53×10^{-4}
B2	9.35×10^{-6}	1.03×10^{-5}	8.77×10^{-6}	5.12×10^{-5}	5.59×10^{-5}
B3	6.58×10^{-5}	7.14×10^{-5}	5.64×10^{-5}	4.17×10^{-4}	2.50×10^{-4}
B4	9.90×10^{-6}	1.04×10^{-5}	6.13×10^{-6}	3.91×10^{-5}	4.98×10^{-5}
B5	7.00×10^{-5}	7.30×10^{-5}	4.07×10^{-5}	3.68×10^{-4}	3.58×10^{-4}
B6	2.80×10^{-4}	2.92×10^{-4}	1.65×10^{-4}	1.08×10^{-3}	1.19×10^{-3}
B7	1.54×10^{-4}	1.61×10^{-4}	9.61×10^{-5}	6.51×10^{-4}	7.32×10^{-4}
B8	1.01×10^{-4}	1.07×10^{-4}	6.76×10^{-5}	4.53×10^{-4}	5.15×10^{-4}
B9	2.64×10^{-5}	2.80×10^{-5}	1.81×10^{-5}	1.22×10^{-4}	1.33×10^{-4}
*BT	8.77×10^{-4}	9.20×10^{-4}	5.54×10^{-4}	3.69×10^{-3}	3.63×10^{-3}
T4	1.50×10^{-3}	1.56×10^{-3}	8.38×10^{-4}	5.24×10^{-3}	5.62×10^{-3}
T4-mission	9.16×10^{-4}	9.46×10^{-4}	4.97×10^{-4}	3.13×10^{-3}	4.90×10^{-3}

*BT = total fatigue damage of all bump segments

7.1.3 Relationship Between Prediction and Experiment

The experimental uniaxial fatigue lives in Table 5.2 were compared with the prediction values in Table 7.1. Figure 7.1 shows the correlation of fatigue lives between experiment and all four strain-life models. Each data point represents a loading condition in Table 5.2 and Table 7.1. The correlated fatigue lives between the ESD model and experiments were distributed around the 1:1 line and within the range of ± a factor of 2. However, the correlation points produced from the data of the three other strain-life models (Coffin-Manson, Morrow and SWT) were located outside the range of ± a factor of 2. This suggests that the ESD model provided the closest correspondences between the predicted fatigue life and the experimental fatigue life.

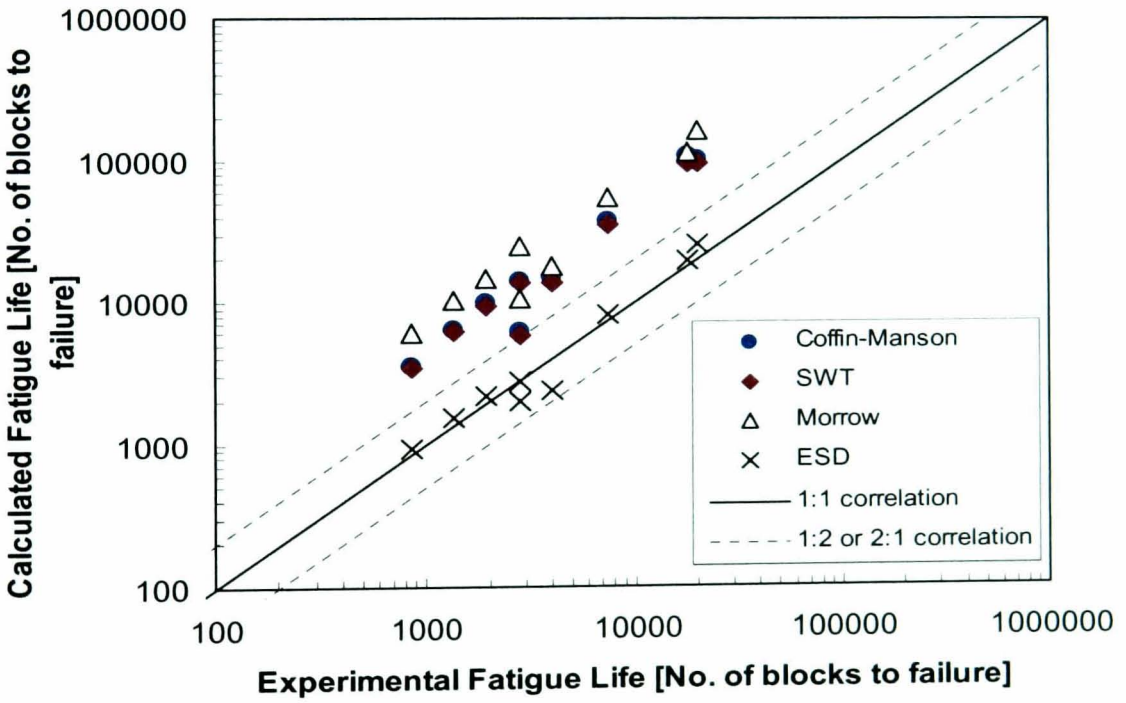

Figure 7.1: Fatigue life correlation between prediction and experiment for the nine bump segments of signal T4.

Numerically, the comparison between fatigue lives determined using the four strain-life models and the experimental findings (Choi 2004) are tabulated in Table 7.2. The table shows the difference (in percent) between the predicted value of a particular strain-life model and the experimental value for a particular bump segment. Then, the differences for the same strain-life model are averaged in order to obtain a single value for

comparison purposes. The results in Table 7.2 show that the difference between the SWT model and the experimental results gave the highest value at 580%, followed by the Coffin-Manson model at 358% and the Morrow model at 333%. Using the ESD model, the average difference was found to be 17%.

Table 7.2: Fatigue life differences between prediction and experiment for nine bump segments of signal T4.

Signal Name	Fatigue Life Differences (%)			
	Coffin-Manson vs. Experiment	Morrow vs. Experiment	SWT vs. Experiment	ESD vs. Experiment
B1	119	111	270	30
B2	498	443	538	9
B3	280	251	343	40
B4	403	380	712	27
B5	412	391	780	3
B6	323	307	620	10
B7	377	355	662	12
B8	409	382	661	14
B9	404	376	636	9
Average	358	333	580	17

Note: Fatigue life (N_f) difference =absolute $\{(N_{f\ predicted} - N_{f\ experiment})/ N_{f\ experiment}\} \times 100\%$

In a separate analysis, Table 7.3 shows the difference in total fatigue damage of the bump segments when comparing the prediction results of the strain-life models and the experiments. Similar to the data in Table 7.2, the SWT model produced the highest difference with respect to the experiment, which was found at 85%. It was followed by the Coffin-Manson and Morrow models, at 76% and 75%, respectively. However, the ESD model produced the smallest difference value at 2%. Using the ESD model, the lowest difference in fatigue life prediction was found as shown in Table 7.2 and Table 7.3. Since the ESD model accounts for mean stress and cycle sequence effects during the fatigue life calculation (DuQuesnay *et al.* 1992a; 1992b; 1993; Topper and Lam 1997; DuQuesnay 2002), the high correlations were to be expected.

Table 7.3: Comparison of total fatigue damage accumulated for all T4 bump segments.

Signal Name	Fatigue Life Differences (%)			
	Coffin-Manson vs. Experiment	Morrow vs. Experiment	SWT vs. Experiment	ESD vs. Experiment
TOTAL	76	75	85	2

Note: Fatigue life (N_f) difference =absolute {($N_{f\ predicted} - N_{f\ experiment}$)/ $N_{f\ experiment}$} x 100%

7.1.4 Concluding Remarks

The comparison of the experimental and analytical results obtained for the T4 bump segments suggested that the ESD model provided more accurate fatigue life predictions for VA fatigue loadings than the three other strain-life models that were considered. Since the smallest fatigue life differences of Tables 7.2 and 7.3 were obtained using the ESD model, it can be concluded that the ESD model is the most suitable for predicting the fatigue damage caused by VA loadings. The combination of ESD and WBE provide a novel wavelet-based fatigue data editing technique which accurately extracts the most fatigue damaging events (bump segments) and which preserves the original load cycle sequence within the fatigue loadings.

7.2 The WBE Algorithm for Fatigue Data Editing

7.2.1 Purpose of the WBE Algorithm

During the durability testing of machines such as automobiles, load histories under particular driving conditions are often collected (Palma and Martins 2004). If these loadings are used in unmodified form for laboratory fatigue testing, a lengthy testing time is required. In order to minimise such testing, accelerated fatigue tests are used. Previous studies (Austen and Gregory 1995; El-Ratal *et al.* 2002) suggest that testing

can often be accelerated by the use of time domain fatigue data editing techniques to produce a shortened loading that contains the high amplitude cycles.

In the research described in this thesis, the WBE algorithm was developed to summarise long VA fatigue loadings by extracting bump segments which cause most of the fatigue damage and which retain the original cycle sequences. The development of WBE involved the application of the orthogonal wavelet transform using 12^{th} order Daubechies wavelets, which permits bump identification to be performed in individual wavelet groups (frequency regions). The bump identification process identified the start and finish points of the bump segments of the original time history of the VA loading. Concatenating the bump segments creates a shortened mission signal that preserves the load sequence. Ideally, the mission signal produced using WBE should have equivalent fatigue damage to the original signal. The WBE algorithm was described in detail in Chapter 4.

In the previous section the effectiveness of the ESD model was demonstrated. Further, the ESD model permits a correct evaluation of cycle sequence effects. The ESD model was thus adopted for performing fatigue life calculations of VA loadings within WBE. This part of the research is the subject of the next section of this thesis.

7.2.2 Limitations of the WBE Algorithm

When applying WBE to the four experimental test signals (refer to Section 4.1.2) WBE was found to highly compress the pavé test track signal. The time length of the mission signal for the T4 and T5 road signals was found to be 40.9% and 53.9% of the original duration, respectively. However, the algorithm was found to be less effective to compress signals containing relatively a mixture of higher amplitude events in small amplitude background or a signal with similar condition to T3. In addition, the algorithm was also found less effective for signals which have most of the vibrational energy

below 1 Hz as observed in the low frequency wavelet group of T3 (Figure 4.7) and T6 (Figure 4.10).

Referring to Figure 7.2 which represents signal T3, the time duration of the mission signal is 83.4% of the original signals, and some of the low amplitude events were retained. Longer time length of the mission signal was caused by the difference value (in percent) of the r.m.s. and kurtosis which were used to determine the trigger levels. This was one of the limitations of the WBE algorithm, and will be the subject of Section 7.2.3. The result shows the difficulty of performing an automatic fatigue mission analysis based only on global signal statistics.

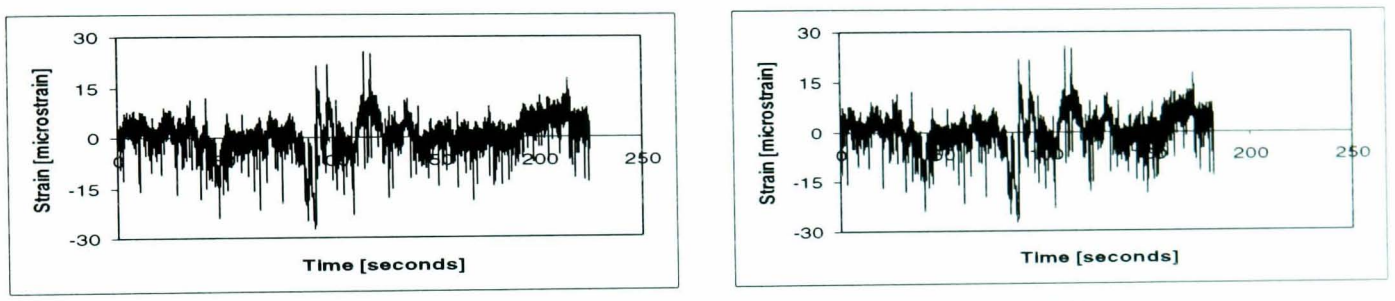

Figure 7.2: The original and mission signals of T3: (a) The 225-second T3 signal; (b) The 182-second T3 mission signal.

Another limitation of the WBE algorithm is its difficulty in dealing with low frequency content in the input signal, as shown in Figure 7.3 for signal T6. In this figure, it can be seen that the low frequency content of the signal has an important role in determining the overall length of the bump segments. In Figure 7.3b, the time length of the first bump is 34.9 seconds and for the second bump is 11.5 seconds. The length of individual bump in Wavelet Group 1 produced the similar length of the bump segments, as illustrated in Figure 7.3d. Accordingly, the bump segments of T6 had longer time extent (46.4 seconds) compared to the bump segments of the other test signals. With WBE it is not easy to heavily compress VA fatigue loadings with a substantial low frequency content because most of the mission time length involves a single bump from a low frequency wavelet group.

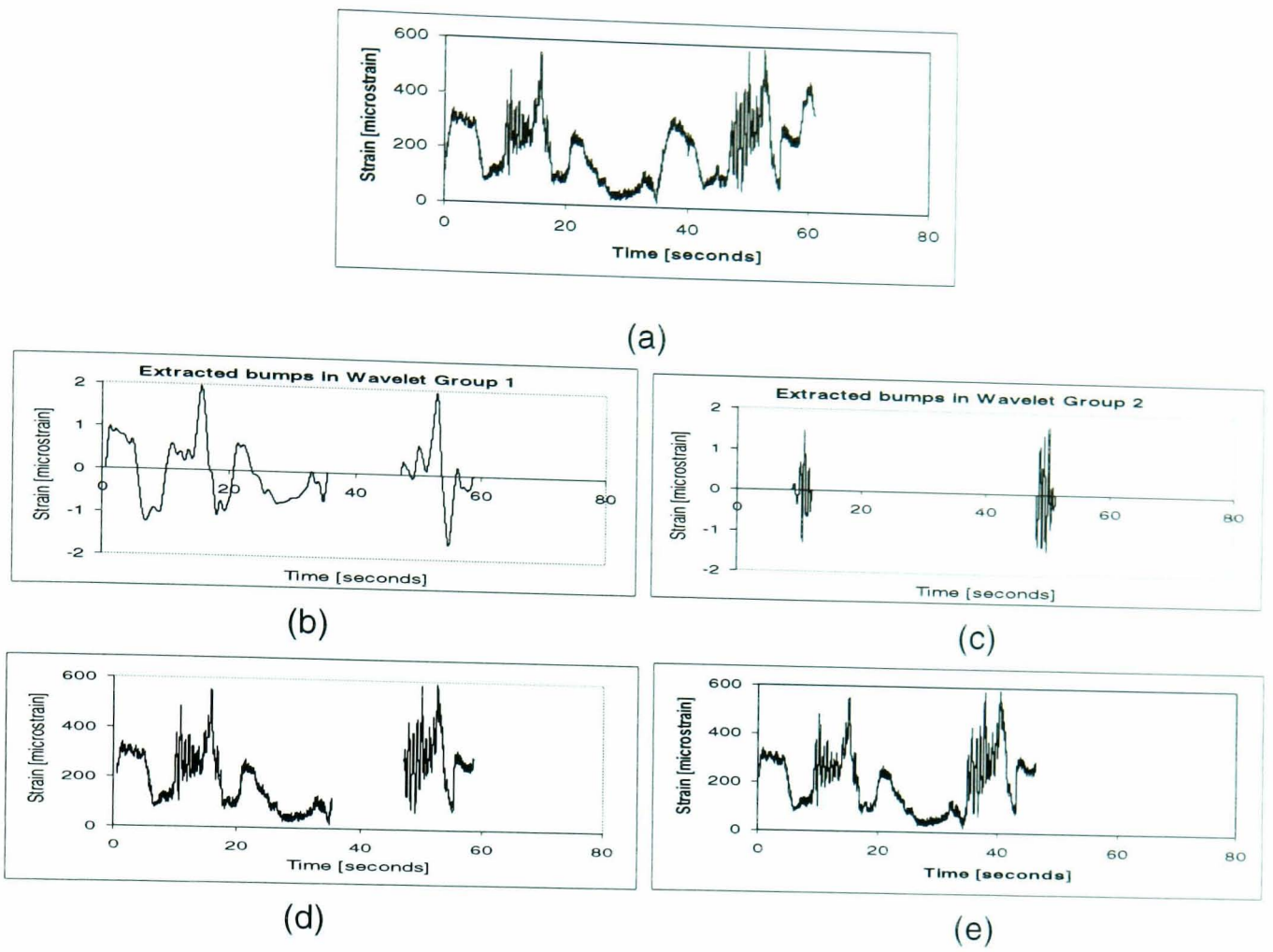

Figure 7.3: T6: (a) The original signal; (b) Bumps in Wavelet Group 1; (c) Bumps in Wavelet Group 2; (d) Extracted bump segments; (e) The 46.4-second mission signal.

7.2.3 Trigger Level as a Control Parameter for WBE

It was discussed in Section 7.2.2 that the trigger level value is a controlling parameter in identifying the bumps in a wavelet group. In order to determine suitable trigger level values, four values are used in the procedure shown in Figure 4.9. The first parameter, *C1*, is the required ratio (in percent) of the initial trigger level to the maximum amplitude for all wavelet groups. The second parameter, *C2*, is the trigger level step and is the ratio (in percent) of the step size to the maximum amplitude in a wavelet group. *C1* was set to a value of 95% when analysing the test signals described in this thesis and a value of 5% was used for *C2*. The initial trigger level value was determined by multiplying the maximum strain amplitude of a wavelet group by *C1*. The trigger level step was set by multiplying the maximum strain amplitude of a wavelet group by *C2*. Other parameters which affect bump identification are *RD* and *KD*. These are the global

statistical parameters. The WBE user is requested to input a desired value of root-mean-square (r.m.s.) difference (*RD*) and kurtosis difference (*KD*) between the mission and original signals. Both parameters are related to the fatigue damage potential, as a higher r.m.s. value produces higher fatigue damage (Hu 1995) and a higher kurtosis value is characteristic of data with many high amplitude peaks, which also produces higher fatigue damage (Qu and He 1986).

In WBE, the r.m.s. and kurtosis difference of the mission and original signals must satisfy the conditions as shown in the flowchart of Figure 3.2,

$$-RD < D1 < +RD \tag{7.1}$$

$$-KD < D2 < +KD \tag{7.2}$$

where *D1* and *D2* are the calculated difference (in percents) r.m.s. and kurtosis between the original and mission signals, respectively. Both parameters must simultaneously meet the *RD* and *KD* values, giving simultaneous check on the vibrational energy (r.m.s. value) and amplitude range (kurtosis value) of the mission and the original signals.

The relationship between the trigger level values and the fatigue damage can be understood from an analysis using the signals measured on different road surfaces: on the public road (T3) and on the pavé test track (T4). These two signals were chosen since both of them were experimentally measured from the lower suspension arm of different vehicles travelling over different road surfaces. Other experimental measured signals are T5 and T6. Since T5 was measured on similar road surface to T4 and T6 has a limitation in the signal compression characteristics (with respect to a low frequency content as discussed in Section 7.2.2), both T5 and T6 were omitted from the analysis of this section. Using T3 and T4, these two signals were processed with WBE and the mission signals with the original bump segment sequences (BS1) were used for the analysis. The ESD model was then used for the prediction of the fatigue life, using the properties of BS 080A42 steel.

The results of the trigger level analysis for both signals are tabulated in Table 7.4, which presents the time and fatigue life ratios at various user defined differences. At ±70°。

r.m.s. and kurtosis difference for T3, a 31-second mission signal (14% of the original signal length) was obtained with 92% of the original fatigue damage retained. For T4, using ±70% statistical difference produced the 9-second mission signal (20% of the original signal length) with 99% of the original fatigue damage was retained. The relationship between time ratio and fatigue life ratio is shown in Figure 7.4. Figure 7.5 presents the T3 and T4 signals alongside the obtained mission signals containing 92% and 99%, respectively, of the total fatigue damage. The ability of the WBE algorithm to shorten fatigue loading time histories by more than half their original length, while simultaneously retaining the majority of fatigue damage, would be expected to prove useful in accelerated fatigue tests.

Table 7.4: Time ratio and fatigue life ratio for signals T3 and T4 processed with WBE using several values of r.m.s. and kurtosis range.

T3 (Original time length = 225 seconds; fatigue life = 96182 blocks to failure)				
r.m.s. and kurtosis range [%]	Mission Signals		Ratio	
	Time [seconds]	Fatigue life using the ESD model [no. of blocks to failure]	Time ratio [%]	Life Ratio [%]
5-10	182	96182	81	100
10-15	131	96182	58	100
15-20	119	105170	53	92
20-25	96	105170	42	92
25-30	66	105170	30	92
30-65	33	105170	14	92
65-70	31	105170	14	92
T4 (Original time length = 46 seconds; fatigue life = 1035240 blocks to failure)				
5-10	19	1035240	41	100
10-20	12	1045172	26	99
20-30	12	1045172	26	99
30-40	9	1045172	21	99
40-70	9	1045172	21	99

Note: Ratio = (mission signal / original signal) x 100%

With reference to Table 7.4 and Figure 7.4, the majority of original fatigue damage was retained in the mission signal at lower difference of r.m.s. and kurtosis values. It shows that the global signal statistics parameters cannot be acted as a single criterion for bump identification and extraction.

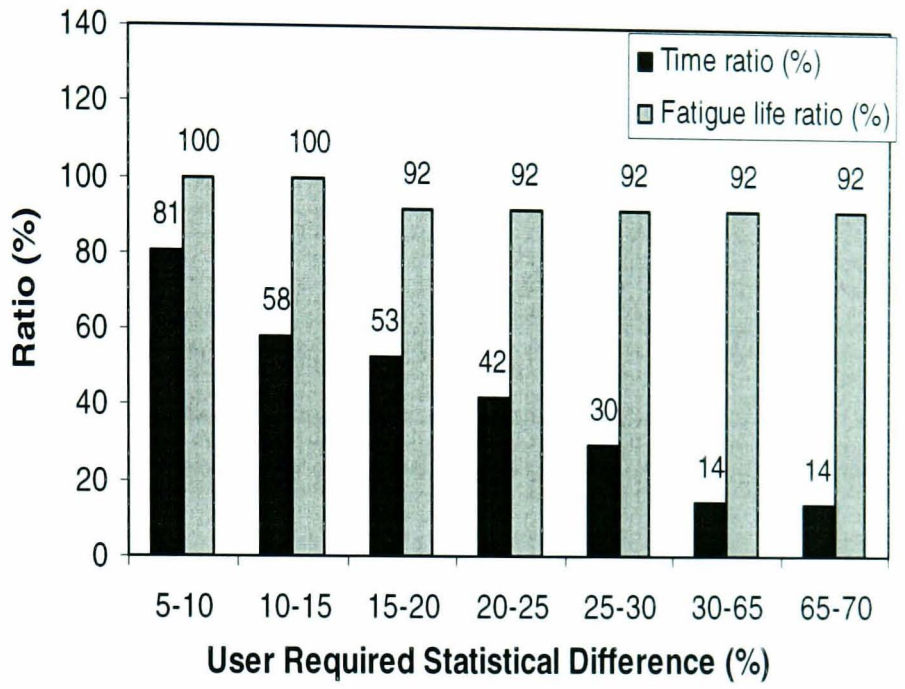

(a)

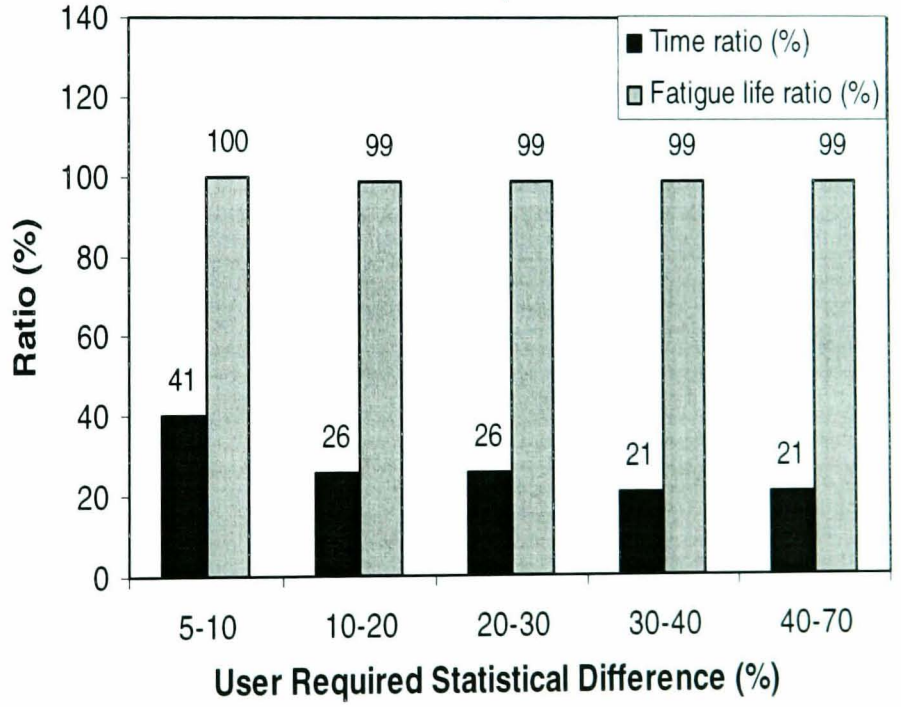

(b)

Figure 7.4: Relationship between time ratio and fatigue life ratio at the user required r.m.s. and kurtosis difference for: (a) T3, (b) T4.

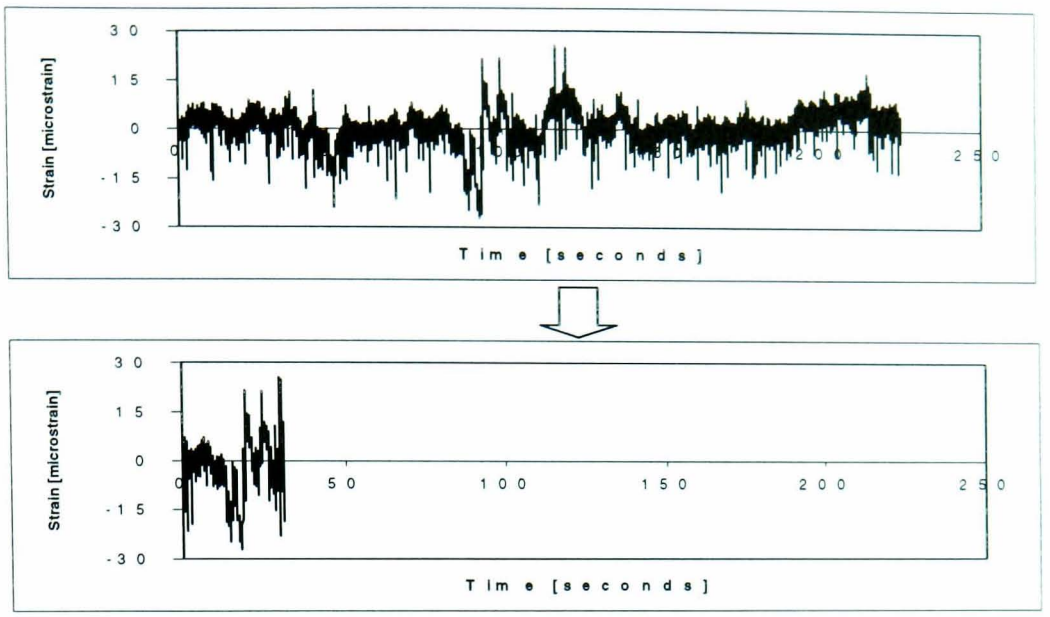

(a)

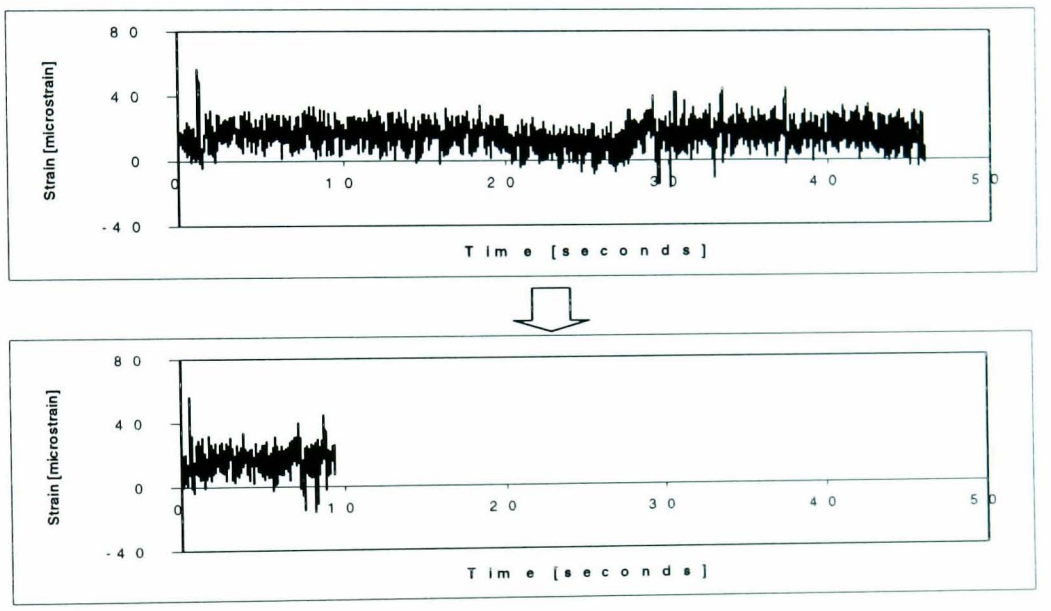

(b)

Figure 7.5: The T3 and T4 mission signals with the majority of fatigue damage:
(a) T3 and its 31-second mission signal (92% damage retained),
(b) T4 and its 9-second mission signal (99% damage retained).

7.2.4 Comparison Between the WBE Algorithm and the Time Correlated Fatigue Damage (TCFD) Method

Since the WBE algorithm is a new fatigue data editing technique, it is important to compare this technique with an established procedure. According to research by El-Ratal *et al.* (2002), the time domain fatigue data editing is recommended for accelerated

fatigue tests. Using the time domain fatigue data editing, the phase and amplitude relationships of the original signal are retained in the shortened signal.

El-Ratal *et al.* (2002) used the time correlated fatigue damage (TCFD) method, as implemented in the nSoft® software package, for editing VA fatigue loadings. Hence, this method was used for comparison with the WBE algorithm. TCFD is used to remove non-damaging sections of the time history on the basis of time correlated fatigue damage windows of the input signal. Windows with low amplitude cycles which contained minimal fatigue damage are removed. Using this approach, either the percentage of damage retention or the required acceleration factor, or both, can be set as editing targets (nSoft® User Manual 2001).

Two test signals were used for the comparison: T3 and T4, for similar reasons explained in Section 7.2.3 were considered for signal selection (Both signals were experimentally measured from lower suspension arm of different vehicles travelling over different road surfaces). These two signals were analysed by TCFD to produce the time-domain compressed signals of a similar time length to the respective WBE mission signals. The original bump segment sequences of the mission signals (T3BS1 and T4BS1) which were produced at the ±10% r.m.s. and kurtosis difference were selected for comparison. The respective plots of T3BS1 and T4BS1 are shown in Figure 4.19b and Figure 4.20b. Using the TCFD method, the time correlated damage profiles for T3 and T4 are shown in Figure 7.6. These profiles were divided into damage time windows for the TCFD editing criterion. In order to have the TCFD compressed signals at similar time-length to the WBE mission signals, the original signals were reduced at 80.8% for T3 and 40.9% for T4. This allowed the required acceleration factors to be set as editing targets i.e. 1.24 for T3 and 2.45 for T4.

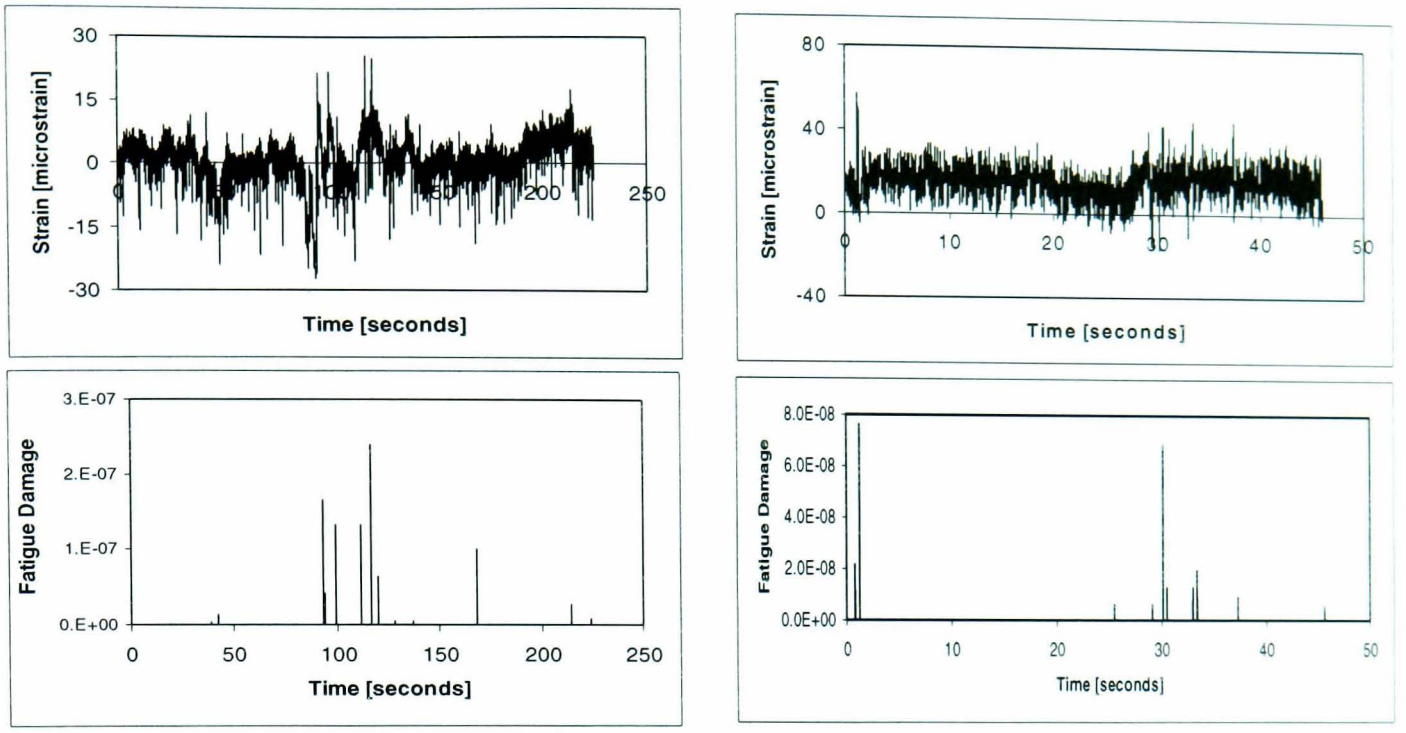

Figure 7.6: The original signal and its time correlated damage profile: (a) T3, (b) T4.

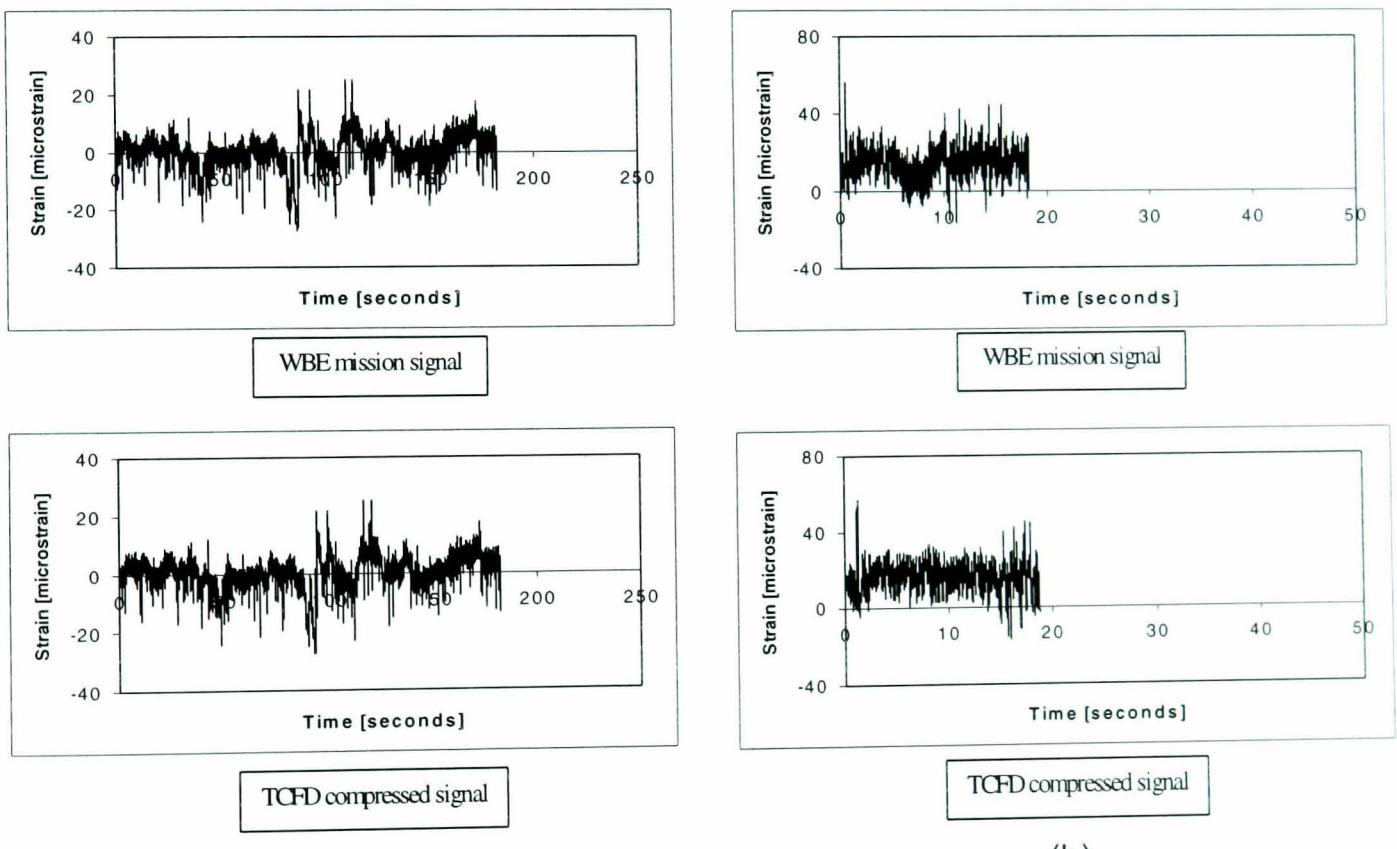

Figure 7.7: Comparison of loading compression achieved with the WBE and TCFD methods for signals: (a) T3, (b) T4.

In order to compare equal abilities of preserving fatigue damage in the compressed signals, the original fatigue damage was preserved at 100% for both signals, as shown in Table 7.4. Figure 7.7 shows the signals of similar time length which were obtained from WBE and TCFD at the decided condition of equal damage. Since the conserved

damage was set to be equal, the shortened signals were compared based on the r.m.s. value, the kurtosis value and the PSD plot. The general idea behind the comparison was to check if the general signal statistics remained unchanged after compression, since this would be a likely indicator that cycle sequence and other fatigue-relevant characteristics remained unchanged. The r.m.s. and kurtosis comparisons were chosen as general statistical measures while the PSD plots were used to observe the vibrational energy distribution of the time series. The comparison results are tabulated in Table 7.5 and Table 7.6.

Table 7.5: Comparison of the signal statistics between the original, WBE mission and TCFD compressed signals.

Signal	Signal length [seconds]	Signal Statistics	
		r.m.s. [microstrain]	kurtosis
T3			
Original Signal	225.0	4.6	8.0
WBE mission signal	181.9	4.9	7.4
TCFD compressed signal	181.9	4.6	8.6
T4			
Original Signal	46.0	16.7	3.4
WBE mission signal	18.8	16.6	3.6
TCFD compressed signal	18.8	17.4	4.1

Table 7.6: Time length and signal statistics normalised by the original signal values.

Signals	Signal length ratio [%]	Signal Statistics [%]	
		r.m.s.	kurtosis
T3			
Original Signal	-	100.0	100.0
WBE mission signal	80.8	106.5	92.5
TCFD compressed signal	80.8	100.0	107.5
T4			
Original Signal	-	100.0	100.0
WBE mission signal	40.9	99.4	105.9
TCFD compressed signal	40.9	104.2	120.6

Mixed results were found in the case of signal T3. The TCFD compression retained the r.m.s. value of the original signal. On the other hand, the r.m.s. value of the WBE mission signal was found to be higher than the original by 6.5%. Similar differences in the kurtosis value for signal T3, of 7.5%, were found for both WBE and TCFD shortened signals. For signal T4, WBE produced a compressed loading with r.m.s. and kurtosis values closest to the original signal. The differences were found to be 0.6% and 5.9% for the r.m.s. and kurtosis values, respectively.

Figure 7.8 and Figure 7.9 present the power spectral densities (PSDs) of the original T3 and T4 signals, and of the WBE and TCFD shortened signals. From these figures, it can be seen that neither compression technique maintains exactly the same PSD distribution as the original signals. The differences are, however, qualitatively different. The results obtained using the WBE algorithm follow the general distribution of resonant frequencies (the peaks), but tends to produce higher amplitudes than the original at the resonant peaks. TCFD, on the other hand, produced qualitatively different energy, occasionally failing to represent some resonances from the original road data. From a PSD perspective, the WBE algorithm appears to provide superior performance.

Considering the general trend of better results observed with the WBE algorithm, it can be suggested that the WBE algorithm is a better approach compared to TCFD.

7.2.5 Preservation of Fatigue Damage by WBE

The purpose of the analysis of this section is to demonstrate the preservation of the original fatigue damage in the WBE mission signal. The material provides an analytical validation of the applicability of the WBE algorithm as a tool for producing accelerated fatigue loading signals. The ESD strain-life fatigue damage model and six test signals (listed in Table 4.1 and Table 4.2) are used.

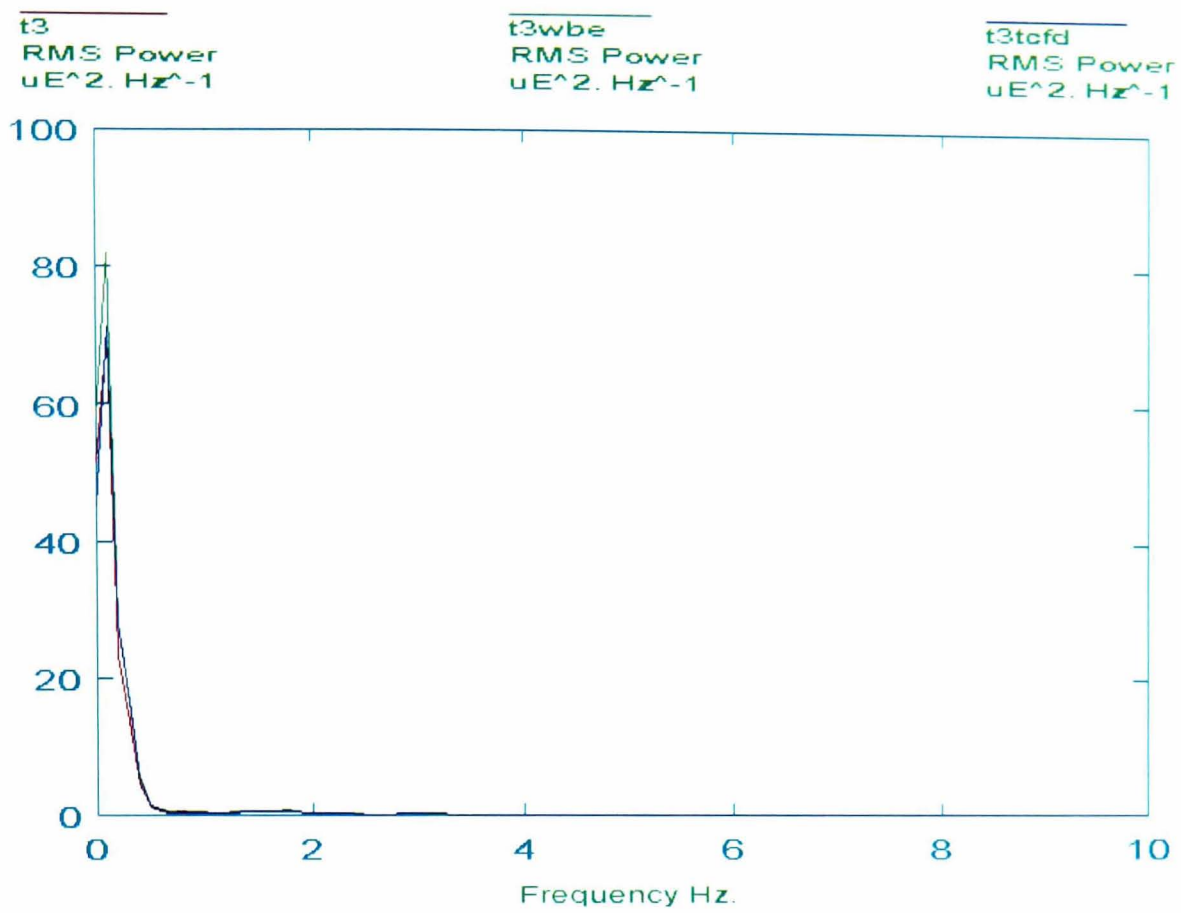

(a)

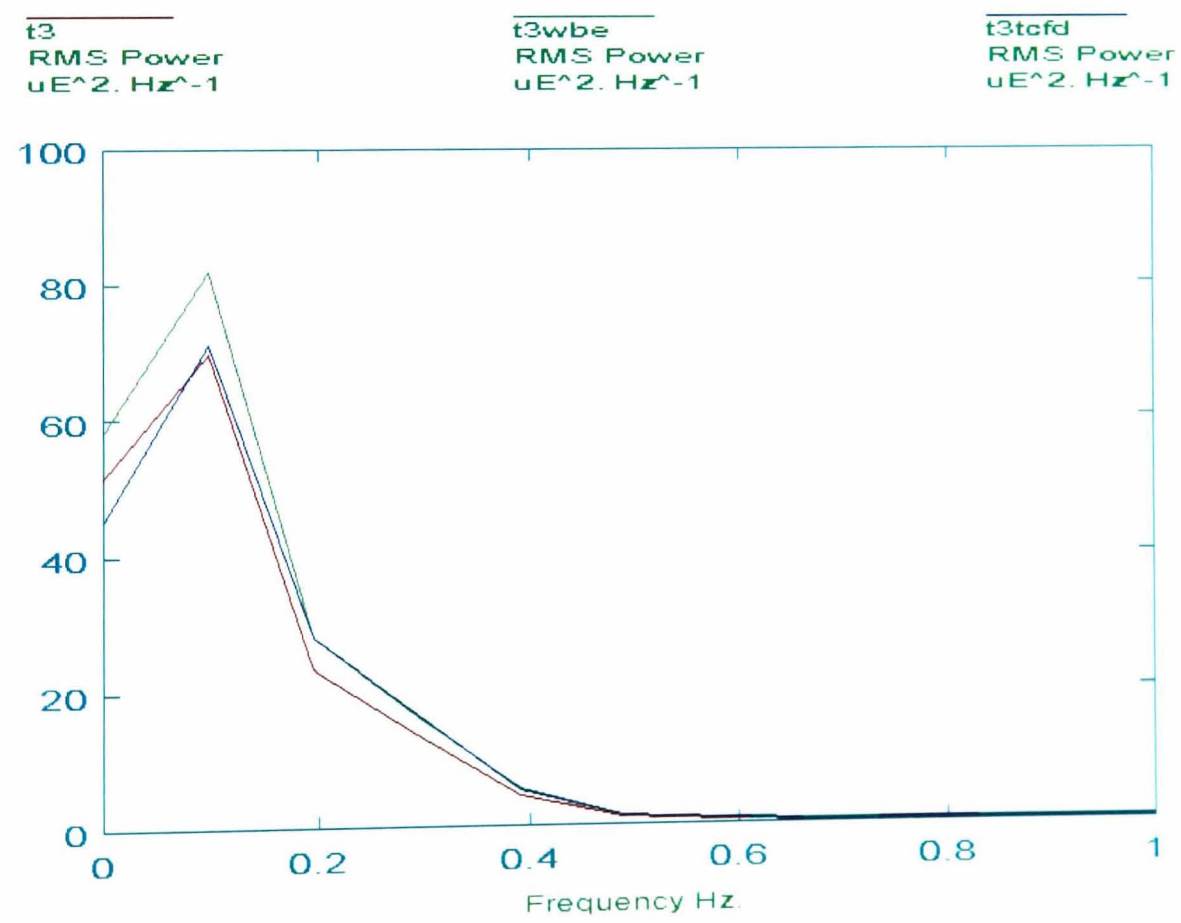

(b)

Figure 7.8: PSD comparison between the T3 original signal (*t3*), the WBE mission signal (*t3wbe*) and the TCFD compressed signal (*t3tcfd*):
(a) Frequency range: 0-10 Hz, (b) Frequency range: 0-1 Hz.

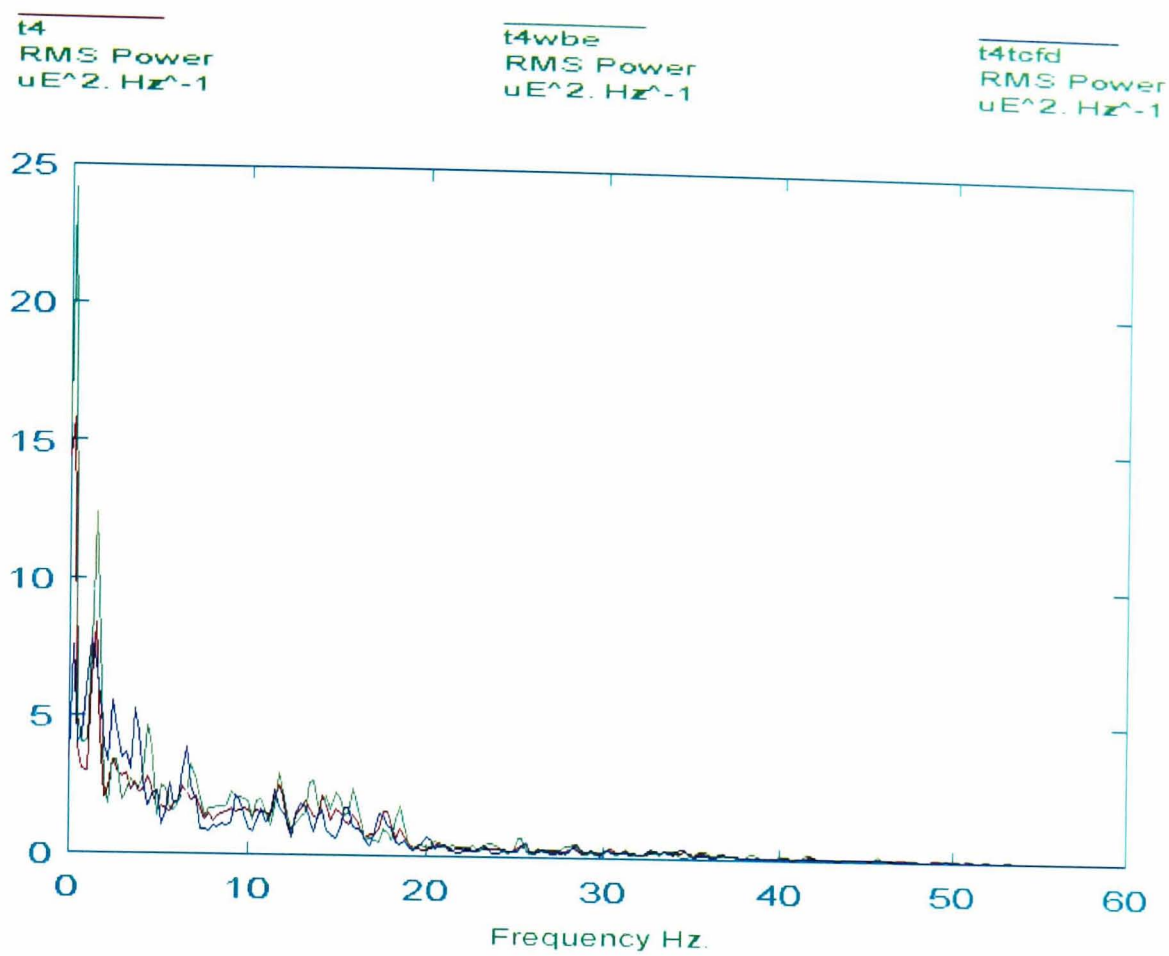

(a)

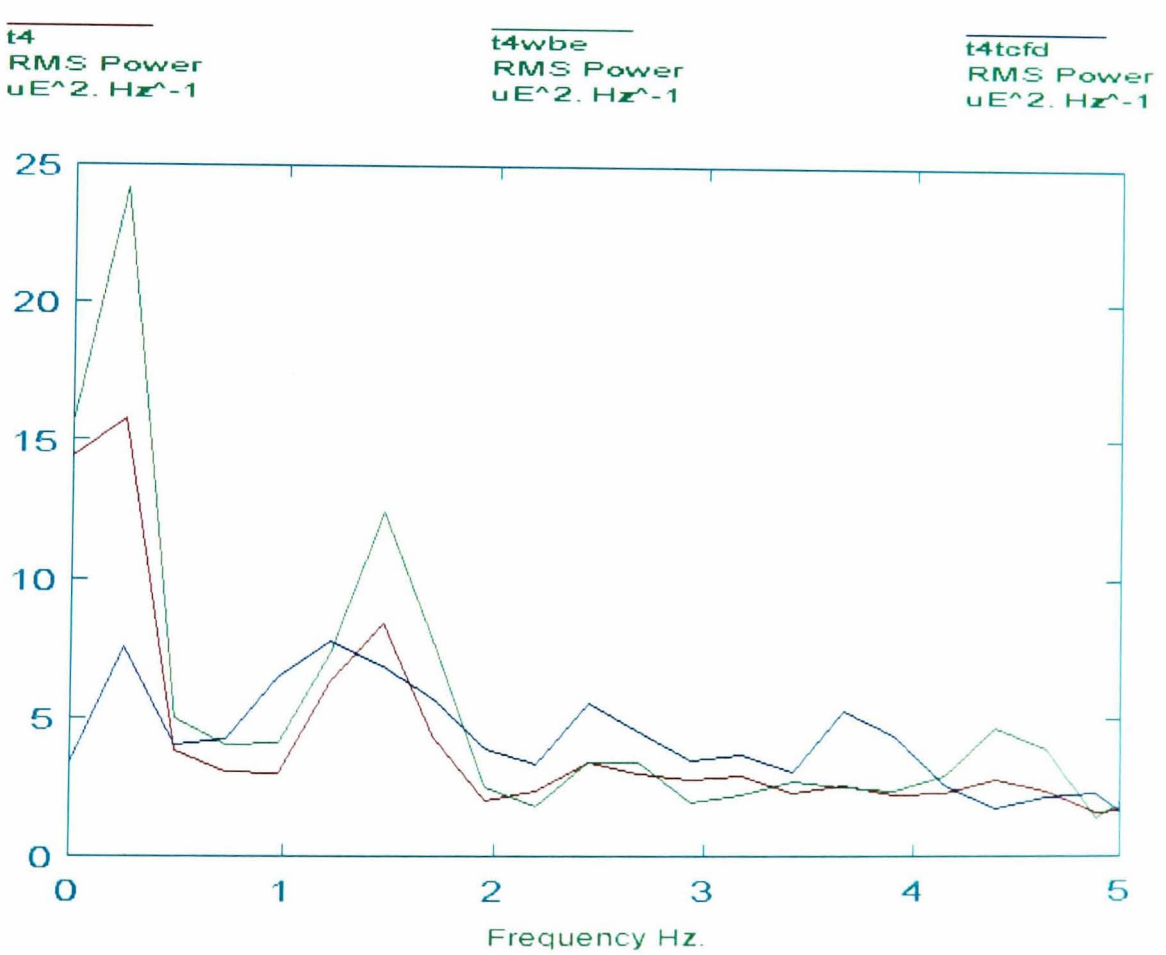

(b)

Figure 7.9: PSD comparison between the T4 original signal (*t4*), the WBE mission signal (*t4wbe*) and the TCFD compressed signal (*t4tcfd*):
(a) Frequency range: 0-60 Hz, (b) Frequency range: 0-5 Hz.

For the fatigue life prediction, firstly, the original and mission signals were rainflow counted (Matsuishi and Endo 1968) to extract fatigue cycles. An example of the rainflow cycle distribution is shown in Figure 7.10 for the original T4 signal and for the mission signal T4BS1. Similar plots for all test signals are presented in Appendix B (Figure B.1 to Figure B.6). Comparing the cycle distribution between the original and mission signal, the majority of original high amplitude cycles which contribute to the fatigue damage were retained in the mission signals.

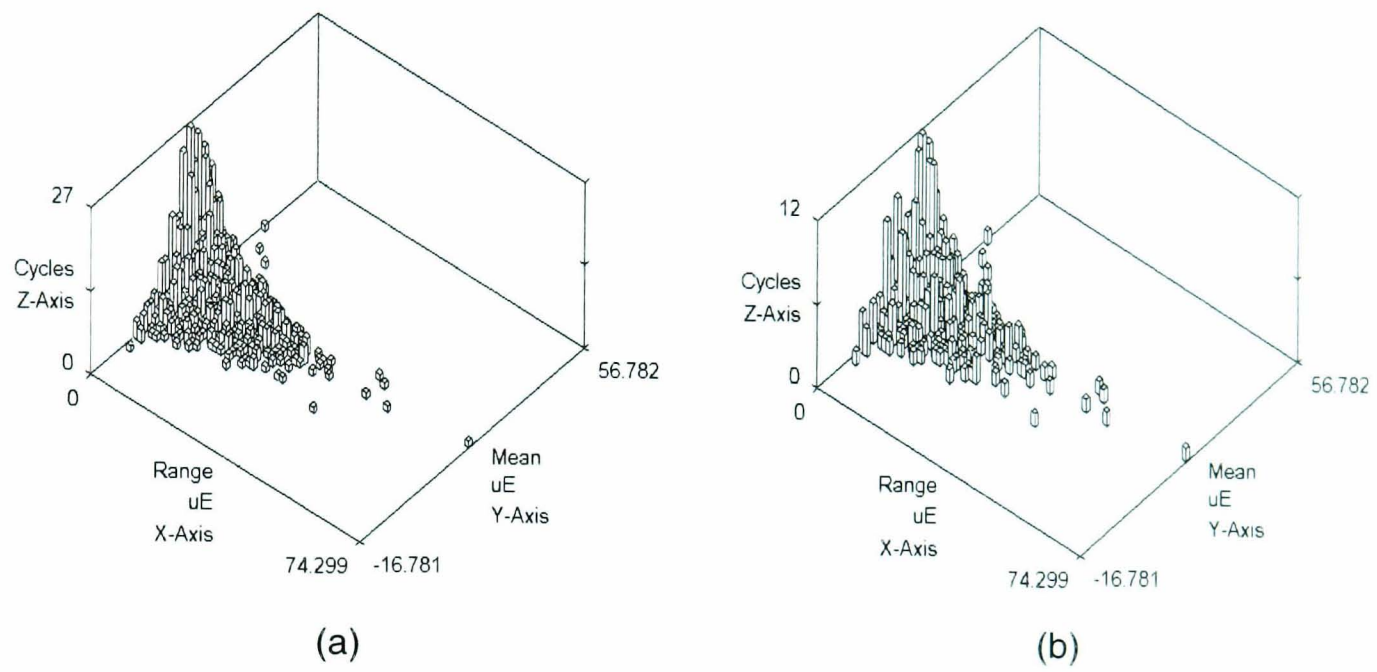

(a) (b)

Figure 7.10: Rainflow cycle histogram: (a) T4, (b) T4BS1.

The fatigue lives for six test signals and for the corresponding six mission signals were calculated using the ESD model and are presented in Table 7.7. Considering all six signals, at least 82% of the original fatigue damage was preserved in the mission signals. In Table 7.7 two values of stress concentration factor K_t were used for the fatigue life calculations. K_t = 1 was used to represent a smooth specimen, as this specimen is illustrated in Figure 5.4. On the other hand, K_t = 1.3 was used to represent a circumferential notch specimen with a root radius 3 mm and this specimen is illustrated in Figure 5.5.

Table 7.7: Fatigue lives predicted for six test signals and for each of 18 mission signals using the ESD model for BS 080A42 steel.

Signals	K_t = 1.0		K_t = 1.3	
	Fatigue Life [No. of blocks to failure]	Fatigue damage ratio (mission/original), [%]	Fatigue Life [No. of blocks to failure]	Fatigue damage ratio (mission/original), [%]
T1	69930		7559	
T1BS1	69930	100	7559	100
T1BS2	69930	100	7559	100
T1BS3	69930	100	7559	100
Average		***100***		***100***
T2	734646		53937	
T2BS1	734646	100	51285	105
T2BS2	734646	100	51285	105
T2BS3	734646	100	51285	105
Average		***100***		***105***
T3	96182		10854	
T3BS1	96182	100	11010	99
T3BS2	87161	110	10328	105
T3BS3	97229	99	11097	98
Average		***103***		***100***
T4	1035240		48610	
T4BS1	1035240	100	49665	98
T4BS2	1025504	101	46251	105
T4BS3	991473	104	48482	100
Average		***102***		***101***
T5	5833		680	
T5BS1	6506	90	862	79
T5BS2	6072	96	709	96
T5BS3	7214	81	908	75
Average		***89***		***83***
T6	793		209	
T6BS1	853	93	220	95
T6BS2	1277	62	367	57
T6BS3	853	93	220	95
Average		***83***		***82***

Based on the information in Table 7.7, T1 to T4 retained all of the original fatigue damage in the mission signals. Different orders of bump segments, and the joining of bump segments in the mission signal, sometimes brought the ratio above 100%. In order to prove this argument, it is suggested in future research that uniaxial fatigue tests should be performed using the mission signals with different bump segment sequences. This would permit the bump sequence effects to be experimentally observed and analysed.

T6, which is the signal with the greatest energy at low frequencies, produced the lowest fatigue damage ratio between the mission signal and the original signal. Since T6 has significant low frequency content in the signal, almost all of the sections contribute to the fatigue damage. Accordingly, more fatigue damage tends to occur at the low frequency of the PSD, as small amplitudes which are not damaging are normally located in high frequency area of the PSD (Austen and Gregory 1995; Morrow and Vold 1997). For signal T6, it was only possible to remove a 23.9-second section, which contained 18% of the original fatigue damage, when producing the mission signal. This result shows the difficulty WBE encounters when attempting to compress a signal characterised by low frequency content.

Figure 7.11 shows the ESD fatigue life comparison between the mission signals and the original signals using the smooth and the notched specimens. In this figure, all correlation points are located around the 1:1 line and within the range of ± a factor of 2. Figure 7.11 suggests a close correlation between the mission and original signals, leading to the suitability of the mission signals for accelerated fatigue tests.

From the analytical results of this section, it is shown that the majority of the predicted fatigue damage was preserved in the WBE mission signal. Therefore, used in combination, the WBE algorithm and the ESD model are able to produce mission signals which retain most of the fatigue damage potential of the original loading while maintaining, unvaried, the original cycle sequences.

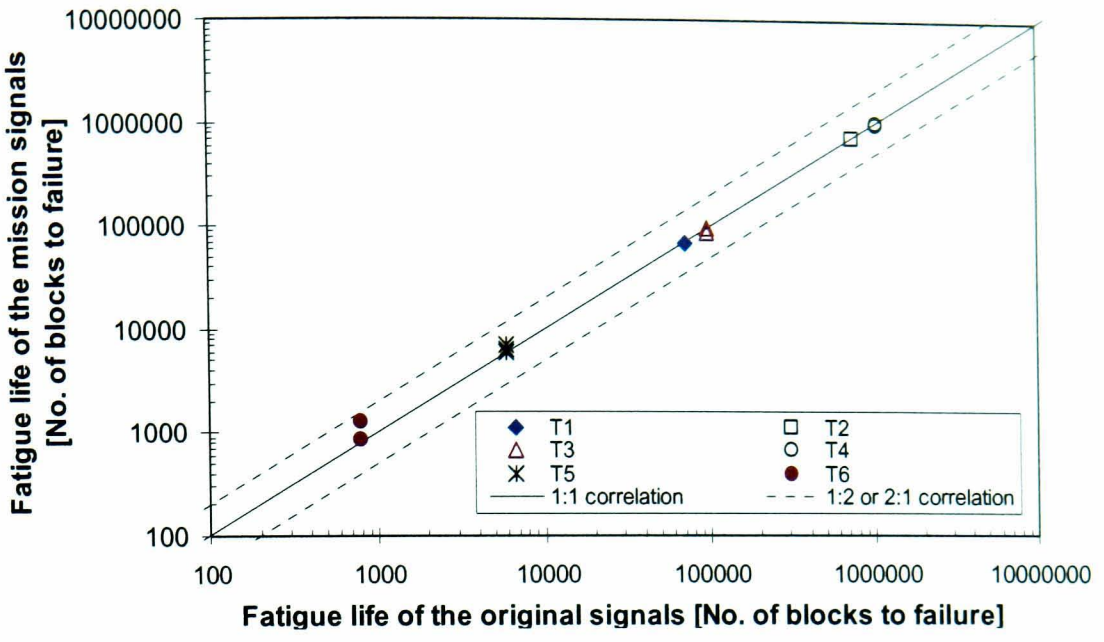

(a)

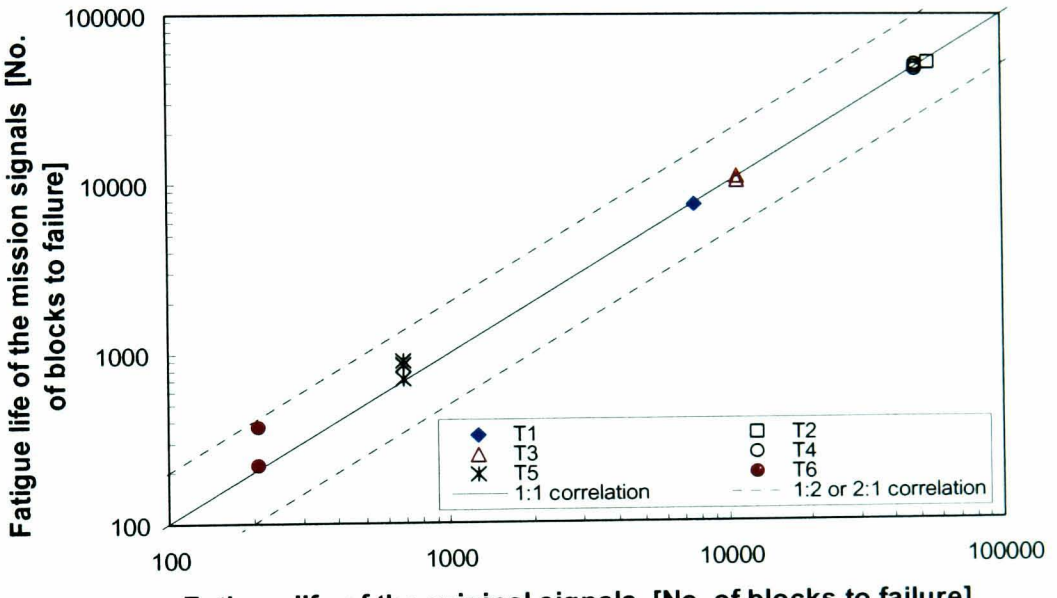

(b)

Figure 7.11: Fatigue life correlation between the mission signals and the original signals based on the ESD model of BS 080A42 steel using two values of the stress concentration factor K_t: (a) $K_t = 1.0$, (b) $K_t = 1.3$.

7.3 Fatigue Life Analysis Using Mission Signals

This section discusses the results obtained from the experiments involving the use of the WBE mission signals of T4. Using the mission signals for the laboratory fatigue tests, the preservation of the experimental fatigue damage could be observed. The results of Section 6.2 are further elaborated upon here to demonstrate the ability of the WBE algorithm to preserve fatigue damaging events.

7.3.1 Fatigue Life Prediction

In order to observe the relationship between the experimental results (refer to Section 6.2) and the analytical findings, the fatigue lives of the T4 original and mission signals were predicted using the ESD model for BS 080A42 steel. Since the experiments were performed using both smooth and notched specimens, predictions were also performed using two values of the stress concentration factor K_t , i.e. K_t = 1.0 and K_t = 1.3 to represent the smooth and notched specimens, respectively. Table 7.8 shows the predicted fatigue life and the predicted fatigue damage using the ESD model for the T4 original and mission signals, together with the experimental results. In the table, T4 is the original signal (Figure 4.20a), T4BS1 is the T4 mission signal with the original order sequence of bump segments (Figure 4.20b), T4BS2 is the T4 mission signal with the bump segment sequence of the highest expected fatigue damage to the lowest (Figure 4.20c) and T4BS3 is the T4 mission signal with the bump segment sequence of the lowest expected fatigue damage to the highest (Figure 4.20d).

7.3.2 Relationship Between Prediction and Experiment

Referring to the results in Table 7.8, the experimental fatigue lives of the T4 original and mission signals were compared with the predicted fatigue lives. The use of smooth specimens would most likely have been sufficient to experimentally observe the preservation of fatigue damage in the mission signals. However, the notched specimens were also used in order to observe the response of the ESD model when calculating the fatigue life using the stress concentration factor value greater than unity (K_t > 1.0). Therefore, the results obtained during the course of current research for the notched specimens or K_t > 1.0 can be compared to the outcomes obtained for the smooth specimens or K_t = 1.0. In all previous applications of the ESD model (DuQuesnay *et al.* 1993; Topper and Lam 1997; DuQuesnay 2002; Khalil *et al.* 2002; Khalil and Topper 2003; Choi 2004) smooth specimens were used for determining the experimental fatigue

life or the use of $K_t = 1.0$ in the fatigue life calculations. Therefore, the results presented in this are to be determined for stress concentration factor (K_t) greater than unity.

Table 7.8: The values of fatigue life and fatigue damage of the T4 original and mission signals using the ESD model.

Signals	Prediction		Experiment 1		Experiment 2	
	$K_t = 1.0$	$K_t = 1.3$	Smooth specimens	Notched specimens	Smooth specimens	Notched specimens
Fatigue Life [Number of blocks to failure]						
T4	200	43	289	45	454	36
T4BS1	329	75	409	60	261	36
T4BS2	295	68	367	153	285	28
T4BS3	304	71	291	111	340	8
Fatigue Damage [Damage per block]						
T4	5.00×10^{-3}	2.33×10^{-2}	3.46×10^{-3}	2.22×10^{-2}	2.20×10^{-3}	2.78×10^{-2}
T4BS1	3.04×10^{-3}	1.33×10^{-2}	2.44×10^{-3}	1.67×10^{-2}	3.83×10^{-3}	2.78×10^{-2}
T4BS2	3.39×10^{-3}	1.47×10^{-2}	2.72×10^{-3}	6.54×10^{-3}	3.51×10^{-3}	3.57×10^{-2}
T4BS3	3.29×10^{-3}	1.41×10^{-2}	3.44×10^{-3}	9.01×10^{-3}	2.94×10^{-3}	1.25×10^{-1}

Figure 7.12 shows the correlation between the fatigue life predicted using the ESD strain-life model and the experimental results. Each data point represents an experimental loading condition of Table 6.3 and Table 6.4, and the corresponding prediction results of Table 7.8. Referring to Figure 7.12a, the majority of fatigue lives were distributed around the 1:1 correlation line and within the range of ± a factor of 2. It shows a close correspondence was observed for the smooth specimens and $K_t = 1.0$, suggesting acceptable results were obtained between the experiment and prediction.

For fatigue life correlation of the notched specimens or $K_t = 1.3$, as shown in Figure 7.12b, three of the eight points are located outside the range of ± a factor of 2. The distribution of correlation points suggests some uncertainties may have occurred during the experiment, such as the room temperature or the machine condition. A more probable explanation is the manufacturing of the notched specimens and the surface finish of the notch area. Since the notch is a stress sensitive area, care must be taken

during the machining of the specimen and during the polishing process in order to avoid any occurrence of preload or residual stress around this location. It is possible that some of the test specimens used in the research described in this thesis suffered some amount of residual stress. Further investigations related to the fatigue life determination using notched specimens are suggested.

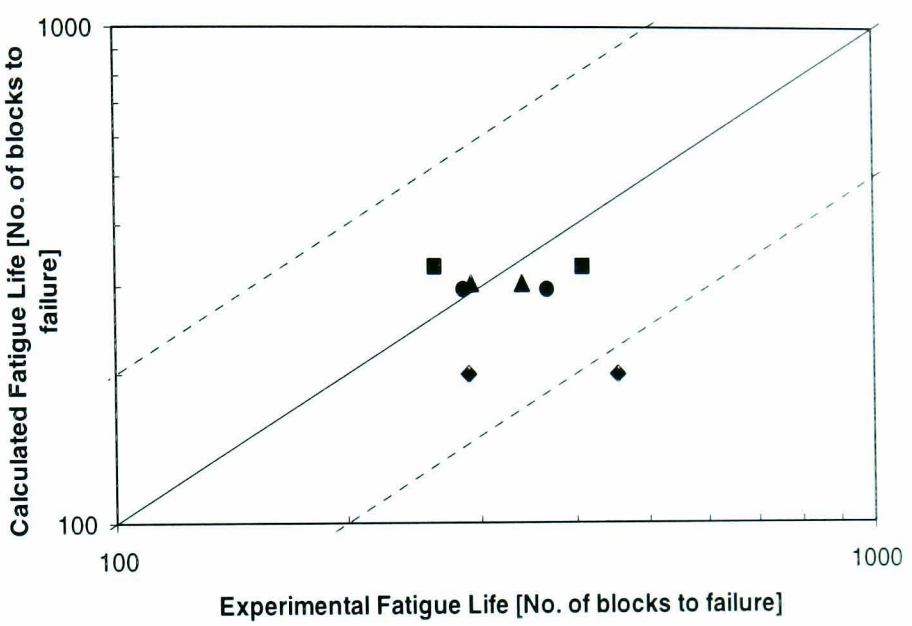

(a)

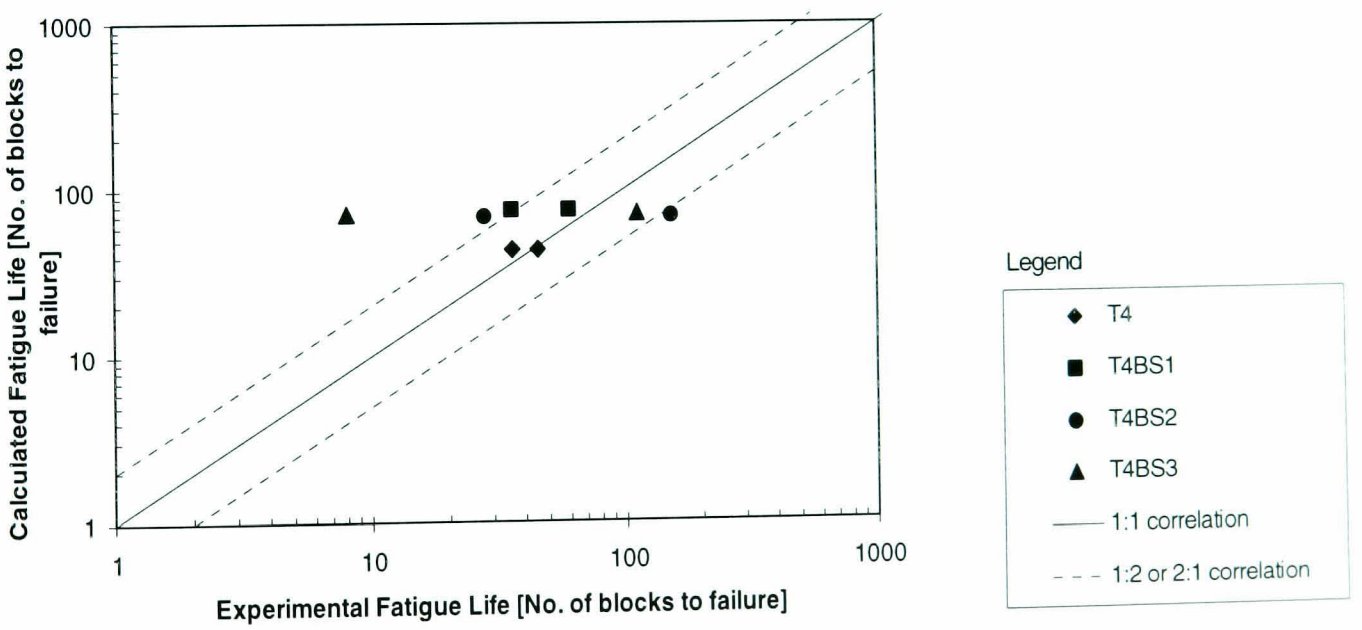

(b)

Figure 7.12: Fatigue life correlation between the ESD model prediction and the experimental test results. The data points represent the results of two experimental tests performed using the T4 signal and two tests performed using each of three WBE generated mission signals:

(a) The smooth specimens or $K_t = 1.0$,

(b) The notched specimens or $K_t = 1.3$.

Figure 7.13 presents a histogram of the fatigue life values obtained in the experiments and those obtained by prediction using the ESD model for BS 080A42 steel. In this figure, the difference between the fatigue life of the original signal and the mission signals with different bump segment sequences (refer to Section 7.3.8 for the notations of bump segment sequences and Section 5.3 for time history plots) can be observed for both the smooth (or K_t = 1.0) and the notched (or K_t = 1.3) specimens. In Figure 7.13, it was observed that majority of the original fatigue damage was retained in the mission signals and within the range of ± a factor of 2.

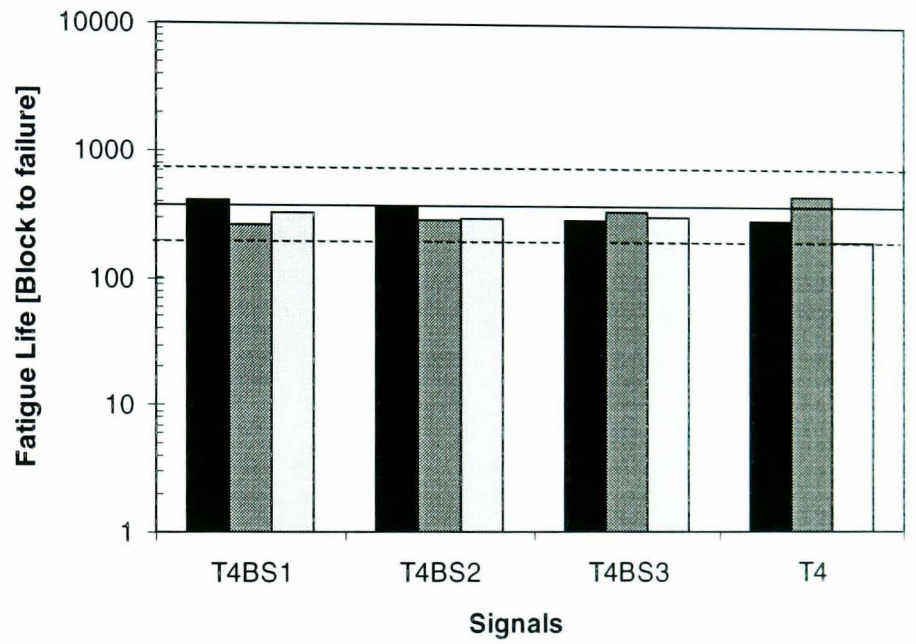

(a)

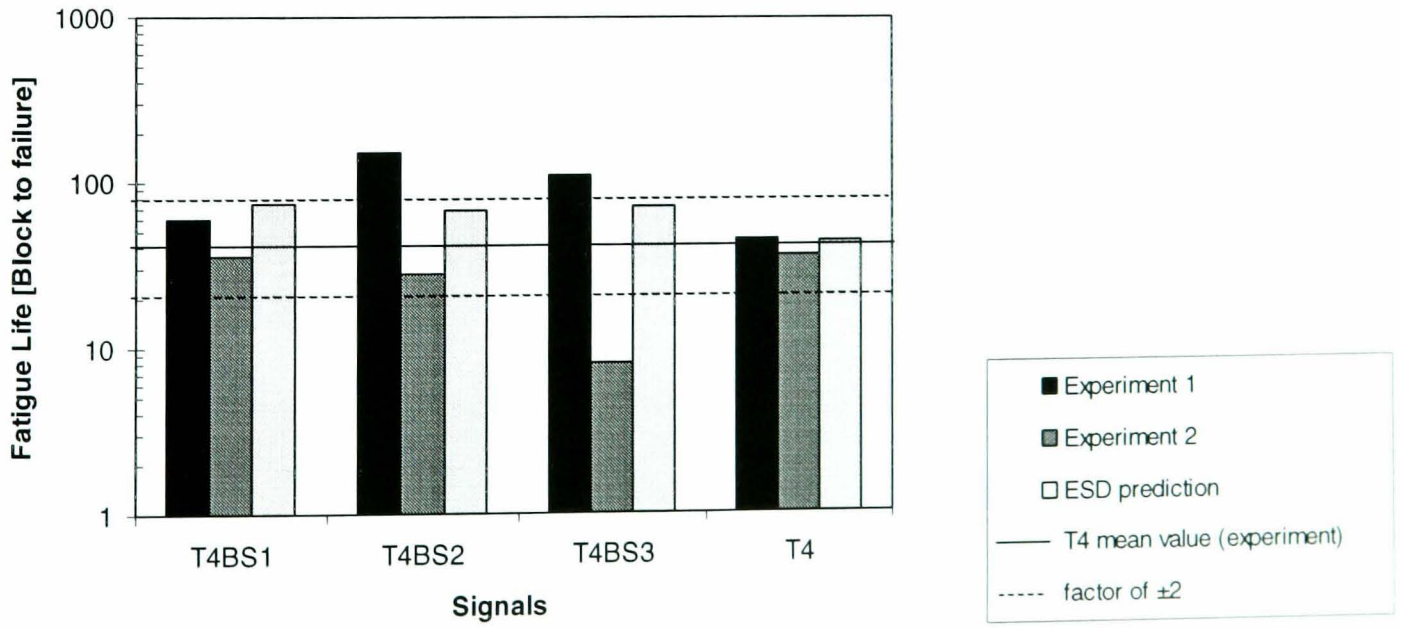

(b)

Figure 7.13: Experimental and prediction fatigue lives of the mission and original signals for: (a) The smooth specimens or K_t = 1.0, (b) The notched specimens or K_t = 1.3.

7.4 Observation of Bump Sequence Effects in the WBE Mission Signals

In this section, bump segment sequence effects are discussed in order to find which ordering of bump segments within a mission signal is better for accelerated fatigue testing. In Table 6.3 for smooth specimens and Table 6.4 for notched specimens, the experimental fatigue lives of the T4 mission signals were listed. In this experiment, two repeats of fatigue tests were performed for both specimen types. The purpose of repeating the fatigue tests was to observe a variation in the experimental fatigue lives as various factors can affect the accuracy of experimental results. The results were used to show the WBE capability in analysing the original fatigue damage preservation and bump segment sequence effects in the mission signals. Ideally, if multiple fatigue tests are run at similar input loading, there is always considerable statistical scatter in fatigue life (Dowling 1999) and therefore, the statistical analysis of fatigue lives can be performed. For the research of this thesis, however, there was not enough experimental data for performing the statistical analysis.

Using the fatigue life values for the smooth specimens or $K_t = 1.0$, as tabulated in Table 7.8, the relationship between the mission signals versus the original signal were shown in Figure 7.13a. In this figure, all the predicted and experimental fatigue lives were located within the range of $\pm$ a factor of 2. This range was calculated based on the mean value of the experimental fatigue lives using the T4 original signal. The results of Figure 7.13a showed that the fatigue lives of the smooth specimens were not sensitive by means of fatigue damage to the different bump segment sequences of the three mission signals.

For notched specimen or $K_t = 1.3$, the fatigue life relationship between all mission and the original signals are shown in Figure 7.13b, using the data in Table 7.8. In this figure, T4BS1 produced the calculated (using the ESD model) and the experimental fatigue lives within the range of $\pm$ a factor of 2. However, different results were obtained for the

T4BS2 and T4BS3 mission signals, i.e. three (out of four) experimental fatigue lives were outside the range of ± a factor of 2. The variation of fatigue lives produced by three mission signals using the notched specimens was due to the bump segment sequence effects in the mission signals. In addition, these fatigue lives variation indicated that the notched specimens were sensitive by means of fatigue damage to the variable amplitude loadings (Dowling 1999) and the specimens were also sensitive to the different load sequences in variable amplitude loadings.

As the concluding remarks, the work discussed in this section shows the importance of the bump segment sequences effects in the WBE mission signal, whilst the original load cycle sequences must be retained in the bump segment. In this section, it is suggested that the ability of the WBE algorithm to produce mission signals with three sets of bump segment sequences. All T4 mission signals showed a good relationship with the original signal, either for analytical or experimental analysis. In Figure 7.13, it is observed that the notched specimens were found to be more sensitive in fatigue damage compared to the smooth specimens. Therefore, the notched specimens produced a significant variation in fatigue lives at different bump segment sequence effects. From Figure 7.13b, it is suggested that T4BS1can be used to replace the original T4 signal for the purposes of the accelerated fatigue tests.

In order to improve the available results, further experimental studies related to this scope should be performed using various materials and signals. Therefore, more convincing fatigue life correlations can be obtained, so as to have further validation of the WBE algorithm.

7.5 The WBE Algorithm for Accelerated Fatigue Tests

The possible usefulness of the WBE algorithm for the purpose of defining accelerated fatigue tests is discussed in two parts, i.e. analytical and experimental studies. Background information can be found in Table 4.4, in Table 7.7 and in summary Table

7.9. Since the original order of bump segment sequences for T4 was experimentally proven to produce an accelerated fatigue test signal, this sequence (BS1) was chosen for this discussion.

Table 7.9: Summary of the accelerated fatigue test signal comparisons on BS 080A42 steel using the ESD model.

Signals		Signal time length, refer to Table 4.3		Fatigue damage ratio [%] between the mission and the original signals	
		Signal length [seconds]	Time ratio [%]	Smooth specimens	Notched specimens
T1	Original	40.0	31.3	100	100
	Mission	12.5			
T2	Original	40.0	76.7	100	105
	Mission	30.7			
T3	Original	225.0	83.4	103	100
	Mission	181.9			
T4	Original	46.0	40.9	102	101
	Mission	18.8			
T5	Original	46.0	53.9	89	83
	Mission	24.8			
T6	Original	61.0	76.1	83	82
	Mission	46.4			

Note: 1) Time ratio (%) = ($t_{mission}$ / $t_{original}$) x 100%;
2) Fatigue life ratio is the average ratio from three mission signals for the particular original signal. Refer to Table 7.8 for the details.

A first set of consideration about the usefulness of WBE for defining accelerated test signals can be drawn by bringing together as Table 7.9 contains the analytical results described in Chapter 4 (refer to Table 4.3). In Table 7.9, signals T1 to T4 preserved all the original fatigue damage in their mission signals. For T5 and T6, the majority of the original fatigue damage was retained of 83-89% for T5 and 82-83% for T6. Figure 7.11 shows that the fatigue life of all mission signals were within an acceptable margin of the

original signals. Preservation of the majority of fatigue damage in the mission signal suggests the suitability of WBE algorithm to produce a shortened signal for accelerated fatigue tests. In terms of the relationship between the time ratio and the fatigue damage ratio, T4 produced the best results compared to other signals, using ±10% r.m.s. and kurtosis differences.

The usefulness of the WBE algorithm for defining accelerated test signals can also be seen in the experimental test results obtained for the T4 signal, which are gathered here as in Table 7.10. From this table it can be seen that the uniaxial fatigue tests were accelerated by 23.4-57.6% for the smooth specimens and at least at 9.1% for the notched specimens. According to the analysis in Section 7.4, such time ratios were obtained with the preservation of the majority of the original fatigue damage in the mission signals. The findings of this section concluded that WBE is able to produce a mission signal with the preservation of the individual cycle sequences within the bump and the bump segment sequences in the mission signal.

Table 7.10: Summary of the accelerated fatigue test signals comparisons based on the experimental tests using BS 080A42 steel specimens.

Signal	No. of PV Points in Signal	Experimental Fatigue Life [blocks to failure]		Specimen Breaking Time* [hours]		Specimen Breaking Time Ratio** [%]	
		Exp. 1	Exp. 2	Exp. 1	Exp. 2	Exp. 1	Exp. 2
Smooth specimens							
T4	981	289	454	78.8	123.7		
T4BS1	399	409	261	45.3	28.9	57.6	23.4
T4BS2	403	367	285	41.1	31.9	52.2	25.8
T4BS3	402	291	340	32.5	38.0	41.3	30.7
Notched specimens							
T4	981	45	36	12.3	9.8		
T4BS1	399	60	36	6.7	4.0	54.2	40.7
T4BS2	403	153	28	17.1	3.1	139.7	32.0
T4BS3	402	111	8	12.4	0.9	101.1	9.1

Exp. 1 = Experiment 1, Exp. 2 = Experiment 2

* An assumption of 1 Hz cyclic frequency was being used during the uniaxial fatigue test in order to calculate a specimen breaking time.

** Specimen breaking time ratio = {(time of the mission signal)/(time of the original signal)} x 100%.

7.6 WBE Applications Using Bump Segments: Future Research

The analysis using the WBE mission signals for accelerated fatigue tests have been analytically and experimentally performed in Section 7.5. Using this method in practice, several fatigue design factors can be minimised such as specimen costs, labour costs, testing time consumption and others. Thus, the production of automotive components associated with fatigue design and testing can be expedited in practice.

Future work which can be performed in the WBE operation is data segmentation. The measured fatigue signal on vehicle components may generate multi-VA loadings, such as an equivalent pattern in Figure 2.18. Currently, the WBE algorithm was not able to edit this type of data because of its suitability to summarise signals with mildly nonstationary characteristics and minimal effects of low frequency content. With the type of signal as in Figure 2.18, it is useful to divide the signal into segments each having mildly nonstationary characteristics or equivalent patterns as the test signals in Table 4.1 and Table 4.2 (exception for T2 and T6). The individual segments will then be extracted using WBE to produce the equivalent mission signals. Finally, these mission signals can be combined to produce the complete final mission signal which represents the original signal. Possible criteria to be considered in segmenting multi-VA loadings are running fatigue damage windows, running global signal statistics windows, the wavelet analysis or cumulative sum (CUSUM) procedures. The theoretical background of time series segmentation, such as the application of CUSUM, can be found in a book by Basseville and Nikiforov (1993).

Another further study related to the WBE algorithm is the analysis of bump segments. The analysis can be done by comparing bump segments extracted from proving test tracks to those extracted from public roads. A public road may contain potholes, pavé, kerb-strike, irregular or smooth surfaces. Thus, a VA loading measured on a public road may have high amplitudes exhibiting these types of bump segment pattern. With the

numerical analysis (either in the form of global signal statistics, fatigue damage values or other analysis), bump segments of the public road can be compared to those similar to the proving ground bump segments. These segments can also be clustered in order to produce a group of bump segments with equivalent fatigue damage values or global signal statistics. This method is known as the classification of bump segments.

For further work of using signals measured on public roads, analysis of the bump segment pattern similarity in the record length is proposed. Therefore, the analysis of similar bump segments repetition, which has an equivalent fatigue damage or signal statistics, can be performed in a block of VA fatigue time history.

A list of future works related to the WBE redevelopment and validation processes, which are proposed by the author, are presented in Section 8.2.

CHAPTER 8

8. Conclusions and Recommendations for Future Research

8.1 Summary of Research Findings

The activities described in Chapters 3 to 7 were performed for the purpose of answering questions relating to the development of a new wavelet-based fatigue data editing technique. This technique is able to solve the problem of retaining sequence information when summarising variable amplitude (VA) loadings. This algorithm, called Wavelet Bump Extraction (WBE), was developed to identify and extract fatigue damaging events or bump segments from an original signal. A shortened mission signal with the load cycle sequence preserved is produced from the combination of the main fatigue damaging events. The mission signal should have equivalent global signal statistics and fatigue damage to the original signal. Since WBE is defined here for the first time, experimental validation of the algorithm is important. Taken as a whole the findings provide a first response to the questions posed in Chapter 1. Therefore it is useful to summarise the findings in light of the originally posed questions.

- *What is a suitable fatigue damage model to calculate the fatigue life of a component under VA loadings?*

Most of the fatigue life calculations performed by means of the commercial software packages involve the Palmgren-Miner rule associated with the Coffin-Manson, Morrow or Smith-Watson-Topper (SWT) models. This approach is not suitable for VA loadings because cycle sequence effects are not accounted for (DuQuesnay *et al.* 1993; Fatemi and Yang 1998). The Effective Strain Damage (ESD) model was identified as the suitable model for VA loadings. It was developed by DuQuesnay *et al.* (1993) based on crack growth and crack closures, with consideration of cycle sequence effects.

Monotonic tensile and uniaxial constant amplitude (CA) loading fatigue tests using BS 080A42 steel were performed to obtain the necessary data to define the ESD model. The fatigue lives of the CA loadings were compared to the prediction achieved using the ESD and Coffin-Manson models, see Table 6.5. Better predictions using the ESD model showed the suitability of this model to calculate fatigue life.

For VA loadings (Table 7.2), the ESD model fatigue lives versus the experimental fatigue lives produced the lowest difference at 17%, compared to other strain-life models. Analysis of the ESD model for BS 080A42 steel using the WBE extracted VA loadings showed that the ESD fatigue lives had a close correspondence to the experimental fatigue lives, see Figure 7.1. Overall results suggest the suitability of the ESD model for predicting the fatigue life associated with VA loadings.

- *What is the most appropriate method to edit VA fatigue loadings for the purpose of accelerated fatigue tests?*

According to research by El-Ratal *et al.* (2002), time domain fatigue data editing was identified as a suitable technique for accelerated fatigue tests. Using this approach, the phase and amplitude relationships of the original signal are retained in the shortened signal. One of the time domain data editing methods is the time correlated fatigue damage (TCFD) method. In this thesis, the comparison of the WBE algorithm with the

TCFD method was performed. Using WBE, the original phase and amplitude relationships were also retained in the mission signal. From the findings, the WBE mission signal has the global signal statistics and frequency content (specifically low frequency) of the original signal. Due to the improved signal statistics in WBE with respect to the TCFD method, the WBE algorithm was found to be a better approach to edit VA loadings for accelerated fatigue tests.

- *Can a new algorithm be developed to improve the accuracy of fatigue data editing with respect to existing techniques?*

The algorithm called Wavelet Bump Extraction (WBE) has been developed here for the first time. It makes intelligent use of the orthogonal wavelet transform, of a wavelet grouping procedure, and of automatic trigger level calculation for extracting transient (bump or fatigue damaging) events. The comparison of the fatigue data editing technique between the WBE algorithm and TCFD method was performed. The results showed WBE to be the better approach for editing VA loadings for the purpose of accelerated fatigue tests. Using WBE, six mission signals at the length of 31-84% were produced from their respective original signals, as presented in Table 4.3. At these lengths, a minimum of 82% of the original fatigue damage was retained in the respective mission signal, as presented in Table 7.8.

- *What are the main factors that influence the identification of fatigue damaging events in the new algorithm?*

In the WBE analysis, several factors were identified which influenced the extraction of fatigue damaging events; for example the choice of wavelet group, the initial maximum values in the wavelet group and differences in global signal statistics (r.m.s. and kurtosis). Among these, the differences in global signal statistics were recognised as the major factor. The use of ±70% r.m.s. and kurtosis differences between the mission and original signals showed that the majority of the original fatigue damage can be

preserved in the mission signals. Lower values of statistical difference between the mission signal and the original signal often provided insufficient damage retention. The trigger level criteria is therefore the main factor influencing the identification of fatigue damaging events in VA loadings by means of the WBE algorithm. This occurrence can clearly be observed in the signals of T3 and T4. Referring to Table 7.4, it shows the retention of original fatigue damage at various global statistics differences. At higher r.m.s. and kurtosis differences, i.e. at ±70%, the minimum of 92% of the original fatigue damage was preserved for both T3 and T4.

- *How important are the sequence effects of fatigue cycles and fatigue damaging events to the fatigue life prediction?*

The importance of fatigue cycle sequence effects in VA fatigue loading is evident from the research results which can be observed in Table 7.2 and Table 7.3. Using the WBE extracted bump segments, the predicted fatigue lives using four strain-life models were compared with those obtained in the experiments by Choi (2004). The lowest average difference between prediction and experiments was found when predicted using the ESD model, i.e. at 17% for the T4 bump segments and 2% for accumulated total fatigue damage of all T4 bump segments. These results were in concordance with the literature background in Chapter 2, where the ESD model was identified as a strain-life model which accounts for cycle sequence effects. An analysis was performed of the experimental fatigue lives obtained from different bump segment sequences defined using the bump segments extracted from the T4 mission signals, as presented in Table 7.11. The original bump segment sequences (T4BS1) produced a mean fatigue life closer to the original signal, i.e. 9.7% for the smooth specimens and 15.0% for notched specimens than a low-to-high or a high-to-low ordering of the bump segments. It shows that the original bump segment sequences (BS1) is a suitable mission signal for performing accelerated fatigue tests in place of the original signal. Using the WBE algorithm to compress the long record of VA fatigue loadings, finally, the bump segments were extracted with the preservation of load cycle sequences. With the

retention of the original bump segment sequences in the mission signal, the fatigue lives in accelerated fatigue tests can be appropriately determined.

- *Are the mission signals produced by the new fatigue data editing algorithm suitable for accelerated fatigue testing of vehicle components?*

This thesis presents numerous analytical analysis, it can be seen that signals were shortened by WBE while preserving most of the fatigue damage. In Table 7.8, the mission signals preserved the minimum of 82% of the original fatigue damage. It showed the usefulness of WBE for performing accelerated fatigue tests. Experimentally, accelerated laboratory fatigue tests were performed using the T4 signal and BS 080A42 steel specimens. The results in Figure 7.13 showed the mission signal fatigue lives for smooth and notched specimens were within the acceptable range (within a range of ± a factor of 2) of the original signals. Table 7.10 presents experimental fatigue test data obtained from the laboratory accelerated fatigue tests. From this table, it is suggested that signal T4BS3 for the smooth specimens and signal T4BS1 for the notched specimens provided, on average, the smallest breaking time ratio of a specimen. However, more uniaxial VA fatigue testing is required in order to provide a better understanding of which bump ordering provides the closest match to the original road loading.

Final concluding remark: Using the WBE algorithm to shorten the VA fatigue loadings, and using the ESD model to calculate the fatigue damage, provided fatigue life predictions which were close to the experimental results. These findings show the importance of retaining load cycle sequences within VA fatigue loadings in order to produce accurate fatigue life predictions. By using the WBE algorithm and the ESD model, the majority of the original fatigue damage is preserved in the mission signal, whilst the time-length of the VA fatigue signal is substantially shortened.

8.2 Future Research of the WBE Algorithm

The wavelet-based fatigue data editing or the WBE algorithm is a new approach that has been developed for applications in automotive research. Considering the limitations and problems of the WBE algorithm, further research works are suggested in order to improve the performance of this algorithm:

1. *Optimisation of trigger level values to identify bump events*: In this research the global signal statistics parameters were used to control the trigger level values determination. Higher differences in the global signal statistics between the original and the mission signals retained the majority of the fatigue damage. Since the original signal fatigue damage is the main element to be preserved in the WBE mission signal, further research is required to produce an optimum trigger level for each wavelet group based on fatigue damage parameters. Such a procedure may produce more accurate results when working with new and unfamiliar data.

2. *Choice of the Wavelet Function for the WBE algorithm:* Currently WBE uses the 12^{th} order of Daubechies wavelet function for decomposing the VA loadings into its frequency bands. According to research by Staszewski (1998b), nonstationary and stationary signals are best evaluated using lower, and higher, orders of Daubechies wavelet, respectively. The choice of 12^{th} order Daubechies wavelet was based on the successful studies in compressing automobile road load data performed by Giacomin *et al.* (1999; 2000; 2001), Grainger (2001), Steinwolf *et al.* (2002) and Abdullah *et al.* (2004). According to these studies, the wavelet choice seems to be a parameter affecting bump identification. Further studies to determine the most suitable wavelet function and wavelet order should be performed.

3. *Development of a signal segmentation algorithm for VA loadings*: The measured fatigue signal on road vehicle components may consist of multiple time segments, each of which may be characterised by different signal statistics. Currently, the WBE algorithm not particularly efficient at editing this type of data because the approach used in the WBE development was to compress mildly nonstationary

signals. It would be appear intuitively useful to use a preprocessing stage to subdivide a complete road loading into individual segments, such that each segment contains mildly nonstationary statistics as required by WBE. Possible criteria to be considered in segmenting long loading histories are running fatigue damage windows, running global signal statistics windows, wavelet analysis, cumulative sum (CUSUM) procedures, etc. The theoretical background of many useful time series segmentation procedures can be found in the text book by Basseville and Nikiforov (1993).

4. *Development of an algorithm for bump clustering and classification*: The WBE extracted bumps each have their own characteristics, both statistically and in terms of fatigue damage. Thus, the author proposes to develop a pattern recognition algorithm for the bumps extracted by WBE from the signals measured on various road surfaces (public roads and proving grounds). Bumps obtained from public roads can then be easily compared to bumps obtained from proving ground surfaces by means of global signal statistics or fatigue damage. The results might be used as a basis for customer correlation analysis.

5. *Comparison with other signal editing techniques*: In this research, the WBE algorithm was compared with the TCFD method. It is suggested to compare the WBE algorithm with other fatigue data editing methods (in the domain of frequency, peak-valley or cycle-histogram). Such comparison would permit a complete evaluation of the effectiveness of the WBE algorithm.

6. *More experimental fatigue tests using the T4 signals*: In this research the author performed two repeats of the accelerated laboratory fatigue tests. In the author's opinion, promising results were observed from the two similar experiments for both the smooth and the notched specimens. In terms of statistical analysis, however, two samples cannot represent a population. In order to have a good representation of the results and to have an accurate experimental validation of the WBE algorithm, more experiments are needed using the same VA loadings (T4 and the T4 WBE mission signals), material, specimen geometry and apparatus.

7. *More analysis (analytically and experimentally) using other signals*: The fatigue tests discussed in the thesis were performed using the T4 signal, which was measured on the lower suspension arm of a road vehicle travelling over a pavé track surface. In many cases road load signals vary widely in length of time, scale, sensor location and the road driven. For example, in the case of signals measured from the component connected to an engine block, the signal will contain the fatigue damage pattern related to the rotation of the engine. This pattern may be different to the pattern produced from other components (lower suspension arm for the research by the author). In order to have general findings, more applications using various signals measured from various road vehicle components are needed for both analytical and experimental studies.

REFERENCES

1. Abdullah, S., Giacomin, J. A. and Yates, J. R., 2004, A mission synthesis algorithm for fatigue damage analysis, *Proc. of the Instn. of Mech. Engrs, Part D, Journal of Automobile Engineering*, Vol. 218, No. D3, pp 243-258.

2. Anthes, R. J., 1997, Modified rainflow counting keeping the load sequence, *Int. J. Fatigue*, Vol. 19, No. 7, pp 529-535.

3. ASTM E1049-85, 1997, Standard practice for cycle counting in fatigue analysis, *American Society for Testing and Materials.*

4. ASTM E466-96, 2000, Standard practice for conducting force controlled constant amplitude axial fatigue tests of metallic materials, *American Society for Testing and Materials.*

5. ASTM E468-90, 2000, Standard practice for presentation of constant amplitude Fatigue test results for metallic materials, *American Society for Testing and Materials.*

6. ASTM E739-91, 1998, Standard practice for statistical analysis of linear and linearised stress-life (S-N) and strain-life (e-N) fatigue data, *American Society for Testing and Materials.*

7. Austen, I. and Gregory, R., 1995, Component test during duration prediction and acceleration by fatigue analysis and fatigue editing, *VTT Symposium*, Vol. 3, Part 157, pp 169-187.

8. Banvillet, A., Łagoda, T., Macha, E., Niesłony, A., Palin-Luc, T. and Vittori, J-F., 2004, Fatigue life under non-Gaussian random loading from various models, *Int. J. Fatigue*, Vol. 26, pp 349-363.

9. Basseville, M. and Nikiforov, I. G., 1993, *Detection of Abruct Changes: Theory and Application*, Prentice-Hall, Ney Jersey.

10. Bendat, J. S. and Piersol, A. G., 1986, *Random Data: Analysis and Measurement Procedures*, 2nd Edition, Wiley-Interscience, New York.

11. Bignonnet, A., 1999, Automotive industry and fatigue design, *Fatigue '99, Proceedings of the Seventh International Fatigue Congress*, edited by Wu, X. R., and Wang, Z. G., Beijing, P. R. China, pp 2627-2634.

12. Bilir, O. G., 1991, Experimental investigation of fatigue damage accumulation in 1100 aluminium, *Int. J. Fatigue*, Vol. 13, No. 1, pp 3-6.

13. Bishop, N. and Caserio, A., 1998, Vibration fatigue analysis in the finite element environment, paper presented in the *Americas User Conference,* California, USA, 5-9 Oct.

14. Bishop, N. W. M. and Sherratt, F., 1989, Fatigue life prediction from power spectral density data. Part 1: traditional approach, *Environmental Engineering*, Vol. 2, pp 11-14.

15. Bishop, N. W. M. and Sherratt, F., 1990, A theoretical solution for the estimation of 'rainflow' ranges from power spectral density data, *Fatigue Fract. Engng. Mater. Struct,* Vol. 13, No. 4, pp 311-326.

16. Bishop, N. W. M. and Sherratt, F., 2000, *Finite Element Based Fatigue Calculations*, NAFEMS, The International Association for the Engineering Analysis Community, Farnham.

17. Bishop, N. W. M., Lack, L. W., Li, T. and Kerr, S. C., 1995, Analytical fatigue life assessment of vibration induced fatigue damage, *Proceedings of MSC 1995 World Users' Conference*, Paper No. 18, California, USA, 8-12th May.

18. Bolotin, V. V., 1999, *Mechanics of Fatigue*, Mechanical Engineering Series, CRC Press, Boca Raton USA.

19. Bonnen, J. J. F. and Topper, T. H., 1999, The effect of bending overloads on torsional fatigue in normalised 1045 steel, *Int. J. Fatigue*, Vol. 21, pp 23-33.

20. Boulahbal, D., Golnaraghi, M. F. and Ismail, F., 1999, Amplitude and phase wavelet maps for the detection of cracks in geared systems, *Mechanical Systems and Signal Processing*, Vol. 13, No. 3, pp 423-436.

21. BS 10002-1, 2001, Metallic material-tensile testing - method of test at ambient temperature, *British Standard*.

22. BS 7270, 1990, Constant amplitude strain controlled fatigue testing, *British Standard*.

23. BS 970-1, 1996, General inspection and testing procedures and specific requirements for carbon, carbon manganese, alloy and stainless steels, Part 1, *British Standard*.

24. Burrus, C. S., Gopinath, R. A. and Guo, H., 1998, *Introduction to Wavelets and Wavelet Transforms: A Primer*, Prentice Hall, New Jersey.

25. Changqing, Z., Yucheng, J. and Guangli Y., 1996, Effect of a single peak overload on physically short fatigue crack retardation in an axle-steel, *Fatigue Fract. Engng. Mater. Struct,* Vol. 19, No. 2-3, pp 201-206.

26. Choi J. C., 2004, *Fatigue Evaluation for the Wavelet Bump Extraction (WBE) Algorithm*, MPhil Thesis, The University of Sheffield, United Kingdom.

27. Chu, C-C., 1998, Multiaxial fatigue life prediction method in the ground vehicle industry, *Int. J. Fatigue*, Vol. 19, Supp. no.1, pp S325-S330.

28. Chui, C.K., *Introduction to Wavelets*, Academic Press, New York, 1991.

29. Ciavarella, M. and Meneghetti, G., 2004, On fatigue limit in the presence of notches: classical and recent unified formulations, *Int. J. Fatigue*, Vol. 26, pp 289-298.

30. Clormann, U. H. and Seeger, T., 1986, Rainflow-HCM, Ein Zählverfahren für Betriebsfestigkeitsnachweise auf werkstoffmechanischer Grundlage, *Stahlbau*, Vol. 55, pp 55-71.

31. Coffin, L. F., 1954, A study of the effect of cyclic thermal stresses on a ductile metals, *Transactions of ASME*, Vol. 79, pp 931-950.

32. Collins, J. A., 1981, *Failure of Materials in Mechanical Design*, Wiley, New York.

33. Conle, A. and Landgraf, R., 1983, A fatigue analysis program for ground vehicle components, *Proceedings of International Conference on Digital Techniques in Fatigue*, London, pp 1-28.

34. Conle, A. and Topper, T. H., 1979, Evaluation of small cycle omission criteria for shortening of fatigue service histories, *Int. J. Fatigue,* Vol. 1, pp 23-28.

35. Conle, A. and Topper, T. H., 1980, Overstrain effects during variable amplitude service history testing, *Int. J. Fatigue*, Vol. 2, No. 3, pp 130-136.

36. Conle, A., Grenier, G., Johnson, H., Kemp, S., Kopp, G. and Morton, M., 1997, Service history determination, *SAE Fatigue Design Handbook AE-22*, Society Automotive Engineers Inc, Warrendale, pp 115-144.

37. Conle, F. A. and Chu, C. -C., 1997, Fatigue analysis and the local stress-strain approach in complex vehicular structures, *Int. J. Fatigue*, 1997, Vol. 19, Supp. No. 1, pp S317-S323.

38. Conle, F. A., 1974, *A Computer Simulation Assisted Statistical Approach to the Problem of Random Fatigue,* M.Sc. Thesis, University of Waterloo, Canada.

39. Cooley, J. W. and Tukey, J. W., 1965, An algorithm for the machine calculation of complex Fourier series, *Math. Comput.,* Vol. 19, pp 297–301.

40. Dabayeh, A. A. and Topper, T. H., 1995, Changes in crack-opening stress after underloads and overloads in 2024-T351 aluminium alloy, *Int. J. Fatigue*, Vol. 17, No. 4, pp 261-269.

41. Dabell, B., 1997, General fatigue design considerations, *SAE Fatigue Design Handbook* (AE-22), Society of Automotive Engineers, Warrendale.

42. Daubechies, I., 1992, *Ten Lectures on Wavelets*, SIAM, Philadelphia.

43. Dowling, N. E., 1972, Fatigue failure prediction for complicated stress-strain histories, *Journal of Materials*, JMLSA, Vol. 7, No. 1, pp 71-87.

44. Dowling, N. E., 1988, Estimation and correlation of fatigue lives for random loading, *Int. J. Fatigue*, Vol. 10, pp 179-185.

45. Dowling, N. E., 1999, *Mechanical Behaviour of Materials: Engineering Methods for Deformation, Fracture and Fatigue*, Second Edition, Prentice Hall, New Jersey.

46. Downing, S. D. and Socie, D. F., 1982, Simple rainflow counting algorithms, *Int. J. Fatigue*, Vol. 4, pp 31-40.

47. Downing, S., Galiart, D. and Berenyi, T., 1977, A Neuber's rule fatigue analysis procedure for use with a mobile computer, in *Fatigue Under Complex Loading: Analyses and Experiment,* edited by Wetzel, R.M., Society of Automotive Engineers (SAE), pp 189-201.

48. DuQuesnay, D. L., 2002, Applications of overload data to fatigue analysis and testing, *Application of Automation Technology in Fatigue and Fracture Testing and Analysis: Fourth Volume*, ASTM STP 1411, edited by Braun, A.A., McKeighan, P.C., Nicolson, A. M. & Lohr, R. D., ASTM, West Conshohocken USA, pp 165-180.

49. DuQuesnay, D. L., MacDougall, C., Dabayeh, A. A. and Topper, T. H., Notch fatigue behaviour as influenced by periodic overloads, *Int. J. Fatigue*, Vol. 17, No. 2, pp 91-99.

50. DuQuesnay, D. L., Pompetzki, M. A. and Topper, T. H., 1993, Fatigue life prediction for variable amplitude strain histories, *SAE Transactions (SAE930400)*, Society of Automotive Engineers (SAE), Vol. 102, No. 5, pp 455-465.

51. DuQuesnay, D. L., Topper, T. H., Pompetzki, M. A. and Jurcevic, R., 1992a, The effective stress range as a fatigue damage parameter, in *The Rainflow Method*, edited by Murukami, Y., Butterworth Heinemann, London, pp 132-141.

52. DuQuesnay, D. L., Topper, T. H., Yu, M. T. and Pompetzki, M. A., 1992b, The effective strain range as a mean stress parameter, *Int. J. Fatigue*, Vol. 14, No. 1, pp 45-50.

53. El-Ratal, W., Bennebach, M., Lin, X. and Plaskitt, R., 2002, Fatigue life modelling and accelerated test for components under variable amplitude loads, in *Symposium on Fatigue Testing and Analysis Under Variable Amplitude Loading Conditions*, Tenth International Spring Meeting of SF2M, Tours, France, 29-31st May.

54. Ermer, D. S. and Notohardjono, D., 1984, Fatigue failure identification by time series model, *Engineering Fracture Mechanics,* Vol. 20, No. 5/6, pp 705-718.

55. Fatemi, A. and Yang, L., 1998, Cumulative fatigue damage and life prediction theories: a survey of the state of the art for homogeneous materials, *Int. J. Fatigue*, Vol. 20, No. 1, pp 9-34.

56. Fowler, K. R. and Watanabe, R. T., 1989, Development of jet transport airframe fatigue test spectra, in *Development of Fatigue Loading Spectra*, edited by Potter, J. M. and Watanabe, R. T., American Society for Testing and Materials (ASTM), Philadelphia, USA.

57. Frost, N. E., Marsh, K. J. and Pook, L. P., 1974, *Metal Fatigue*, Clarendon Press, Oxford.

58. Fuchs, H. O. and Stephens, R. I., 1980, *Metal Fatigue in Engineering*, John Wiley and Sons, New York.

59. Fuchs, H. O., Nelson, D. V., Burke, M. A. and Toomay, T. L., 1977, Shortcuts in cumulative damage analysis, in *Fatigue Under Complex Loading: Analyses and Experiment,* edited by Wetzel, R.M., Society of Automotive Engineers (SAE), pp. 145-162.

60. Giacomin, J., Steinwolf, A. and Staszewski, W. J., 1999, A vibration mission synthesis algorithm for mildly nonstationary road data, *ATA 6th Int. Conf. on the*

New Role of Experimentation in the Modern Automotive Product Development Process, Florence, Italy, 17-19 November.

61. Giacomin, J., Steinwolf, A. and Staszewski, W. J., 2000, An algorithm for Mildly Nonstationary Mission Synthesis (MNMS), *Engineering Integrity*, Vol. 7, January, pp 44-56.

62. Giacomin, J., Steinwolf, A. and Staszewski, W. J., 2001, Application of Mildly Nonstationary Mission Synthesis (MNMS) to Automotive Road Data, *ATA 7th Int. Conf. on the New Role of Experimentation in the Modern Automotive Product Development Process*, Florence, Italy, 23-25 May.

63. Glinka, G. and Kam, J. C. P., 1987, Rainflow counting algorithm for very long stress histories, *Int. J. Fatigue*, Vol. 3, pp 223-228.

64. Goswani, T., 1997, Low cycle fatigue life prediction – a new model, *Int. J. Fatigue,* Vol. 19, No. 2, pp 109-115.

65. Goupillaud, P., Grossman, A. and Morlet, J., 1984, Cycle-octave and related transform in seismic signal analysis, *Geoexploration*, Vol. 23, pp 85-102.

66. Grainger, J. J., 2001, *Application of Mildly Nonstationary Mission Synthesis (MNMS) to Maserati Wheel Hub Road Data*, M.Eng Dissertation, The University of Sheffield, United Kingdom.

67. Graps, A., 1995, An introduction to wavelets, *IEEE Computational Science and Engineering,* Vol. Summer, pp 50-61.

68. Grossmann, A. and Morlet, J., 1984, Decomposition of Hardy functions into square integrable wavelets of constant shape, *SIAM J. Math.* Vol. 15, pp 723-736.

69. Gunger, J. E. and Stephens, R. I., 1997, Variable amplitude history editing and accelerated testing of SAE 1045 steel, SAE950704 in *Recent Developments in Fatigue Technology*, edited by Chernenkoff, R.A. and Bonnen, J.J., Society of Automotive Engineers (SAE), USA.

70. Halfpenny, A. and Bishop, N. W. M., 1997, *Vibration Fatigue*, nCode International Ltd., Sheffield UK.

71. Halfpenny, A., 1999, A frequency domain approach for fatigue life estimation from finite element analysis, paper presented at *International Conference on Damage Assessment of Structures (DAMAS 99)*, Dublin, Ireland.

72. Harvey, A.C., 1981, Time Series Model, Philip Allan Publishers Limited, Oxford.

73. Hawkyard, M., Powell, B. E., Hussey, I. and Grabowski, L., 1996, Fatigue crack growth under the conjoint action of major and minor stress cycles, *Fatigue Fract. Engng. Mater. Struct,* Vol. 19, No. 2-3, pp 217-227.

74. Heuler, P. and Seeger, T., 1986, A criterion for omission of variable amplitude loading histories, *Int. J. Fatigue,* Vol. 8, pp 225-230.

75. Hinton, P. R., 1995, *Statistics Explained: A Guide for Social Science Students*, Routledge, London.

76. Hong, N., 1991, A modified rainflow counting method, *Int. J. Fatigue*, Vol. 13, pp 465-469.

77. Hu, J.M., 1995, Life prediction and damage acceleration based n the power spectral density of random vibration, *Journal of the IES*, Vol. 38, No. 1, pp 34-40.

78. Hubbard, B. B., 1996, *The World According to Wavelets*, A K Peters, Massachusetts.

79. Jurcevic, R., DuQuesnay, D. L., Topper, T. H. and Pompetzki, M. A., 1990, Fatigue damage accumulation in 2024-T351 aluminum subjected to periodic overloads, *Int. J. Fatigue*, Vol. 12, No. 4, pp 259-266.

80. Juvinall, R. C. and Marshek, K. M., 1991, *Fundamentals of Machine Component Design,* 2nd Edition, John Wiley, New York.

81. Kay, S. M., 1993, *Fundamentals of Statistical Signal Processing: Estimation Theory*, Prentice Hall International Inc., New Jersey.

82. Khalil, M. and Topper, T. H., 2003, Prediction of crack-opening stress levels for 1045 as-received steel under service loading spectra, *Int. J. Fatigue*, Vol. 25, pp 149-157.

83. Khalil, M., DuQuesnay, D. L. and Topper, T. H., 2002, Prediction of crack-opening stress levels for service loading spectra, *Application of Automation Technology in Fatigue and Fracture Testing and Analysis*: Fourth Volume, ASTM STP 1411, edited by Braun, A. A., McKeighan, P. C., Nicolson, A. M. and Lohr, R. D., ASTM, West Conshohocken USA, pp 165-180.

84. Kliman, V, 1985, Fatigue life estimation under random loading using the energy criterion, *Int. J. Fatigue*, Vol. 7, No. 1, pp 39-44.

85. Lambert, R. G., 1976, Analysis of fatigue under random vibration, *The Shock and Vibration Bulletin*, Vol. 46.

86. Landgraf, R. W., 1987, Durability by design – an overview, In *Durability by Design: Integrated Approaches to Mechanical Durability Assurance of Ground Vehicles,* Passenger Car Meeting and Exposition, Dearborn, Michigan, USA, 19th-22nd October, pp 23-28.

87. Lee, Y-L., Raymond, M. N. and Villaire, M. A., 1995, Durability design process of a vehicle suspension component, *Journal of Testing and Evaluation (JTEVA)*, Vol. 23, No. 5, pp 354-363.

88. Leese, G. E. and Mullin, R. L., 1991, The role of fatigue analysis in the vehicle test simulation laboratory, *Recent Development in Fatigue Technology*, *SAE Transactions (SAE910166)*, Society of Automotive Engineers (SAE), pp 57-68.

89. Leser, C., 1993, *On Stationary and Nonstationary Fatigue Load Modeling Using Autoregressive Moving Average (ARMA) Models,* Ph.D. Thesis, Virginia Polytechnic Institute and State University, USA.

90. Leser, C., Juneja, L., Thangjitham, S. and Dowling, N. E., 1998, On multi-axial random fatigue load modeling, SAE 980696, paper presented in *SAE World Congress,* Detroit USA, 23rd – 26th February.

91. *Leyland Technical Centre (LTC),* Aston Way, Leyland, Preston, PR5 3TZ, United Kingdom.

92. Li, Q., Minnetyan, L. and Chamis, C. C., 2001, Computational simulation under PSD fatigue loading, *Proceedings of Structures Structural Dynamics and Materials Conference*, Seattle, USA, 16-19th April, pp 3147-3154.

93. Li, X., Dong, S. and Yuan, Z., 1999, Discrete wavelet transform for tool breakage monitoring, *Int. J. of Machine Tools & Manufacture*, Vol. 39, pp 1935-1944.

94. Lin, J. and Zuo, M. J., 2003, Gearbox fault diagnosis using adaptive wavelet filter, *Mechanical Systems and Signal Processing*, Vol. 17, No. 6, pp 1259-1269.

95. Lin, X. B. and Heyes, P. J., 1999, Some aspects of automotive durability analysis, *Fatigue '99, Proceedings of the Seventh International Fatigue Congress*, edited by Wu, X. R., and Wang, Z. G., Beijing, P.R. China, pp 2641-2646.

96. Liou, H. Y., Wu, W. F. and Shin, C. S., 1999, A modified for the estimation of fatigue life derived from random vibration theory, *Probabilistic Engineering Mechanics,* Vol. 14, pp 281-288.

97. Mann, J. Y., 1967, *Fatigue of Materials: An Introductory Text*, Melbourne University Press, Melbourne.

98. Manson, S. S., 1965, Fatigue: a complex subject – some simple approximation, *Experimental Mechanics*, Vol. 5, pp 193-226.

99. Marco, S. M. and Starkey, W. L., 1954, A concept of fatigue damage, *Transaction of the ASME*, Vol. 76, pp 627-632.

100. *Matlab User's Guide*, Matlab 5.2, The Math Works, 1998.

101. Matsuishi, M. and Endo, T., 1968, Fatigue of metals subjected to varying stress, *Proceedings of the Kyushu Branch of Japan Society of Mechanics Engineering*, Fukuoka, Japan (in Japanese), pp 37-40.

102. Memon, I. R., Zhang, X. and Cui, D., 2002, Fatigue life prediction of 3-D problems by damage mechanics with two block loading, *Int. J. Fatigue*, Vol. 24, pp 29-37.

103. Mercer, I., Malton, G. and Draper, J., 2003, The effect of user decisions on the accuracy of fatigue analysis from FEA, *16th Annual ABAQUS Users' Conference,* Munich, Germany, June 4-6.

104. Meyer, Y., 1993, *Wavelets: Algorithm and Applications*, SIAM, Philadelphia USA.

105. Miner, M. A., 1945, Cumulative damage in fatigue, *Journal of Applied Mechanics*, Vol. 67, pp A159-A164.

106. Mitchell, M. R., 1996, Fundamentals of modern fatigue analysis for design, *Fatigue and Fracture, ASM Handbook*, Vol. 19, ASM International, USA.

107. Morrow, D. and Vold, H., 1997, Compression of Time Histories Used for Component Fatigue Evaluation, SAE930403 in PT-67, in *Recent Developments in Fatigue Technology*, edited by Chernenkoff, R. A. and Bonnen, J. J., Society of Automotive Engineers (SAE), USA.

108. Morrow, J. D., 1968, *Fatigue Properties of Metal Fatigue Design Handbook*, Society of Automotive Engineers.

109. Neuber, H., *Kerbspannungslehre*, Springer-Verlag, Vienna, 1987 (Reprinted in translation as *Theory of notch stresses*, Springer Publisher, Berlin, 1958).

110. Newland, D. E., 1993, *An Introduction to Random Vibrations Spectral and Wavelet Analysis*, 3rd Edition, Longman Scientific and Technical, New York.

111. nSoft® User Manual, 2001, *nSoft V5.3 Online Documentation*, nCode International Ltd., Sheffield.

112. Oh, C-S., 2001, Application of wavelet transform in fatigue history editing, *Int. J. Fatigue,* Vol. 23, pp 241-250.

113. Palma, E. S. and Martins, M. G. M., 2004, Durability test analysis in a passenger vehicle, *Proceedings of the 12th International Conference on Experimental Mechanics (ICEM12)*, Bari, Italy, 29th August – 2nd September, paper no. 237.

114. Palmgren, A., 1924, Die Lebensdauer von Kugellagern, *Verfahrenstechinik*, Berlin, Vol. 68, pp 339-341.

115. Patsias, S., 2000, *Extraction of Dynamic Characteristics from Vibrating Structures Using Image Sequences,* Ph.D. Thesis, The University of Sheffield, United Kingdom.

116. Peterson, R. E., 1959, Notch sensitivity, in *Metal Fatigue*, edited by Sines, G. and Waisman, J. L., McGraw-Hill, New York, pp 293-306.

117. Peterson, R. E., 1974, *Stress Concentration Factors,* John Wiley & Sons, New York.

118. Plumtree, A. and Shen, G., 1990, Cyclic deformation and life prediction using damage mechanics, *Constitutive Laws of Plastic Deformation and Fracture*, edited by A.S. Krause et al, Kluwer Academic Publishers, The Netherlands, pp 77-85.

119. Pompetzki, M. A., 1993, *Variations in Fatigue Damage During the Measurement and Reconstruction of Service Load Histories,* Ph.D. Thesis, University of Waterloo, Canada.

120. Pompetzki, M. A., Topper, T. H. and DuQuesnay, D. L., 1990a, The effect of compressive underloads and tensile overloads on fatigue damage accumulation in SAE 1045 steel, *Int. J. Fatigue*, Vol. 12, No. 3, pp 207-213.

121. Pompetzki, M. A., Topper, T. H., DuQuesnay, D. L. and Yu, M. T., 1990b, Effect of compressive underloads and tensile overloads on fatigue damage accumulation in 2024-T351 aluminum, *Journal of Testing and Evaluation,* JTEVA, Vol. 18, No. 1, pp 53-61.

122. Qu, L. and He, Z., 1986, *Mechanical Diagnostics*, Shanghai Science and Technology Press, Shanghai, P. R. China.

123. Raath, A. D. and Van Waveren, C. C., 1998, A time domain approach to load reconstruction for durability testing, Engineering Failure Analysis, Vol. 5, No. 2, pp 113-119.

124. Ridder, R. L., Landgraf, R. W. and Thangjitham, S., 1993, Reliability analysis of an automotive wheel assembly, *SAE Transactions (SAE930406)*, Society of Automotive Engineers (SAE), pp 225-235.

125. Rotem, A., 1981, Accelerated fatigue testing method, *Int. J. Fatigue*, Vol. 3, No. 4, pp 211-215.

126. Shabana, A. A., 1998, *Dynamics of Multibody Systems*, John Wiley and Sons, New York.

127. Shang, D-G. and Yao, W-X., 1999, A nonlinear damage cumulative model for uniaxial fatigue, *Int. J. Fatigue*, Vol. 21, pp 187-194.

128. Shigley, J. E. and Mischke, C. R., 1989, *Mechanical Engineering Design*, 5th Edition, McGraw-Hill, New York.

129. Smith, K. N., Watson, P. and Topper, T. H., 1970, A stress-strain function for the fatigue of metals, *Journal of Materials*, JMLSA, Vol. 5, No. 4, pp 767-778.

130. Smith, R. A., 1999a, Fatigue in transport: Background, Solutions and Problems, *Fatigue '99, Proceedings of the Seventh International Fatigue Congress*, edited by Wu, X. R., and Wang, Z. G., Beijing, P.R. China, pp 2583-2590.

131. Smith, S. W., 1999b, *The Scientist and Engineer's Guide to Digital Signal Processing*, 2nd Edition, California Technical Publishing, San Diego.

132. Socie, D. F., 1977, Fatigue-life prediction using local stress/strain concept, *Experimental Mechanics,* Vol. 17, No. 2, pp 50-56.

133. Staszewski, W. J., 1998a, Structural and mechanical damage detection using wavelets, *The Shock and Vibration Digest*, Vol. 30, No. 6, pp 457-472.

134. Staszewski, W. J., 1998b, Wavelet based Compression and Feature Selection for Vibrational Analysis, *Journal of Sound and Vibration*, Vol. 211, No. 5, pp 735-760.

135. Stearns, S. D. and David, R. A., 1993, *Signal Processing Algorithms in Fortran and C*, Prentice-Hall, New Jersey.

136. Steinwolf, A., Giacomin, J. and Staszewski, W. J., 2002, On the need for bump event correction in vibration test profiles representing road excitations in automobiles, *Proc. of the Instn. of Mech. Engrs, Part D, Journal of Automobile Engineering*, Vol. 216, No. D4, pp 279-295.

137. Stephens, R. I., Dindinger, P. M. and Gunger, J. E., 1997, Fatigue damage editing for accelerated durability testing using strain range and SWT parameter criteria, *Int. J. Fatigue*, Vol. 19, pp 599-606.

138. Suresh, S., 1991, *Fatigue of Materials*, Cambridge University Press, Cambridge.

139. Tacer, B. and Loughlin, P. J., 1998, Nonstationary signal classification using the joint moments of time-frequency distributions, *Pattern Recognition*, Vol. 31, No. 11, pp 1635-1641.

140. Taheri, F., Trask, D. and Pegg, N., 2003, Experimental and analytical investigation of fatigue characteristics of 350WT steel under constant and variable amplitude loading, *Marine Structures*, Vol. 16, pp 69-91.

141. Taylor, D. and Wang, G., 2000, The validation of some methods of notch fatigue analysis, *Fatigue Fract. Engng. Mater. Struct.*, Vol. 23, pp 387-394.

142. Topper, T. H. and Lam, T. S., 1997, Effective strain-fatigue life data for variable amplitude loading, *Int. J. Fatigue*, Vol. 19, No. Supp. No.1, pp S137-S143.

143. Topper, T. H., DuQuesnay, D. L., Pompetzki, M. A. and Jurcevic, R., 1991, A crack closure based model for mean stress and overload effects on fatigue damage, *International Symposium on Fatigue Damage Measurement and Evaluation Under Complex Loadings,* Fukuoka, Japan, Vol. July.

144. Tucker, L. and Bussa, S, 1977, The SAE cumulative fatigue damage test program, In *Fatigue Under Complex Loading: Analysis and Experiments,* edited by Wetzel, R. M., Warrendale, PA, Society of Automotive Engineers, pp 3-14.

145. Veers, P. S., Winterstein, S. R., Nelson, D. V. and Cornell, C. A., 1989, Variable amplitude load models for fatigue damage and crack growth, in *Development of Fatigue Loading Spectra*, edited by Potter, J. M. and Watanabe, R. T., American Society for Testing and Materials (ASTM), Philadelphia, USA.

146. Vormwald, M. and Seeger, T., 1991, The consequences of short crack closure on fatigue crack growth under variable amplitude loading, *Fatigue Fract. Eng. Mater. Struct.*, Vol. 14, No. 3, pp 205-225.

147. Waisman, J. L., 1959, Factor affecting fatigue strength, in *Metal Fatigue*, edited by Sines, G. and Waisman, J. L., McGraw-Hill, New York, pp 7-39.

148. Walker, J. S., 1999, *A Primer on Wavelets and Their Scientific Applications*, Chapman & Hall/CRC, Boca Raton, USA.

149. Wang, C. H. and Brown, M. W., 1993, Inelastic deformation and fatigue under complex loading, in *Structural Mechanics in Reactor Technology: Transactions of the 12th International Conference on Structural Mechanics in Reactor Technology*, Vol. L, pp 159-170.

150. Wang, C. H. and Brown, M. W., 1996, Life prediction technique for variable amplitude multiaxial fatigue part 1: Theories, *Journal of Engineering Materials and Technology*, Vol. 118, pp 367-370.

151. Wang, Z. and Chen, Z. W., 1999, Influence of small load cycle omission on fatigue damage accumulation, *Fatigue '99, Proceedings of the Seventh International Fatigue Congress*, edited by Wu, X. R., and Wang, Z. G., Beijing, P.R. China, pp 1113-1118.

152. Wetzel, R. N., 1971, *A method for fatigue damage analysis*, Ph.D. Thesis, University of Waterloo, Canada.

153. Wheeler, O. E., 1972, Spectrum loading and Crack Growth, *J. Basic Eng., Trans. ASME*, Vol. D94, No. 1, pp 181-186.

154. Willenborg, J., Engle, R. M. and Wood, H. A., 1971, *A Crack Growth Retardation Model Using an Effective Stress Concept*, AFFDL TM-71-1-FBR.

155. Williams, C. R., Lee, Y. -L. and Rilly, J. T., 2003, A practical method for statistical analysis of strain-life fatigue data, *Int. J. Fatigue*, Vol. 25, pp 427-436.

156. Wöhler, A., 1860, Versuche über die Festigkeit der Eisenbahnwagenachsen, *Zeitschrift* für *Bauwesen,* Vol. 10; English summary*, Engineering*, Vol. 4, 1867, pp 160-161.

157. Woolman, J. and Mottram, R. A., 1969, *The Mechanical and Physical Properties of the British Standard EN Steels (B.S. 970-1955)*, compiled for the Steel User Service of the British Iron and Steel Research Association. - Vol.3: EN 40 to EN 363, Pergamon, Oxford.

158. Yan, J. H., Zheng, X. L. and Zhao, K., 2001, Experimental investigation on the small-load-omitting criterion, *Int. J. Fatigue*, Vol. 23, pp 403-415.

159. Yan, X., Cordes, T. S., Vogel, J. H. and Didinger, P. M., 1992, A property fitting approach for improved estimates of small cycle fatigue damage, *SAE Transactions (SAE920665),* Society of Automotive Engineers (SAE), Philadelphia USA.

160. Zheng, X., 2001, On some basic problems of fatigue research in engineering, *Int. J. Fatigue*, Vol. 23, pp 751-766.

APPENDIX A: Properties of BS 080A22 Steel

Table A.1: Designation of a steel specification according to BS 970-1 (1996).

Designation	Description
The first three digits	
000-199	Carbon and carbon-manganese steels.
200-240	Free cutting steels with sulphur content.
250	Silicon-manganese spring steels.
300-399	Stainless, heat resisting and valve steels.
500-999	Alloy steels in groups according to alloy type.
The fourth digit	
A	The steel will be supplied to close limits of chemical composition (no mechanical or hardenability properties specified).
H	A combination of hardenability and chemical analysis.
M	A combination of mechanical properties and chemical analysis.
S	A stainless steel specification.

Table A.2: Nominal chemical composition of BS 080A42 steel (BS 970-1 1996).

Carbon		Silicone		Manganese		Sulphur		Phosphorus	
min	max	min	max	min	max	min	max	min	max
0.40	0.45	0.05	0.35	0.70	0.90	-	0.060	-	0.060

Table A.3: Equivalent grades in the international standards (BS 970-1 1996).

BS	EN	SAE	AISI	DIN
080A42	EN8D	1042	C1042	17200

APPENDIX B: Rainflow Cycle Histogram of Six Test Signals

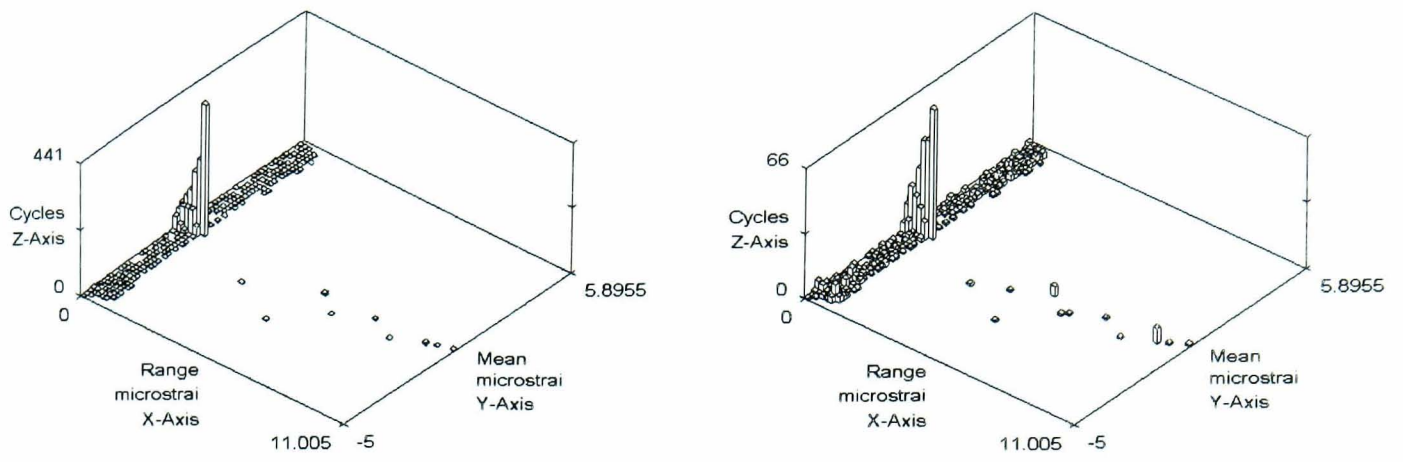

(a) (b)

Figure B.1: Rainflow cycle histogram: (a) T1, (b) T1BS1.

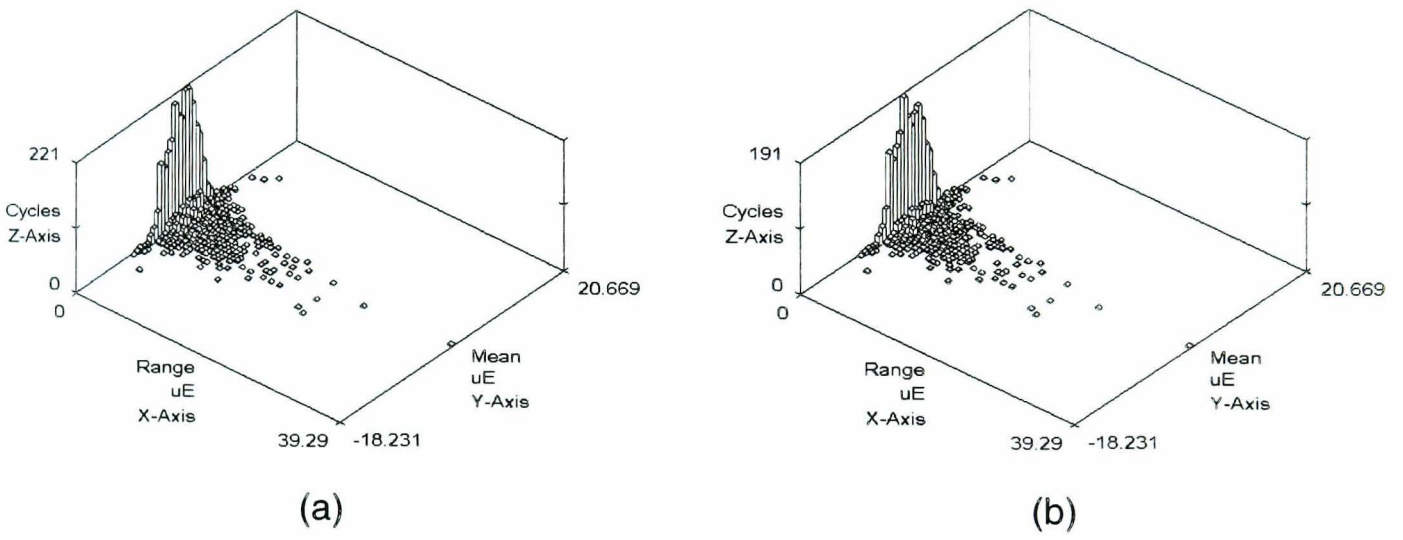

(a) (b)

Figure B.2: Rainflow cycle histogram: (a) T2, (b) T2BS1.

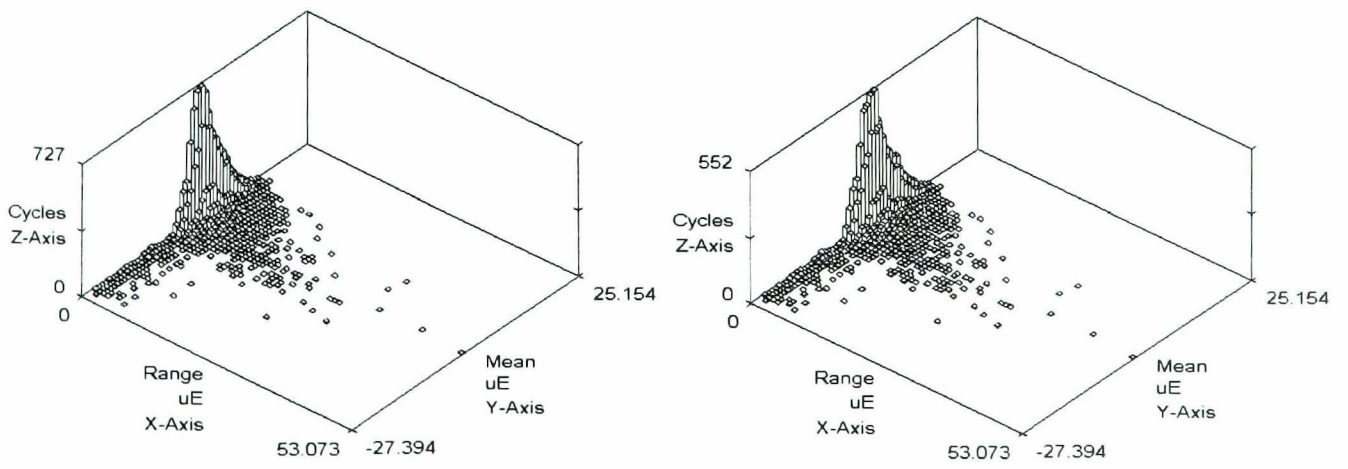

(a) (b)

Figure B.3: Rainflow cycle histogram: (a) T3, (b) T3BS1.

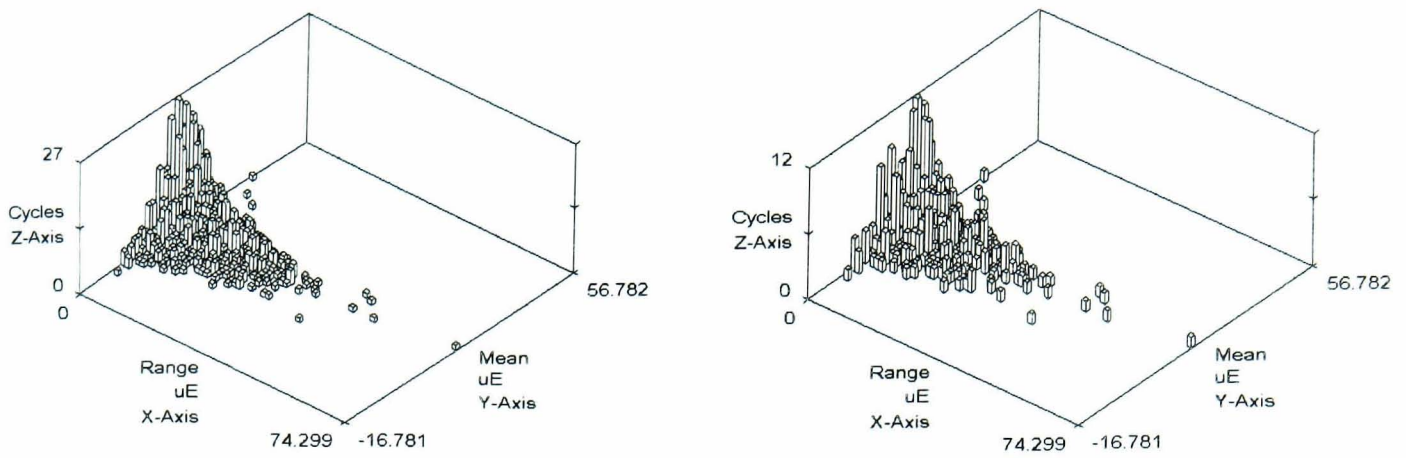

(a) (b)

Figure B.4: Rainflow cycle histogram: (a) T4, (b) T4BS1.

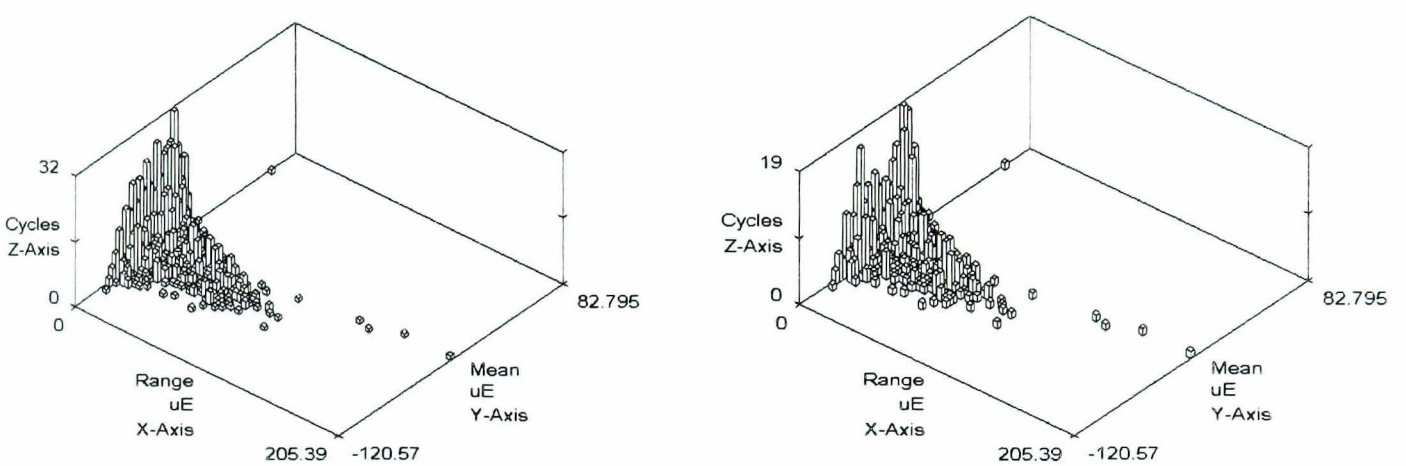

(a) (b)

Figure B.5: Rainflow cycle histogram: (a) T5, (b) T5BS1.

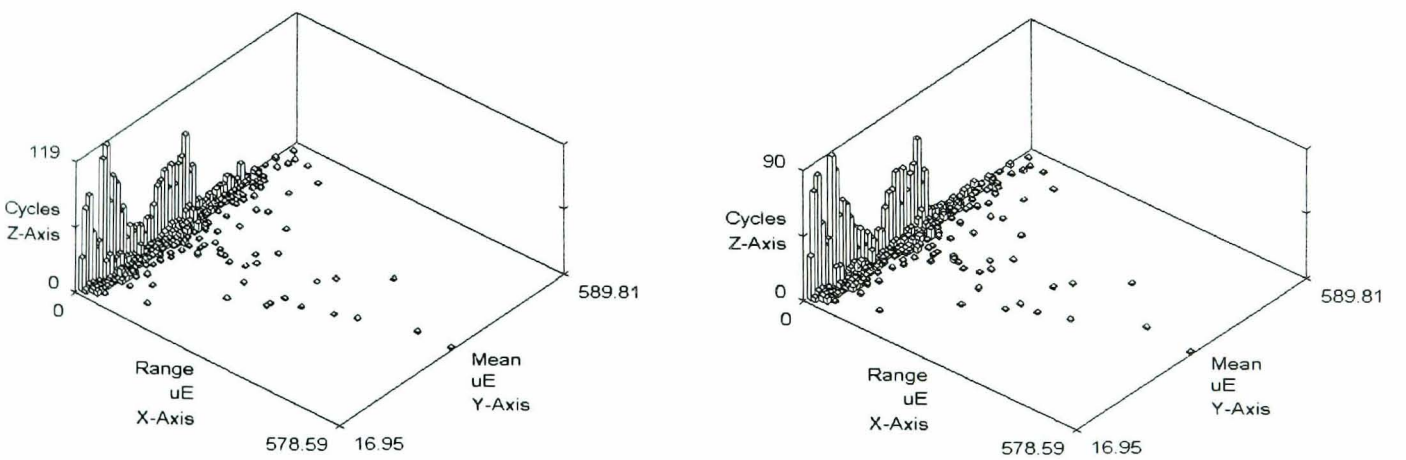

(a) (b)

Figure B.6: Rainflow cycle histogram: (a) T6, (b) T6BS1.